EE-M-MSFC-1774

Final Report

SPACE VEHICLE ENGINE AND HEAT SHIELD ENVIRONMENT REVIEW

SPACE VEHICLE ENGINE AND HEAT SHIELD ENVIRONMENT REVIEW

Volume I - Engineering Analysis

December 1973

BOEING ENGINEERING

Cummings Research Park • Huntsville, Alabama 35807

FINAL REPORT
EE-MSFC-1774

SPACE VEHICLE ENGINE AND HEAT SHIELD ENVIRONMENT REVIEW

VOLUME I - ENGINEERING ANALYSIS

By

W. B. McAnelly
C. T. K. Young, Ph.D.

December 1973

Prepared For

PROPULSION AND THERMODYNAMICS DIVISION
ASTRONAUTICS LABORATORY
GEORGE C. MARSHALL SPACE FLIGHT CENTER
HUNTSVILLE, ALABAMA

Contract No. NAS8-27802

Prepared By

ELECTRONICS AND ENGINEERING
TELEDYNE BROWN ENGINEERING
HUNTSVILLE, ALABAMA

ABSTRACT

Results, conclusions, and recommendations derived from an in-depth review of Saturn rocket base heat transfer are contained in three volumes.

- Volume I - Engineering Analysis - Discusses some of the theoretical and real aspects of the rocket base heat transfer problem. It presents an in-depth critique of the problems associated with instrumentation and measurements of the inflight base heat transfer; compares and discusses typical Saturn flight test, scale model test, and analytically generated base heating and environmental parameters. It also attempts to identify, delineate, and explain the differences between the experimentally observed and analytically produced results.

- Volume II - Engineering Data - Gives description of the Saturn flight vehicles, engine specifications, and operating parameters, descriptions of the base instrumentation and vehicle flight trajectories. The collected, normalized, and correlated Saturn flight test data is presented in this volume.

- Volume III - Flow Reversal Program - Discusses the theoretical aspects of the flow reversal program, and presents parametric comparison between the base environmental parameters and experimentally obtained results.

Approved:

N. E. Chatterton, Ph. D.
Manager
Research Department

TABLE OF CONTENTS - VOLUME I

TABLE OF CONTENTS - VOLUME I - Concluded

TABLE OF CONTENTS - VOLUME II

TABLE OF CONTENTS - VOLUME II - Concluded

TABLE OF CONTENTS - VOLUME III

LIST OF ILLUSTRATIONS

LIST OF ILLUSTRATIONS - Continued

LIST OF ILLUSTRATIONS - Continued

LIST OF ILLUSTRATIONS - Continued

LIST OF ILLUSTRATIONS - Continued

LIST OF ILLUSTRATIONS - Continued

LIST OF ILLUSTRATIONS - Continued

LIST OF ILLUSTRATIONS - Continued

LIST OF ILLUSTRATIONS - Concluded

LIST OF TABLES

LIST OF SYMBOLS

A	Area
C	Convective heat transfer correlation coefficient
C_p	Constant pressure specific heat
D	Discriminating streamline
E	Emissive power
F	View factor
$\mathfrak{F}$	Radiation interchange factor
g	Gravitational constant
h	Heat transfer coefficient
$I_{b\nu}$	Planck function
J	Boundary of undisturbed jet
K	Conductivity
ℓ	Mean beam length
M	Mach number
m	Reynolds number exponent
N	Refractive index
N_{nu}	Nusselt number
N_{pr}	Prandtl number
N_{re}	Reynolds number
N_{st}	Stanton number
n	Prandtl number exponent

O/F	Oxygen-to-fuel mixture ratio
P	Pressure
Q_n	Conduction heat transfer
q	Heat flux
R	Gas constant
R_o	Vehicle radius
r	Radius, gas temperature recovery factor
r'	Gas temperature recovery factor
S	Optical path
T	Temperature
u	Velocity
w	Weight
x	Characteristic dimension

Greek Symbols

α	Absorptivity
γ	Ratio of specific heats
ϵ	Emissivity
κ	Absorption coefficient
λ	Wavelength
μ	Dynamic viscosity
ν	Wave number

Greek Symbols - Concluded

ρ	Density, reflectivity
σ	Stephan-Boltzmann constant
τ	Time, transmissivity
τ'	Angular transmissivity without reflection
ω	Solid angle

Subscripts

b	Base
c	Convective heating, chamber
conv	Convective
eff	Effective
ex	Exit
f	Film
ir	Incident radiation
in	Net flux
ℓ	Phase Change
n	Normal
o	Stagnation condition
p	Plume
r	Recovery temperature
rr	Reradiation

Subscripts - Concluded

s	Surface, static condition
sen	Sensing element
std	Standard calo
w	Wall
∞	Ambient

EXECUTIVE SUMMARY

In current missile designs, it is common practice to form the main propulsive system by clustering together several rocket engines. The clustered engine concept is advantageous to many missile design disciplines in that it tends to optimize the vehicle. However, this design creates a very complex thermal fluid problem commonly referred to as the "Base Heating Problem". Heating of the base region results from radiation which is emitted by the high-temperature rocket exhausts and convection from gases circulating in the base region. As a result, a severe thermal environment usually exists in the base region. Vital engine components and sensitive base structure must be protected from this environment. This is accomplished by determining the thermal response of the components to the base environment and designing an adequate protection system. Since this must be accomplished prior to any flight tests, the ability to predict the environment is a necessity.

As a result of experience gained in the design of previous rocket vehicles, several methods of predicting the base region thermal environment have evolved. These can be generally categorized as:

- Scale model testing
- Extrapolation of previous and related flight test results
- Semiempirical analytical techniques.

A study of both the theoretical and experimental aspects of the problem will show, however, that all techniques are still in the development stage.

A NASA-funded review of the base heating experienced by the Saturn Apollo vehicles was initiated in July 1971. The objectives of this study were the following:

- Collect, review, correlate, and compare all relevant Saturn flight test, scale model test data, and analytically produced base environmental parameters

- Identify, delineate, and explain the deficiencies and differences in the experimental and analytical methodologies

- Develop improved analytical and experimental procedures for predicting and evaluating the base environment.

Results, conclusions, and recommendations derived from the study are contained in three volumes. The accomplishments and conclusions resulting from this study are summarized in the following paragraphs.

Pertinent Saturn vehicle flight and scale model test data were collected, correlated, compared, and are presented in the reports.

The review of the scale model test results indicated the following:

- Scale model testing of the type used during the Saturn program does not predict the full scale vehicle radiant environment (Note: The Saturn model test program was designed only to provide information about the convective environment.)

- Scale model testing tends to over-predict the convective environment

- Test results need to be scaled or otherwise altered in developing full-scale base thermal design criteria. At present, the scaling procedures produce uncertain predictions of full scale results.

- Scale model test data have been used with better results in establishing the design criteria for upper stages than for booster stages.

- Scale model tests have been found useful in establishing the relative effects of some of the off-nominal vehicle operating conditions (Note: Exceptions to this can be found.).

It was concluded that although scale model tests are expensive and often leave much to be desired in establishing the full-scale vehicle base thermal design criteria, if properly used, they can provide guidance and a degree of confidence in the technique which is being used.

Work associated with the analytical methodologies produced the following:

- A procedure for predicting the convective cooling during the aspiration phase of flight was developed. Comparisons with the flight test results are presented in the report.

- The computer technique for predicting the base environment during flow reversal was improved, expanded, and computed results compared to measured flight and scale model test data. The comparisons which are presented in the report generally indicate that the program tends to conservatively over-predict the base convective flux, over-predict the gas temperature, and under-predict the pressure. Coupled with the comparisons contained in the report, the flow reversal program should provide an alternate method for developing full-scale vehicle base design criteria.

- The use of NASA-developed gaseous radiation computer programs appears to offer an appropriate method for predicting plume radiation. However, this method is somewhat complicated and time-consuming.

- A simplified radiation prediction technique used successfully to predict the Saturn and Titan base radiation is easier to use, but requires a knowledge of the plume ground-level emissive power. A computer program was developed to compute the radiant flux in the base region using measured plume emissive power as input. Partially occluded plumes and blockage by nonparticipating surfaces can be included. The change in radiation with altitude is obtained by extrapolating results measured during flight tests of similar vehicles, which is one of the limitations with this technique.

- Studies of cryogenically cooled engines indicated that condensation of the exhaust gases along the engine wall can occur when the wall temperature is below the saturation temperature of the exhaust gases. The effects of condensation on the base environment could be significant.

Review of the flight test results produced the following:

- Useful qualitative and quantitative trends and characteristics can be obtained from the measured flight test data.

- All instruments used to measure the Saturn inflight base heat transfer parameters had the potential for erroneous indications. The quantitative accuracy of some of the instruments could not be determined with the information available.

- Techniques were developed for correcting some of the measured results. For future flight tests it is recommended that the instruments be calibrated in an environment similar to that anticipated during the flight, i.e., a combined radiant and convective environment. The necessary flight parameters can then be evaluated, approximately, from the calibration data.

The procedures and methodologies for predicting the base environment and developing thermal design criteria are basically developed; however, many of the complexities of the problem will never be significantly simplified. Many improvements can be made and further research is recommended. Areas and specific problems which should be studied are listed at the end of each section in Volume I of this report.

ACKNOWLEDGMENT

The results of this study and the data contained in the three volumes of the final report represent contributions by many individuals in addition to those listed on the title sheets. Specifically acknowledged are the NASA Marshall Space Flight Center technical sponsors: Messrs. C. C. Wood, J. L. Vaniman, R. R. Fisher, and D. E. Price. Former or present Teledyne Brown Engineering personnel are Dr. N. E. Chatterton, Mr. E. H. Ingram, Dr. T. S. Fu, Mr. T. D. Harper, and Mr. D. Allen. In addition to the above, a special acknowledgment is made to the Teledyne Brown Engineering Publications Department personnel for the difficult task of preparing the many illustrations and manuscript of these reports.

1. INTRODUCTION AND SUMMARY

1.1 INTRODUCTION

In current missile designs, it is common practice to form the main propulsive system by clustering together several rocket engines. Figure 1-1 shows two typical arrangements which have been employed. The clustered engine concept is advantageous to many missile design disciplines, in that it tends to optimize the vehicle by resulting in a relatively compact, minimum weight, and dynamically stable system. However, this design creates a very complex thermal-fluid problem commonly referred to as the "Base Heating Problem". The heating results from the radiation emitted by high-temperature rocket exhausts and convectively from gases circulating in the base region. This phenomenon is shown schematically in Figure 1-2. In summary, the heating in the base region varies significantly with altitude and can be characterized as follows: at low altitudes, the supersonic exhausts, in conjunction with the freestream flow, pulls the ambient air into the base region which provides cooling to offset the usually high thermal radiation. At high altitudes, where the ambient pressure is low, the exhaust jets expand and interaction between adjacent engine plumes occurs. This causes some of the high-temperature exhaust gases to reverse back into the base region, resulting in convective heating. Generally, heating rates and gas temperatures in the base region are relatively high, and fluxes of 10 to 30 Btu/ft^2-sec and temperatures of 2,000°F are not uncommon.

As a result of the severe thermal environment, vital engine components and sensitive base structure must be protected. This is accomplished by determining the thermal response of the components to the base thermal environment and designing an adequate protection system.

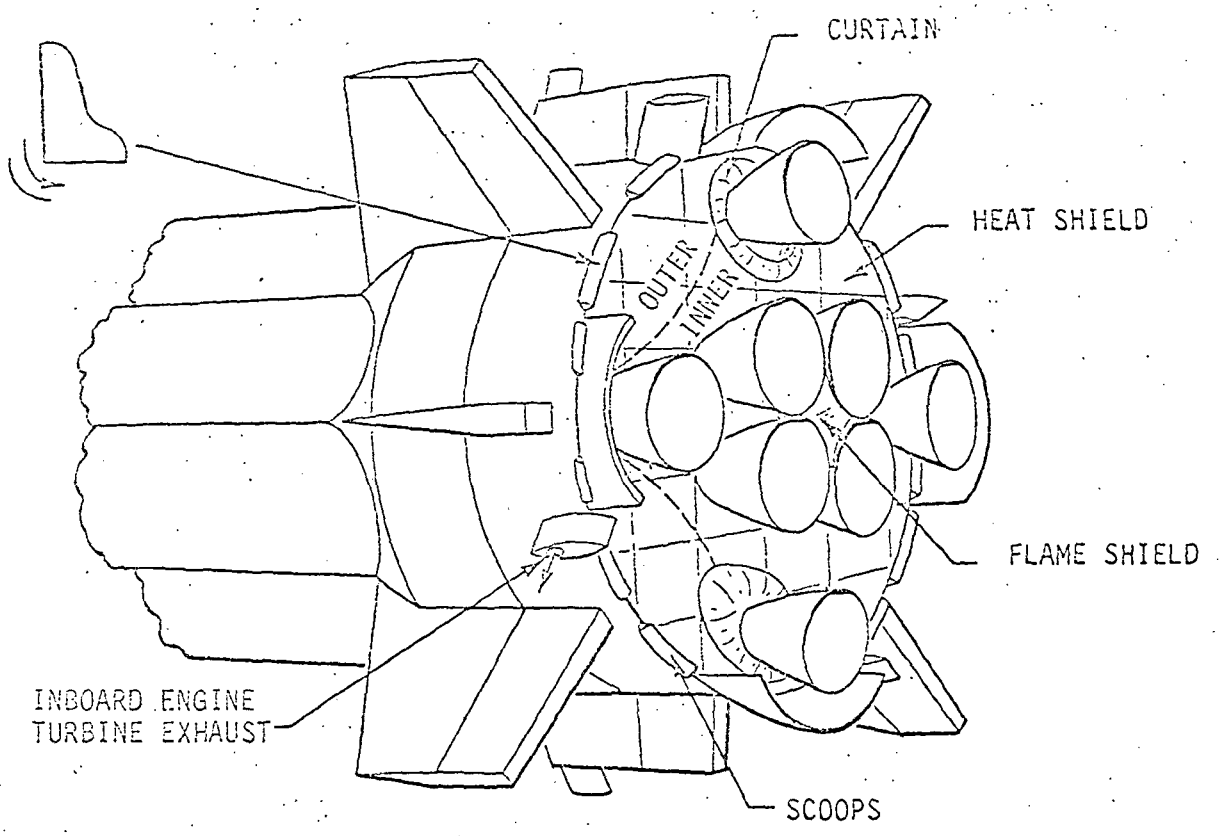

SATURN S-1 BASE REGION

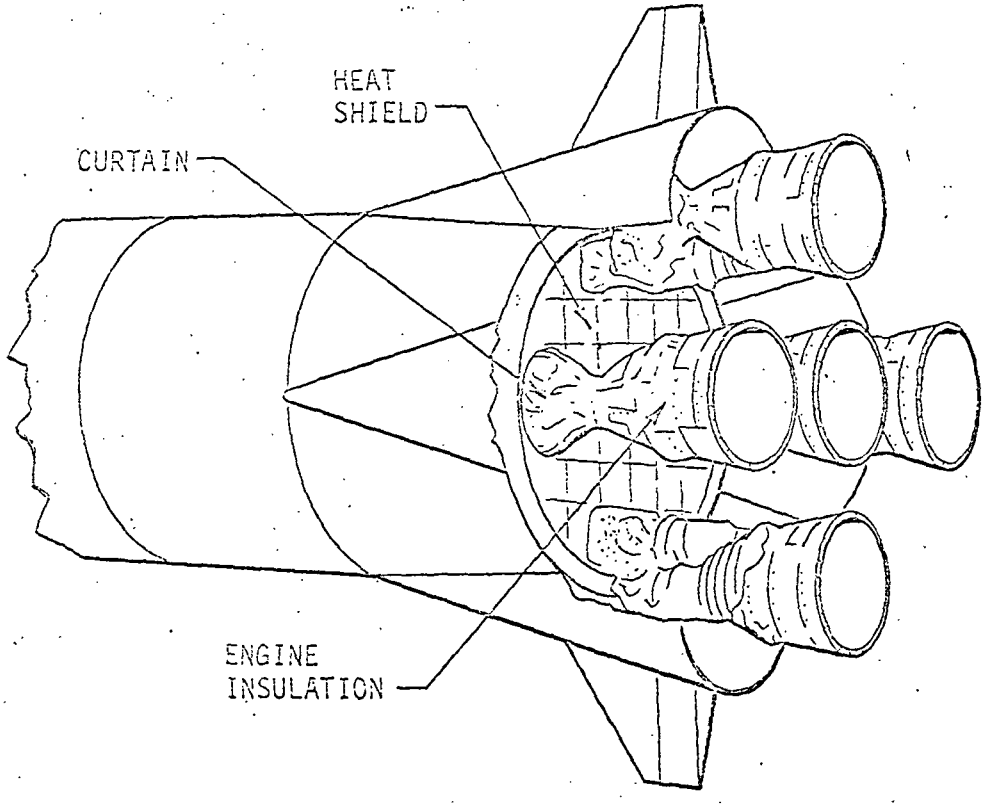

SATURN S-1C BASE REGION

FIGURE 1-1. TYPICAL MULTIENGINE CONFIGURATIONS

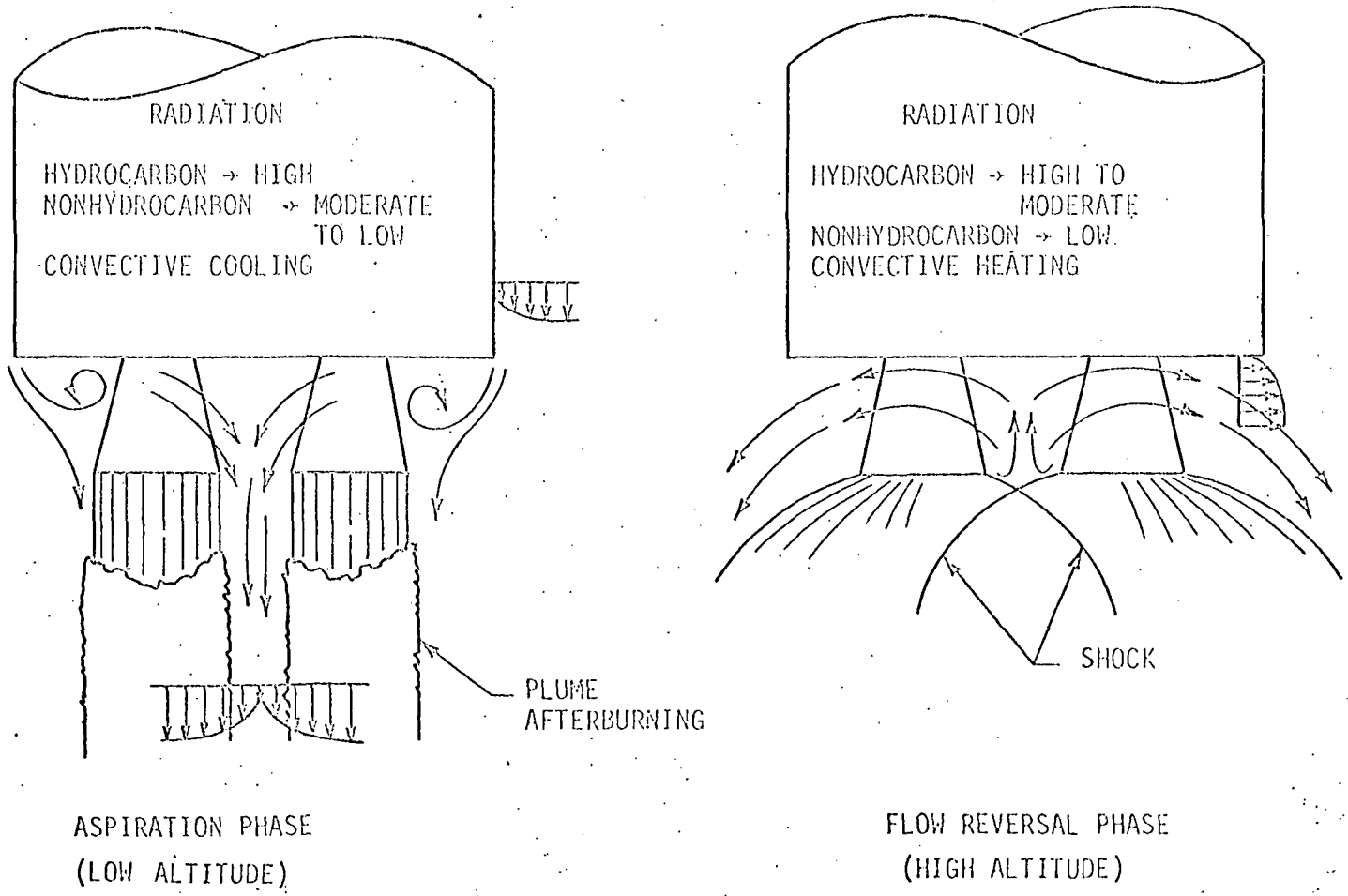

ASPIRATION PHASE
(LOW ALTITUDE)

FLOW REVERSAL PHASE
(HIGH ALTITUDE)

FIGURE 1-2. BASE FLOW REGIMES

Since this must be accomplished prior to any flight tests, the ability to predict the environment is a necessity. Unfortunately, because of the very complex nature of the base heating problem, the predictability of the environment is very limited, even though much time and money have been devoted to researching the various aspects of the problem during the past 10 years.

As a result of previous efforts, several methods of predicting the base region thermal environment have evolved. These methods can be generally categorized as: 1) Scale model testing; 2) Extrapolation of previous and related flight test results; 3) Semi-empirical analytical techniques.

However, in studying both the theoretical and experimental aspects of the problem, it becomes obvious that all techniques for predicting the base heat transfer are still in the development stage. This is not surprising when the extremely complex nature of the problem is considered. The theories associated with such problems as fully separated and interacting three-dimensional compressible viscous fluid flows, multiphase turbulent and chemically reacting boundary layers and coupled radiation, and convection and conduction heat transfer (to mention just a few) are currently limited and complicated. However, these problems are commonly encountered in the base heating problem. In the development of the analytical techniques, these complex problems are solved using much simpler theories which ultimately introduce inaccuracies into the calculated results. The basic idea in the analytical model development is to approximate the insolvable problems by simple theories and then to adjust the computed results until agreement with experimental results is obtained. Thus, the final analytical model would be a semi-empirical solution to the problem. Trouble is encountered using this approach when considering the experimental data which is to be used as the basis for modifying the

analytical model. If scale-model test results are used, these results often do not agree with the flight test results because of the inability to simulate full-scale vehicle conditions. The flight test results, on the other hand, are suspected of being in error at various times during the flights. As a result, if the analytical models are forced to agree with the available experimental data, a general solution of the base heating problem is not obtained. What does emerge is a model which fails to properly predict the environment for vehicle configurations which are significantly dissimilar.

Other factors also contribute to the general lack of base heat transfer predictability. Such realistic factors as multiphase (i.e., engine wall condensation) engine boundary layers, surfaces with temperatures controlled by cryogenic liquids, and water absorption by porous heat shield materials appear to affect the base environment directly. These factors are not the same on all vehicles, and the predictability of the effect is often speculative.

1.2 SUMMARY

In this study all available analytical techniques, Saturn flight test results and scale-model test data were to be reviewed. The purpose of this review was to determine how well these results agree

to provide guidance in establishing acceptable techniques for

ating the base thermal environment and base thermal protection

- Task 1 - Review of Analytical Methods and Evaluation of Important Parameters - All available analytical methods (for both solid and liquid propellant systems) for calculation of base heating data were reviewed and evaluated. The validity of assumptions made in the analytical methods was investigated. The most influential parameters were determined. Condensation, turbine exhaust gas injection, shroud, chemical kinetics, and other effects that may influence base heating were considered.

- Task 2 - Evaluation of Computer Programs - Available computer programs and manuals for calculation of base heating were reviewed. Representative analytical methods and Teledyne Brown Engineering's base heating manual were used to generate analytical data for Saturn vehicles which were compared with flight and experimental data in Task 6.

- Task 3 - Collection and Review of Experimental and Flight Data - All available Saturn I, IB, and V flight data, static test data, and scale model test data, including both hot and cold flow tests, were collected and reviewed. These data were separated and categorized for the required correlations, scaling, and corrections which were performed in Tasks 4 and 5.

- Task 4 - Correlation of Flight and Experimental Data - Measured data associated with each stage (Saturn I, IB, and V) that best characterizes the base heating phenomenon were selected for evaluation. Off-nominal conditions were identified and investigated. Data correlation, correction, and comparison techniques were studied. Errors associated with measurements and instrumentation were investigated. The most suitable technique was used to correlate and compare the measured data. Factors which cause correlation deficiencies and which create off-nominal conditions were identified and investigated.

- Task 5 - Scaling of Model Test Data - All existing scaling methods were reviewed and evaluated. The deficiencies of existing scaling methods were determined and improvements made. The model test data were then scaled (by the best available scaling method) to full-scale flight data.

- Task 6 - Comparisons of Data, Conclusions, and Recommendations - The analytical data from Task 2, the correlated flight and experimental data from Task 4, and the scaled model test data from Task 5 were compared and studied. Base heating rates, recovery temperatures, base pressures, and other variables or phenomenon, e.g., condensation effects, found to be important in the study were included in the comparisons. The objective of these comparisons is to explain the large differences between predicted and flight base heating data.

- Task 7 - Preparation of Final Report - A final technical report that describes in detail the results, conclusions, and recommendations of the base heating studies has been prepared.

In Section 2, the basic theoretical aspects of the rocket base heating problem are discussed. The fundamental equations, which show in simple terms what must be known in order to arrive at an analytical solution of the base heating problem, are discussed.

In Section 3, the problems associated with the instrumentation used to measure the inflight base heat transfer are discussed. The design of accurate instruments for measuring the base heat transfer is a difficult problem which has not been solved. Many of the instruments used during the Saturn flight tests had the potential for error and appear to have produced measured results which cannot be completely correlated and evaluated.

In Section 4, some typical Saturn flight test results are compared, analyzed, and discussed.

In Section 5, the scale model test results are compared to the measured flight data and discussed.

Base heat transfer diagnostic and prediction techniques are discussed in Section 6. Base heat transfer environmental parameters predicted by some of the analytical techniques are compared to the scale model and flight test results.

During the course of the study, several quarterly progress reports were published and are listed as References 1-1 through 1-6. Additional information concerning the Saturn base heat transfer can also be obtained from Reference 1-7.

REFERENCES - SECTION 1

1-1. Young, C. T. K., W. B. McAnelly, and E. H. Ingram, "Space Vehicle Engine and Heat Shield Review", Teledyne Brown Engineering 1st Quarterly Report SE-MSFC-1431, October 1971

1-2. McAnelly, W. B., C. T. K. Young, and T. D. Harper, "Space Vehicle Engine and Heat Shield Environment Review", Teledyne Brown Engineering 2nd Quarterly Report SE-MSFC-1461, January 1972

1-3. McAnelly, W. B. and T. D. Harper, "Space Vehicle Engine and Heat Shield Environment Reveiw", Teledyne Brown Engineering 3rd Quarterly Report SE-MSFC-1514, April 1972

1-4. McAnelly, W. B. and T. D. Harper, "Space Vehicle Engine and Heat Shield Environment Review", Teledyne Brown Engineering Interim Report SE-MSFC-1592, July 1972

1-5. McAnelly, W. B., T. S. Fu, and T. D. Harper, "Space Vehicle Engine and Heat Shield Environment Review", Teledyne Brown Engineering Fourth Quarterly Report SE-MSFC-1655, October 1972

1-6. McAnelly, W. B. and T. S. Fu, "Space Vehicle Engine and Heat Shield Environment Review", Teledyne Brown Engineering Fifth Quarterly Report, SE-MSFC-1682, January 1973

1-7. Mullen, C. R., R. L. Bender, R. L. Bevill, J. Reardon, and L. Hartley, "Saturn Base Heating Handbook", NASA-CR-61390, May 1, 1972

2. DISCUSSION OF THE BASE HEATING PROBLEM

2.1 BASIC HEAT TRANSFER CONSIDERATIONS

The heat transfer to the base of a clustered-engine rocket vehicle is a result of incident thermal radiation and convection combined with the conduction, heat storage, reradiation, and possibly phase changes associated with the base region materials. Consider the differential material volume arbitrarily located in a base region as shown in Figure 2-1. The differential area, dA_s, is assumed to be exposed to the convective flux, q_c, and to the radiant flux, q_{ir}. Assuming that the material is a porous medium, such as an insulation that could have absorbed moisture, the phase change which would take place as the material is heated at the saturation temperature represents an energy loss, q_ℓ. The reradiation, q_{rr}, from the surface to the surroundings will also represent an energy loss. A simply energy balance shows that the net heat crossing the unit differential area, dA_s, is

$$q_{in} = q_c + \alpha q_{ir} - q_l - q_{rr} \qquad (2\text{-}1)$$

where

q_{in} - net heat flux crossing dAs

q_c - convective heat flux

q_{ir} - incident radiant flux

q_{rr} - reradiation flux

q_l - heat loss by phase change

α - surface absorptivity.

The temperature of the differential volume can be computed by solving Equation 2-2, the Fourier conduction equation:

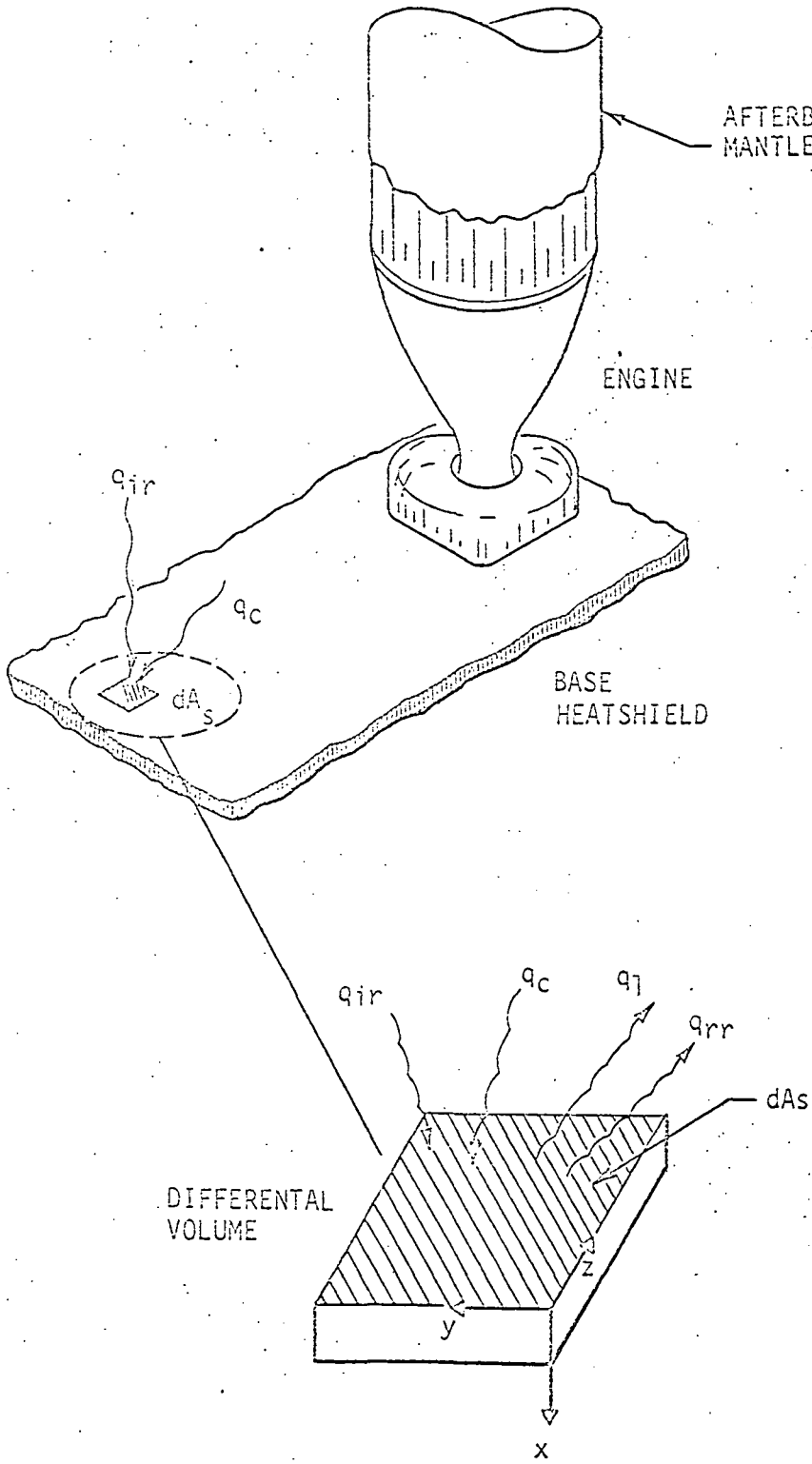

FIGURE 2-1. DIFFERENTIAL VOLUME ELEMENT

$$\rho c_p \frac{\partial T}{\partial \tau} = \nabla(k \nabla T) + Q_l \qquad (2\text{-}2)$$

$$= \frac{\partial}{\partial x}\left(k \frac{\partial T}{\partial x}\right) + \frac{\partial}{\partial y}\left(k \frac{\partial T}{\partial y}\right) + \frac{\partial}{\partial z}\left(k \frac{\partial T}{\partial z}\right) + Q_l$$

where

ρ - density

c_p - specific heat

T - temperature

τ - time

k - thermal conductivity

Q_l - heat lost by phase change or gained because of heat generation.

Equation 2-1 is related to Equation 2-2 through the boundary conditions of the problem. For example, the conduction heat flux is defined as

$$q_x = - k \frac{\partial T}{\partial x} \; . \qquad (2\text{-}3)$$

At the surface, dAs (see Figure 2-1), this is equal to the heat flux entering the volume element and gives the boundary condition;

$$q_x\Big)_{x=0} = - k \frac{\partial T}{\partial x}\Big)_{x=0} = q_{in} \qquad (2\text{-}4)$$

$$= q_c + \alpha q_{ir} - q_l - q_{rr} \; .$$

Normally Equation 2-2 cannot be solved by closed-form integration for complicated heat transfer problems. As a result, most problems are solved using a computer program such as the Chrysler Improved Numerical Differencing Analyzer (CINDA). This particular program is very versatile and has the capabilities to include the effects of phase change heat losses. With regard to Equations 2-2 and 2-4, the driving potential which causes the heat transfer is the convective and the radiant heat flux. As opposed to this, in a transient problem, the conduction, reradiation, and the heat loss by phase change are controlled mostly by the internal properties of the material. With respect to base heat transfer, it is usually the convective and radiant heating rates which are the most difficult to specify.

2.2 BASIC PARAMETERS IN CONVECTIVE HEAT TRANSFER

To show what must be known in order to specify the convective flux, consider the following. The convective flux is defined by Newton's law of cooling as

$$q_c = h\,(T_r - T_w) \tag{2-5}$$

where

h - heat transfer coefficient

T_r - gas recovery temperature

T_w - surface temperature.

Also, it is known that the convective coefficient can be derived using a modified form of the Reynolds analogy given as,

$$N_{nu} = C\,N_{re}^{m} N_{pr}^{n} \tag{2-6}$$

where

N_{nu} - Nusselt number = hx/k

N_{re} - Reynolds number = $\rho ux/\mu$

N_{pr} - Prandtl number = $\mu c_p/k$

C, m, n - experimentally determined coefficients

and

x - characteristic dimension

k - thermal conductivity

ρ - gas density

u - velocity

μ - dynamic viscosity

c_p - specific heat.

Because convective heat transfer is a boundary layer problem, property gradients exist between the outer fluid and that near the wall. As a result, the evaluation of the transport properties is dictated by correlating experimental data using Equation 2-6. The coefficients c, m, n are also determined as a result of this correlation. Thus, it can be said that solutions to the convective heating are always semi-empirical.

Substitution of the physical quantities into Equation 2-6 gives

$$h = (C) \cdot \left(\frac{C_p^{\,n} k^{1-n} \rho^m u^m}{\mu^{m-n}} \right) \cdot \left(x^{m-1} \right) \quad (2\text{-}7)$$

Further simplification of Equation 2-7 is possible if the velocity, u, and the density, ρ, can be related to the local freestream variables,

using ideal gas and isentropic relations. Then,

$$\rho = \frac{P_s}{R\,T_s} \tag{2-8}$$

and

$$u = M\,(\gamma g R T_s)^{\frac{1}{2}} \tag{2-9}$$

$$= \left\{ \frac{2\gamma}{\gamma-1} \left[\left(\frac{P_o}{P_s} \right)^{\frac{\gamma-1}{\gamma}} - 1 \right] g R T_s \right\}$$

where

P_s - static pressure

P_o - total pressure

T_s - static temperature

γ - ratio of specific heats

R - gas constant

M - local Mach number

g - gravitational constant.

Then, using the isentropic relation

$$\frac{T_o}{T_s} = \left(\frac{P_o}{P_s} \right)^{\frac{\gamma-1}{\gamma}} \tag{2-10}$$

where T_o is the total temperature, Equation 2-7 can be written as

$$h = \left[C(2g)^{m/2}\right] \cdot \left[\frac{C_p{}^{n} k^{1-n} \left(\frac{\gamma}{\gamma-1}\right)^{m/2}}{R^{m/2} \mu^{m-n}}\right] \qquad (2\text{-}11)$$

$$\cdot \left(x^{m-1}\right) \cdot \left\{\frac{P_s}{T_o} \left(\frac{P_o}{P_s}\right)^{\frac{\gamma-1}{\gamma}} \left[\left(\frac{P_o}{P_s}\right)^{\frac{\gamma-1}{\gamma}} - 1\right]\right\}^{m/2}$$

which is

$$h = \begin{pmatrix}\text{constant}\\ \text{terms}\end{pmatrix} \cdot \begin{pmatrix}\text{transport}\\ \text{properties}\end{pmatrix}$$

$$\begin{pmatrix}\text{characteristic}\\ \text{dimension}\end{pmatrix} \cdot \begin{pmatrix}\text{flow field}\\ \text{properties}\end{pmatrix} .$$

Equation 2-11 represents only one of the many relations which are possible. This equation relates the heat transfer coefficient to the most basic properties of the flow. The computation of the heat transfer coefficient using Equation 2-11 requires the following knowledge:

- The type of fluid must be known in order to evaluate the transport properties C_p, k, μ, γ, and R
- The flow field must either be known or be possible to compute in order to specify the thermodynamic properties P_s, P_o, T_o, and T_s
- The coefficients c, m, n and characteristic dimension, x, must be known or assumed.

The latter implies that some geometrically similar problem must have been investigated and correlated using Equation 2-6.

With respect to the base heating problem, the following characteristics are known:

- Because the base flow changes throughout the flight, all terms on the right side of Equation 2-11 are transient
- The gas in the base region during the aspiration phase of the flight consists primarily of the free-stream ambient air
- During the flow reversal phase, the base gases consist primarily of the reversed engine exhaust products
- Regardless of how it is accomplished, a base gas temperature and a component surface temperature must be determined in order to solve Equation 2-1.

Therefore, because the transport properties are primarily a function of temperature, it can be assumed that these properties will be known when a solution is possible. Knowing this fact, the functional relations can be written

$$q_c(\tau) = f[\, h(\tau),\ Tr(\tau)\,] \qquad (2\text{-}12)$$

where

$$h(\tau) = f[\, c,\ m,\ n,\ P_o,\ P_s,\ T_o,\ x] \qquad (2\text{-}13)$$

or

$$h(\tau) = f[\, c,\ m,\ n,\ P_s,\ T_s,\ u,\ x]$$

and

$$Tr(\tau) = f[T_o(\tau)] \quad . \qquad (2\text{-}14)$$

The relations on the right side of Equation 2-13 are also time-dependent.

Equations 2-12 through 2-14 are by no means a major simplification. However, these equations do show, in simple terms, what must be known to derive an analytical solution. The analytical model must be devised so that the transient values of the pressure (P_o, P_s) and temperature (T_o, T_r) can be evaluated from the known vehicle and thermodynamic conditions. Also, the available experimental data must be correlated (using Equation 2-6) to determine c, m, n, and the characteristic dimension x.

2.3 ASPIRATION PHASE CONVECTIVE COOLING

After engine ignition and release, the vehicle rises through the atmosphere with increasing velocity. During the first phase of the ascent, the supersonic exhaust jets, in conjunction with the freestream, tend to create an ejector effect in the base region (see Figure 1-2). This action pulls the ambient air into the base region. The ambient air's having a relatively low total temperature during this phase of the flight provides a source of convective cooling to offset the usually high radiation. The aspiration phase usually persists only at low altitudes during the first half of the flight. Because of its positive effects, convective cooling has been largely ignored in base region thermal analyses. However, some attempts have been made to more effectively utilize this potential by placing scoops and flow deflectors around the base of the vehicle (see Figure 1-1). The development of an engineering model of the convective cooling during this phase will be discussed in another section of this document.

2.4 FLOW REVERSAL PHASE CONVECTIVE HEATING

At high altitudes, where the ambient pressure is low, the exhaust jets expand until interactions between adjacent engine plumes occur. As a result of these interactions a very complex shock structure and flow

field is established (see Figure 2-2). Briefly, what happens is the following.

As the supersonic jet leaves the nozzle, turbulent mixing between the jet-free boundary and the surrounding gas takes place. As the jet approaches the impingement point, the mixing zone has spread to a relatively thick layer. Because of the momentum exchange associated with the mixing porcess, the velocity (and, therefore, the streamwise momentum) varies significantly across the mixing layer. As the flow approaches the impingement point, some of the low-energy gases in the mixing layer cannot penetrate the oblique shock wave and are therefore reversed.

The criteria which establishes the portion of the mixing layer which is reversed is to determine the minimum energy streamline (i.e., the discriminating "D" streamline in Figure 2-2) which can penetrate the shock. This can be established by finding the streamline with a stagnation pressure equal to the static pressure behind the oblique shock. Likewise, the location of the undisturbed jet boundary (i.e., "J" streamline in Figure 2-2) determines if any of the main jet is reversed. If the "J" streamline of Figure 2-2 has a stagnation pressure greater than that of the discriminating "D" streamline, then the net flow is out of the base region (i.e., no flow is reversed). However, when the "J" streamline stagnation pressure is less than that of the "D" streamline, then the high-energy main jet exhaust gases are reversed back into the base region.

This criteria was developed by studying two-dimensional flow across a rearward facing step. Chapman (Ref. 2-1), studying laminar flow, was the first to develop a theoretical model of the flow reversal mechanism. Korst, et al (Ref. 2-2) developed a similar model for turbulent flows. Goethert (Ref. 2-3), studying flow reversal from clustered rocket engines, was the first to apply these theoretical models

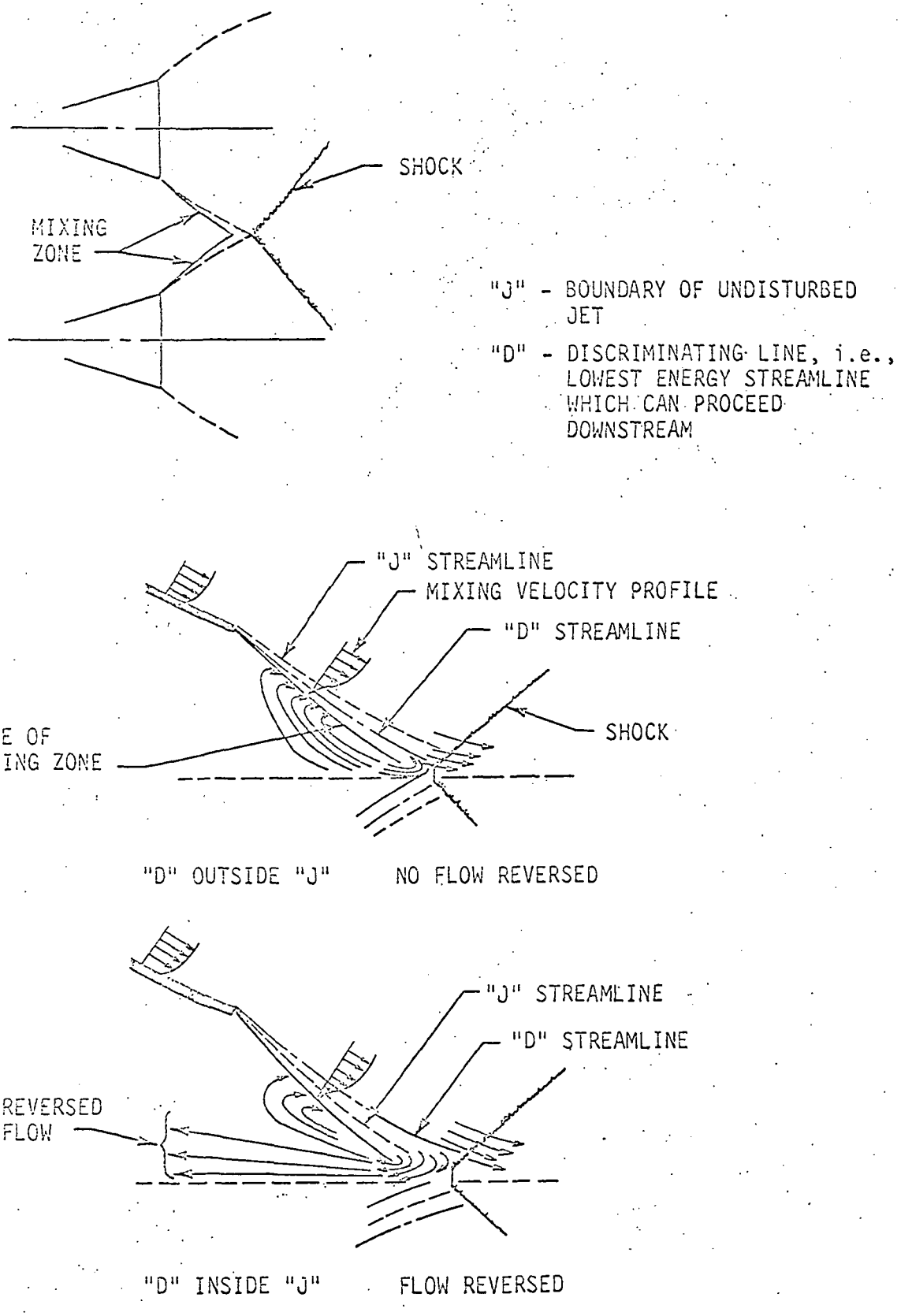

FIGURE 2-2. FLOW REVERSAL CONDITIONS

directly to the rocket base flow problem. The use of back step flow models as diagnostic techniques for predicting the base environment has not received wide acceptance because of disagreements obtained with equivalent experimental results. One of the reasons cited is that in order to apply the relatively simple two-dimensional back step flow model to the very complex three-dimensional rocket base flow reversal problem, many significant simplifications and approximations must be made. These are thought to introduce errors in the computed results.

One of the tasks of this study was to determine the accuracy and utility of the flow reversal analytical models. For this purpose, a computer program was developed and is discussed in detail in Volume III of this report. Comparison between the analytical flow reversal model and the measured results obtained during scale model and flight test are shown in Section 6 and in Volume III of this report.

2.5 PLUME RADIATION

The thermal radiation emitted by rocket exhausts depends on many factors. The basic factors are associated with the propellant combinations and engine operating conditions. To achieve maximum specific impulse (thrust-to-mass-flow ratio), engine operating conditions are required which directly influence the plume radiation. For liquid-propellant engines, the maximum specific impulse is obtained when the mixture ratio is fuel rich. For solid-propellant motors, metallic particles are mixed with the fuel to increase the specific impulse. Large liquid engines also have very fuel-rich turbopump gases discharged into the outer periphery of the main exhaust streams near the exits. As a result, liquid engines discharge large amounts of excess

fuel which can and do mix with the ambient air and burn under the correct conditions. The afterburning appears to be quite significant at low altitudes and produces a high temperature mantle which surrounds the exhaust plumes. At high altitudes, the afterburning either decreases to a very low level or ceases altogether. For liquid engines where the fuel is a hydrocarbon (RP-1), the chemically inefficient combustion process (i.e., excess fuel) taking place within the engine system produces significant amounts of particulate carbon (soot). This condition, in conjunction with the afterburning, causes the plumes to radiate similarly to a high-temperature blackbody. Because of the solid particles, the radiation from large, hydrocarbon-fueled engines and solid-propellant engines is similar. If the fuel is a nonhydrocarbon (hydrogen), the exhaust gases are semiopaque and the radiation is, therefore, much lower.

Rocket exhaust plumes are nonisothermal, nonisobaric, and nonhomogeneous gas bodies. The equation which governs such a radiating gaseous body is (see Figure 2-3)

$$q_{ir} = \int_{\nu} \int_{\omega} \int_{s} \rho \, \kappa_{\nu} \, I_{b\nu} \exp\left(- \int_{s} \rho \, \kappa_{\nu} \, dS'\right) \cdot \cos \phi \, dS \, d\omega \, d\nu \qquad (2\text{-}15)$$

where

q_{ir} - incident radiant flux

ρ - local density

κ_{ν} - spectral absorption coefficient

$I_{b\nu}$ - Planck function

S - optical path

ω - solid angle

ν - wave number

ϕ - see Figure 2-3.

Computer programs for calculating the rocket exhaust plume radiation using Equation 2-15 are available (see Reference 2-4 for example). However, the computer programs require, as input, the complete spatial definition of all thermodynamic and radiation properties along all optical paths. This type of information is seldom available and is difficult to generate theoretically for multiple plumes with afterburning.

For an isothermal, isobaric, and homogeneous gas, Equation 2-15 can be reduced to

$$q_{ir} = E_b \epsilon_p \int_{A_p} F_{dAs - dAp} \tag{2-16}$$

where

$E_b = \sigma T_p^4$ - plume blackbody emissive power

$\epsilon_p = f(T_p, \rho, \ell)$ - effective volumetric gas emissivity

$F_{dA_s - dA_p} = \frac{\cos \phi \, d\omega}{\pi}$ - view factor between dA_s and dA_p

T_p - plume temperature

ℓ - mean beam length.

To derive Equation 2-16, the emissivity was assumed to be a function of the gas temperature, density, and some characteristic dimension (ℓ) of the gaseous body. This concept developed by H. C. Hottel is discussed in most engineering heat transfer texts. The characteristic dimension for circular cylinders and spheres can be obtained from Reference 2-5. The restriction that the gas is isothermal, isobaric,

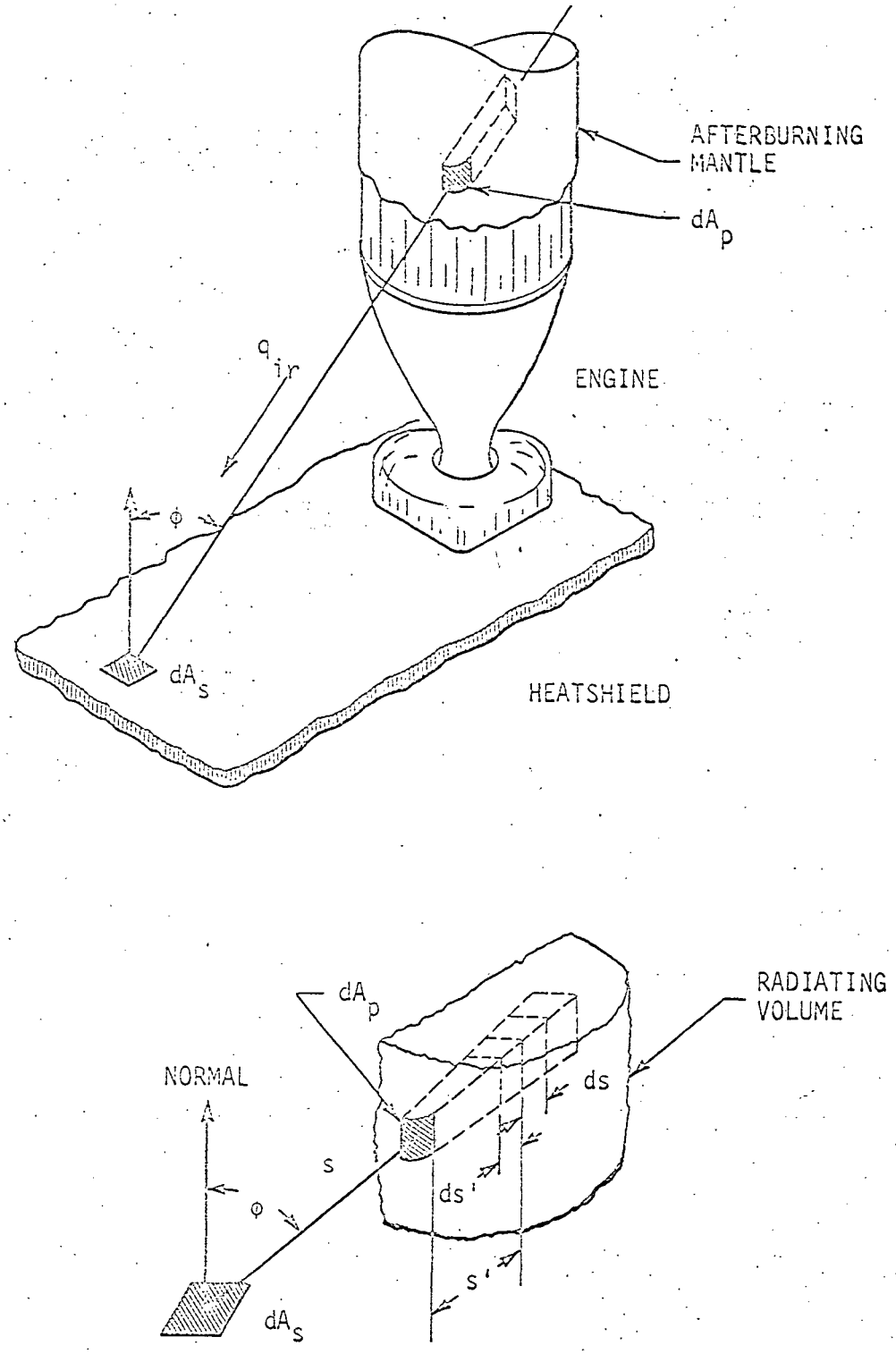

FIGURE 2-3. ROCKET PLUME RADIATION SCHEMATIC

and homogeneous severely limits the use of this approach when computing the radiation from rocket exhausts.

Because of the solid particles in the exhaust plumes, the optical depth is very short for both hydrocarbon-fueled liquid and solid-propellant engines operating at low altitudes. Therefore, the radiation is very nearly a surface phenomenon. For this condition, Equation 2-15 can be reduced to the usual equation for radiation between a finite radiating surface and a differential receiver. In finite difference form, this equation can be written as

$$q_{ir} = \sum_{p} E_p F_{\Delta A_s - \Delta A_p} \cdot \qquad (2\text{-}17)$$

To use this equation to compute the radiation, it is necessary to know the spatial variation of the plume emissive power (E_p).

Because of the very complex nature of the problem, accurate radiation predictions are very difficult to make.

2.6 MISCELLANEOUS EFFECTS

Considering the discussions of the convective and radiant heating in a rocket base region, some of the obvious factors which establish the base environment are

- Engine spacing
- Base structural arrangement
- Propellant combination
- Vehicle operation conditions.

However, many other (not-so-obvious) factors also exist which can influence the thermal environment in direct ways. These factors are often unique to one specific vehicle configuration and/or to one specific flight. Some of these are discussed below.

Base heat shields are usually coated with a high-performance, lightweight insulation material. These materials are often quite porous. As a result of the humid atmosphere in conjunction with surfaces at or near cryogenic temperatures, a considerable amount of condensation is in contact with the vehicle prior to launch. It is often possible for some of this condensate to collect above the heat shield and/or be absorbed into the porous insulation material. During flight the pressure surrounding the base region is constantly decreasing, and thermal energy is constantly being added to the materials in the base region. As a result, any moisture changes phase from a liquid to a gas or sublimes directly between the solid and vapor state. The heat shield absorbed moisture outgasses directly into the convective boundary layer and appears to influence the convective environment during the early phase of booster flights. Because of the large energy required in changing phase, the temperature of the heat shield is lower than that which would be expected for a dry heat shield.

Another example of phase-change-related environmental effects is associated with cryogenically cooled engine walls. Typically, liquid propellant rocket engines are constructed of thin wall tubes brazed together along the axial direction. Wall cooling is provided by pumping some of the fuel through the tubes. Since the Saturn upper stages used LOX/H_2 propellants, hydrogen was pumped through the tubes. It is important to the coolant circuit flow rates that the coolant enter and leave the cooling circuit as a liquid. For hydrogen, this means temperatures of approximately -250 to -400° F. Flowing hydrogen at these temperatures produces gas side wall temperatures well below the saturation temperatures of the mostly water vapor exhaust products. As a result, condensation and even solidification of the water vapor adjacent to the wall appears to have taken place. Since the engine boundary layer

fluid is the first portion of the fluid which is reversed into the base region, it would appear that the condensate could have significantly influenced the temperature of the base gas.

Extreme engine gimbal patterns and/or inoperative engines can also significantly influence the base environment. During a nominal flight, the engines gimbal (i. e., pivot about an apex) only slightly to make minor adjustments in the vehicle trajectory. However, such things as inoperative engines, gimbal actuator failures or events which create severe vehicle side loads (e.g., loss of the micrometeoroid shield during launch of the Skylab) cause severe engine movements. All of these conditions have been experienced during some of the Saturn vehicle flights. When these conditions exist, the base environment is usually influenced significantly. As a result, the vehicle base thermal protection system design environment is often dictated by one of these more severe conditions.

The existence of soot from hydrocarbon propellants is another factor which complicates the base heating problem. Since the base region is a high radiant heating environment, it would be very desirable to use surfaces which have a low absorptivity. Although it is customary to employ low absorptivity surface coating, for added insurance, the effect can seldom be relied on because of the possibility of degradation resulting from soot deposition. Photographic observations have shown that the base region is almost engulfed in thick exhaust gases just after engine ignition, and occasionally during the release and launch phases of the mission. Other photographic observations of the vehicles at extreme altitudes have shown what appears to be soot deposition along the cylindrical afterbody. This is explained by the reversed gas flowing out of the base region and forward along the vehicle in a highly separated

flow region. This amount of soot deposition along the side of the vehicle implies an even larger amount within the base region. Needless to say, the problem of soot deposition creates serious instrumentation problems when attempts are made to measure radiative and convective heating parameters.

Several of these effects will be discussed in more detail in the following sections.

REFERENCES - SECTION 2

2-1. Chapman, D. R., "An Analysis of Base Pressure at Supersonic Velocities and Comparison with Experiments", NACA-1051, 1951

2-2. Korst, H. H., W. L. Chow, and G. W. Zumwalt, "Research in Transonic and Supersonic Flow of a Real Fluid at Abrupt Increases in Cross Section", University of Illinois, ME-TN-392-5, December 1959

2-3. Goethert, B. H., "Base Flow Characteristics of Missiles with Cluster-Rocket Exhausts", Aerospace Engineering, Vol. 20, pp. 108-117, March 1961

2-4. Huffaker, R. M., "A General Program for the Calculation of Radiation from an Inhomogeneous, Nonisobaric, Nonisothermal Rocket Exhaust Plume", NASA-TMX-53622, 1967

2-5. McAnelly, W. B., "Radiant Heat Transfer from Some Simple Geometric Bodies of Gaseous Carbon Dioxide or Water Vapor to a Different Area", M.S. Thesis, University of Alabama, 1969

3. FLIGHT VEHICLE INSTRUMENTATION PROBLEMS

3.1 INTRODUCTION

Because of the extreme complexity of the base heating problem, one would expect to gain a considerable understanding and insight into the problem by studying and comparing the in-flight test results. To a degree, the latter is possible; however, certain instrumentation-related problems have thus far prevented the full use of the flight-test results.

With respect to efforts made in measuring the base environment, the Saturn vehicles were probably the most well-instrumented vehicles ever flight-tested. Over 200 individual instrument types and locations were used in the base region. Many of these were carried on several of the 30 individual, well-instrumented, flight-test vehicles. However, these efforts appear to have fallen short of producing results which can be used to evaluate many of the parameters that are important and necessary in understanding the base heating problem. If a single factor could be identified as a major cause for the general lack of understanding of the base heat transfer, it would most surely have to be the inability to accurately measure the in-flight base environmental conditions. The latter might imply criticism of those responsible for the design and selection of the individual instruments. This is not necessarily intended. The truth of the matter lies in the fact that conditions existing within the base region produce requirements which are nearly impossible to meet with instruments designed along conventional lines.

The instrumentation used in the base region was intended to serve a dual purpose. First, it was to establish the adequacy of the base thermal protection system. Second, it was to provide basic information with regard to the base heating phenomenon. The types of instruments used

were thermocouples, gas temperature probes, pressure probes, and heat flux meters. The high radiation and convective heating environment; the high-frequency, high-g conditions; and transient, possibly contaminating (i.e., soot from engine exhausts) environments produced difficult conditions for the instruments to meet.

The basic requirements for the instrumentation were that it be lightweight, compact, and rugged. Early in the program it was realized that accurate, responsive, and reliable instruments were not available to meet these requirements. As a result, an extensive instrument development program was carried on over the entire program at significant expense. The instruments used on the later flights represent the most well-developed instruments. However, as will be shown, even these leave much to be desired with respect to individual instrument accuracy.

3.2 GAS TEMPERATURE PROBES

3.2.1 Physical Descriptions

Shown in Figures 3-1 through 3-7 are sketches of some of the probes used to measure gas temperatures in the base regions. Generally, the probes consisted of specially designed and constructed thermocouples.

The probes shown in Figures 3-1 and 3-2 were used in the Saturn I through Saturn IB base regions. These probes consisted of a chromel-alumel thermocouple mounted in an insulating case. Various radiation shields were used in an effort to reduce the effects of absorbed radiation on the temperature reading. On the Saturn IB vehicle, the probes were mounted so that the distance from the surface to the probe sensing element was varied as shown in Figure 3-3.

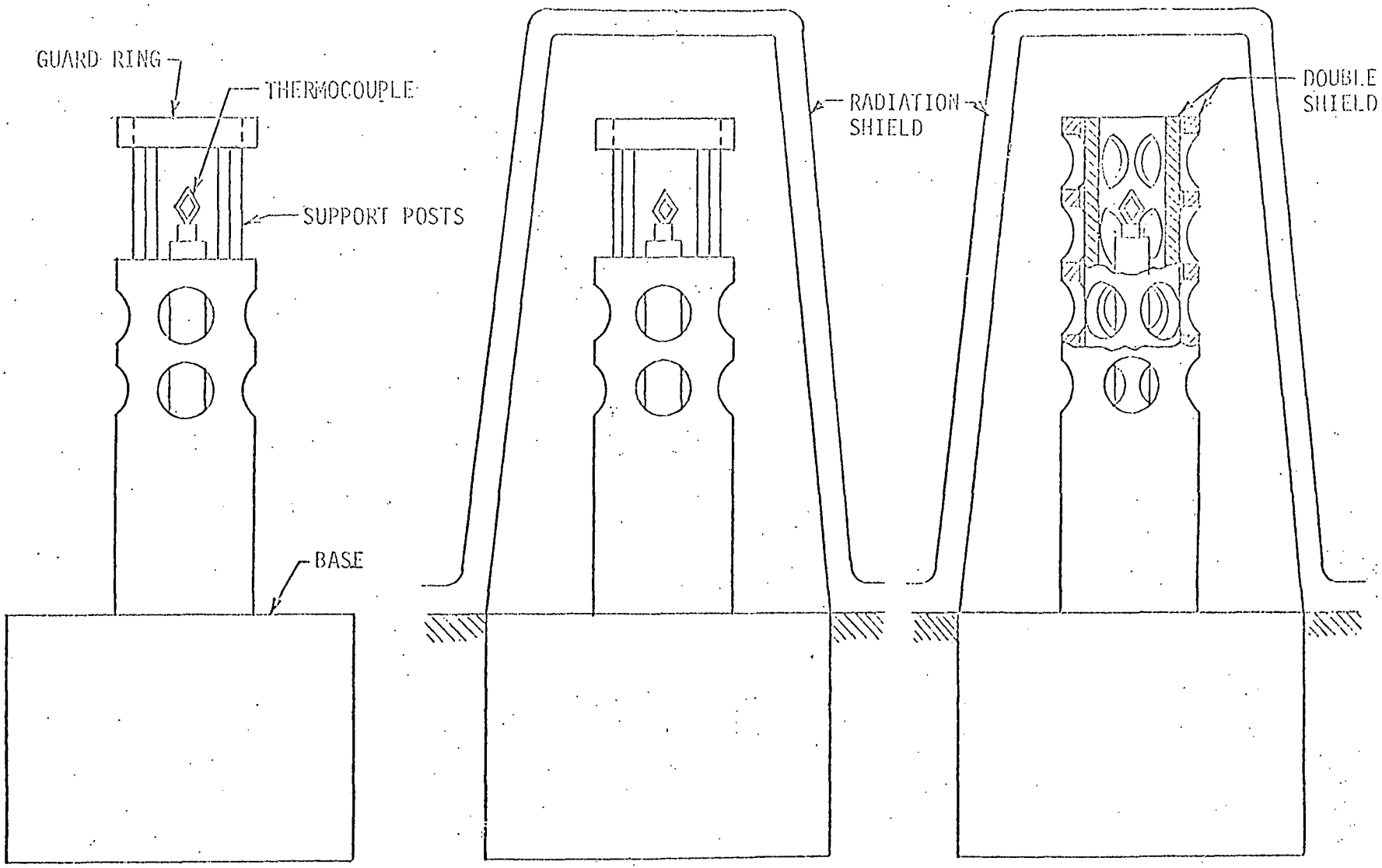

FIGURE 3-1. TYPICAL SATURN I GAS TEMPERATURE PROBES

NOTE: ALL DIMENSIONS IN INCHES

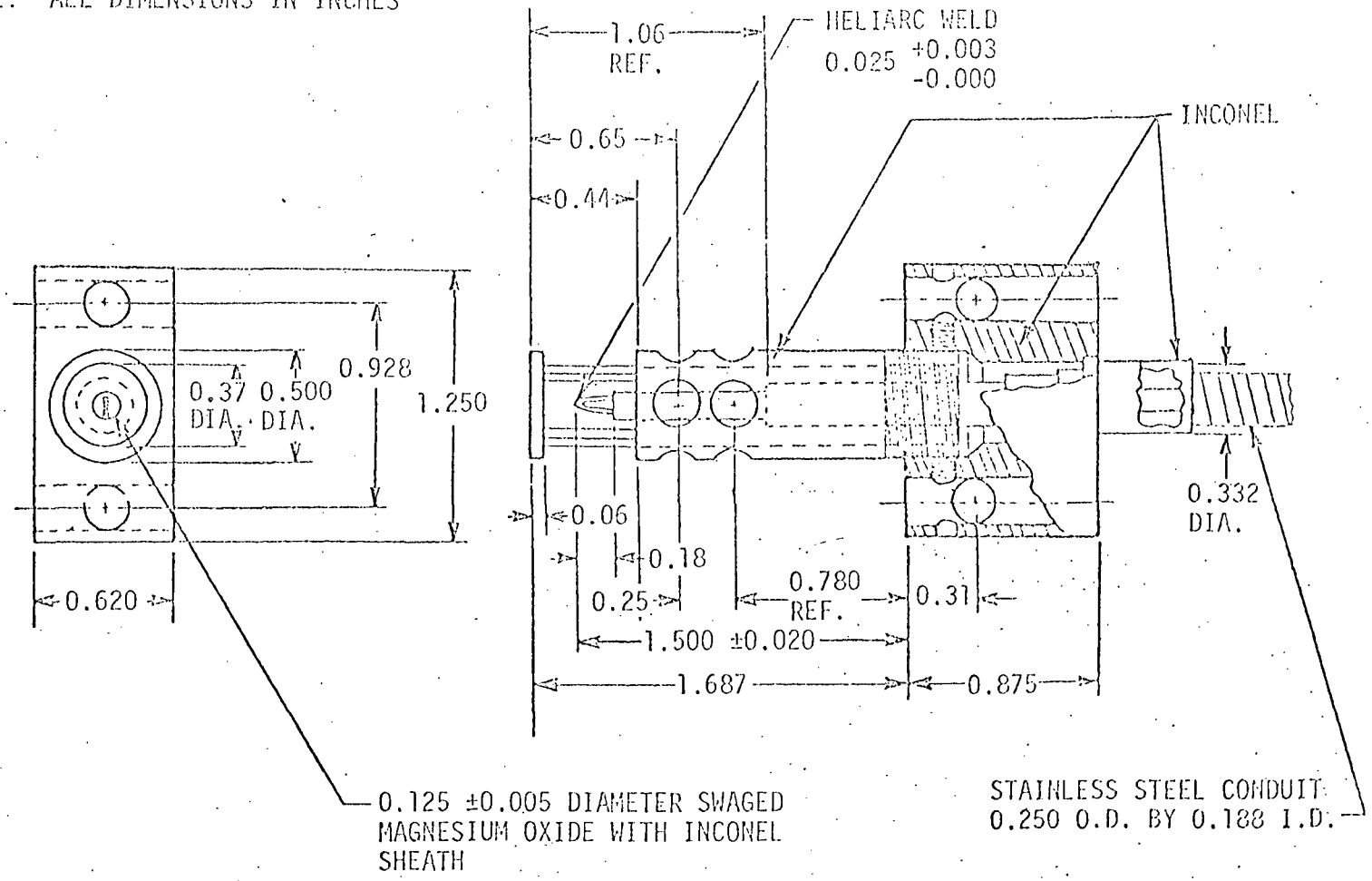

FIGURE 3-2. SCHEMATIC OF SATURN I GAS TEMPERATURE PROBE

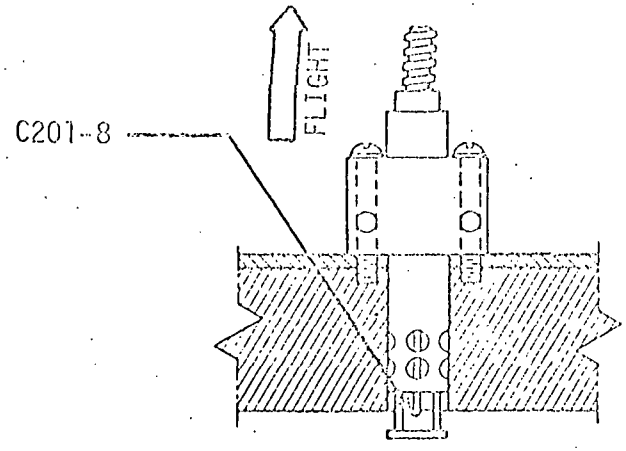

ZERO EXTENSION GAS TEMPERATURE PROBE

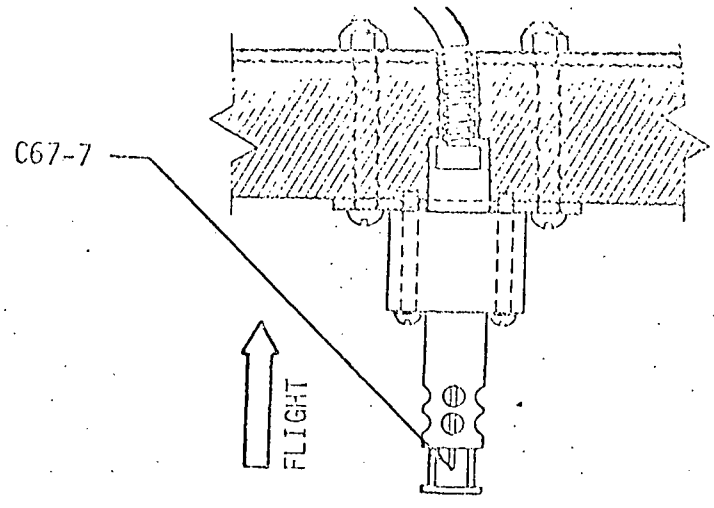

2.5-in. GAS TEMPERATURE PROBE

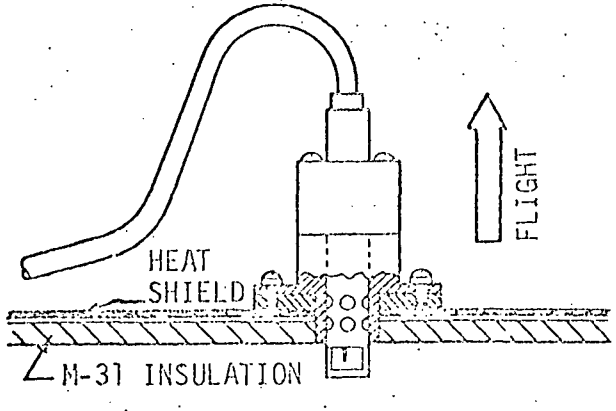

0.25-in. GAS TEMPERATURE PROBE

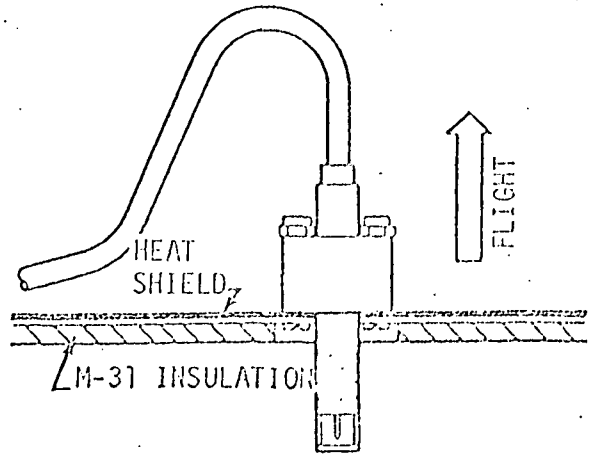

1.25-in. GAS TEMPERATURE PROBE

FIGURE 3-3. TYPICAL SATURN IB GAS TEMPERATURE PROBE INSTALLATIONS

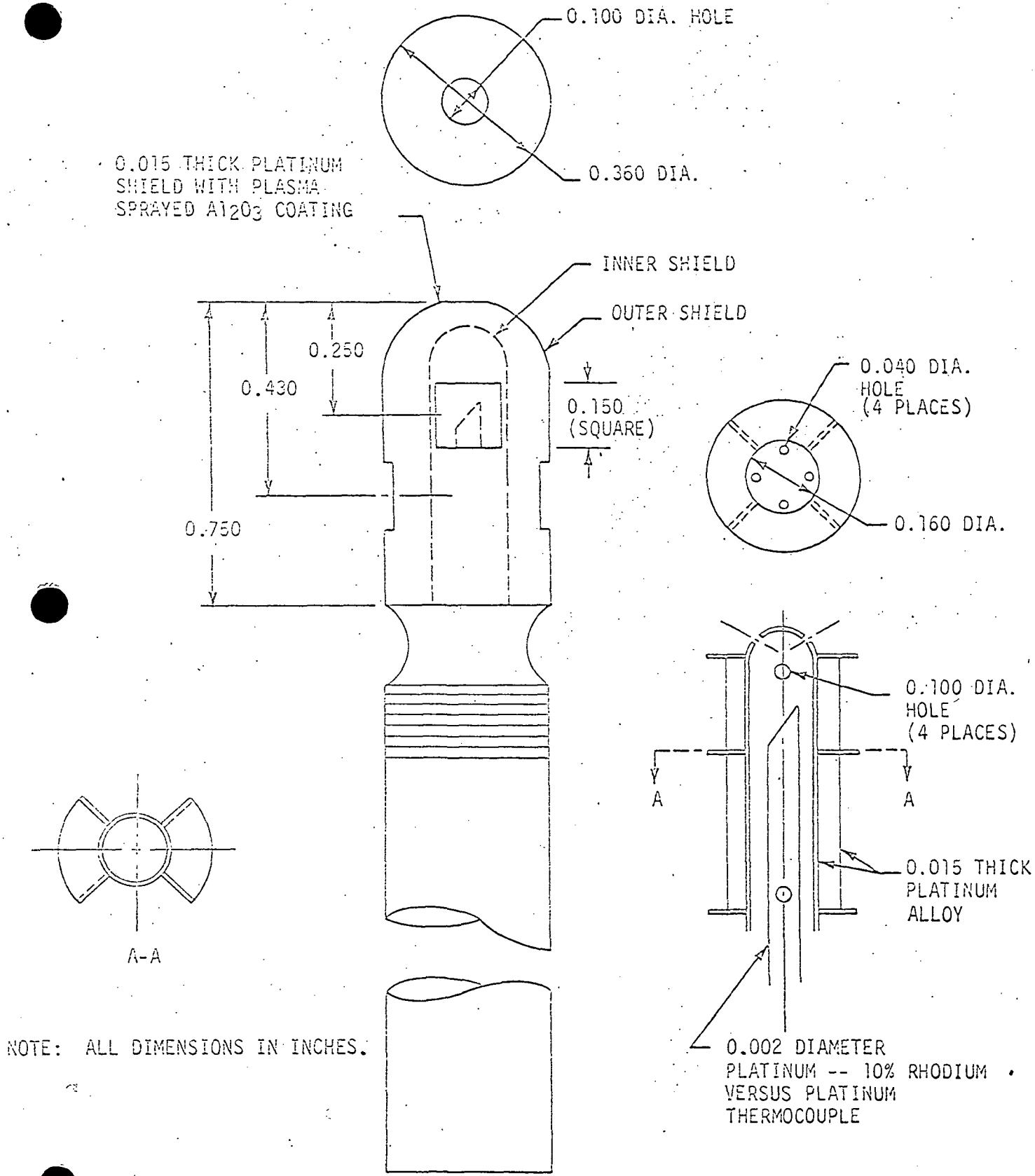

FIGURE 3-4. SCHEMATIC OF SATURN S-IC ENGINE GAS TEMPERATURE PROBE

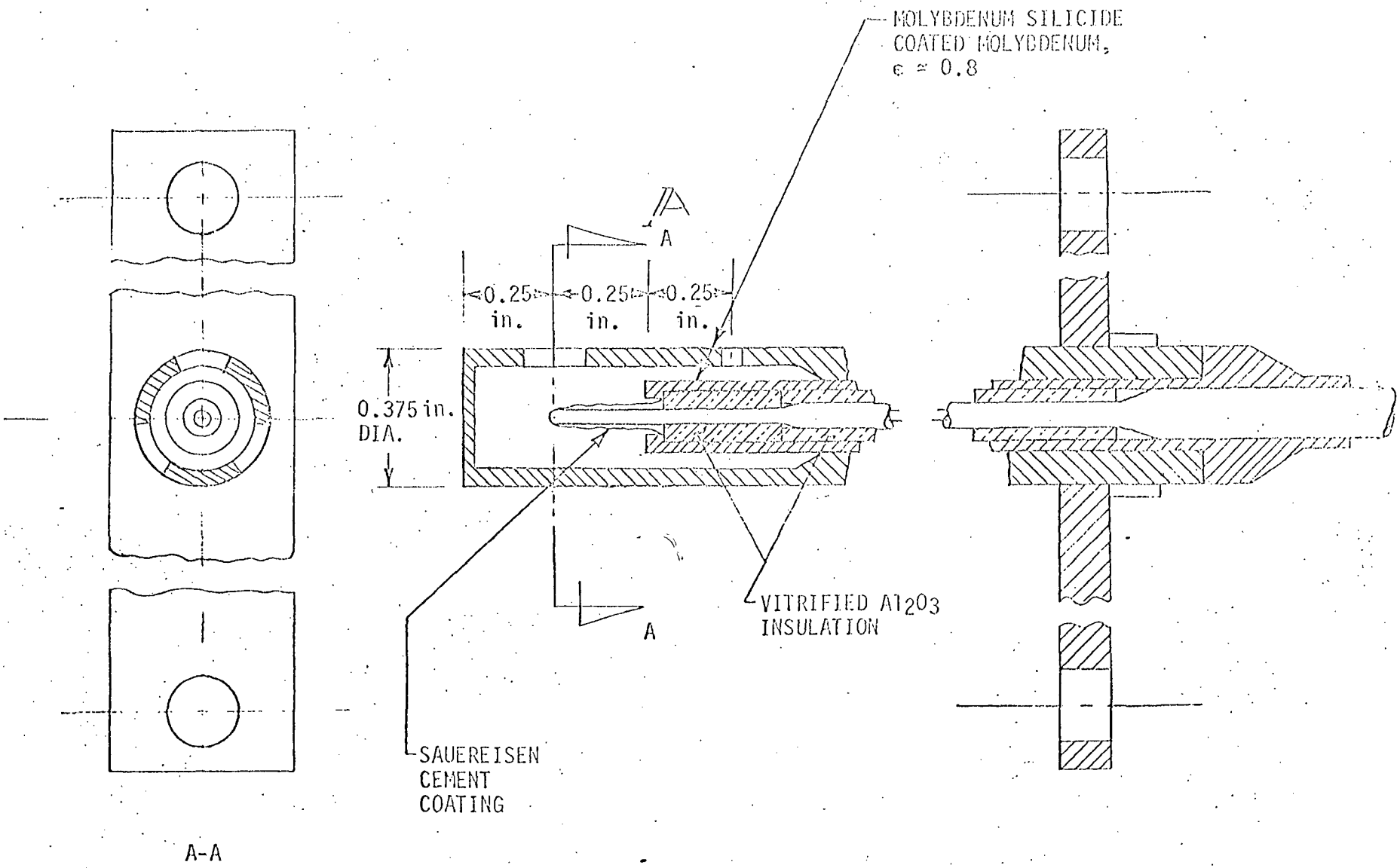

FIGURE 3-5. SCHEMATIC OF SATURN S-IC HEAT SHIELD GAS TEMPERATURE PROBES

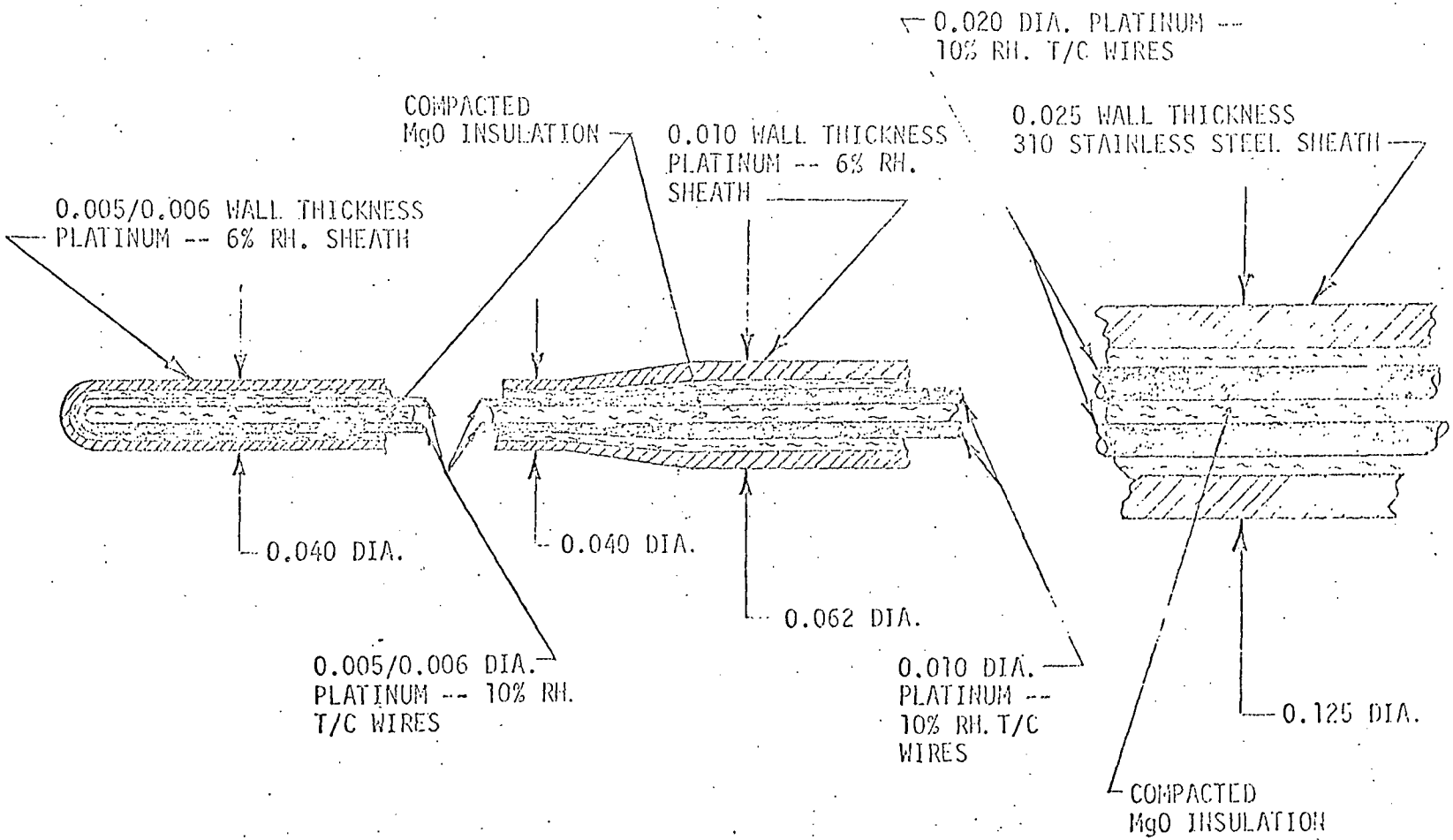

FIGURE 3-6. SCHEMATIC OF SATURN HEAT SHIELD GAS PROBE SENSING ELEMENT

Shown in Figures 3-4 through 3-6 are sketches of the probes used in the Saturn V, S-IC base region. The probe shown in Figure 3-4 was used exclusively around the engines, while that shown in Figure 3-5 was used on the heat shield. The heat shield probes were mounted through the heat shield with the distance from the surface to the sensing element varying between 0.25, 1.0, and 2.5 inches.

As seen in the figures the designs of the sensing elements of the S-IC heat shield and engine gas temperature probes are distinctly different. The engine probe consisted of a bare 0.002-inch-diameter platinum/10 percent rhodium thermocouple surrounded by a double radiation shield. The inner and outer radiation shields were plasma spray coated with aluminum oxide to prevent catalytic reactions. Gas contacted the thermocouple junction by traveling a circuitous route through a 0.15-inch square hole in the outer shield and through 0.040-inch or 0.10-inch-diameter holes in the inner shield.

The heat shield probe consisted of a fine platinum/10 percent rhodium thermocouple wire encased in a platinum/6 percent rhodium sheath filled with compacted magnesium oxide insulation (see Figures 3-5 and 3-6). To reduce thermal radiation, the sensing element was surrounded by a single outer shield. To prevent catalytic reactions, the exposed surfaces were coated with molybdenum silicide, and the sensing element was coated with ceramic cement. Gas entered the outer shield through three equally spaced radial holes 0.1625 inch in diameter (approximate).

Figure 3-7 shows a schematic of the gas temperature probe used in the base region of the Saturn S-II stage. These probes were unshielded and extended approximately 2 inches from the heat shield surface. The design of the sensing element which contained the

thermocouple was considered proprietary by the manufacturer. However, the information which could be obtained suggests that the design of the S-II stage sensing element was similar to that of the S-IC heat shield probe shown in Figure 3-6. No doubt different materials such as the alumina sheath were used in construction; otherwise, the design was probably similar.

Further information regarding details of constructing and qualification tests of the Saturn gas temperature probes can be obtained from References 3-1 through 3-8.

3.2.2 Gas Temperature Probe Accuracy

Based upon the data available, it must be concluded that the ability of the gas temperature probes to measure accurately the temperature of the base gases is very questionable. For some conditions the probes may have indicated the true temperature within a few percent, however, this is a result of fortuitous circumstances. Furthermore, it does not appear possible at this time to correct the erroneous inflight-measured results with any degree of confidence and/or accuracy. The reasons for these unfortunate conclusions are many and varied and are discussed in detail in the following sections.

Briefly stated, the gas temperature probe errors appear to be a result of the following factors:

- Coating the surfaces of the probes to prevent catalytic reactions produced surfaces with high radiation absorbtivities and caused the probes to be overly sensitive to incident radiation and reradiation at high temperatures.

- Capsulating the thermocouple inside the insulated sheath would appear to have had several deleterious effects: the heat transfer path between the gas and the thermocouple was increased; the sensible heat capacity of the thermocouple/insulation/sheath system was considerably

higher than it would have been for the thermocouple alone; and the conduction path between the body of the probe and the thermocouple was increased.

The net effect of these factors could have caused the probes to measure both higher or lower depending entirely upon the instantaneous equilibrium conditions which prevailed. When these probes are used in the base region some of the effects tend to cancel each other, providing some reason to speculate that the overall accuracy might be better than that indicated by considering each source of error separately.

3.2.3 Gas Temperature Probe Theoretical Evaluation

Considering the schematic of the gas temperature probe shown in Figure 3-8, a heat balance about the thermocouple junction gives

$$Q_s = Q_r + Q_c - Q_K \qquad (3\text{-}1)$$

where

Q_s - net heat in the junction

Q_r - net radiation absorbed or rejected by the junction

Q_c - convective heating to the junction

Q_K - heat conducted into or out of the junction.

Assuming the junction to be an isothermal mass, the net heat in the junction at any time is the sensible heat; therefore

$$Q_s = w_j C_{p_j} \frac{dT_j}{d\tau} \qquad (3\text{-}2)$$

where

w_j - weight of the junction

C_{p_j} - specific heat of the junction

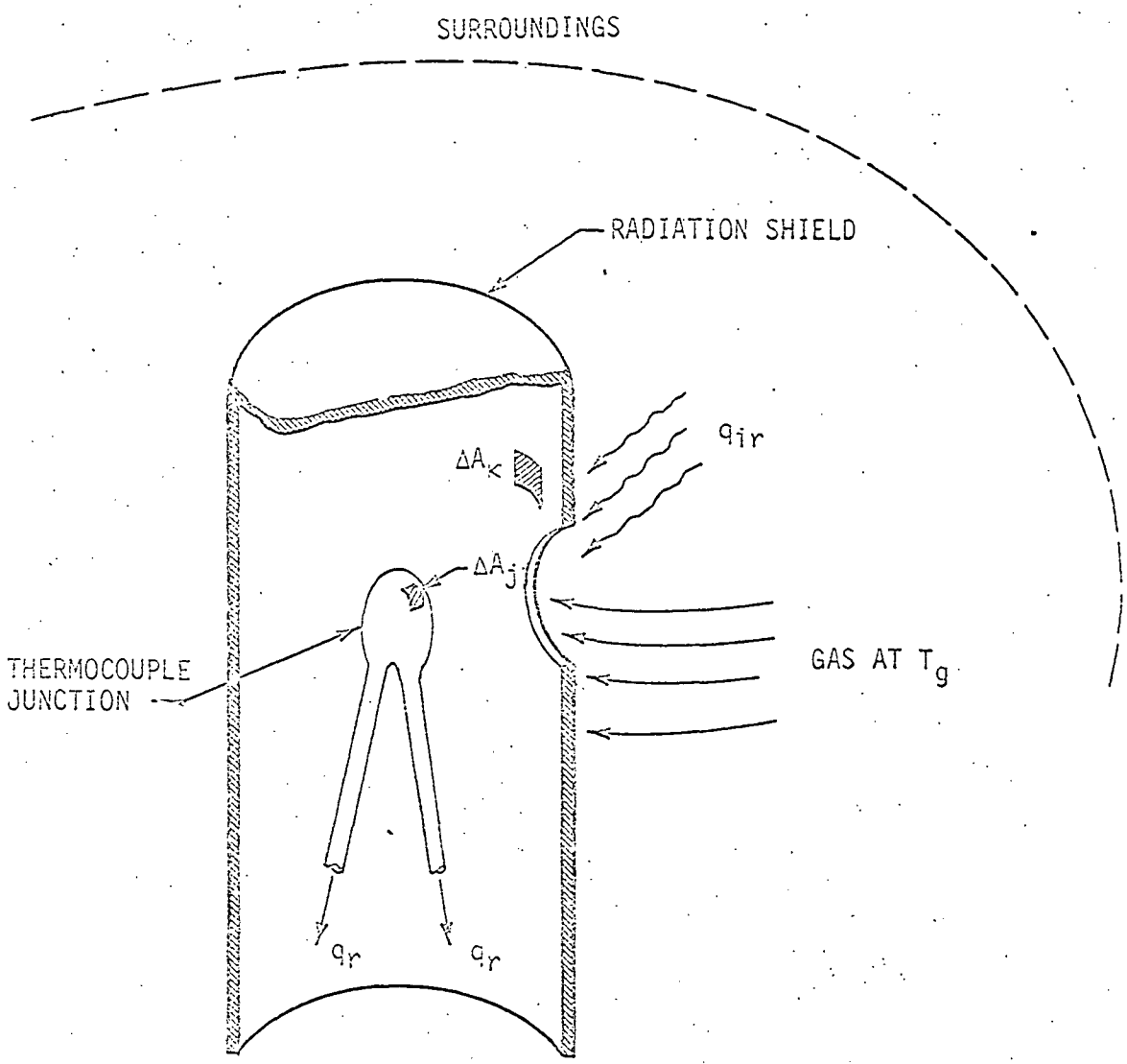

FIGURE 3-8. SCHEMATIC OF A TYPICAL THERMOCOUPLE GAS TEMPERATURE PROBE

T_j - temperature of the junction

τ - time .

Considering the radiation interchange between some small but finite junction area, ΔA_j, and an arbitrarily picked surrounding area, ΔA_κ, the radiant energy emitted by ΔA_j which is absorbed by ΔA_κ is

$$Q_{j-\kappa} = \mathcal{F}_{j-\kappa} \Delta A_j E_{bj} \tag{3-3}$$

where

$Q_{j-\kappa}$ - net radiant energy emitted by ΔA_j and absorbed by ΔA_κ

$\mathcal{F}_{j-\kappa}$ - radiation interchange factor

E_{bj} - blackbody emissive power of ΔA_j

$E_{bj} = \sigma T_j^4$.

The radiation interchange factor includes not only the direct radiation between ΔA_j and ΔA_κ but, also, any reflected and rereflected energy. The net radiant energy exchange, i.e., the amount emitted by ΔA_κ and received by ΔA_j minus the amount received by ΔA_κ that was emitted by ΔA_j (Ref. 3-9), is given by

$$Q_{j \rightleftarrows \kappa} = Q_{\kappa \rightarrow j} - Q_{j \rightarrow \kappa} \quad . \tag{3-4}$$

Then, if all of the surrounding (which at this point includes the shield, radiant sources, etc.) are divided into n arbitrary area elements, the net energy exchange between ΔA_j and the n radiating elements is

$$Q_{net,\ j} = \sum_{\kappa=1}^{n} Q_{n \rightleftarrows j} \tag{3-5}$$

$$= \sum_{\kappa=1}^{n} Q_{\kappa-j} - \sum_{\kappa=1}^{n} Q_{j-\kappa} \tag{3-6}$$

$$= \sum_{\kappa=1}^{n} \mathcal{F}_{\kappa-j}\, \Delta A_{\kappa}\, E_{b\kappa} - \sum_{\kappa=1}^{n} \mathcal{F}_{j-\kappa}\, \Delta A_{j}\, E_{bj} \quad . \tag{3-7}$$

Then, using the reciprocity theorem (Ref. 3-9),

$$\Delta A_{\kappa}\, \mathcal{F}_{\kappa-j} = \Delta A_{j}\, \mathcal{F}_{j-\kappa} \tag{3-8}$$

gives

$$Q_{net,\,j} = \sum_{\kappa=1}^{n} \Delta A_{j}\, \mathcal{F}_{j-\kappa}\, (E_{b\kappa} - E_{bj}) \quad . \tag{3-9}$$

Letting the thermocouple junction be subdivided into m elemental areas, ΔA_j, the net radiant energy exchange between the junction and all of the surroundings is

$$Q_r = \sum_{j=1}^{m} \sum_{\kappa=1}^{n} \Delta A_{j}\, \mathcal{F}_{j-\kappa}\, (E_{b\kappa} - E_{bj}) \quad . \tag{3-10}$$

Equation 3-10 can be simplified by the following:

$$Q_r = \sum_{j=1}^{m} \sum_{\kappa=1}^{n} \Delta A_{j}\, \mathcal{F}_{j-\kappa}\, E_{b\kappa} - \sum_{j=1}^{m} \sum_{\kappa=1}^{n} \Delta A_{j}\, \mathcal{F}_{j-\kappa}\, E_{bj}$$

$$= \sum_{j=1}^{m} \sum_{\kappa=1}^{n} \Delta A_{j}\, \mathcal{F}_{j-\kappa}\, E_{b\kappa} - \sum_{j=1}^{m} \Delta A_{j}\, E_{bj} \sum_{\kappa=1}^{n} \mathcal{F}_{j-\kappa} \quad . \tag{3-11}$$

Then, since

$$\sum_{\kappa=1}^{n} \mathcal{F}_{j-\kappa} = \epsilon_j \qquad (3\text{-}12)$$

the second term in Equation 3-11 can be written as

$$\sum_{j=1}^{m} \sum_{\kappa=1}^{n} \Delta A_j \mathcal{F}_{j-\kappa} E_{bj} = \sum_{j=1}^{m} \Delta A_j \epsilon_j E_{bj} . \qquad (3\text{-}13)$$

Then, assuming $\epsilon_j E_{bj} = \epsilon_j \sigma T_j$ to be constant over the junction, Equation 3-13 becomes

$$\sum_{j=1}^{m} \Delta A_j \epsilon_j E_{bj} = \epsilon_j E_{bj} \sum_{j=1}^{m} \Delta A_j$$

$$= A_j \epsilon_j E_{bj} = A_j \epsilon_j \sigma T_j^4 \qquad (3\text{-}14)$$

where

A_j - surface area of the junction

ϵ_j - emissivity of the junction

T_j - temperature of the junction.

Equation 3-14 is the thermocouple radiant emission term and accounts for all of the energy lost by radiation that is absorbed by the surroundings. Thus, the net radiation can be written as

$$Q_r = \sum_{j=1}^{m} \sum_{\kappa=1}^{n} \left(\Delta A_j \mathcal{F}_{j-\kappa} E_{b\kappa} \right) - A_j \epsilon_j \sigma T_j^4 . \qquad (3\text{-}15)$$

The first term on the right of Equation 3-15 represents all the sources which radiate to the junction. For convenience, this can be subdivided into the separate sources of radiation. Therefore, dividing the plumes into p radiant sources, the radiation shield into ℓ sources, and letting a represent all other sources which radiate to the junction gives

$$Q_r = \sum_{j=1}^{m} \left(\sum_{g=1}^{p} \Delta A_j \mathcal{F}_{j-g} E_{bg} + \sum_{S=1}^{\ell} \Delta A_j \mathcal{F}_{j-S} E_{bS} + \sum_{e=1}^{a} \Delta A_j \mathcal{F}_{j-e} E_{be} \right) - A_j \epsilon_j \sigma T_j^4 \qquad (3\text{-}16)$$

which is

$$= \left[\begin{pmatrix} \text{net plume} \\ \text{radiation} \end{pmatrix} + \begin{pmatrix} \text{net shield} \\ \text{radiation} \end{pmatrix} + \begin{pmatrix} \text{net surroundings} \\ \text{radiation} \end{pmatrix} \right] - \begin{pmatrix} \text{net} \\ \text{reradiation} \end{pmatrix} .$$

The convective heat flux to the junction can be written as

$$Q_c = A_j h_j (T_r - T_j) \qquad (3\text{-}17)$$

where

$T_r = r T_g$

r - recovery factor .

Then, substitution of Equations 3-2, 3-16, and 3-17 into Equation 3-1 gives

$$w_j C_{pj} \frac{dT_j}{d\tau} = \sum_{j=1}^{m} \left(\sum_{g=1}^{p} \Delta A_j F_{j-g} E_{bg} \right.$$

$$\left. + \sum_{S=1}^{\ell} \Delta A_j F_{j-S} E_{bS} + \sum_{e=1}^{a} \Delta A_j F_{j-e} E_{be} \right)$$

$$- A_j \epsilon_j \sigma T_j^4 + A_j h_j (r T_g - T_j) - Q_K \quad . \quad (3\text{-}18)$$

The individual terms of Equation 3-18 represent the following:

$w_j C_{pj} \frac{dT_j}{d\tau}$	-	sensible heat capacity of the junction
$\sum_{j=1}^{m} \sum_{g=1}^{p} \Delta A_j F_{j-g} E_{bg}$	-	net radiation emitted by the plumes that is absorbed by the junction
$\sum_{j=1}^{m} \sum_{S=1}^{\ell} \Delta A_j F_{j-S} E_{bS}$	-	net radiation emitted by the radiation shield that is absorbed by the junction
$\sum_{j=1}^{m} \sum_{e=1}^{a} \Delta A_j F_{j-e} E_{be}$	-	net radiation emitted by all other radiant sources that is absorbed by the junction
$A_j \epsilon_j \sigma T_j^4$	-	net radiation given up by the junction
$A_j h_j (r T_g - T_j)$	-	convective heating to the junction
Q_K	-	conduction heat lost or gained by the junction .

For an ideal probe, all terms of Equation 3-18 are identically zero, giving $T_j = r T_g \approx T_g$; thus, measuring the emf output of the probe gives the approximate gas temperature. For an actual probe,

all terms in Equation 3-18 are not zero and the result is

$$(r\,T_g - T_j) \neq 0 \; ; \tag{3-19}$$

likewise,

$$T_j \neq r\,T_g \; .$$

By studying Equation 3-18 it can be seen that in the design of an accurate gas temperature probe it is desirable to have the following:

- The sensible heat capacity of the junction (or specifically the mass of the junction) should be as small as possible [i.e., $w_j\, C_{pj}\, (dT_j)/(d\tau) \rightarrow 0$]. This gives a rapid response to changes in temperature.
- The conduction path between the thermocouple junction and the probe body should be as small as possible. This reduces the heat lost or gained by the junction via conduction (i.e., $Q_K \sim 0$).
- The net effects of absorbed and emitted radiation should be made negligible.
- The gas should contact the probe junction with low flow velocities so that the recovery factor, r, would be as close to unity as possible.
- The heat transfer coefficient should be made as high as possible so that the convective flux to the junction (and therefore the sensitivity to the gas temperature), would be high relative to the other sources of heat transfer.

The requirements for which the Saturn gas probes were designed, such as the ability to withstand high-g, high-frequency vibrations; high-absorbtivity surface coatings; etc., made these idealistic requirements almost impossible to approach.

Shielding the junction reduces the net effects of absorbed and emitted radiation. By following the derivation given on page 311 of Reference 3-9 for the net radiant flux transferred between two shielded surfaces, it can be shown that the net flux transferred between the outer shield and the inner shield is given by

$$q_{net_1} = \frac{E_{bn} - E_{bj}}{\frac{n}{2} + \sum_{\kappa=1}^{n} \frac{\rho_\kappa}{\epsilon_\kappa}} \quad , \tag{3-20}$$

where

n - number of surfaces between the junction and the outer shield including both of these surfaces

E_{bn} - emissive power of the outer shield

ρ - reflectivity

ϵ - emissivity.

Considering a single- and a double-shielded thermocouple (see Figure 3-9), the effect of shielding the junction can be shown. For the single-shielded thermocouple junction, Equation 3-20 gives

$$q_{net_1} = \frac{E_{b2} - E_{b1}}{1 + \frac{\rho_1}{\epsilon_1} + \frac{\rho_2}{\epsilon_2}} \quad . \tag{3-21}$$

For the double-shielded junction, Equation 3-20 gives

$$q_{net_1} = \frac{E_{b4} - E_{b1}}{2 + \frac{\rho_1}{\epsilon_1} + \frac{\rho_2}{\epsilon_2} + \frac{\rho_3}{\epsilon_3} + \frac{\rho_4}{\epsilon_4}} \quad . \tag{3-22}$$

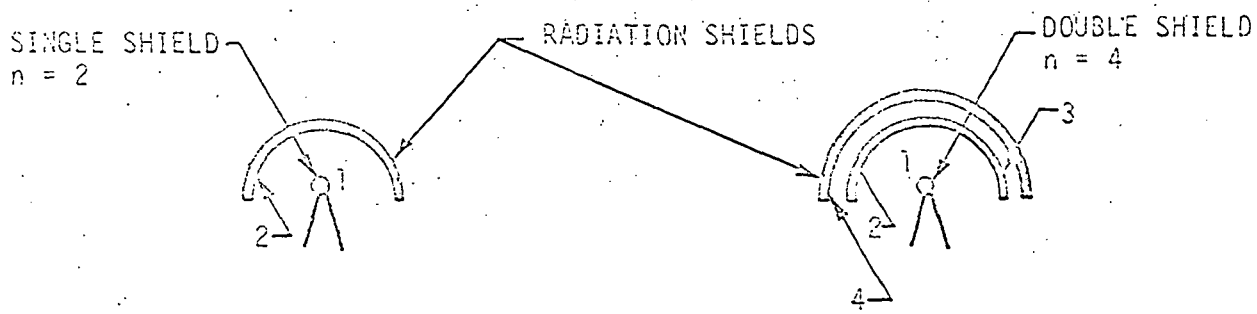

FIGURE 3-9. SHIELDED THERMOCOUPLE JUNCTIONS

It can be seen from Equations 3-21 and 3-22 that even if the surface reflectivities were zero (i.e., blackbody surface), using a double shield reduces the net flux by a factor of two below that of the single-shielded probe. Experimentally, the effects of radiation-shielded thermocouples and conduction influences are reported on pages 263 and 264 of Reference 3-10.

3.2.4 Gas Temperature Probe Qualification Test Results

Qualification tests conducted on the Saturn gas temperature probes (Refs. 3-3, 3-4, and 3-7) show conclusively that the in-flight measured temperatures must be considered questionable. The purpose of the qualification tests was to demonstrate by actual testing that the instruments could meet the mechanical and functional requirements. The thermal tests consisted of exposing the probes to a hot gas flow and a radiant flux. The orientation of the probes as well as the flow velocity, gas temperature, density, and radiant flux were systematically varied.

A typical hot-gas test consisted of exposing a heat shield probe to a flowing gas with known velocity, stagnation temperature, and density. A test fixture was designed so that the probe could be rapidly

injected into the gas stream once the gas flow condition was established. The temperature of the probe was monitored until well after steady-state conditions were reached.

Some typical results obtained during the qualification tests are shown in Figure 3-10. After exposure, the probe would rise to a steady-state value that was well below the actual gas temperature. For condition 4 of Figure 3-10, the actual gas temperature was approximately 2054°F; at steady state the probe indicated a temperature of 1190°F. During this test the flow velocity was 1928 ft/sec, the stagnation pressure was 0.81 psia, and the density was 0.00097 lb/ft^3. The 864°F temperature difference represents a probe error of approximately 34 percent (based on degrees Rankine). As may be seen in the figure, the errors are less at higher flow rates and lower temperatures.

In addition to varying the mass flow rates, the probes were injected into the flow with different orientations with respect to the centerline flow direction. Probe positions were varied from: probe axis normal to the flow (Position I); probe axis 60 degrees to the flow (Position II); probe axis 30 degrees to the flow (Position III); and probe axis parallel to the flow (Position IV).

The results of approximately 44 tests conducted in the hot-gas environment are reported in Reference 3-4. These test results were evaluated to determine the probe error as a function of mass flow rate, position, and gas temperature. The test results are tabulated in Table 3-1. The probe temperature, T_p, is the apparent steady-state value. Also shown in Table 3-1 are the average conditions indicated for all Position I tests. These results are plotted in Figure 3-11. Across the abscissa of this plot are shown the approximate times that the flow in the S-IC base region had the same mass flow flux (ρu).

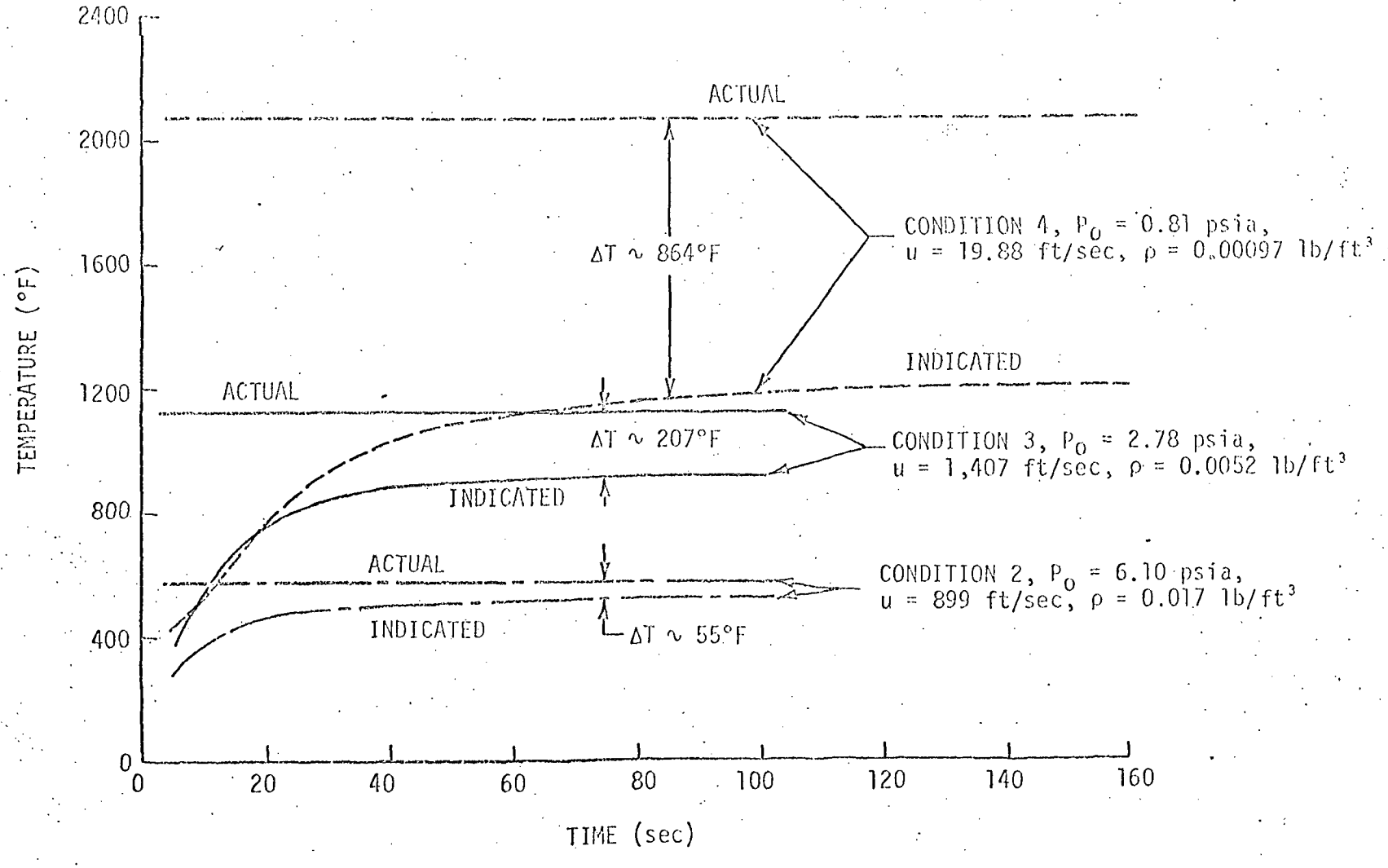

FIGURE 3-10. TYPICAL HOT GAS FLOW TEMPERATURE PROBE QUALIFICATION TEST RESULTS .

TABLE 3-1. HEAT SHIELD GAS TEMPERATURE PROBE STEADY-STATE ERROR

TEST NO.	POSITION	ρ (lb/ft^3)	u (ft/sec)	ρu	T_0 (°R)	T_R (°R)	$\frac{T_0 - T_p}{T_0}$	$T_0 - T_p$
48	I*	0.00084	2433	2.044	2515	1720	0.316	795
48	I*	0.0050	1465	7.325	1589	1345	0.154	244
47	I*	0.016	934	14.944	1034	960	0.716	74
46	I*	0.045	338	15.21	789	758	0.039	31
45	I*	0.00078	2415	1.884	2521	1771	0.298	750
45	I*	0.0050	1482	7.41	1585	1370	0.136	215
44	I*	0.016	939	15.024	1014	955	0.058	59
43	I*	0.046	331	15.226	774	752	0.028	22
42	I*	0.0010	1809	1.809	2519	1777	0.295	742
42	I*	0.0052	1418	7.3736	1593	1392	0.126	201
41	I*	0.017	942	16.014	1039	978	0.059	61
40	I*	0.045	337	15.165	791	765	0.033	26
39	II	0.00097	1943	1.885	2518	1800	0.285	718
39	I*	0.00097	1928	1.870	2514	1650	0.344	864
39	II	0.0052	1407	7.3164	1584	1398	0.117	186
39	I*	0.0052	1407	7.3164	1584	1377	0.131	207
38	II	0.017	904	15.368	1031	980	0.049	51
38	I*	0.017	899	15.283	1030	975	0.053	55
37	II	0.046	331	15.226	784	763	0.026	21
37	I*	0.046	332	15.272	782	760	0.028	22
33	III	0.00085	2220	1.887	2498	1885	0.245	613
36	I*	0.00085	2220	1.887	2498	1808	0.276	690
36	III	0.0051	1443	7.3593	1573	1445	0.081	128
36	I*	0.0051	1449	7.3899	1573	1340	0.148	233
35	III	0.016	960	15.360	1023	990	0.032	33
35	I*	0.016	961	15.376	1022	958	0.063	64
34	III	0.046	335	15.41	782	767	0.019	15
34	I*	0.045	336	15.12	781	756	0.032	25
32	I	0.00038	1917	0.7285	2482	1500	0.396	982
32	I*	0.0052	1404	7.3008	1583	1399	0.116	184
31	I*	0.016	975	15.60	1024	971	0.052	53
30	I*	0.046	334	15.364	785	768	0.022	17
29	I	0.0010	1789	1.789	2318	1875	0.191	443
29	I	0.0053	1376	7.2928	1545	1460	0.055	85
28	I	0.016	960	15.360	1011	987	0.024	24
27	I	0.047	326	15.322	769	760	0.012	9
26	I	0.0011	1728	1.9008	2469	2035	0.176	434
26	IV	0.0011	1709	1.8799	2494	2040	0.182	454
26	IV	0.0050	1462	7.31	1580	1515	0.041	65
26	I	0.0052	1408	7.3216	1568	1460	0.069	108
25	IV	0.016	955	15.28	1019	1001	0.018	18
25	I	0.017	909	15.453	1009	980	0.029	29
24	IV	0.042	363	15.246	782	765	0.022	17
24	I	0.043	358	15.394	777	765	0.015	12
				AVERAGE VALUES				
	I	0.000888	2161.0	1.919	2513.4	1745.2	0.306	768.2
	I	0.00513	1437.2	7.373	1574.5	1370.5	0.130	204.
	I	0.0163	941.67	15.35	1027.17	966.17	0.059	61.
	I	0.0455	334.67	15.2275	783.67	759.83	0.030	23.8

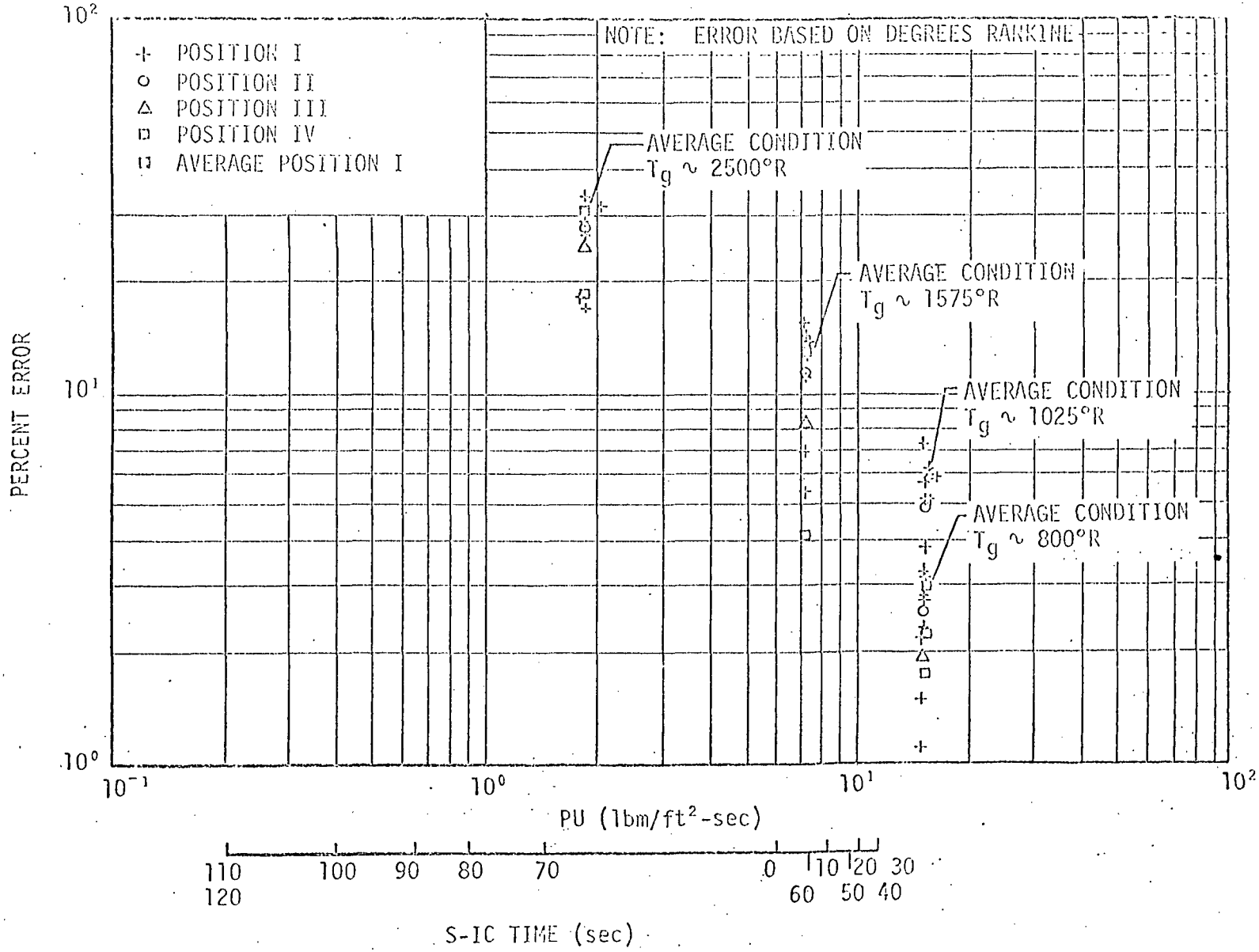

FIGURE 3-11. HEAT SHIELD GAS TEMPERATURE PROBE HOT GAS TEST ERRORS

The test results shown in Figure 3-11 were obtained by exposing the probe to hot gas only. The test chamber was a water-cooled pipe. The temperature of the chamber wall is not reported in Reference 3-4; however, some radiation exchange between the pipe wall and the probe could have influenced the results.

During another part of the qualification tests the probe was exposed to a radiant flux in the absence of any forced convection. The results of these tests are shown in Figure 3-12. When the probe was irradiated with a 40-Btu/ft^2-sec flux from all sides the probe indicated a steady-state temperature of 2500° F. Exposure to a 15-Btu/ft^2-sec flux (approximately the magnitude of the S-IC heat shield incident flux) produced an indicated steady-state temperature of approximately 1400° F. When the sides of the probe were shielded with a special reflective shield and the end was exposed to a 40-Btu/ft^2-sec radiant flux, the probe indicated a steady-state temperature of approximately 450° F.

A similar set of tests was conducted using the S-IC engine gas temperature probe. The engine probe was exposed to hot gas at varying flow rates and to combined radiant flux and gas flow. During the hot-gas flow tests the gas temperature was varied between 300 and 2100° F (Figure 3-13). During the combined radiant and gas flow tests the probes were exposed to incident heating rates of 19.3 and 10.6 Btu/ft^2-sec in a gas flow having temperatures of 20 to 60° F. The probe was also exposed to a 400° F gas temperature flux in conjunction with the 10.6-Btu/ft^2-sec radiant flux.

Based upon the steady-state conditions, the engine probes consistently indicated low when exposed to hot gas flow only, and high when exposed to the combined radiant and gas flow. During the radiation tests, when the probe was exposed to a 10.6-Btu/ft^2-sec radiant flux, the indicated error was less when the gas temperature was 400° F than when the

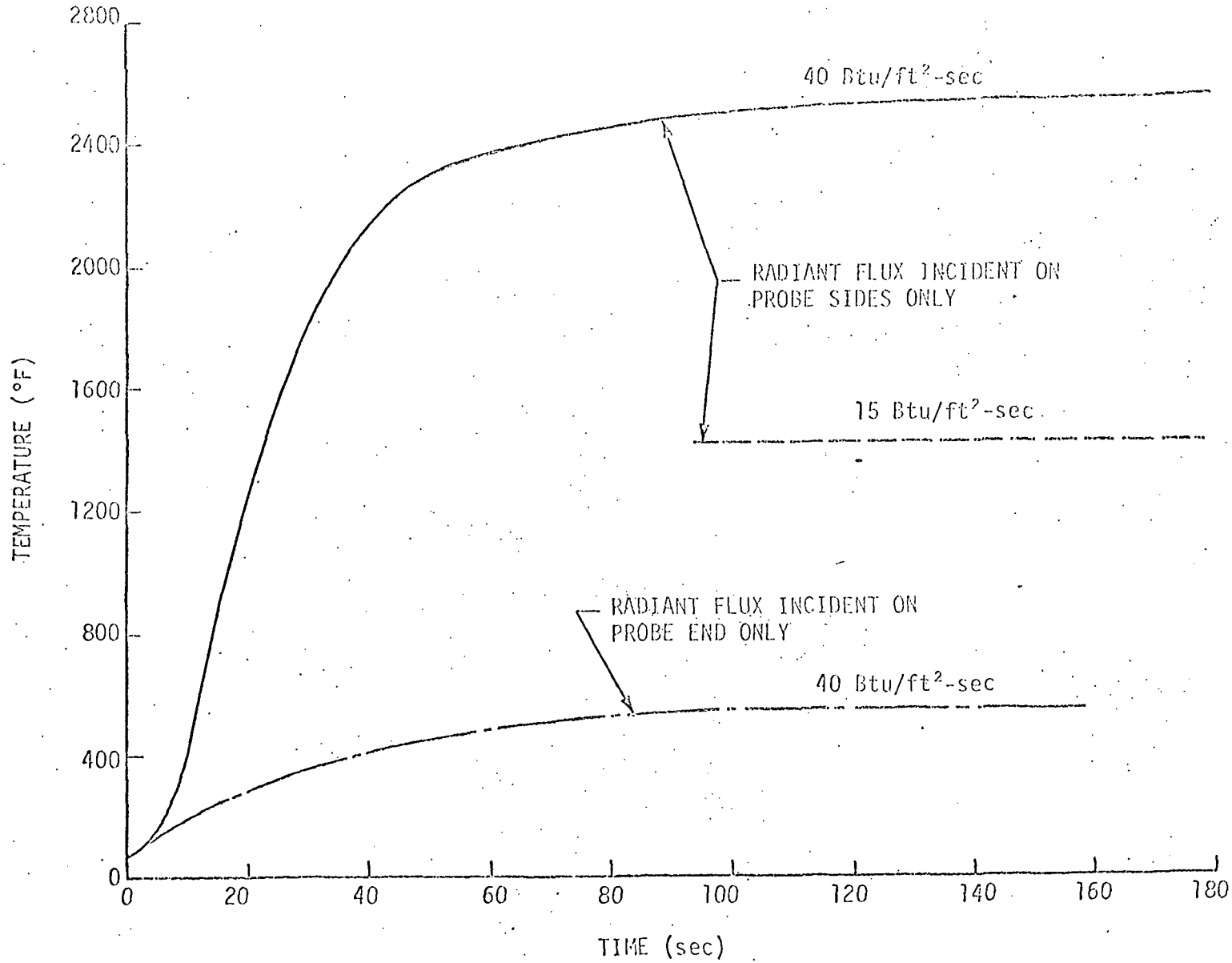

FIGURE 3-12. HEAT SHIELD GAS TEMPERATURE PROBE RESPONSE EXPOSED TO A RADIANT FLUX

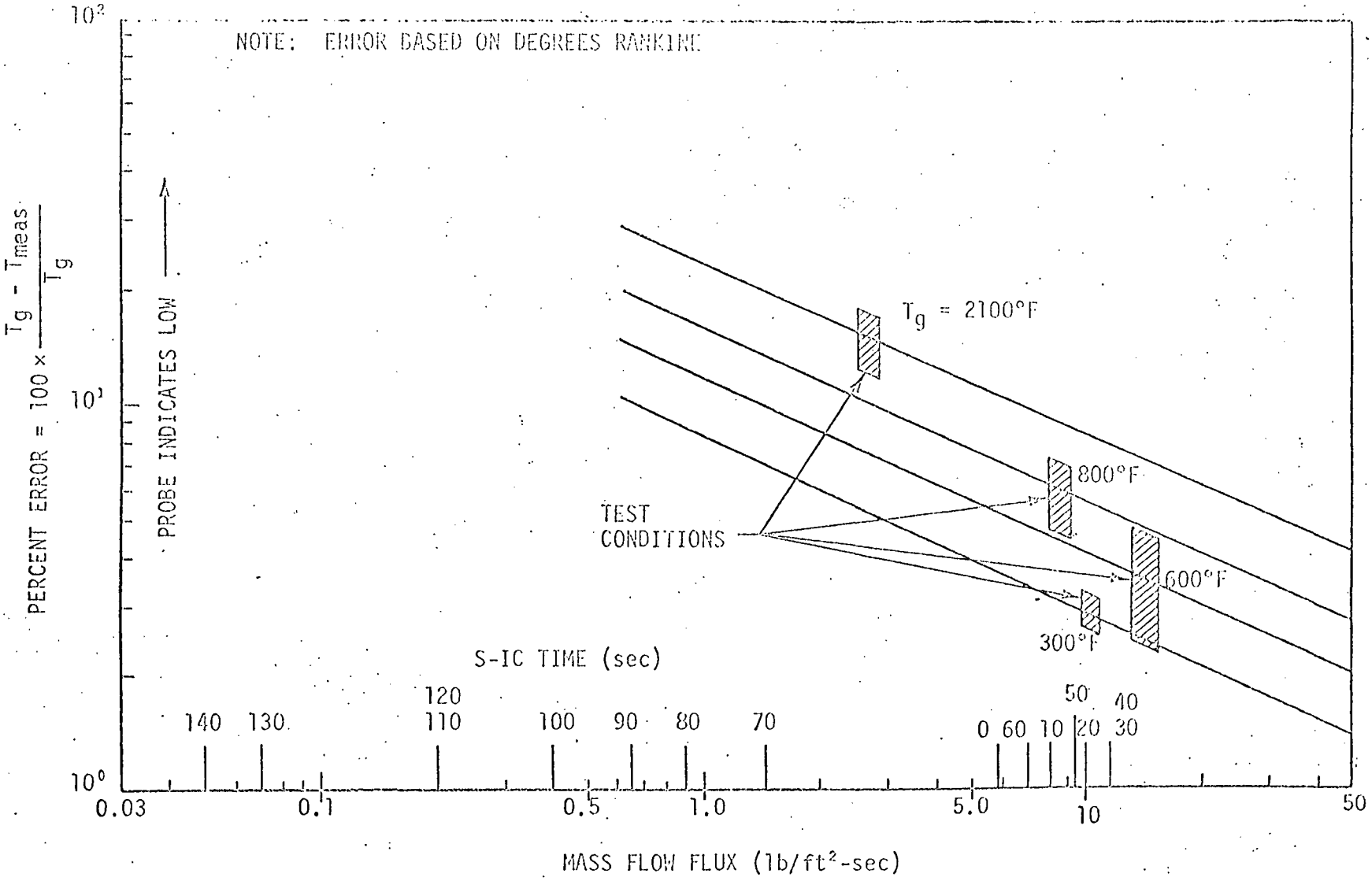

FIGURE 3-13. ENGINE GAS TEMPERATURE PROBE HOT GAS TEST ERRORS

gas temperature was between 20 and 60°F. The latter may appear to be somewhat misleading since it indicates improved accuracy at higher gas temperatures; however, these results actually indicate that with the probe exposed to a 10.6 Btu/ft^2-sec radiant flux the junction equilibrium temperature is closer to the 400°F gas temperature than to the 20 or 60°F gas temperature. This also illustrates that the probe errors tend to be reduced when the probe is exposed to a combined radiant and hot-gas environment.

The Saturn S-II stage gas temperature probes (Figure 3-14) were also tested in a gaseous environment (Ref. 3-7). These tests consisted of exposing the S-II gas temperature probes to the flame of a plasma spray nozzle. The actual gas temperature was measured with a so-called standard thermocouple located in close proximity to the probe junction. All tests were conducted at sea-level, ambient pressure, and the results are shown in Table 3-2. As can be seen in the table, the temperature indicated by the probe is significantly less than that indicated by the standard, particularly at the high-gas temperatures. Another factor which should be considered in these tests is the probable increase in error which would occur with decreased density. Hot gas tests of the other Saturn probes indicated an increase in error as the mass flux (ρu) was decreased. Since the S-II stage probe tests were carried out at sea-level, ambient pressure, it is probable that the density and likewise, the mass flux (ρu), were considerably higher than that which would have been associated with the S-II stage during flight. Therefore, the error in the gas temperature measured by these probes during the flight might be higher than that suggested by Table 3-2.

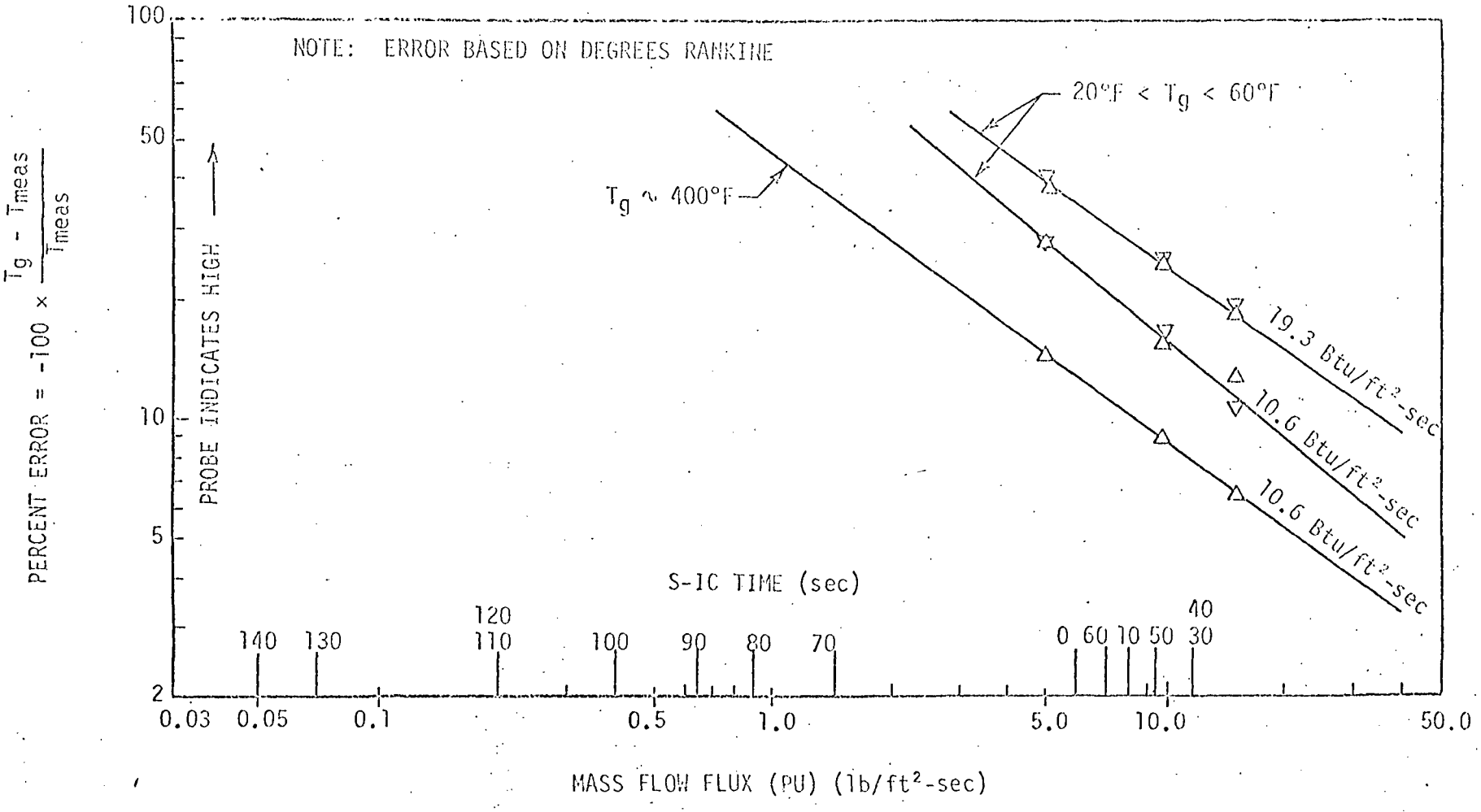

FIGURE 3-14. ENGINE GAS TEMPERATURE PROBE RADIATION TEST ERRORS

TABLE 3-2. SATURN S-II GAS TEMPERATURE PROBE QUALIFICATION TEST RESULTS

GAS TEMPERATURE INDICATED BY STANDARD (°F)	GAS TEMPERATURE INDICATED BY PROBE (°F)	DEVIATION (°F)
1072	930	142
1333	1210	133
1821	1530	291
2172	1800	372
2879	2340	539

During this study attempts were made to correct the flight data by developing very detailed thermal models of the gas temperature probes and surrounding heat shield. The measured flight test data was intended to be used as inputs to the analytical model. These attempts were abandoned when, in the course of the study, it was concluded that so many of the variables necessary for a solution could not be specified with any degree of accuracy and that the computed gas temperature would be at least as questionable as the measured value. As an example, the heat transfer coefficient for the heat shield probe sensing element could be evaluated from the qualification test data.

Figure 3-15 shows a dimensionless Nusselt number/Reynolds number plot of the convective heat transfer to the probe sensing element obtained from the qualification test results. Also shown in this figure is the convective heating to a cylinder normal to the flow obtained from Reference 3-10. As seen in the figure, the qualification test results indicate (approximately) an order of magnitude variation in the convective heat transfer coefficient. The convective heat transfer to a cylinder normal to the flow is one to two orders of magnitude above the results obtained from the qualification tests. The large variation in convective heat transfer to the probe sensing element was possibly caused by the radiation shield. The large deviation in the convective heat transfer

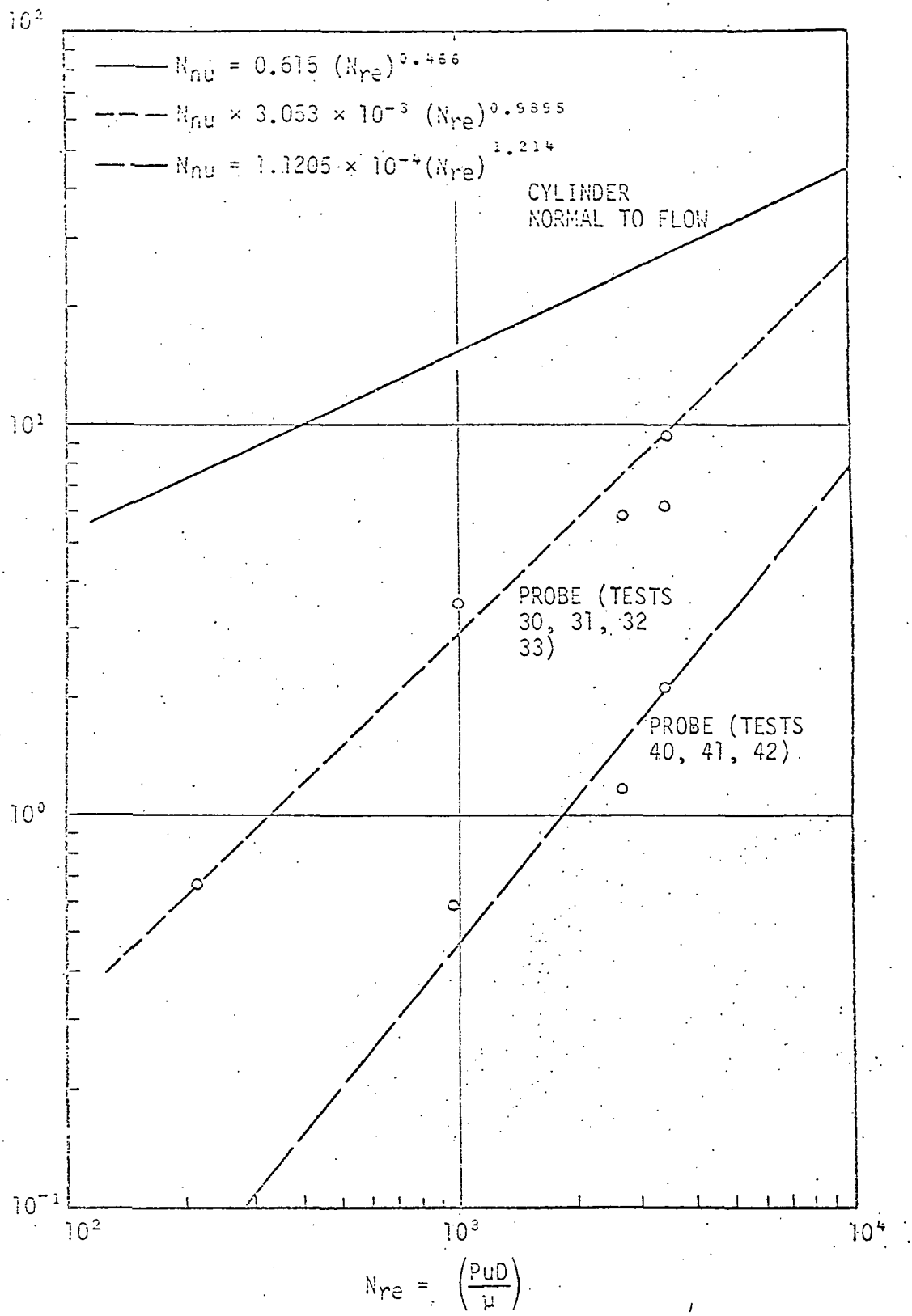

FIGURE 3-15. S-IC HEAT SHIELD GAS TEMPERATURE PROBE CONVECTIVE HEAT TRANSFER RELATIONS

coefficient which would result from this data would make the computed results very questionable.

Sudunas (Refs. 3-5 and 3-6) evaluated the S-II gas temperature probe results using an analytical model of the probe. In this analysis the probe convective coefficients were computed by a circuitous route which involved relating the convective flux measured by the heat flux meters to the probe convective flux. Several important assumptions were necessary in making the analysis and the final results depend upon the correctness of these assumptions; however, the computed gas temperatures were within ±100°F of the measured gas temperatures. The analysis of the S-II stage probes was considerably easier than that required for the S-IC probes because of the absence of a radiation shield and the low incident radiation in the S-II base region.

3.3 TOTAL HEAT FLUX METERS

3.3.1 Physical Description

During the course of the Saturn flight test programs several different types of total and radiant heat flux meters were used. Sketches of some of the different meters and techniques used in evaluating the heat flux from these meters are contained in Volume II, Section 4 of this report. Briefly, two basic types of heat flux meters were used to measure the total heat flux in the Saturn base regions. Some of the characteristics of these meters are presented in the following paragraphs.

Early in the program the so-called slug-type heat flux meter was used. This instrument consisted of a thin, metal slug which was insulated from its surroundings and a thermocouple attached to the slug. The heat flux was evaluated by using various calibration methods which were related to the slope of the measured temperature-time history.

This type of meter was used early in the Saturn program. Continued use disclosed several problems that were inherent to the slug-type meter. The slug could not be completely isolated from the mounting structure; thus, the meters had sizeable conduction losses, particularly at high temperatures. Changes in the thermal properties of the surface coatings limited the maximum temperature to which the meters could be calibrated. Often, during flight use, the meter temperature would exceed the maximum calibration temperature by several hundred degrees, requiring extrapolation of the calibration curves. This caused some doubt as to the validity of the extrapolations because of possible changes in the surface properties and the higher conduction losses. Also, because of the temperature limitations and the high-g environment, a relatively large slug was used. This caused the instrument to have a relatively slow response to the highly transient base environment.

Later in the Saturn program an instrument was developed which did not appear to have most of the undesirable qualities of the slug-type meters. This instrument used a completely different principle for measuring and evaluating the heat flux. This instrument, schematically shown in Figure 3-16, consisted of a thin, constantan foil disk bonded at its periphery to a copper cavity. The copper-constantan formed a thermocouple pair which generated an emf in proportion to the temperature difference between the center of the foil and the edge. The temperature difference is almost proportional to the heat flux incident upon the foil. The mass and heat capacity of the copper was made relatively large in comparison to the mass and exposed area of the foil. As a result, the heat absorbed by the foil was rapidly conducted into the copper. Even when exposed to a relatively high heat flux, this technique prevents the

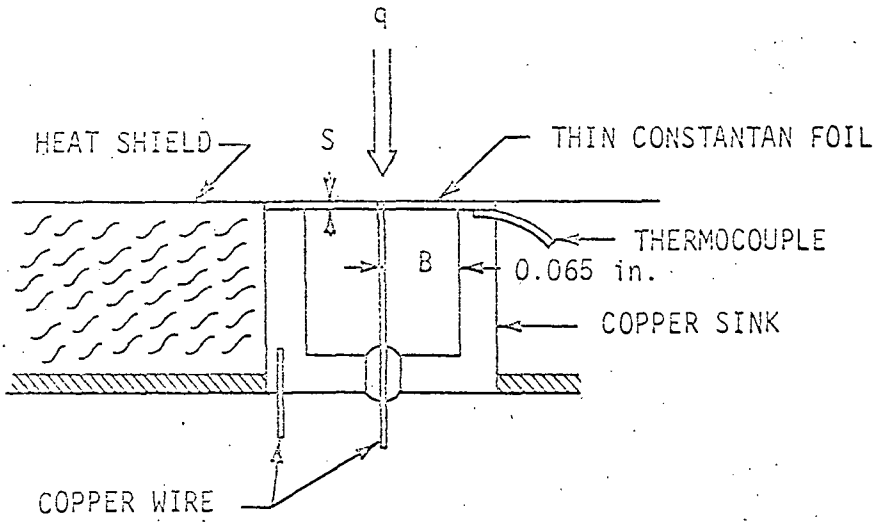

TYPICAL SATURN S-IC TOTAL HEAT FLUX METER CHARACTERISTICS:

RANGE: 0 to 60 Btu/ft^2-sec

0.0645 in. < B < 0.0655 in.

S $\sim$ 0.003 in.

$$q = \sum_{n=0}^{5} A_n C^n \rightarrow \text{(Btu/ft}^2\text{-sec)}, \quad C \text{ - emf output}$$

$A_0 = -0.102$, $A_1 = 6.462$, $A_2 = -0.00959$

$A_3 = 0.00149$, $A_4 = -0.000116$, $A_5 = 0.358 \times 10^{-5}$

FIGURE 3-16. SCHEMATIC OF THIN-FOIL HEAT FLUX METER

center temperature of the foil from rising more than one or two hundred degrees above the temperature of the copper sink, which changes only slightly.

This type of instrument can be made very responsive to changes in heat flux. (The Saturn instruments had response times on the order of 0.150 second.) Another advantage of this instrument is that the heat flux is almost linear with emf over a wide range of heat flux. These instruments were also calibrated and a curve fit of the results has shown that the incident flux for instruments of the same type could be obtained using a fifth order polynomial with variations of less than ±0.3 percent.

Because the surface temperature is important in evaluating the convective flux heat transfer coefficient and cannot be determined from the calorimeter emf output, a separate thermocouple was attached between the foil and the copper (Figure 3-16).

3.3.2 Total Heat Flux Meter Accuracies

When slug-type heat flux meters were utilized, three different techniques were often used to evaluate the heat flux. Each of these techniques gave different results which should be compared when considering the accuracy of the meters. Several comparisons of the measured flux evaluated using the different methods are shown in Volume II (see Figure 7-21 for an example). The data band represented by these methods has often been taken as the realistic accuracy of the individual instruments. However, based upon the techniques used, it would appear that the preflight calibration results should be more realistic during the early portions of the flight, and the cutoff decay results more reliable during the latter phases of the flight.

The stated accuracy of the thin-foil total heat flux meters is ±10 percent; however, the qualification test results (Refs. 4-16 through 4-19 of Volume II) show that accuracies considerably better than ±10 percent can normally be expected from these instruments.

3.3.3 Total Heat Flux Meter Surface Temperature Mismatch Problem

One factor which may have affected all of the total heating rate measurements is the so-called "temperature mismatch problem". This problem, shown schematically in Figure 3-17, is a result of the temperature difference between the surrounding insulation and the heat flux surface. This problem is that if, during the flight, the surface temperature of the insulation is significantly different from the surface temperature of the heat flux meter, the gas boundary layer is perturbated as it crosses the meter; and, since the convective flux is related to the temperature gradient and the thickness of the boundary layer, it is also perturbated. The available experimental and theoretical investigation into this problem (Ref. 3-11) indicates that the Saturn total calorimeters probably indicated a higher heat flux than would have actually existed if the surface had been isothermal and at the same temperature as the heat flux meters. Experimental support for this conclusion can be seen in Figure 3-18.

Figure 3-18 shows some of the experimental results reported in Reference 3-11. These tests were conducted by mounting a membrane calorimeter in an isothermal surface and using an oxyacetylene flame to convectively heat both the isothermal surface and the calorimeter. The location of the calorimeter from the leading edge was varied from 6 to 31.6 inches. Shown in the figure is the ratio of calorimeter heat transfer coefficient to the undisturbed surface coefficient. The

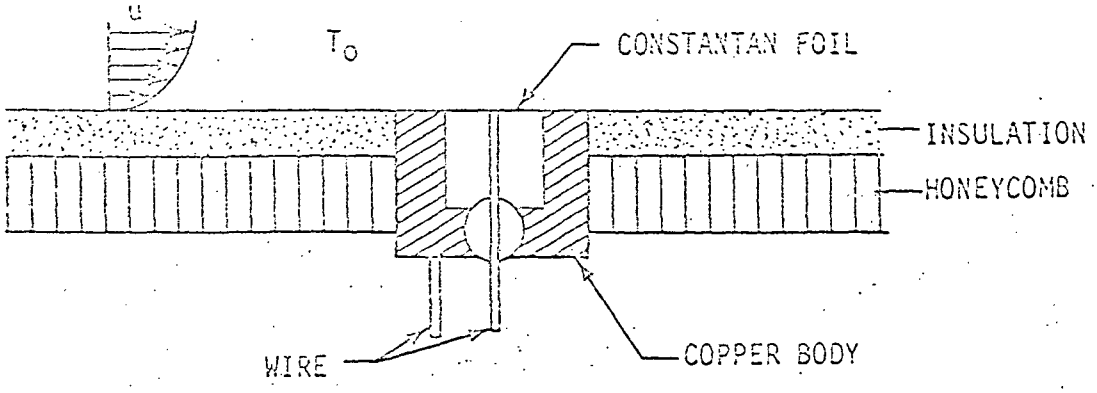

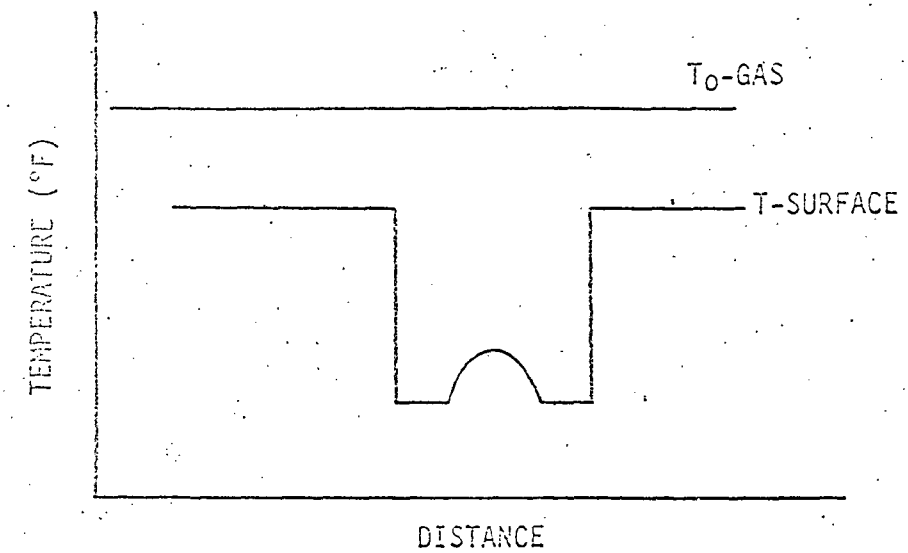

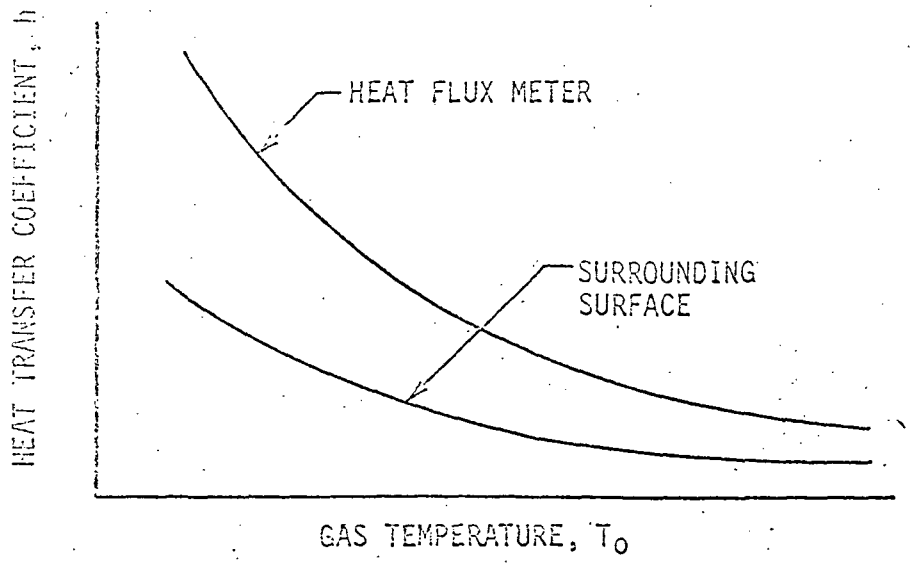

FIGURE 3-17. SCHEMATIC OF HEAT FLUX METER TEMPERATURE MISMATCH PROBLEM

○ $T_1 - T_2$ = 800°F, L = 31.6 in.
△ $T_1 - T_2$ = 1000°F, L = 15 in.
□ $T_1 - T_2$ = 1000°F, L = 6 in.

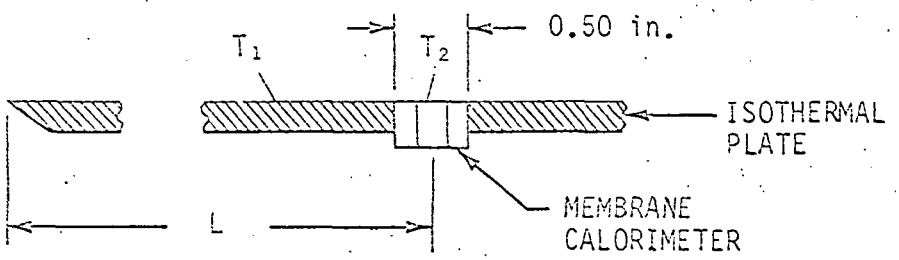

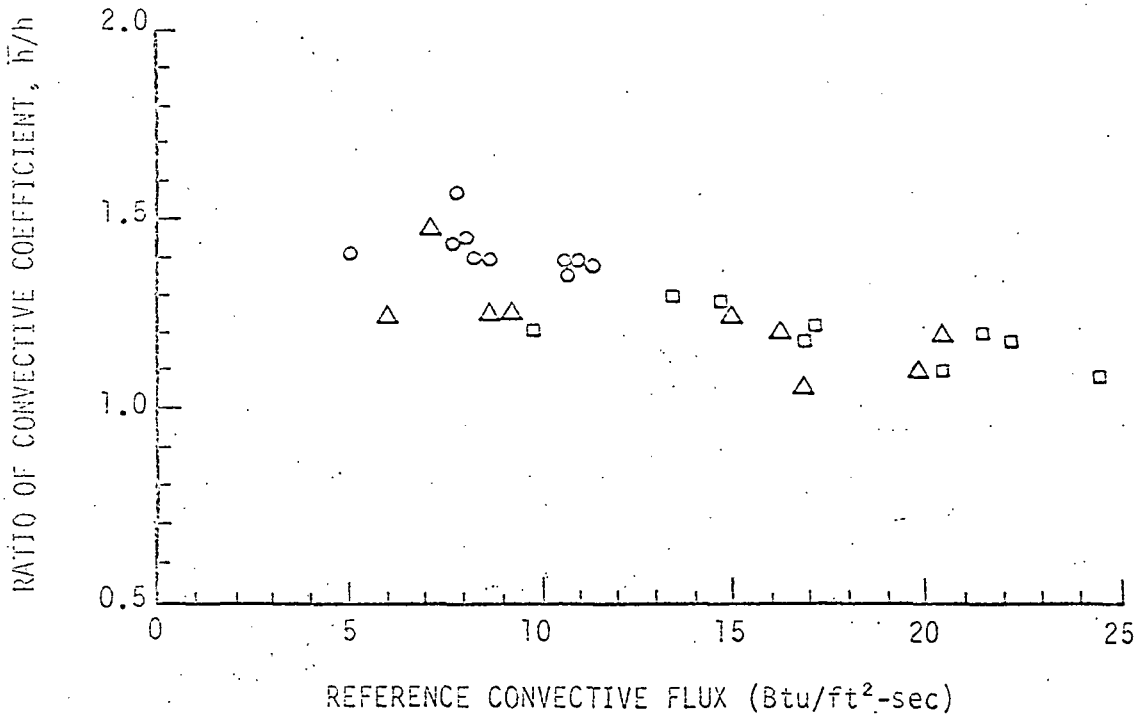

FIGURE 3-18. EFFECT OF TEMPERATURE MISMATCH ON CONVECTIVE COEFFICIENT

The reference convective flux (i.e., convective flux to an undisturbed surface) is shown along the abscissa. The convective flux coefficient indicated by the membrane calorimeter was approximately 1.2 to 1.5 times as great as that of an undisturbed surface.

Some of the Saturn flight test data also tends to support the possibility of higher convective flux measured by the membrane calorimeters. During the Saturn I, Block II flights, one of the instruments was changed from a slug-type heat flux meter to a membrane-type meter, resulting in a different surface temperature. Figure 3-19 shows the predicted surface temperature of the insulation and the measured temperatures of the heat flux meters. According to the temperature mismatch theory, the heat flux indicated by the membrane-type calorimeter should have been higher than that indicated by the slug-type calorimeter. Figure 3-20 shows the total heat flux measured by these meters and tends to indicate that the membrane-type meter did give a higher indication.

3.3.4 Heat Shield Moisture Effects

The effects of moisture absorbed by the heat shield was another factor which probably affected the total heat flux meter measured results. Prior to flight moisture could be and probably is absorbed by the porous heat shield material. During flight the decreasing pressure and heat transferred to the heat shield vaporizes the moisture. The moisture leaving the heat shield insulation enters the boundary layer and contacts the total heat flux meter. Since the temperature of the membrane-type calorimeter is below the saturation temperature of the moisture (see Figure 3-19), the possibility exists that the vapor will condense. Condensation of the moisture on the calorimeter surface would have a pronounced effect upon the measured heat flux. This problem was investigated for NASA by The Boeing Company and the results are reported

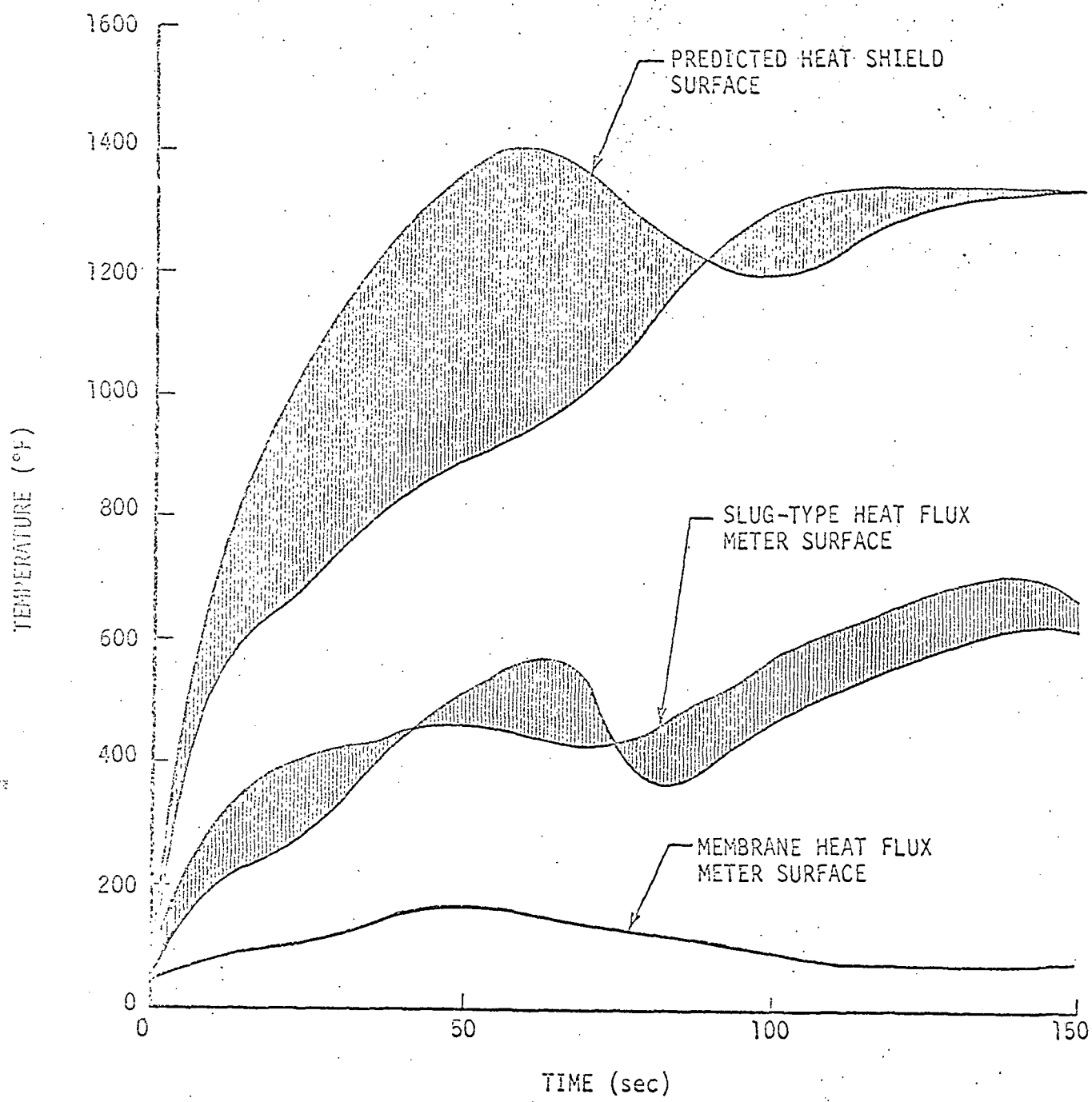

FIGURE 3-19. SATURN I, BLOCK II, CALORIMETER AND HEAT SHIELD SURFACE TEMPERATURES

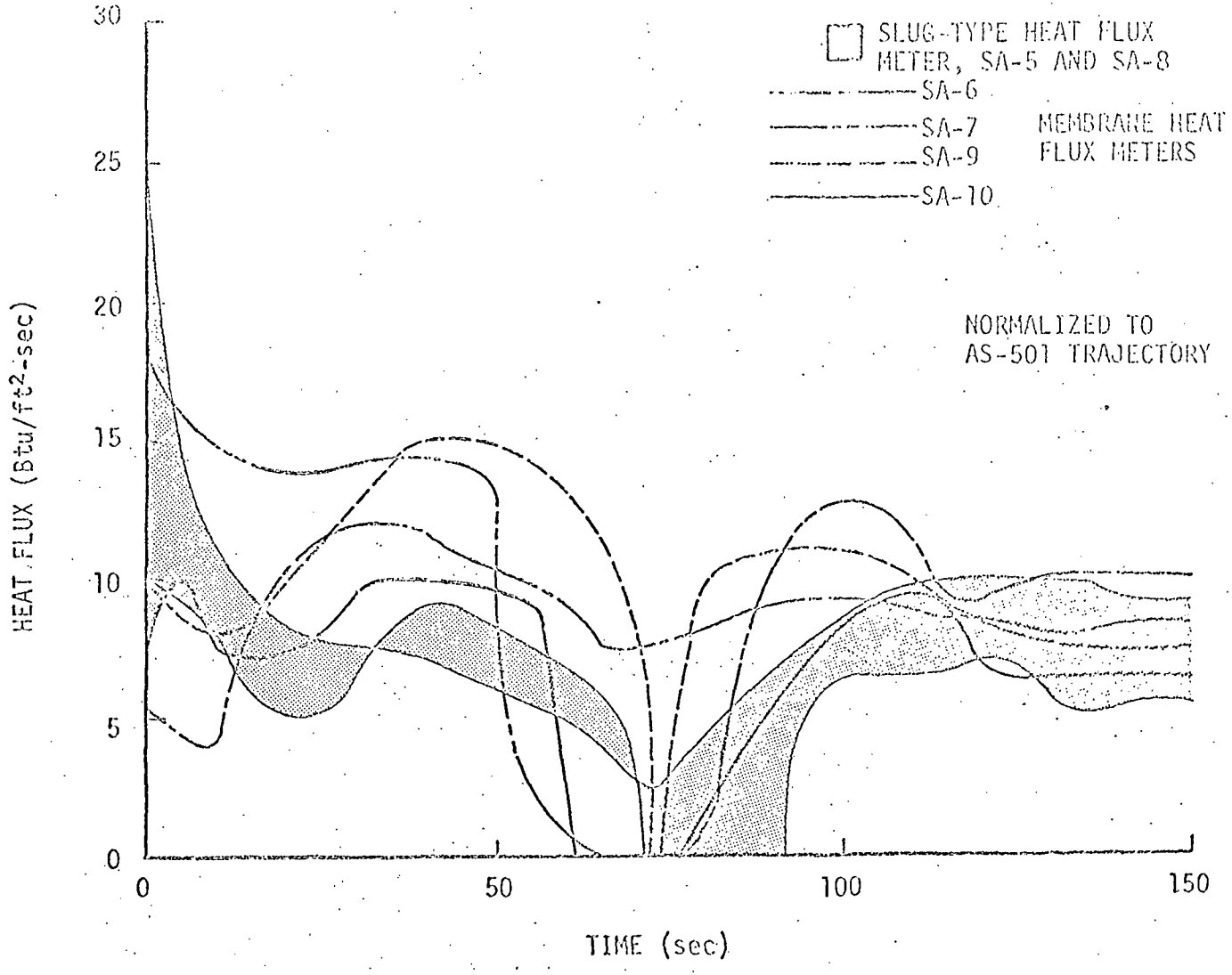

FIGURE 3-20. SATURN I, BLOCK II TOTAL HEAT FLUX MEASURED BY C63-1

Page Intentionally Left Blank

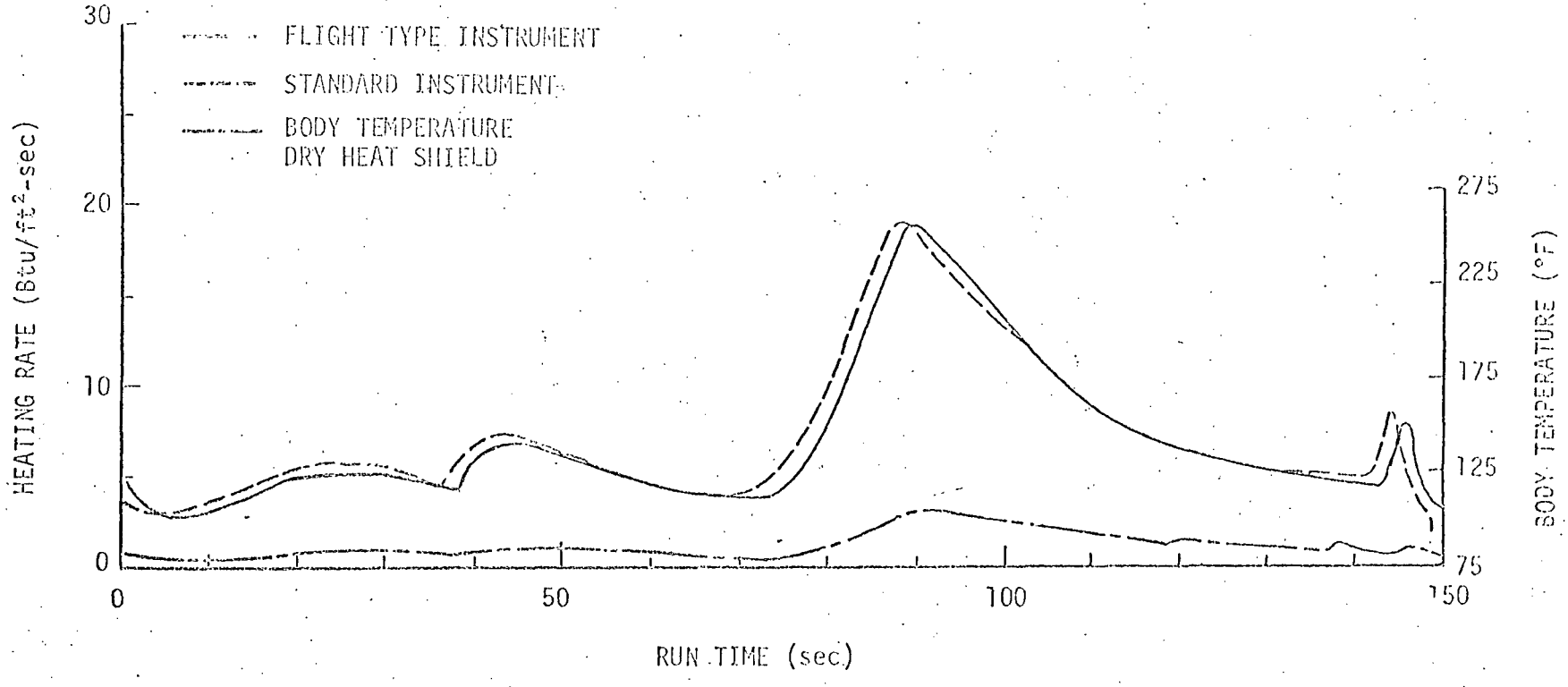

FIGURE 3-21. TOTAL HEAT FLUX MEASURED WITH A DRY HEAT SHIELD

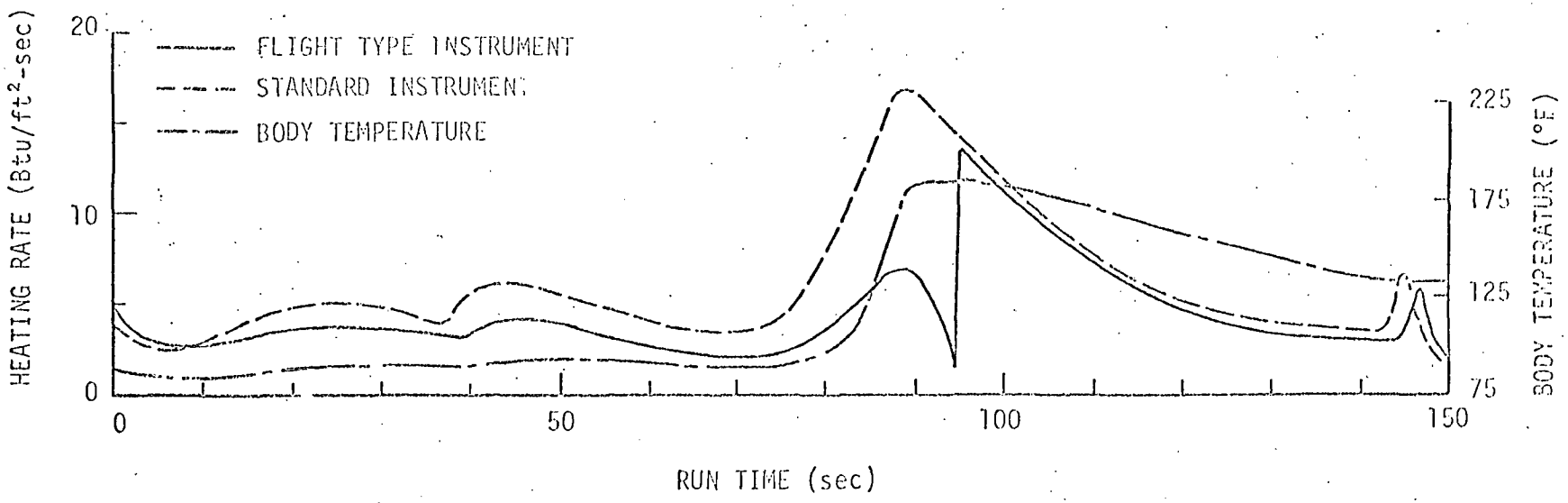

FIGURE 3-22. TOTAL HEAT FLUX MEASURED WITH A WET HEAT SHIELD

During the Saturn program the radiant heat flux was evaluated from these instruments in a manner similar to that used for the total heat flux meters.

3.4.2 Window Transmission Errors

During this investigation, a previously undetected error in the measured flight radiant flux was discovered. This error is related to the manner in which the radiation calorimeters are calibrated, the angular dependence of the sapphire window, and the way in which the instruments are used on the vehicle. Theoretically, it can be shown that the radiation indicated by the S-IC radiation calorimeters is at least 10 percent higher than the actual incident radiation. An explanation of the reason for introduction of the error is presented in the following paragraphs.

During calibration a standard water-cooled calorimeter and a test instrument are simultaneously exposed to an electrically heated graphite plate. The graphite heater is specially designed to radiate spectrally like a very good greybody. Both instruments are placed in close proximity to the plate, giving a view factor of very near unity (i.e., the view factor from the front surface of the test instrument is unity, not the view factor to the sensing element).

Because of the window transmissivity and its angular dependence, the radiant energy reaching the sensing element is much less than that reaching the standard calorimeter. Calibration of the instrument is carried out by equating the emf output of the test instrument to the heat flux being measured by the standard calorimeter. This equates the radiant energy which was absorbed by the sensing element to that which was incident upon the front of the instrument.

If the radiation which is excluded from the radiation sensing element is considered in some detail, it becomes obvious how the errors occur. First, the spectral transmissivity of the sapphire window (in the normal direction) is high ($\tau \sim 0.9$) between $\lambda \approx 0.2$ micrometer and $\lambda \sim 5.0$ micrometers. Beyond these wavelengths the transmissivity rapidly drops to zero; therefore, any radiant energy emitted by the calibration source which is less than $\lambda \approx 0.2$ micrometer, greater than $\lambda \approx 5.0$ micrometers, and approximately 10 percent of that between these limits is excluded from the sensing element by the window. Second, the sensing element is slightly below the front face of the meter and, therefore, views the calibration source through a hole. The resulting effective view angle through which the sensor sees the calibration source for the S-IC calorimeters was approximately 150 degrees. Therefore, any radiant energy approaching the calorimeter at an angle of more than 75 degrees to the normal would not reach the sensor but would be intercepted by the calorimeter housing. Third, the transmissivity of the sapphire window normal to the surface is approximately $\tau \sim 0.9$; however, window transmissivity has an angular dependence. When the angle to the normal is 60 degrees, the transmissivity had dropped from $\tau \sim 0.9$ to $\tau \sim 0.775$ and at 70 degrees, $\tau \sim 0.6$. When the angular transmissivity is integrated over the entire effective view angle of a radiation calorimeter the effective transmissivity obtained in $\tau \sim 0.79$. Therefore, the difference between $\tau \sim 0.9$ and $\tau \sim 0.79$ is an additional amount of radiant energy which does not reach the sensing element.

When the radiation calorimeters are used to measure the radiation in an unknown environment, the three excluded radiant energy sources are automatically included in the calibration. If the view factor to the radiation source is near unity, and the source radiates like a greybody, then the incident radiation indicated by the instrument

is approximately correct. However, if the instrument is exposed to a source which has a view factor significantly less than unity, an error is introduced by the calibration in which excluded radiant energy had been automatically included. The Saturn heat shield radiation calorimeters experienced this problem, resulting in an error which has been estimated to be approximately 10 to 12 percent.

An additional error can be introduced if the radiant source does not emit like a greybody. Greybody radiation suggests that the source emits radiation which is spectrally a constant percent of the corresponding blackbody radiation (i.e., the emissivity is independent of wavelength). The calorimeter window allows only radiation between 0.2 micrometer $\lesssim \lambda \lesssim$ 5.0 micrometers to pass through; however, the excluded energy is included in the calibration because radiation over all wavelengths is absorbed by the standard instrument. Therefore, if the test instrument is exposed to a radiant source which emits radiation significantly different from greybody radiation in the regions 0.2 micrometer $> \lambda$, $\lambda \gtrsim 5.0$ micrometers (i.e., outside of the spectral range of sapphire), this will not be accurately indicated in the calibration. For vehicles using LOX/RP-1 propellants, this may or may not be a significant source of error since the plumes appear to emit approximately greybody radiation (see Figure 6-13b). However, for vehicles using LOX/H_2 propellants, the error could be significant because the radiant energy from these plumes is not of the greybody type (see Figure 6-13a).

3.4.3 Derivation of the Window Angular Transmission Effects

Figure 3-23 shows schematically a calibration test arrangement that depicts the window angular transmissivity dependence. The radiant energy emitted by dA_1 that passes through the window and is directly incident upon dA_2 is given by

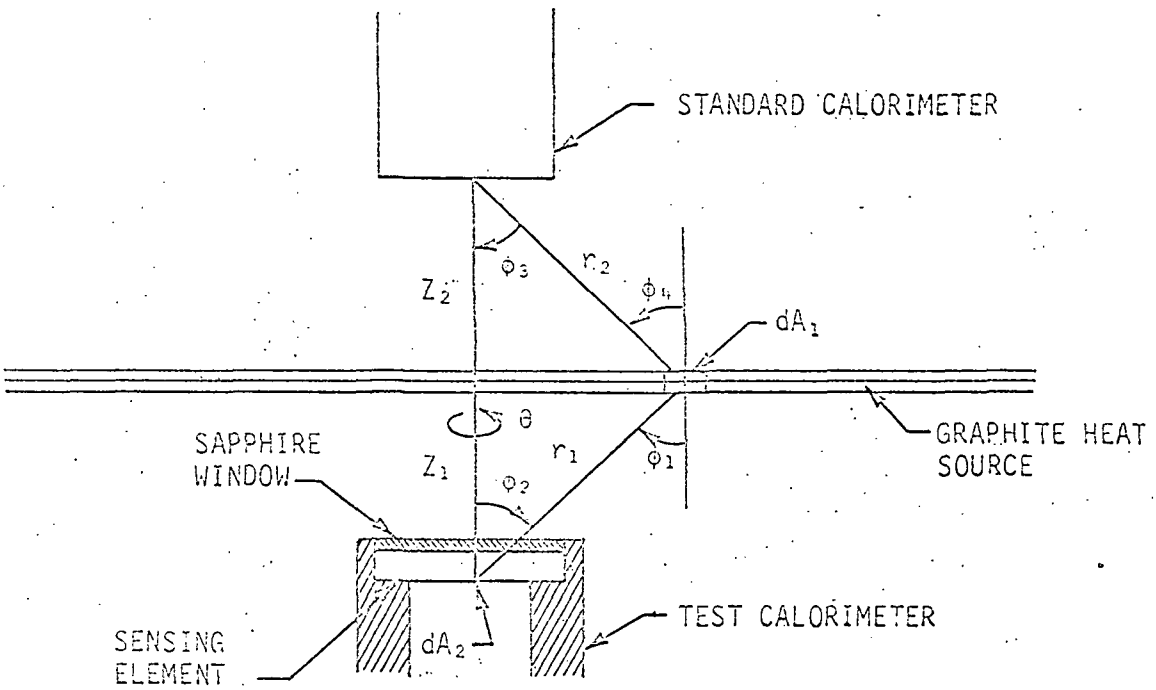

FIGURE 3-23. SCHEMATIC OF RADIATION CALORIMETER CALIBRATION

$$dQ_{A_1-A_2} = \tau_W(\phi_2, \lambda)\, I_1(\phi_1, \lambda)\, dA_1\, d\omega_{1-2}\, d\lambda \qquad (3\text{-}23)$$

where

$dQ_{A_1-A_2}$ - radiant energy emitted by dA_1 and incident upon dA_2

τ_W - window transmissivity

I_1 - radiant intensity of dA_1

$d\omega_{1-2}$ - solid angle intercepted by dA. as seen from dA_1.

Using Lambert's cosine law

$$I_1(\phi_1, \lambda) = I_1(\lambda) \cos \phi_1$$

the Stephan-Boltzmann relation

$$I_1(\lambda) = \frac{E_1(\lambda)}{\pi} \qquad (3\text{-}24)$$

and the definition of solid angle

$$d\omega_{1-2} = \frac{\cos \phi_2\, dA_2}{r_1^2}\,, \qquad (3\text{-}25)$$

Equation 3-23 can be written as

$$dQ_{A_1-A_2} = \frac{\tau_W(\phi_2, \lambda)\, E_1(\lambda) \cos \phi_1 \cos \phi_2\, dA_1\, dA_2\, d\lambda}{\pi r_1^2}\,. \qquad (3\text{-}26)$$

By making the following substitutions

$$dq_{A_1-A_2} = \frac{dQ_{A_1-A_2}}{dA_2}$$

and (see Figure 3-23)

$$\phi_1 = \phi_2 = \phi_3 = \phi_4 = \phi$$

$$dA_1 = Z^2 \frac{\sin\phi}{\cos^3\phi} \, d\theta \, d\phi \ ,$$

and

$$r_1^2 = \frac{Z^2}{\cos^2\phi} \ .$$

Equation 3-26 becomes

$$q_{A_1 - dA_2} = \int_\lambda \int_\theta \int_\phi \frac{\tau_W(\phi, \lambda) \, E_1(\lambda) \cos\phi \ \sin\phi \, d\phi \, d\theta \, d\lambda}{\pi} \tag{3-27}$$

where

$q_{A_1 - dA_2}$ - radiant energy emitted by A_1 that is directly incident upon sensor differential element dA_2

θ - angle about the axis (see Figure 3-23).

Equation 3-27 is the basic equation giving the radiant energy emitted by the calibration source that passes through the window and strikes the sensing element.

For the standard instrument which is assumed to be a minor image of the test instrument with $\tau_\omega = 1$, Equation 3-27 can be integrated in closed form to give

$$q_{A_1 - Std} = \int_{\lambda=0}^{\lambda=\infty} E_1(\lambda) \, d\lambda \int_{\theta=0}^{\theta=2\pi} \int_{\phi=0}^{\phi=\frac{\pi}{2}} \frac{\cos\phi \ \sin\phi \ d\phi \ d\theta}{\pi}$$

$$q_{A_1\text{-Std}} = \int_{\lambda=0}^{\lambda=\infty} E_1(\lambda)\, d\lambda = \epsilon_1 \sigma T_1^4 \quad . \tag{3-28}$$

Equation 3-27 for the radiant flux meter cannot be separated because the transmissivity of the window is a function of the polar angle, ϕ, and the wavelength, λ. Shown in Figure 3-24 are the sensor absorptivity, and the window transmissivity and refractive index. From this figure it can be seen that the transmissivity can be roughly approximated by a square wave with

$$\begin{aligned} &0 \leqq \lambda \leqq 0.2\ \mu, && \tau_W = 0 \\ &0.2\ \mu \leqq \lambda \leqq 5.0\ \mu, && 0.84 \leqq \tau_W \leqq 0.9 \\ &5.0 \leqq \lambda \leqq \infty, && \tau_W = 0 \quad . \end{aligned} \tag{3-29}$$

Since the transmissivity of the window is a function of the polar angle, ϕ, this must also be considered. Figure 3-25 shows how an incident beam of radiation is refracted and reflected as it passes through the window. A portion of the energy is reflected at both the front and rear surfaces of the window.

From the theory of optics (Ref. 3-16), the angular transmittance is given by

$$\tau(\phi) = \tau'(\phi)\ [1 - \rho(\phi)]^2 \tag{3-30}$$

where

$$\tau'(\phi) = \exp\left(-\frac{\kappa\ x}{\cos\phi'}\right) \tag{3-31}$$

$$\phi' = \sin^{-1}\left(\frac{\sin\phi}{N}\right) \tag{3-32}$$

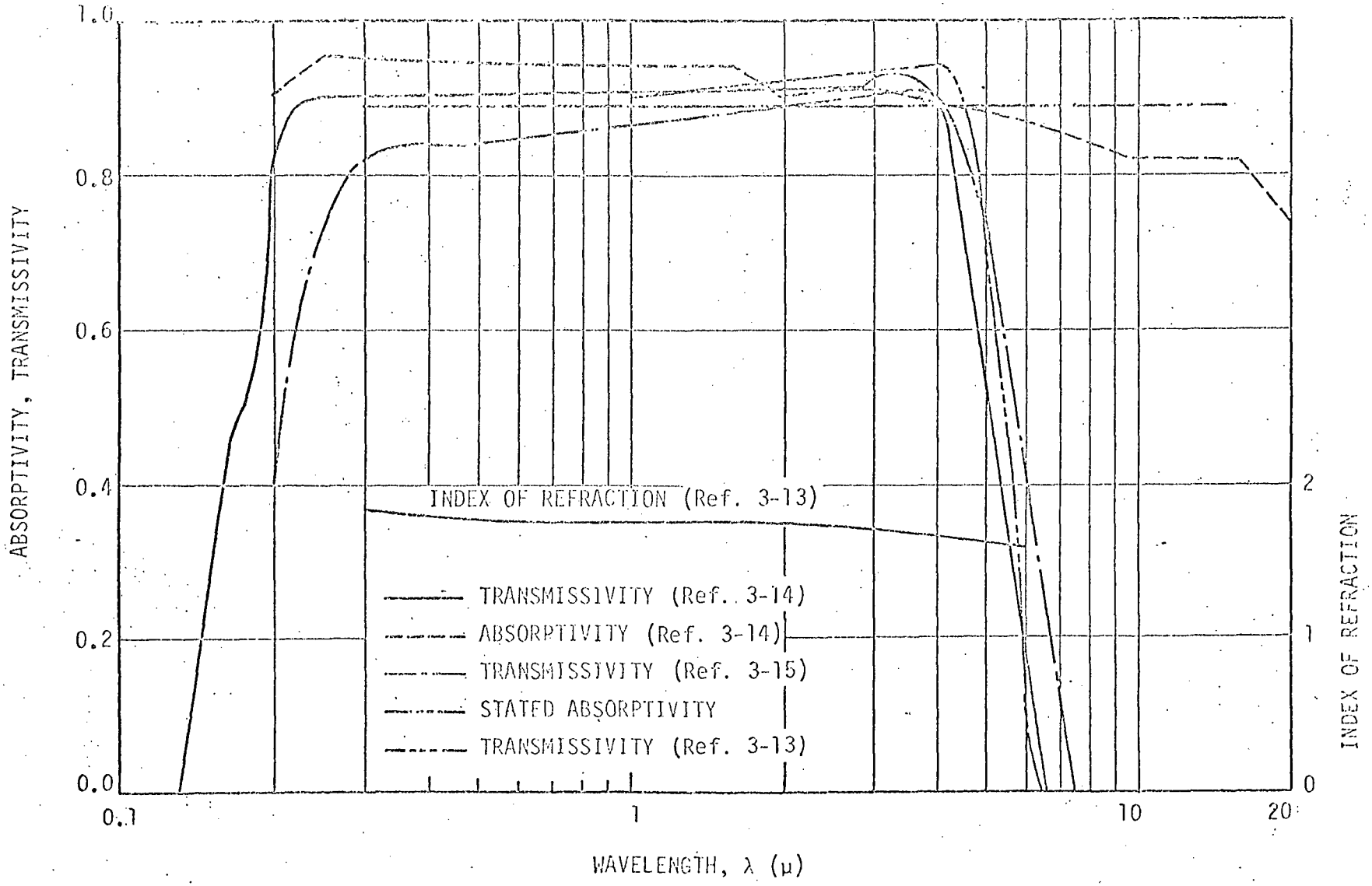

FIGURE 3-24. RADIATION CALORIMETER, SENSOR ABSORPTIVITY, AND WINDOW TRANSMISSIVITY AND REFRACTIVE INDEX

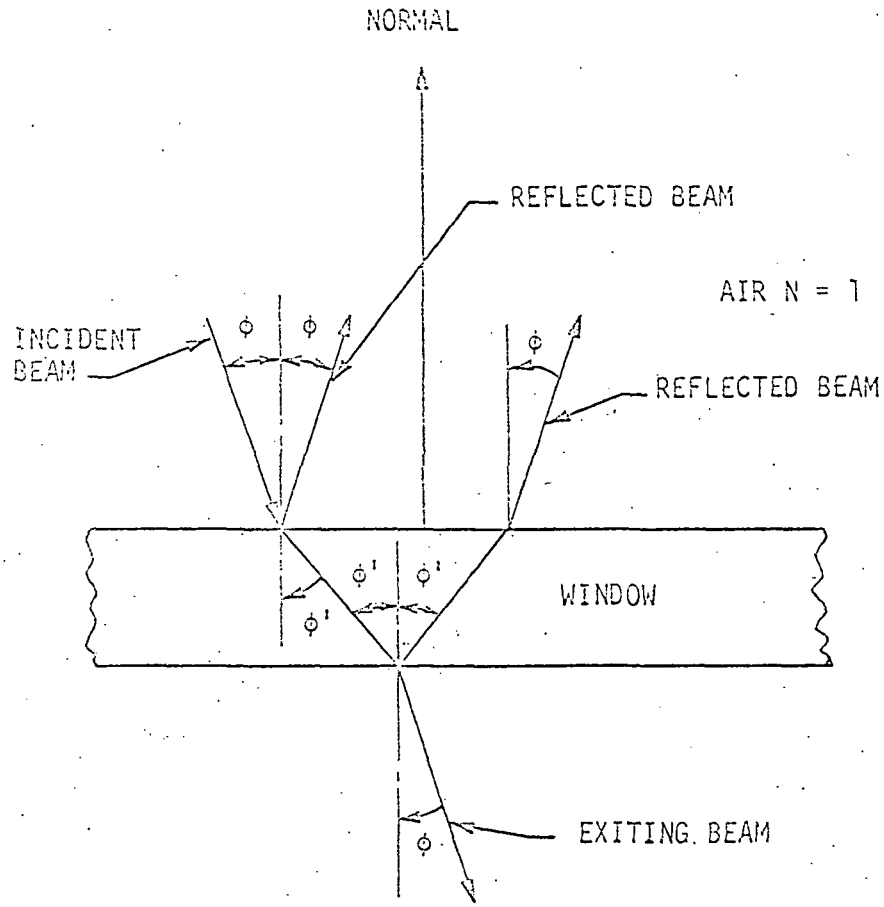

FIGURE 3-25. WINDOW REFRACTIONS AND REFLECTIONS

$$\rho(\phi) = \frac{1}{2}\left[\frac{\sin^2(\phi - \phi')}{\sin^2(\phi + \phi')} + \frac{\tan^2(\phi - \phi')}{\tan^2(\phi - \phi')}\right] \quad (3\text{-}33)$$

$$\rho_n = \left(\frac{N - 1}{N + 1}\right)^2 \quad (3\text{-}34)$$

$$\kappa = -\frac{\ell n\left[\frac{\tau_n}{(1 - \rho_n)^2}\right]}{x} \quad (3\text{-}35)$$

and

$\tau(\phi)$ - angular transmittance

τ_n - transmittance in the normal direction

τ' - angular transmittance without reflections

$\rho(\phi)$ - angular reflection

ρ_n - normal reflection

N - refractive index

κ - absorption coefficient

x - thickness in the normal direction.

Using a window thickness of 0.020 inch and normal transmissivities of $\tau_n = 0.84$ and $\tau_n = 0.9$, the radiation calorimeter window angular transmissivity was computed using Equations 3-30 through 3-35; the results are shown in Figure 3-26.

Equation 3-27, which gives the radiant energy incident upon the sensor, still cannot be integrated directly. Letting τ_{eff} be an effective transmissivity of the window which depends on the geometry of the source with respect to the test instrument, Equation 3-27 can be written as

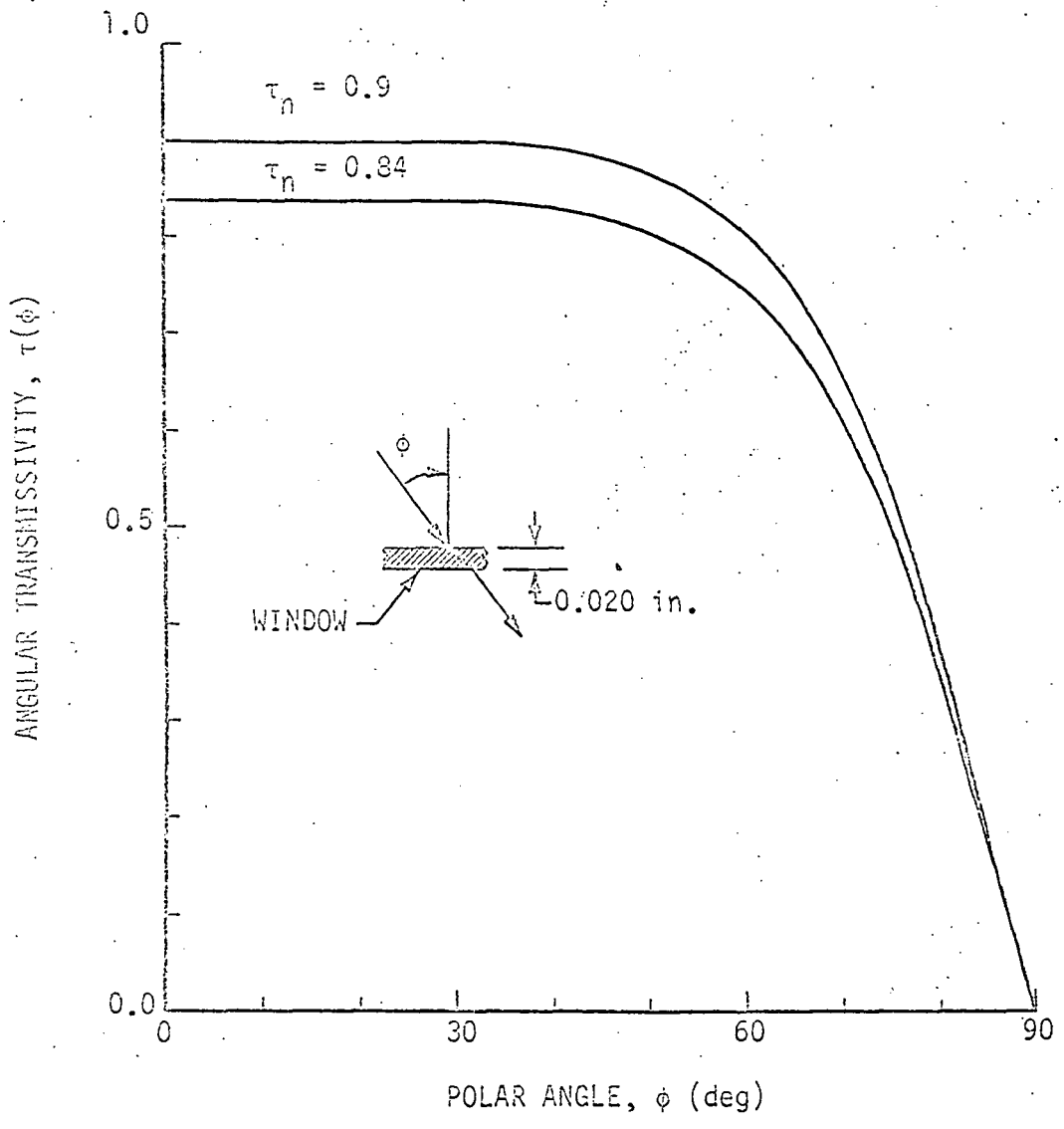

FIGURE 3-26. RADIATION CALORIMETER WINDOW ANGULAR TRANSMISSIVITY

$$q_{A_1 - dA_2} = \int_{\lambda=0.2}^{\lambda=5.0} E_1(\lambda)\, d\lambda \int_{\theta=0}^{\theta=2\pi} \frac{d\theta}{\pi} \int_{\phi_1}^{\phi_2} \tau(\phi) \cos\phi \sin\phi \, d\phi$$

$$= \tau_{eff} \int_{\lambda=0.2}^{\lambda=5.0} E_1(\lambda)\, d\lambda \int_{\theta=0}^{\theta=2\pi} \int_{\phi_1}^{\phi_2} \frac{\cos\phi \sin\phi \, d\phi \, d\theta}{\pi}$$

$$= \tau_{eff} \; F_{A_1 - dA_2} \int_{\lambda=0.2}^{\lambda=5.0} E_1(\lambda)\, d\lambda \; . \qquad (3\text{-}36)$$

Then by comparing the first and third equations and integrating over θ it can be seen that

$$\tau_{eff} = \frac{2 \int_{\phi_1}^{\phi_2} \tau(\phi) \cos\phi \sin\phi \, d\phi}{F_{A_1 - dA_2}} \qquad (3\text{-}37)$$

where τ_{eff} is the effective transmissivity of the window considering angular dependence.

Numerically integrating Equation 3-37 over the effective view angle of the calorimeter gives

$\tau_n = 0.90$, $\quad \tau_{eff}^{(\phi = 90)} = 0.7895$

$\tau_n = 0.84$, $\quad \tau_{eff}^{(\phi = 90)} = 0.734$.

From the results above it can be seen that the transmissivity of the calorimeter window is reduced significantly as a result of the angular dependence.

During calibration the standard instrument and the test calorimeter are exposed to the same heat flux and the emf output of the test instrument is recorded. By assuming that the standard calorimeter

was itself calibrated so that it actually indicates the true incident flux and, assuming a test instrument sensor absorptivity of $\alpha = 0.9$ (Figure 3-22), a relation similar to the calibration can be developed. Using a view factor of unity and multiplying Equation 3-36 by the absorptivity gives the heat flux absorbed by the instrument sensor during calibration as

$$q_{A_1\text{-Sen}} \approx \alpha_S \tau_{eff} \int_{\lambda=0.2}^{\lambda=5.0} E_1(\lambda)\, d\lambda \qquad (3\text{-}38)$$

which gives, for the conditions $\tau_n = 0.9$, $\tau_n = 0.84$, and $\tau_{eff} = \tau_{eff}$ $(\phi = 90)$

$$\tau_n = 0.9, \quad \alpha_S = 0.9, \quad q_{A_2\text{-Sen}} = 0.711 \int_{\lambda=0.2}^{\lambda=5.0} E_1(\lambda)\, d\lambda$$

and

$$\tau_n = 0.84, \quad \alpha_S = 0.9, \quad q_{A_2\text{-Sen}} = 0.66 \int_{\lambda=0.2}^{\lambda=5.0} E_1(\lambda)\, d\lambda$$

where $q_{A_2\text{-Sen}}$ is the approximate heat flux absorbed by the sensor during calibration.

Assuming an emissivity of $\epsilon_1 = 1.0$ for the calibration heat source, Equation 3-28 gives the incident flux indicated by the standard instrument. From the latter and Equation 3-38 the calibration relation, which is shown in Figure 3-27, can be established. By considering the flux absorbed by the sensor, both during calibration and during exposure in the unknown environment, the error introduced can be identified and approximately corrected.

Page Intentionally Left Blank

During calibration the test instrument is exposed to a heat source with a view factor of unity. Using the standard instrument's indication of the incident flux and the measured emf, the flux absorbed by the sensor is related to that incident on the window. During exposure to an unknown flux, the process is reversed. The flux absorbed by the instrument generates an emf which is then related to the incident flux indicated during calibration. An error can be introduced because the unknown incident flux is equal to the incident flux during calibration only when the conditions are identical, i.e., when the emitted flux is of the grey-body type and the view factor is unity.

For the conditions which existed during calibration, the effective transmissivity of the window has been shown to vary between $0.734 \leqq \tau_{eff}\ (\phi = 90) \leqq 0.7895$ because of the angular dependence of the window transmissivity. During exposure in an unknown environment it must be assumed that the instrument will be exposed to a source which does not fill the complete field of view of the instrument. For this condition the effective transmissivity is different from that which existed during calibration and, as a result, more of the energy incident upon the window will arrive at the sensor. In order to correct for this difference, it is necessary to know the emf-incident flux characteristics of the instrument for effective transmissivities other than that associated with the original calibration (i.e., $0.734 \leq \tau_{eff}\ (\phi = 90) \leq 0.7895$). An approximate correction procedure can be developed by determining how the incident flux would have varied with changes in the effective transmissivity while holding the flux absorbed by the sensor constant.

By integrating Equation 3-37 over limits which range from $\phi_1 = 0$ to ϕ_2, the effective transmissivity as a function of ϕ_2 can be obtained. Thus

$$\tau_{eff}(\phi_2) = \frac{\int_{\phi=0}^{\phi_2} \tau(\phi) \cos\phi \sin\phi \, d\phi}{\int_{\phi_1=0}^{\phi_2} \cos\phi \sin\phi \, d\phi} \qquad (3\text{-}39)$$

which becomes

$$\tau_{eff}(\phi_2) = \frac{2\int_{\phi=0}^{\phi_2} \tau(\phi) \cos\phi \sin\phi \, d\phi}{\sin^2 \phi_2} \qquad (3\text{-}40)$$

The results obtained by numerically integrating Equation 3-40 for τ_n = 0.84 and τ_n = 0.9 are shown in Figure 3-28.

From the condition that the absorbed flux must be the same for any effective transmissivity, Equations 3-36 and 3-38 give

$$(q_{A_1}\text{-Sen})_{cal} = \left[\alpha_S \tau_{eff}(\phi_2 = 90) \int_{\lambda=0.2}^{\lambda=5.0} E_1(\lambda) \, d\lambda\right]_{cal}$$

$$= \left[\alpha_S \tau_{eff}(\phi_2) \int_{\lambda=0.2}^{\lambda=5.0} E_1(\lambda) \, d\lambda\right]_{test} \qquad (3\text{-}41)$$

where

$(q_{A_1}\text{-Sen})_{cal}$ - flux absorbed by the sensor during the calibration evaluated from Figure 3-27 or Equation 3-38

$\tau_{eff}(\phi_2)$ - the effective transmissivity corresponding to radiation incident upon the instrument window from a source subtending angle ϕ_2.

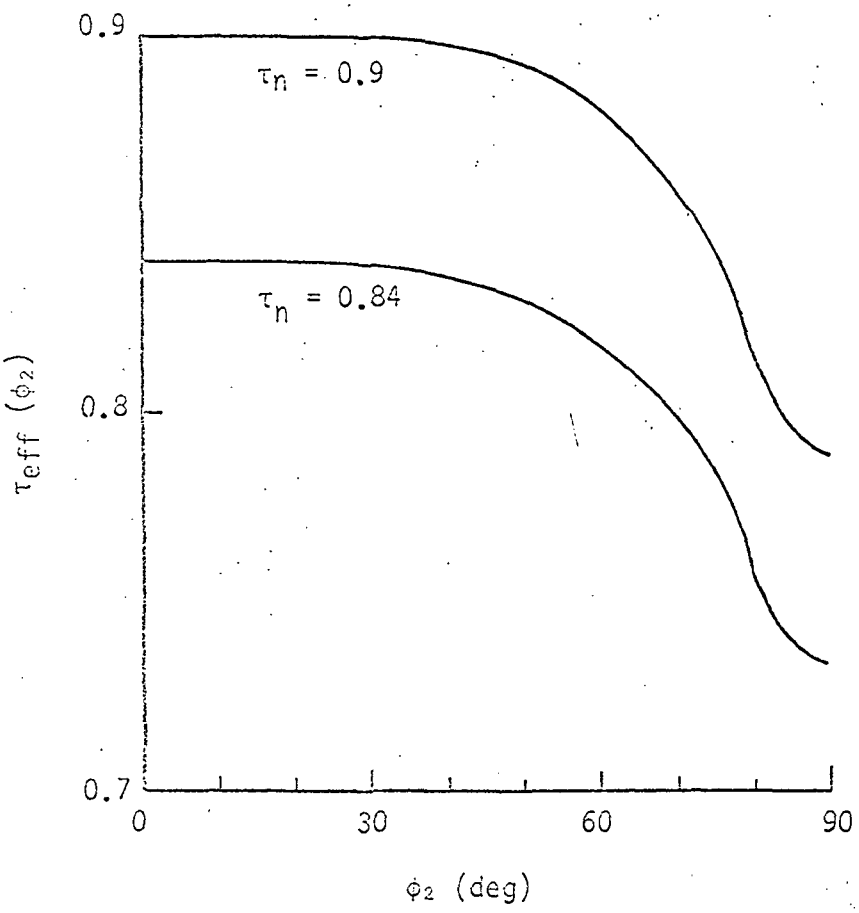

FIGURE 3-28. RADIATION CALORIMETER ANGULAR EFFECTIVE TRANSMISSIVITY

Rewriting Equation 3-41 gives

$$\left[\int_{\lambda=0.2}^{\lambda=5.0} E_1(\lambda)\, d\lambda\right]_{test} = \frac{(q_{A_1} - Sen)_{cal}}{\alpha_S\, \tau_{eff}(\phi_2)} \qquad (3\text{-}42)$$

where $\left[\int_{=0.2}^{=5.0} E_1(\lambda)\, d\lambda\right]_{test}$ is the flux over the interval $0.2 \leqq \lambda \leqq 5.0$ that would be incident upon the window of an equivalent instrument with $\tau_{eff}(\phi_2)$ during calibration to produce the same absorbed flux. Knowing the incident flux over the interval $0.2 \leqq \lambda \leqq 5.0$, it is then possible to compute the incident flux over all wavelengths using Planck functions, thus

$$q_{ir} = \left[\int_{\lambda=0}^{\lambda=\infty} E_1(\lambda)\, d\lambda\right]_{test} = \left[\int_{\lambda=0}^{\lambda=0.2} E_1(\lambda)\, d\lambda + \int_{\lambda=0.2}^{\lambda=5.0} E_1(\lambda)\, d\lambda + \int_{\lambda=5.0}^{\lambda=\infty} E_1(\lambda)\, d\lambda\right]_{test} \qquad (3\text{-}43)$$

To assist in evaluating the incident flux from Equation 3-43, the Planck function over the intervals $0 \geqq \lambda \leqq \infty$ and $0.2 \leqq \lambda \leqq 5$ is plotted in Figure 3-29.

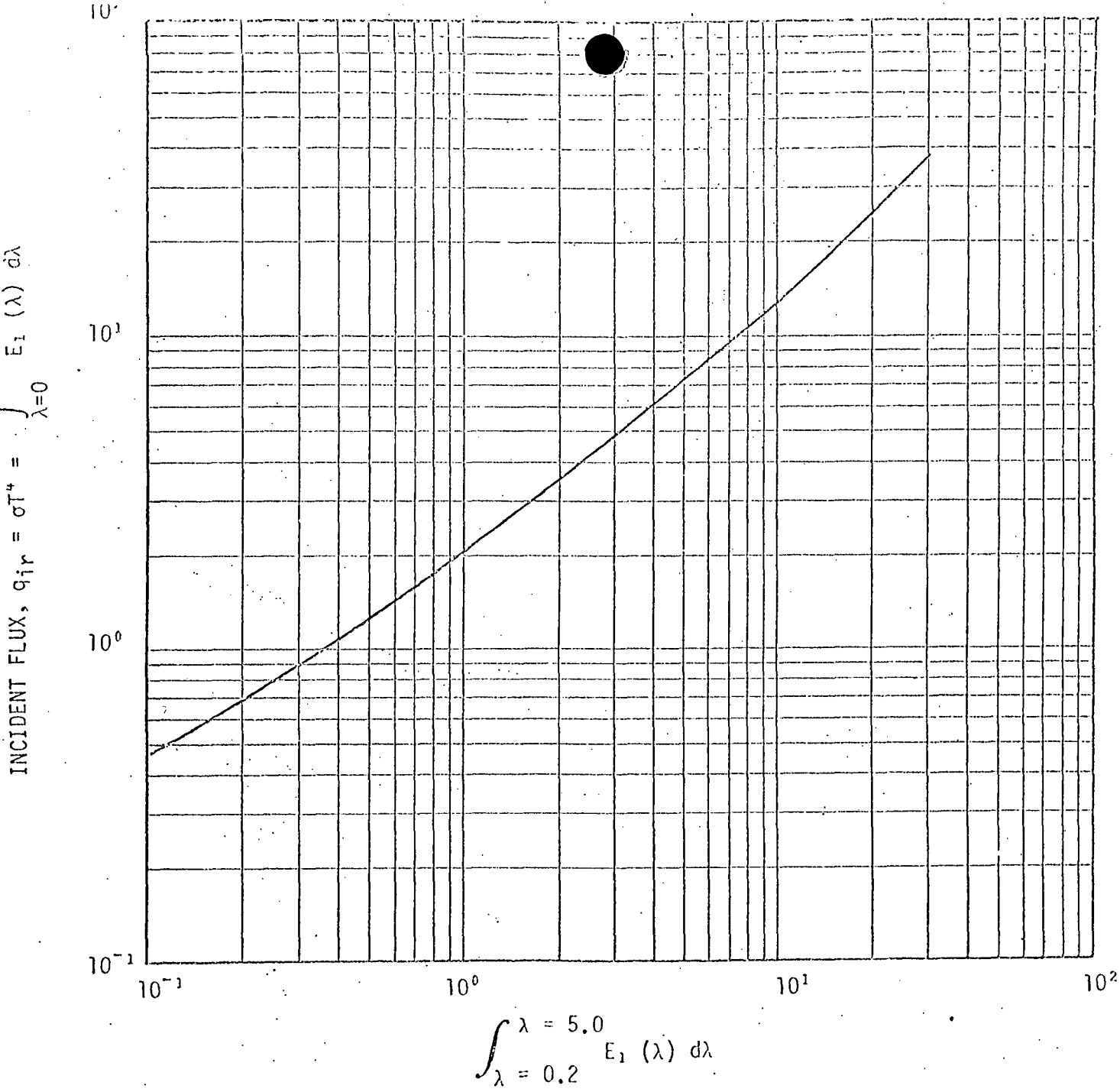

FIGURE 3-29. INCIDENT FLUX RADIATION FUNCTION

A sample problem can best illustrate how the indicated flux can be corrected. Support, for the disk of Figure 3-30, with $\phi_2 = 25$ degrees, the emf output of the instrument indicated an incident flux of 10 Btu/ft^2-sec. From Equation 3-38 or Figure 3-27 the true absorbed flux for the calibration condition would have been

$$\tau_n = 0.84, \qquad (q_{A_1} - Sen)_{cal} = 4.8 \text{ Btu/ft}^2\text{-sec}$$

and

$$\tau_n = 0.9, \qquad (q_{A_1} - Sen)_{cal} = 5.2 \text{ Btu/ft}^2\text{-sec}$$

By assuming that the emf output of the instrument is proportional to the absorbed flux, the flux absorbed by the sensor, when $\phi_2 = 25$ degrees, is the same as the above.

For $\phi_2 = 25$ degrees, the effective transmissivity of the window obtained from Figure 3-28 is

$$\tau_n = 0.84, \qquad \tau_{eff}\,(\phi_2 = 25°) = 0.84$$

or

$$\tau_n = 0.9, \qquad \tau_{eff}\,(\phi_2 = 25°) \approx 0.9.$$

Then, using Equation 3-42, the true incident radiation function gives

$$\tau_n = 0.84, \left[\int_{\lambda=0.2}^{\lambda=5.0} E_1\,(\lambda)\,d\lambda\right]_{test} = \frac{4.8}{0.9 \times 0.84}$$

$$= 6.35 \text{ Btu/ft}^2\text{-sec}$$

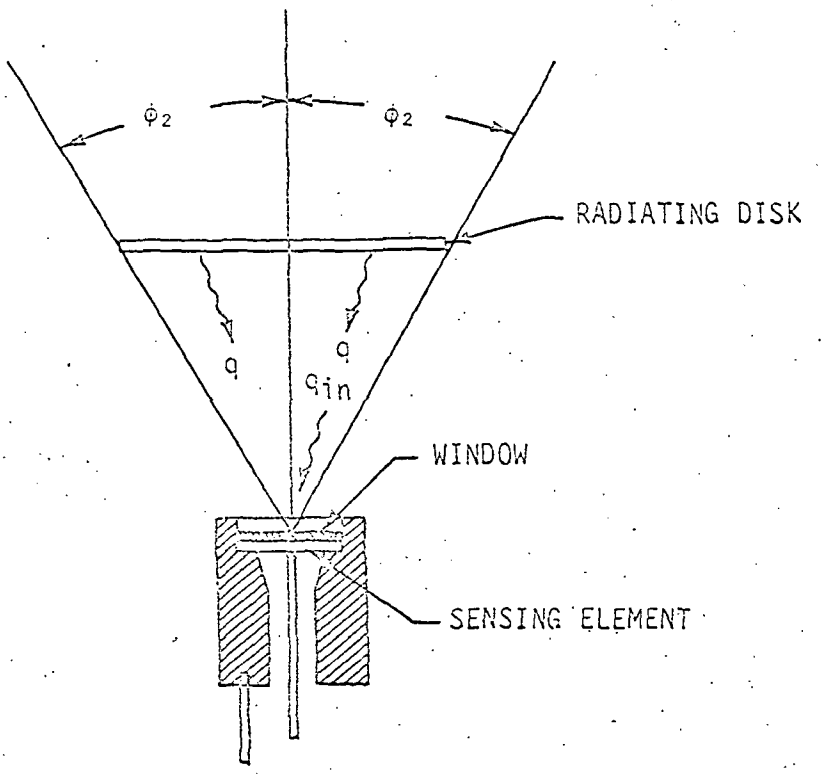

FIGURE 3-30. DISK RADIATING TO CALORIMETER

and

$$\tau_n = 0.9, \quad \left[\int_{\lambda=0.2}^{\lambda=5.0} E_i\ (\lambda)\ d\lambda\right]_{test} = \frac{5.2}{0.9 \times 0.9}$$

$$= 6.42\ \text{Btu/ft}^2\text{-sec} .$$

From the plot of the radiation function, $\int_{\lambda=0.2}^{\lambda=5.0} E_i\ (\lambda)\ d\lambda$ (shown in Figure 3-29), the correct incident flux can be obtained:

$$\tau_n = 0.84, \qquad q_{ir} \approx 8.9\ \text{Btu/ft}^2\text{-sec}$$

$$\tau_n = 0.9, \qquad q_{ir} \approx 9.0\ \text{Btu/ft}^2\text{-sec} .$$

In this example, the error in the indicated incident flux is

$$\tau_n = 0.84, \qquad e = 100 \times \frac{10 - 8.9}{8.9} = 12.4\%$$

$$\tau_n = 0.9, \qquad e = 100 \times \frac{10 - 9}{9} = 11.1\% .$$

Following the same procedure as indicated in the preceding example, the ratio of indicated incident flux to actual incident flux for various included half angles was computed. (The results are plotted in Figure 3-31.) As seen in the figure, the difference between the indicated flux and the actual flux is highest when the included half is less than 25 degrees and increases slightly with the incident flux.

The included half angles of the Saturn S-IC heat shield radiation calorimeters were evaluated and are shown schematically in Figure 3-32. The maximum included half angle of the heat shield radiation

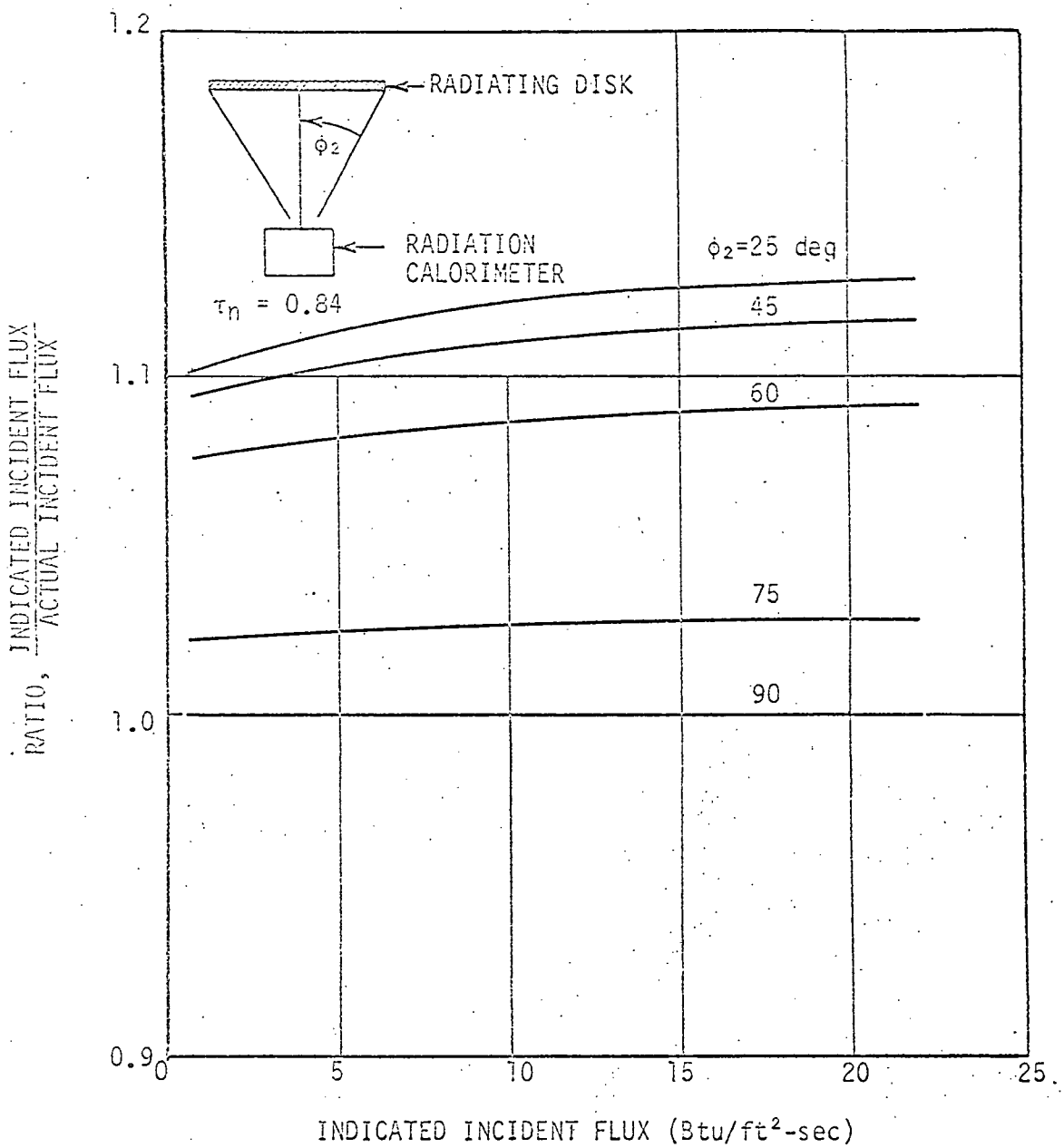

FIGURE 3-31. RATIO OF RADIATION CALORIMETER INDICATED FLUX TO ACTUAL INCIDENT FLUX

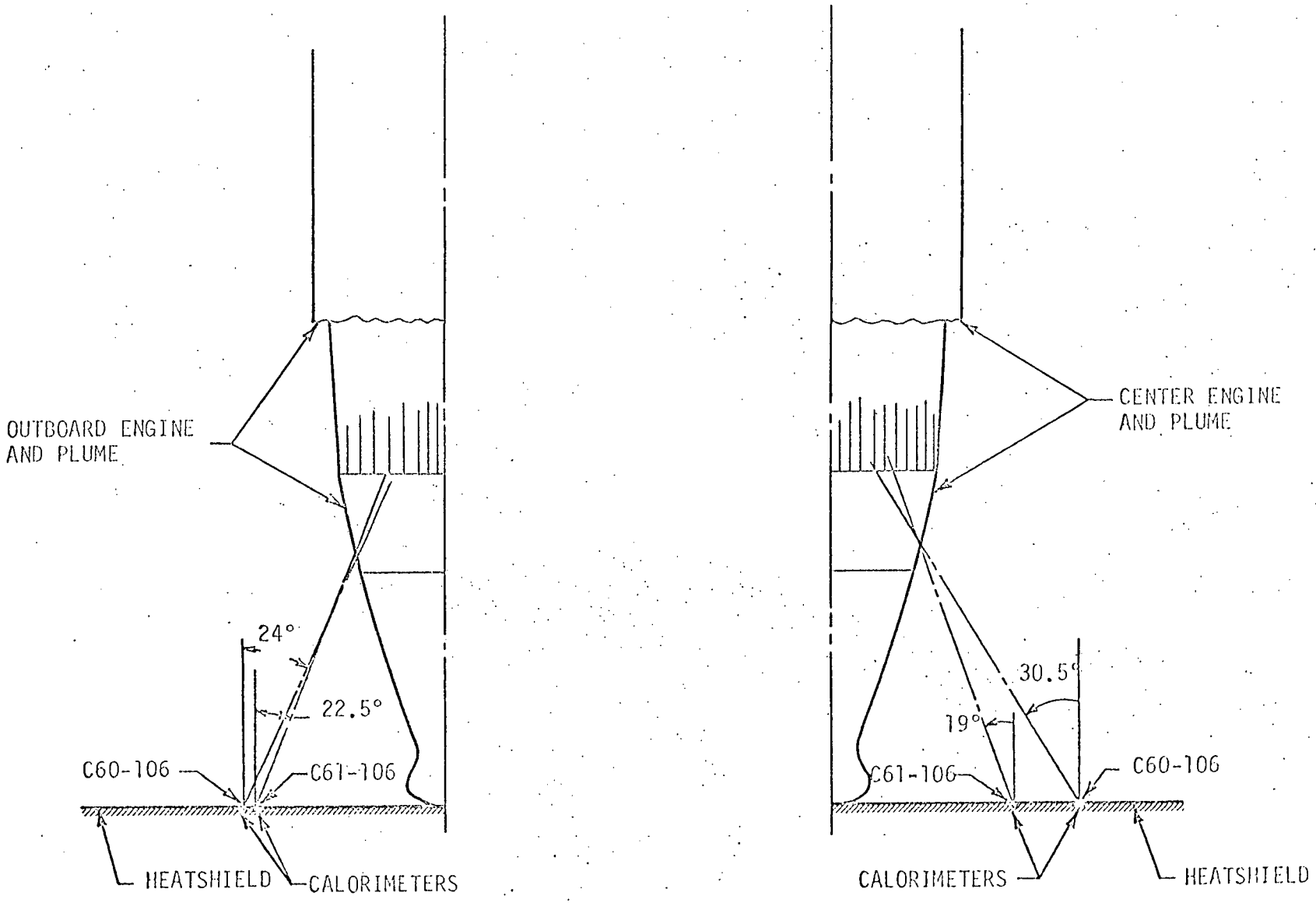

FIGURE 3-32. S-IC HEAT SHIELD RADIATION CALORIMETER INCLUDED HALF ANGLES

calorimeters was approxin ated to be 30.5 degrees at sea level. Because of the orientation of the calorimeters with respect to the engines, significant plume expansion would be required to increase the included angle beyond 30.5 degrees; therefore, it must be concluded that the S-IC indicated radiation heating rates probably were in error by at least 11 to 12 percent throughout most of the flight.

An additional error could have been produced by the nongrey plume radiation. Figure 3-29 shows the blackbody radiation contained within the wavelength range of 0.2 micrometer $\leqq \lambda \leqq$ 5.0 micrometers compared to the corresponding blackbody incident flux. If the plume radiation was not continuous but emitted radiation with significant spectral windows characteristic of radiating gases, then a significant error could result. Considering the previous example, when the incident flux was 10 Btu/ft^2-sec, the radiant energy contained within the wavelength range 0.2 micrometer $\leqq \lambda \leqq$ 5.0 micrometers was 6.35 Btu/ft^2- sec (with τ_n = 0.84). If the disk were such that it radiated energy in the amount of 6.35 Btu/ft^2-sec only within the range 0.2 micrometer $\leqq \lambda \leqq$ 5.0 micrometers, the radiation calorimeter would respond approximately the same as if the disk were a blackbody radiating at the rate of 10 Btu/ft^2-sec. As seen by the difference, this could product a significant error in the indicated results.

3.5 BASE PRESSURE PROBES

3.5.1 Physical Descriptions

The Saturn base pressures probes consisted of a tube connected to an electromechanical transducer. The transducer translated the pressure being sensed by the tube into an electrical signal. All pressure instruments were calibrated prior to flight use.

3.5.2 Base Pressure Measurement Errors

The measured pressures are another source of error. When the raw flight data is reviewed, it is seen that the pressure probes indicate pressures prior to vehicle lift-off and after engine cutoff which do not agree with the known ambient conditions. In some cases, negative absolute pressures are indicated after engine cutoff. These measurements are well within the specified accuracy of the instrumentation, but are not suitable for determining the base flow Mach numbers without correction.

Figure 3-33 shows a typical S-IC base pressure measurement. At the top of the figure is shown the raw measured data obtained from measurement D36-106, AS-502 flight. As seen in the figure, the indicated pressure is too high prior to lift-off and too low after engine cutoff. By averaging the measured values taken from the digitized printout of this measurement, it can be shown that the indicated value prior to engine ignition was approximately 15.025 psia, whereas the ambient pressure was 14.75 psia. Likewise, the indicated value at 130 seconds was approximately -0.1308 psia, whereas the ambient pressure at this time was 0.0276 psia. The specified accuracy of this instrument was ±3 percent of the full scale range which gives a possible error of ±0.6 psia. By comparing the indicated error (i.e., 0.275 psia at lift-off) to the specified accuracy, it is seen that the actual error is much less and, although this is encouraging, does not eliminate the probability of analyzing the flight data.

One of the basic parameters of interest in analyzing the base convective heating is the base flow Mach number. In subsonic compressible flow, the Mach number can be computed if the static and total pressure (P_S, P_o) and the specific heat ratio (γ) are known. The equation which gives the Mach number is

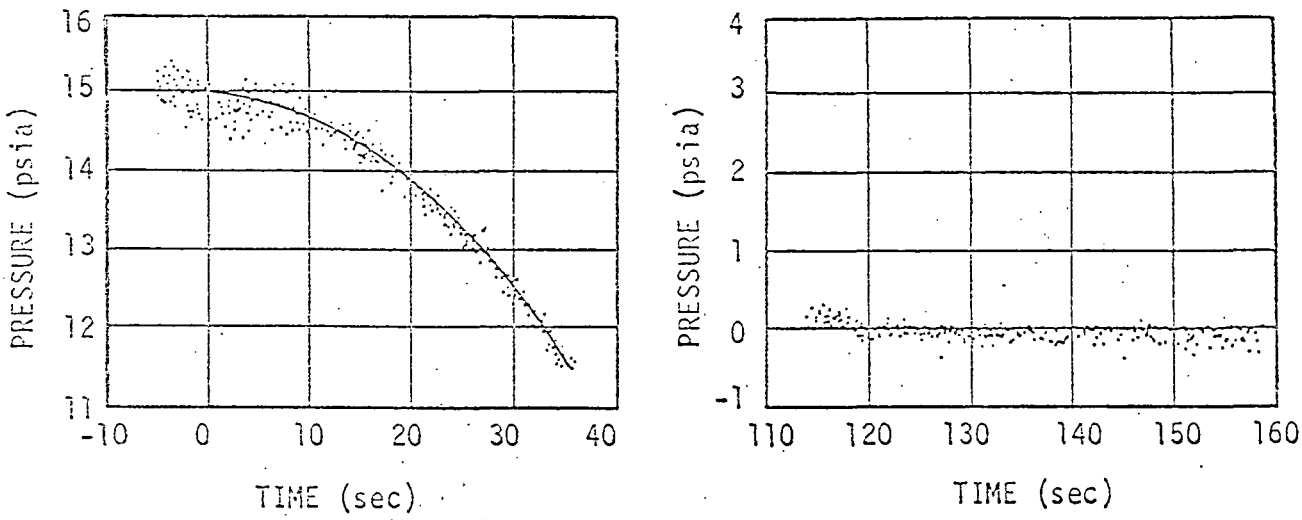

AMBIENT PRESSURE AT LIFT-OFF = 14.75 psia

MEASURED PRESSURE PRIOR TO LIFT-OFF (D36-106) = 15.025 psia

DELTA PRESSURE = 0.275 psia

MEASURED PRESSURE AT 130 sec = - 0.1308 psia

AMBIENT PRESSURE 130 sec = 0.0276 psia

IECO = 144.39 sec

OECO = 147.34 sec

AMBIENT PRESSURE AFTER ENGINE CUTOFF = $0.006 > P_{\infty} > 0.003$ psia

FIGURE 3-33. AS-502 BASE PRESSURE MEASURED AT LIFT-OFF AND CUTOFF

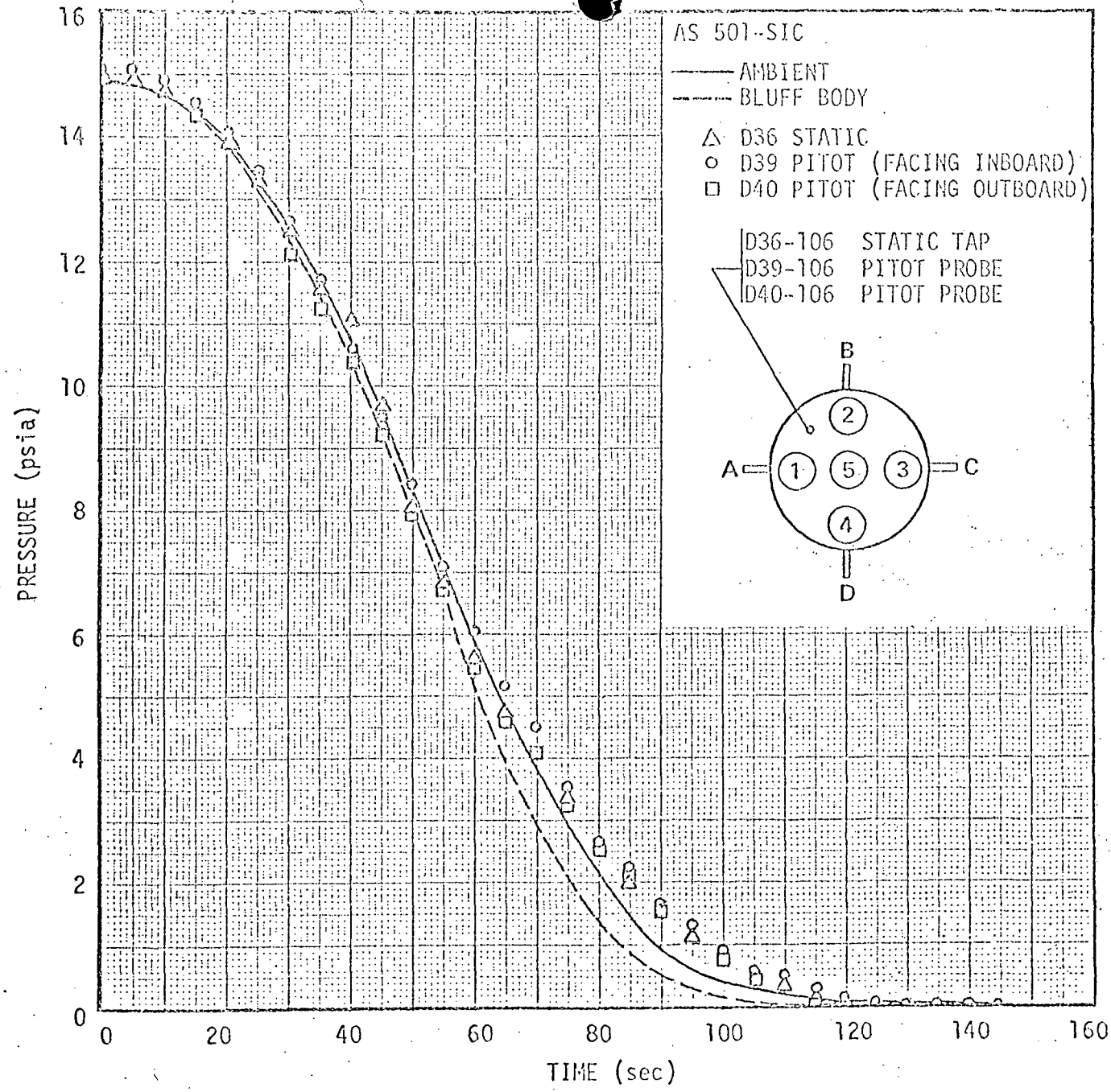

FIGURE 3-34. AS-501 MEASURED BASE PRESSURES

$$M^2 = \frac{2}{\gamma - 1}\left[\left(\frac{P_o}{P_s}\right)^{\frac{\gamma - 1}{\gamma}} - 1\right] \quad . \qquad (3\text{-}44)$$

In base flow the specific heat ratio is known since the gas is primarily ambient air ($\gamma = 1.4$) during the aspiration phase and engine exhaust products ($\gamma \sim 1.2$ for LOX-RP-1) during the flow reversal phase. Therefore, if the total and static pressures can be measured during the flight, the Mach number can be evaluated, approximately, using Equation 3-44. For this purpose, static and pitot probes were located in the base region of the S-IC vehicles. The pressure measured by one set of pitot and static probes during the AS-501 flight is shown in Figure 3-34. The ambient pressure and the experimentally obtained pressure in the base of a bluff body are also shown in the figure. If these measured values are used in Equation 3-44, they indicate a base flow Mach number of 0.1 to 0.2 shortly after lift-off; however, the indicated flow direction is out of the base, which is opposite to the understood characteristics of the base flow. This trend also persists for a significant time over the first phase of the flight. Obviously, the raw measured pressures are not accurate enough to allow the computation of the Mach number and flow direction; this situation can be improved, however, if the measured values can be corrected. Since the actual pressure is known (approximately) prior to engine ignition and after engine cutoff, these two end points can provide a means of correcting the measured values. The correction technique is shown schematically in Figure 3-35. The technique consists of determining the difference between the measured value and the ambient pressure prior to lift-off and after engine cutoff. If the indicated error is plotted versus the measured pressure and a linear relation is assumed between the end points, the measured values can be corrected. The measured

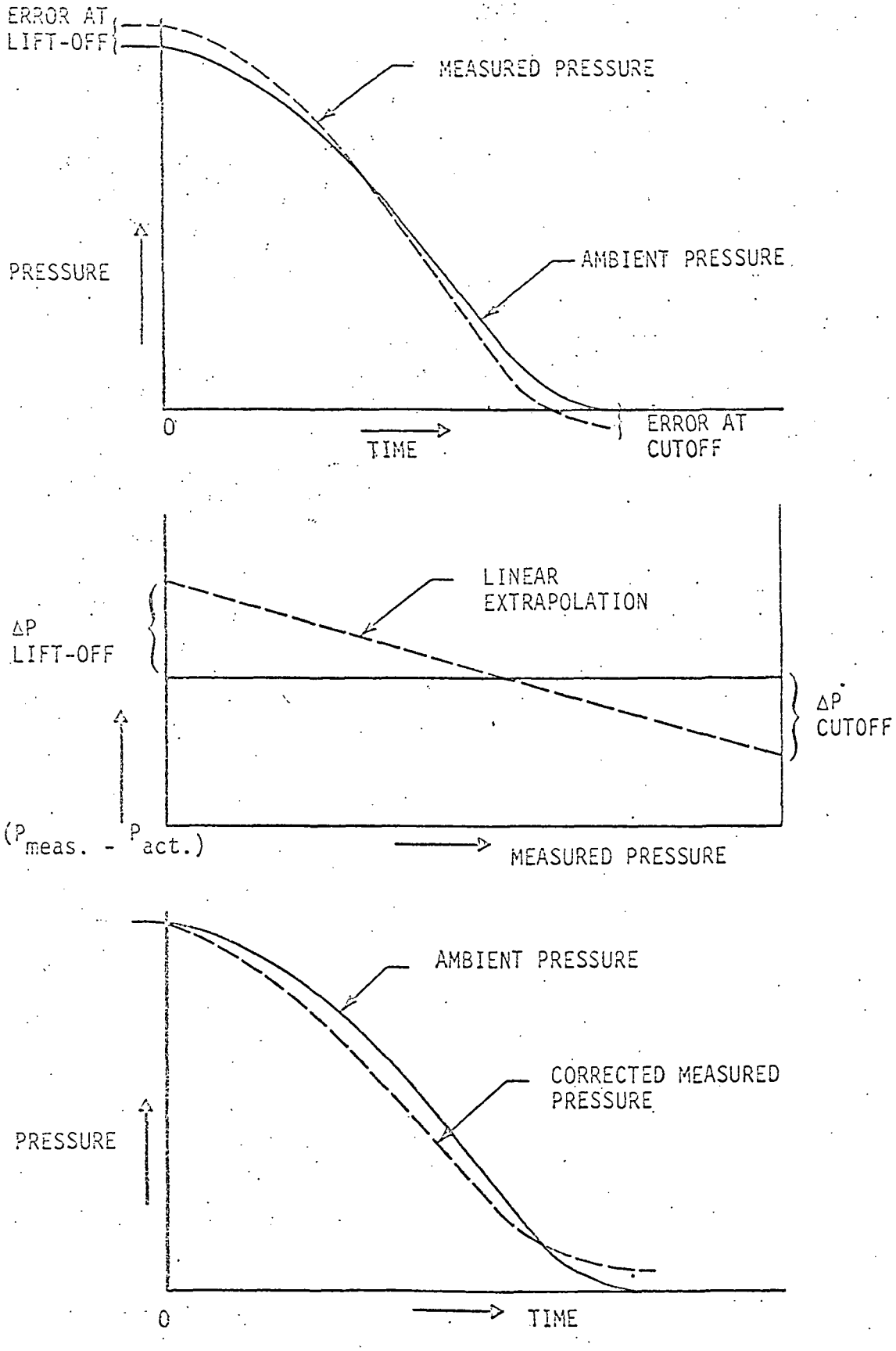

FIGURE 3-35. MEASURED PRESSURE CORRECTIONS SCHEMATIC

pressures shown in Figure 3-34 were corrected in this way and are shown in Figure 3-36. Because of the nature of the technique, the final results are only approximately correct; however, the obvious errors have been eliminated.

The base flow Mach number can be approximated from these corrected pressures by assuming that the maximum absolute pressure is the total pressure and the minimum pressure is the static pressure. The computed results are shown in Figure 3-37. The Mach number, computed using the bluff-body base and ambient pressure, is also shown in this figure.

3.6 CONCLUSIONS AND RECOMMENDATIONS REGARDING INSTRUMENTATION

The results of this study have produced the following conclusions:

- All instruments used to measure the Saturn inflight base heat transfer parameters appear to have had a significant potential for erroneous indications.
- The gas temperature probes were sensitive to radiation heating and lacked response in a low-mass flow rate environment; as a result, the indicated gas temperatures could be higher or lower than the actual gas temperatures.
- The total heat flux meters were sensitive to the mismatch in surface temperature between the sensor and the surroundings; this could have produced a high indicated convective flux. Condensation of moisture on the surface of the instrument could have produced a low indicated convective flux.
- The radiation calorimeter window combined with the calibration results to produce indicated incident heating rates which were higher than the actual flux.
- The measured results indicate the magnitude of the individual base heating parameters but, to an unknown and indeterminable accuracy.

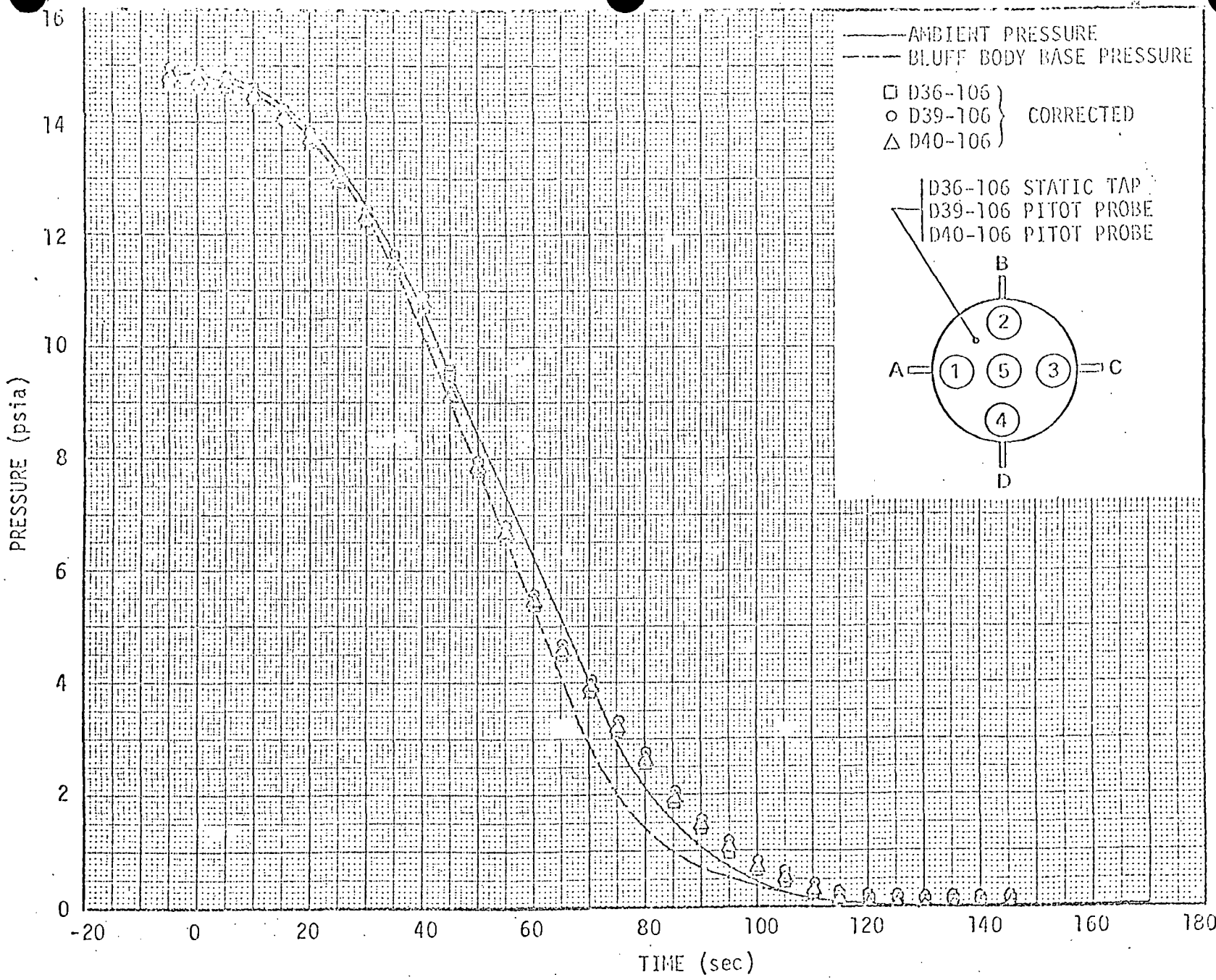

FIGURE 3-36. AS-501 CORRECTED BASE PRESSURES

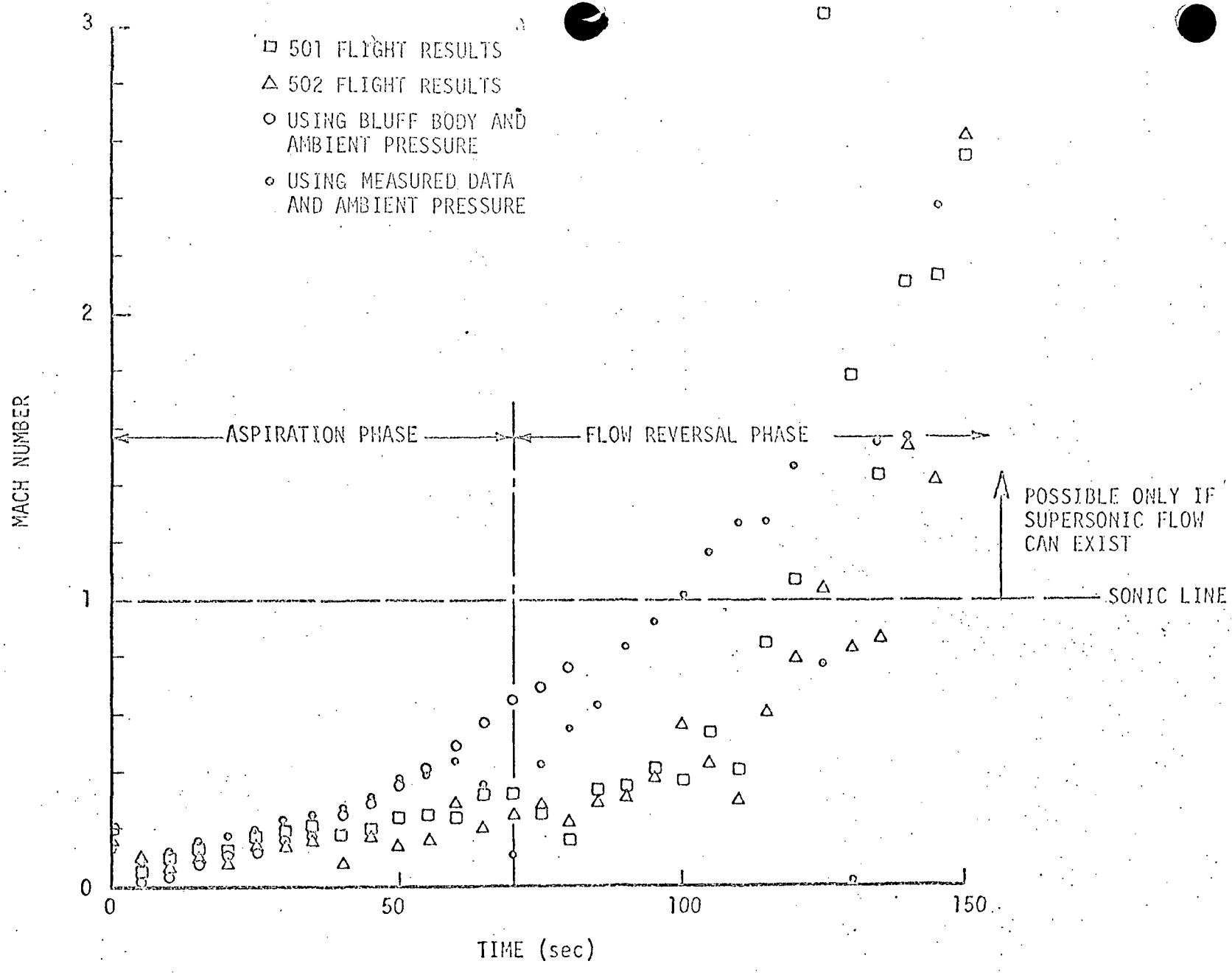

FIGURE 3-37. BASE FLOW MACH NUMBER

- In general, the inflight measured results cannot be combined without liberal modification to delineate important aspects of the base heating problem

- The results point up a serious need for the development of accurate gas temperature probes and heat flux meters which can be used in an environment similar to that of the Saturn base region.

With respect to future flight test instrumentation, the following recommendations are made:

- For booster stages where the radiant flux is significant and the mass flow flux probably changes by several orders of magnitude during the flight, it is doubtful if an accurate gas temperature probe can be developed using a conventional thermocouple. However, more accuracy and greater confidence in the results can be obtained by calibrating the instrument in a combined radiant and convective environment and using the calibration results for evaluating the approximate base gas recovery temperature. For upper stages where the radiant flux and mass flow flux are both low, the probe should also be calibrated because the reradiation from the probe junction may still cause erroneous indications.

- For the total heat flux meters, a properly designed ring which surrounds the instrument at the exposed surface could reduce the effects of moisture condensation and surface temperature mismatch. This instrument should also be tested in a combined radiant and convective environment to determine if empirical correction procedures are necessary.

- For the radiant flux meter it is doubtful if an instrument can be developed which does not have errors caused by variations in the window transmissivity. A method of approximately correcting the measured results has been outlined in Section 3.4. This method should be verified experimentally and on future flight vehicles the instruments should be oriented with respect to the radiant source so that a correction procedure can be used.

- For pressure measurements, the existing instrumentation is probably as accurate as can reasonably be expected. Therefore, for future flight tests it is recommended that the same type instruments be used and corrected as outlined in Section 3.5.

REFERENCES - SECTION 3

3-1. Benedict, B. U., et al, "Evaluation Test of Thermocouple Types 9 and 35 ORD P/Ns 8960085 and 50M10099", Chrysler Corporation Technical Memorandum EER-147, Prepared under Task Order G&C-C-29, Contract NAS8-6, December 1961

3-2. Connell, H. A., "Evaluation of Saturn SA-1 Base Heating", NASA Report MTP-P&VE-P-61-21, December 1961

3-3. "Qualification Test Report for Sensor (Transducer) Gas Temperature", Boeing Document REC46727A, Rev. A, Attachment to 5-1118-M-71-342, August 1967 (Qualification Test Report on S-IC Engine Gas Temperature Probes, retained in MSFC Document Repository)

3-4. "Report of Test on Transducer, Temperature, Ambient Gas", Boeing Document QTR-33F, Revision A, June 1966 (Qualification Test Report on S-IC Heat Shield Gas Temperature Probes, retained in MSFC Document Repository)

3-5. Sudunas, J. A., "AS-503 S-II Base Region Gas Recovery Temperature Evaluation", North American Rockwell Corporation, Internal Letter S-II-190-700-69-21, March 1969

3-6. Sudunas, J. A., "S-II Base Region Gas Recovery Temperature Probe Analysis Program, YF0028", North American Rockwell, Internal Letter LEVA-190-405-70-35, June 1970

3-7. "Design and Development, Testing of Transducer Temperature Thermocouples", RdF Corporation Development Test Report No. 91, April 1966. (Test Report on S-II Stage Gas Temperature Probe)

3-8. "Major Design Review Supporting Data, North American Aviation, Inc., S&ID Procurement Specification MC449-0006, Thermocouple Temperature Transducer", RdF Corporation, May 31, 1966

3-9. Wiebelt, J. A., Engineering Radiation Heat Transfer, Holt, Rinehart and Winston, Inc., 1965

REFERENCES - SECTION 3 - Concluded

3-10. McAdams, W. H., Heat Transmission, 3rd Edition, McGraw-Hill Publishing Company, 1954

3-11. Buchmann, R. C., J. T. Chambers, and W. H. Giedt, "Investigation of Surface Heat - Flux Measurements with Calorimeters", ISA Transactions, pages 143 through 151, April 1965

3-12. Bender, R. L. and W. L. Shaffer, "Examination of Saturn V First Stage Thermal Environment Flight Measurements 501-511", Boeing Company Document 5-9410-H-448, September 1972

3-13. Nueringer, L. J., "Infrared Fundamentals and Techniques", Electrical Manufacturing, pages 101 through 128, March 1960

3-14. "Thermal Instrumentation", Hy Cal Bulletin, No. A-102, 1970

3-15. "Properties of Infrared Transmitting Materials", Servo/Infrared Bulletin, Servo Corporation of America, 1961

3-16. Garbuny, M., Optical Physics, Academic Press, Inc., 1965

4. FLIGHT TEST RESULTS

4.1 BASE ENVIRONMENT MEASURED DURING SATURN FLIGHT TESTS

The Saturn flight test data have been reviewed with regard to the evaluation of the in-flight base heating. As anticipated, a voluminous amount of Saturn flight test data was available for evaluation. The measured data was obtained from the following sources:

- Raw Flight Data - This data, consisting of plotted or tabulated time histories of the measured parameters, was obtained from the MSFC Computation Laboratory flight data microfilm laboratory. In general, this data was used in the study where possible.

- Contractor Flight Reports - For some of the flight tests, the stage contractors published separate aerothermodynamic flight evaluation reports. Some of these data were used in the evaluation, primarily where the raw flight data was not available.

- Original Flight Evaluation Working Papers - These data consisted of raw flight data, as well as calibration curves and original flight evaluation not published in other reports. These data were obtained from the MSFC Astronautics Laboratory, Thermal Engineering Branch files.

- FEWG Reports - These are flight test reports published by the MSFC Flight Evaluation Working Group. These reports contain a summary of the vehicle's flight performance and measured parameters.

- Trajectory Reports - These reports contain the trajectory of the flight vehicle and ambient conditions at or near the time of launch. These reports are maintained in the MSFC Aero-Astrodynamics Laboratory files.

- o IP and C List - These are documents which list the type and location of all instruments that are on the vehicle. Most of these documents were available in the MSFC Document and Drawing Repository.

A review of the flight test data indicated that it would be beneficial to plot the measured results of each measurement for all flight tests on a single plot. This was found to be beneficial because any given parameter measured at the same location in the base region was found to vary slightly from flight to flight. For some flight tests these variations could be attributed to minor variations in vehicle configuration. For most, however, no obvious reason for these random variations appeared to exist. Therefore, plotting the data measured at one location during several test flights could be used to identify measurements which probably failed and/or those which indicated excessively high or low values during the flight.

For the upper stages the measured data could be plotted directly from the raw flight test results. For the booster stages, however, it was necessary to normalize the results. This was found to be necessary because most flight test vehicles flew slightly different trajectories. Because the vehicles were at different altitudes at the same flight time and because a majority of the base heating parameters measured were primarily a function of local ambient pressure, these differences had to be accounted for to obtain consistent data for comparison. As a means of normalizing this data, all of the measured results were related to the Saturn V, AS-501 trajectory by using altitude as the common factor. In this way, all of the booster flight test data could be plotted as if the vehicles had all flown the AS-501 trajectory (for more details of the normalizing procedure see Reference 4-1). This was found to be a painstaking procedure, but resulted in data that could be compared.

All of the important flight test data was plotted in the manner described above and is presented in Volume II. For this report, only representative data for each stage is presented. For an alternate analysis, see Reference 4-2.

4.2 ANALYSIS AND COMPARISONS OF SOME OF THE MEASURED SATURN FLIGHT TEST DATA

4.2.1 Saturn I Flight Results

Figure 4-1 shows the bands of gas temperature measured in the base region of the Saturn I, block II vehicle. The apparent times of the start of flow reversal are also shown in this figure. The time of flow reversal can only be approximately established and the particular times shown in Figure 4-1 were chosen because of significant increases in the measured temperatures.

Typical pressures measured in the base region of the Saturn I, block II vehicle are shown in Figure 4-2. In this figure, it can be seen that the heat shield pressure is very nearly the same as the local ambient pressure. It is also seen in this figure that the flame shield pressure is significantly different from the ambient or base pressure. Since pressure is indicative of the flow field, these measured pressures appear to indicate a weak flow field in the region of the heat shield and a strong flow field in the flame shield region. Another factor which is indicated by the flame shield measured pressure is the probability of a so-called "choked" flow condition (i.e., condition where the mass flow rate is unaffected by any further decrease in the ambient pressure). When the choked condition is reached the temperature (see Figure 4-1), pressure (see Figure 4-2), and heating rate (see Figure 4-3) become constant.

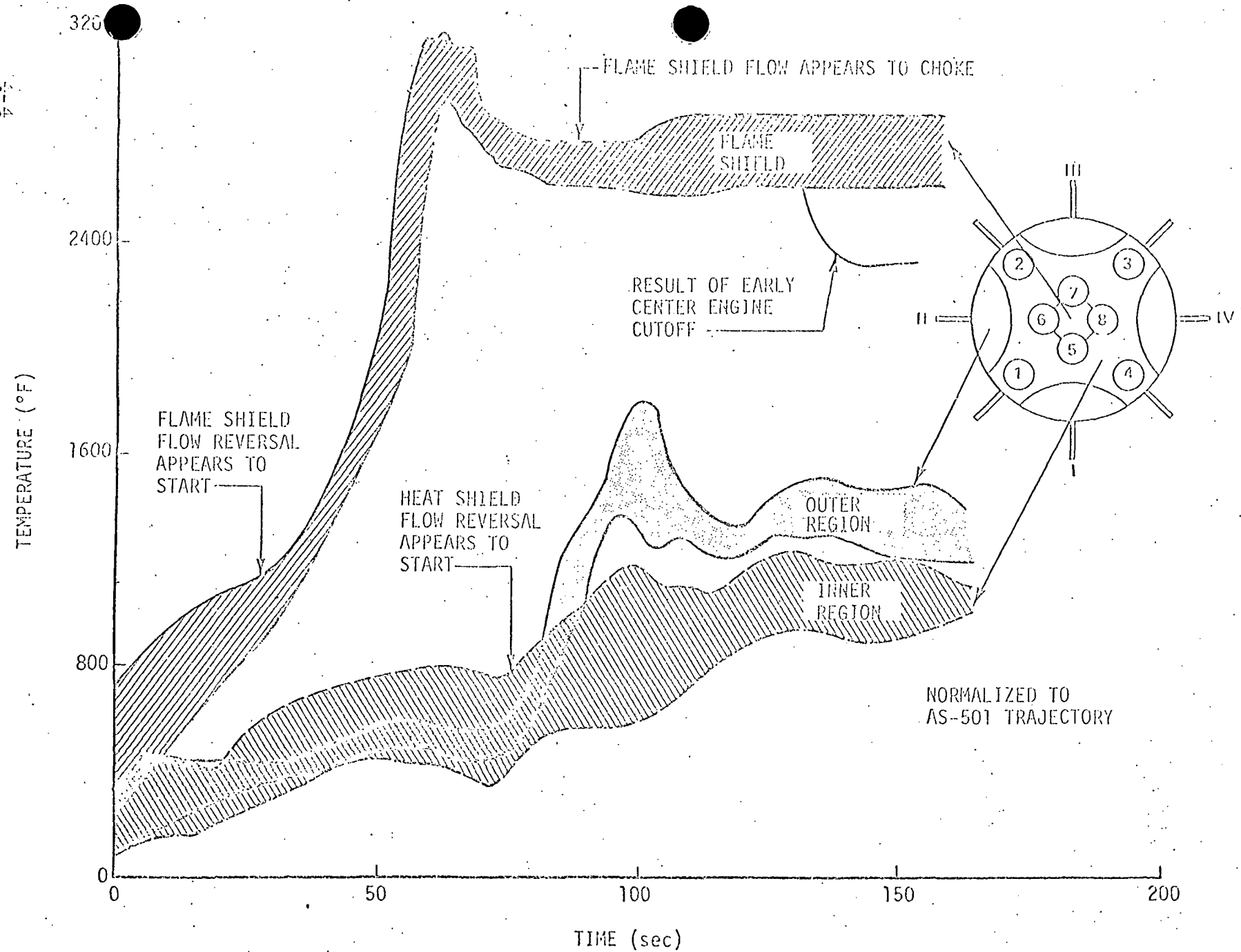

FIGURE 4-1. SATURN I, BLOCK II GAS TEMPERATURES

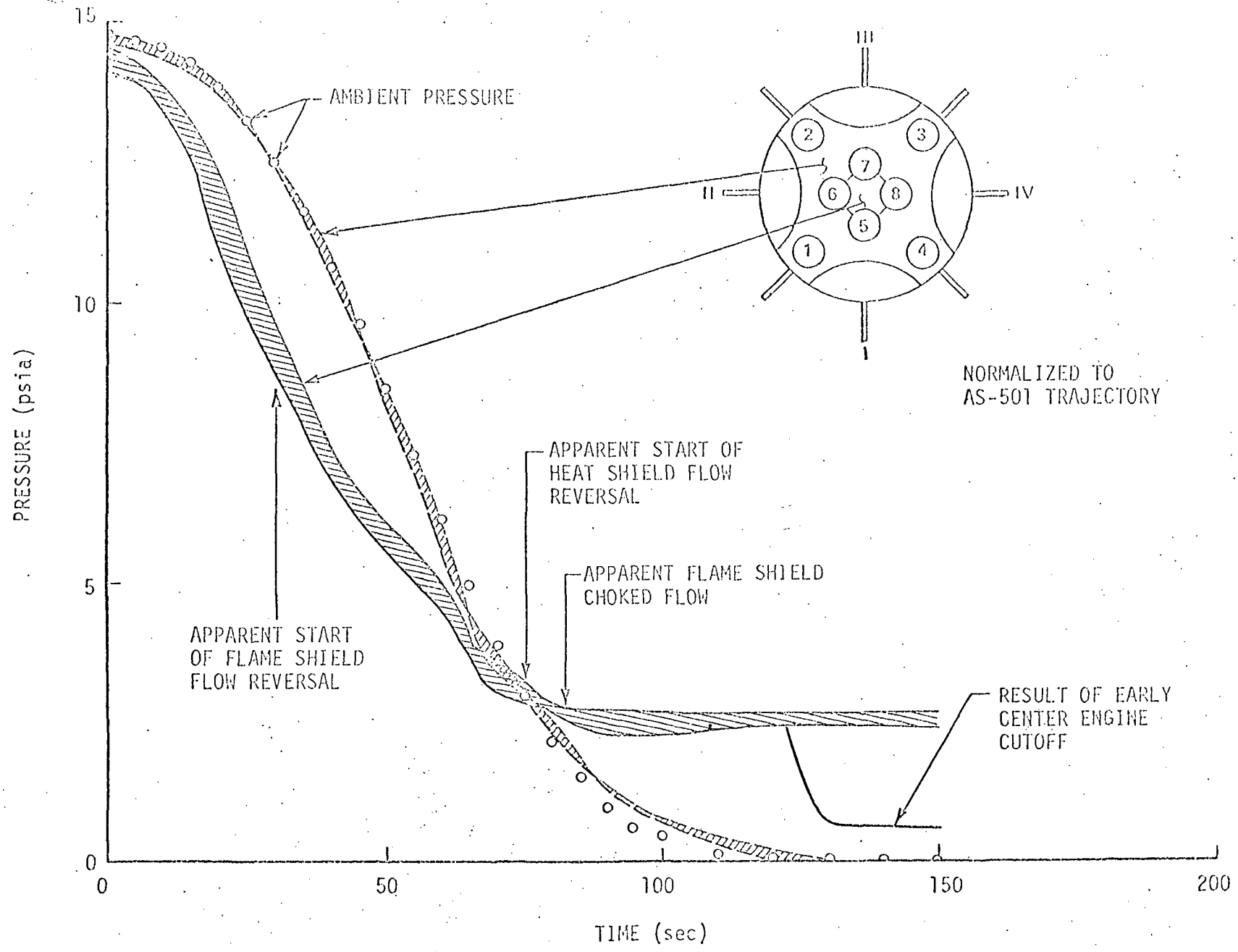

FIGURE 4-2. SATURN I, BLOCK II BASE PRESSURES

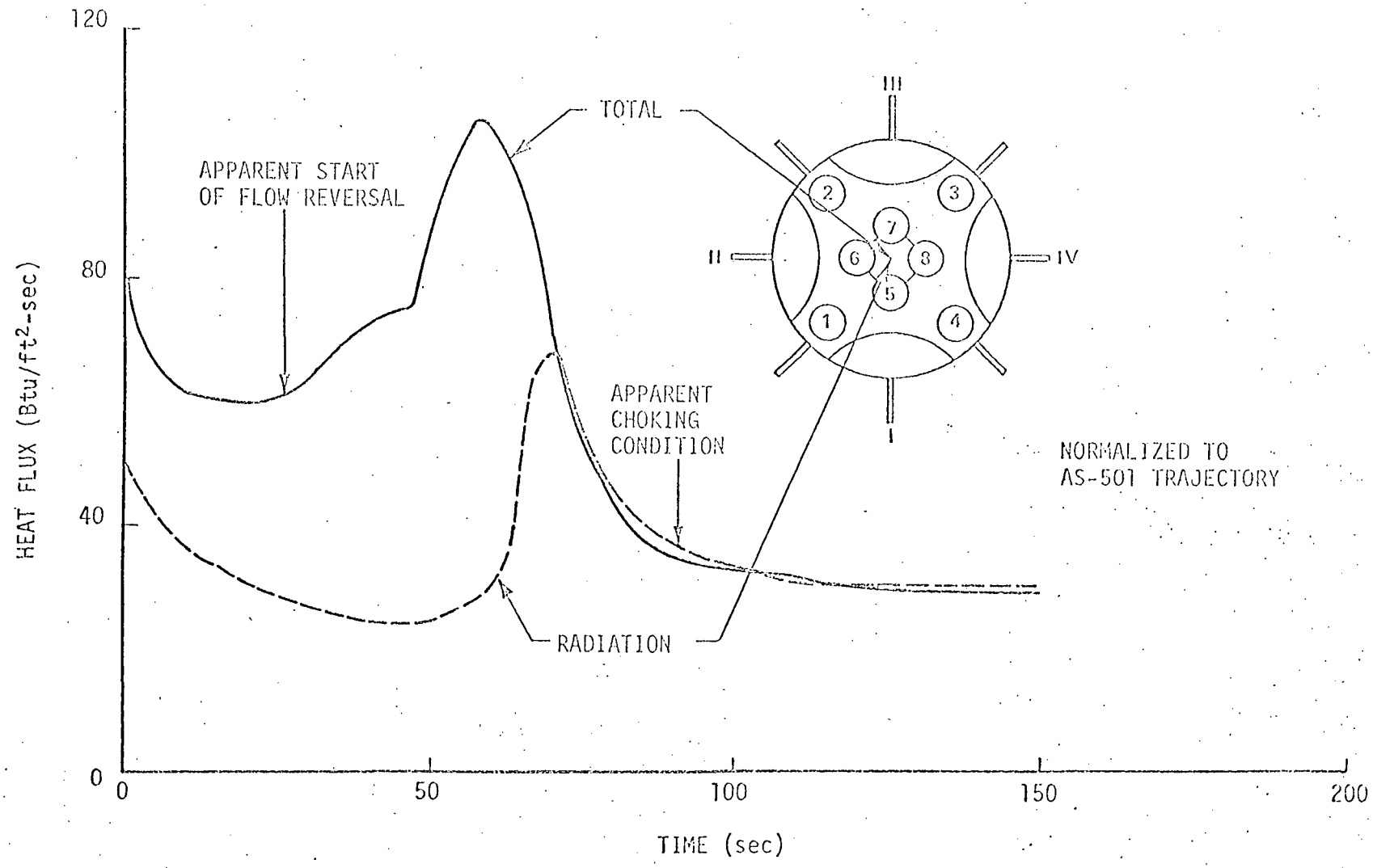

FIGURE 4-3. TYPICAL FLAME SHIELD HEATING RATES

Typical flame shield heating rates measured on one of the Saturn I, block II flight tests are shown in Figure 4-3. The total heat flux includes both the radiant flux (also shown in the figure) and the convective flux. The difference between the total and radiation flux gives the convective flux. The results shown in Figure 4-3 indicate that a significant amount of convective heating occurred both prior to and after the apparent start of flow reversal. By observing the results of this figure, it can be seen that the convective heating (i.e., the difference between the total and radiant flux) was much higher after the flow reversal than prior to flow reversal. However, the fact that the measured gas temperature is high and the convective heating starts at lift-off and continues over the first half of the flight suggests that some of the high temperature exhaust gases are being reversed even at lift-off. Figure 4-3 also shows that the radiant flux is the only mode of heat transfer after 60 seconds. This might not be a completely accurate conclusion since there were problems encountered in evaluating the total heat flux which are explained in Reference 4-3. However, it does appear that radiation was the dominant mode of heat transfer.

Another interesting characteristic can be observed in Figures 4-1 and 4-2. During one of the flight tests, a center engine was cut off approximately 20 seconds earlier than the other three engines. The resulting reduction in the flame shield temperature and pressure are shown in the figures. The gas temperature dropped approximately 300°F and the pressure dropped approximately 2 psi. The heat flux (not shown) dropped only slightly and the choked flow condition appears to have been reestablished.

Shown in Figures 4-4 and 4-5 are representative bands of radiation and total heat flux measured in the outer and inner zones of the Saturn I heat shield. In the figures, it can obviously be seen that

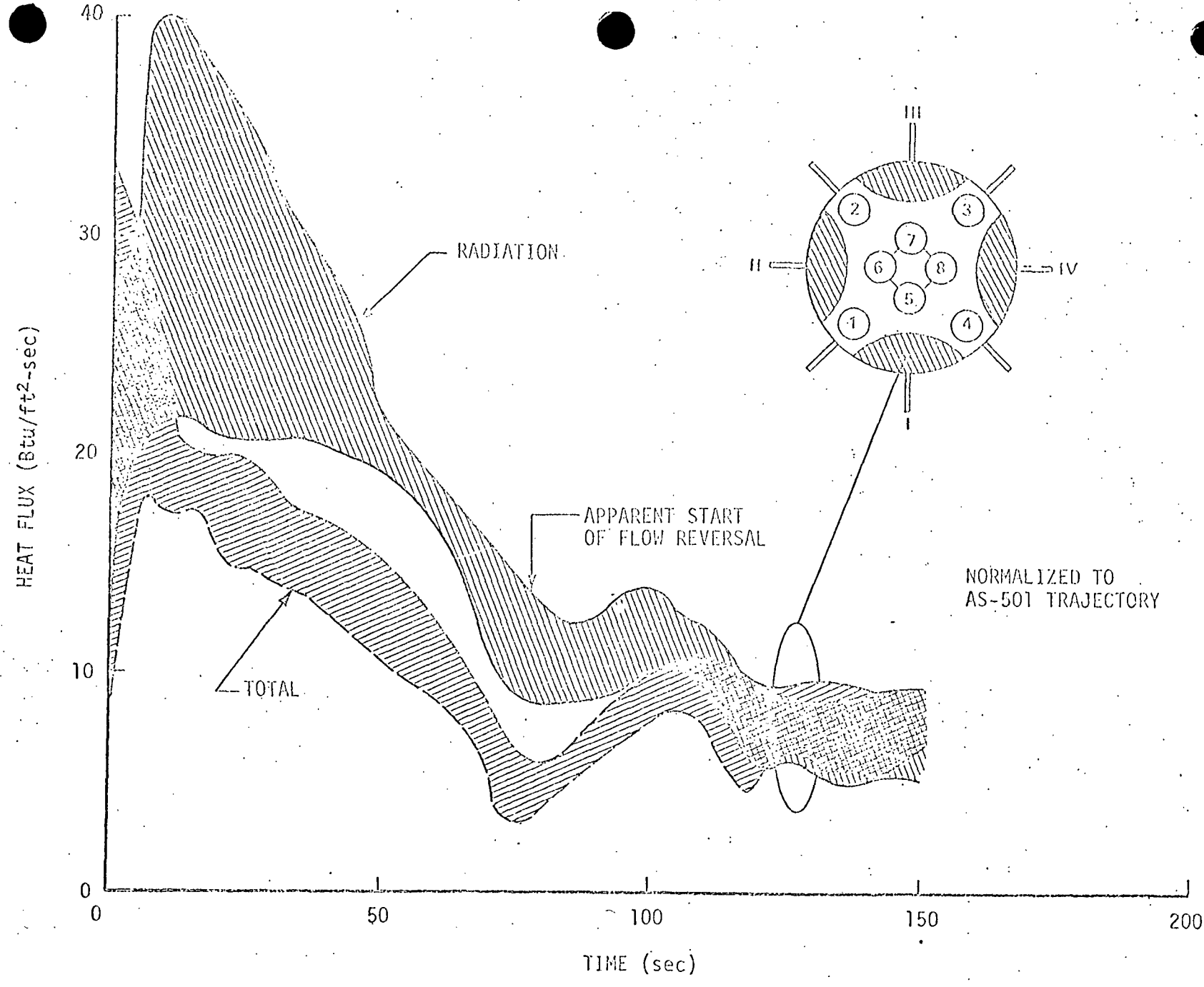

FIGURE 4-4. SATURN I, BLOCK II OUTER REGION HEAT FLUX

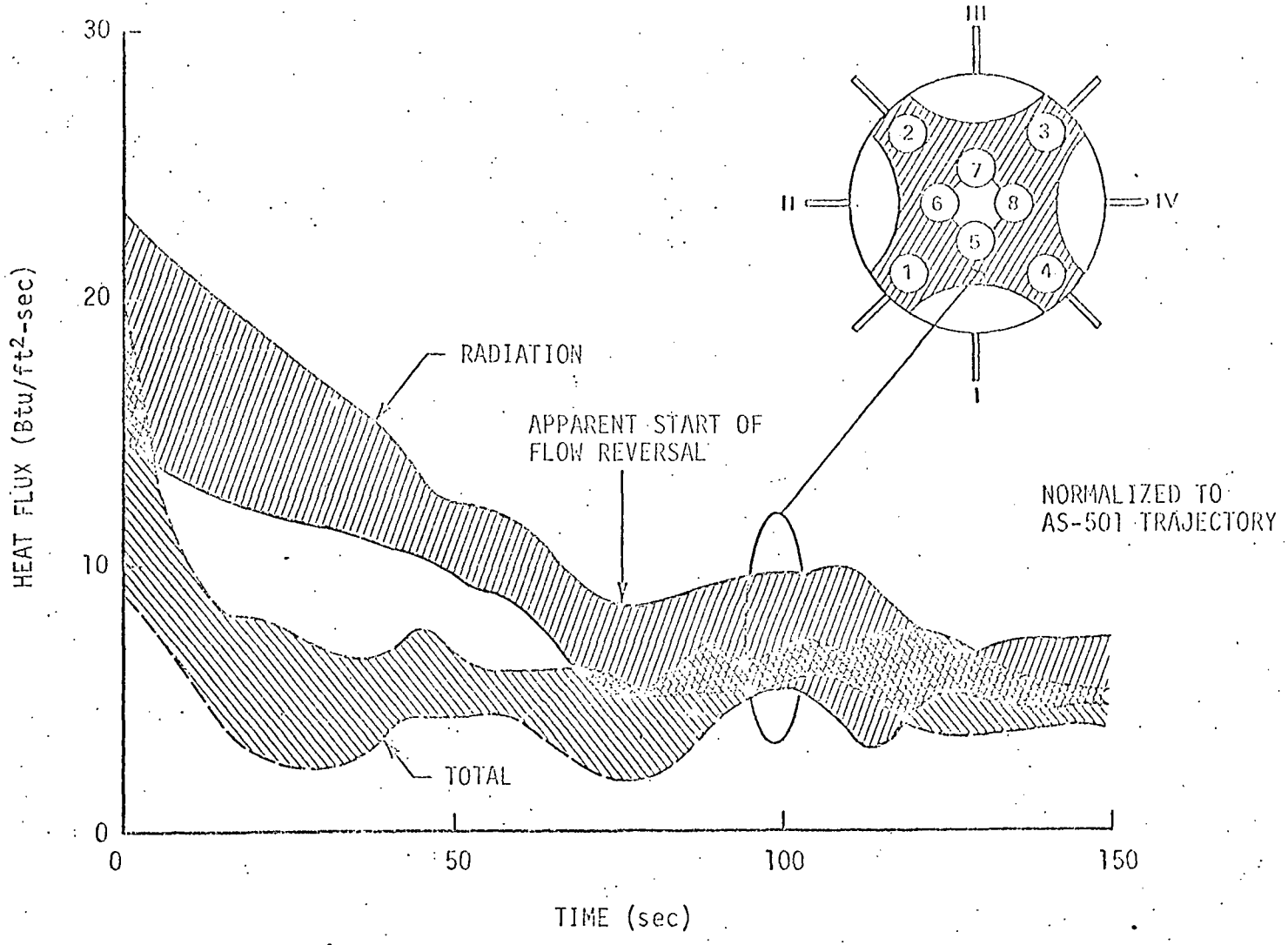

FIGURE 4-5. SATURN I, BLOCK II INNER REGION HEAT FLUX

radiation was the dominant source of heat input throughout the flight. By comparing the total heat flux and the radiant flux, it can be seen that a significant amount of convective cooling exists, particularly during the early phase of the flight.

4.2.2 Saturn S-IC Flight Results

One of the main advantages of normalizing the flight test results is that it allows direct comparison of the same data for different vehicles. Figures 4-5, 4-6, and 4-7 show comparisons between Saturn I and Saturn V, S-IC base thermal environment. Figure 4-6 is a comparison between the Saturn I (outer region) and the Saturn V, S-IC base gas temperature. Surprisingly this shows the gas temperature and the apparent time of flow reversal to be similar even though significant configuration differences existed between the two vehicles.

Figure 4-7 shows a comparison of the radiant flux measured in the base region of these two vehicles. The radiant flux incident upon the S-IC heat shield was much lower than that incident upon the Saturn I heat shield. This difference was primarily due to the relative location of the heat shields and the location of the engines with respect to each other. The heat shield on the Saturn I vehicle was located approximately 2.4 engine radii above the exit plane, whereas the S-IC heat shield was 3.26 engine radii. The Saturn I engines were spaced farther apart, with respect to a point in the outer region of the heat shield, than the S-IC engines. Both of these factors tended to increase the radiation view factor (see Equation 2-17) between the plumes and the heat shield resulting in higher incident radiation to the Saturn I heat shield.

Another interesting characteristic of the S-IC radiation is the sharp increase measured after the apparent time of flow reversal. This same characteristic was evident in the Saturn I flame shield

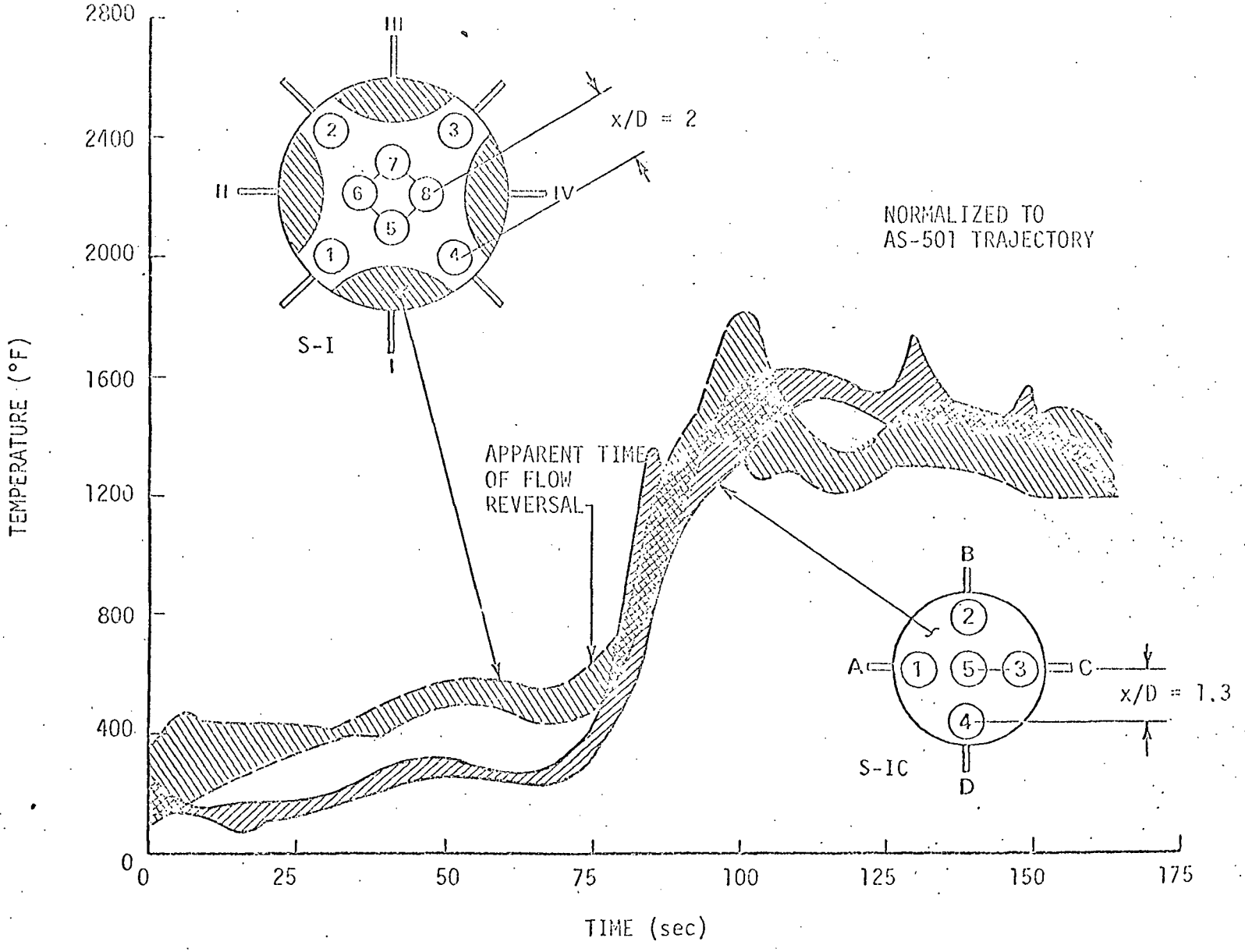

FIGURE 4-6. SATURN I, BLOCK II, AND SATURN V, S-IC BASE GAS TEMPERATURES

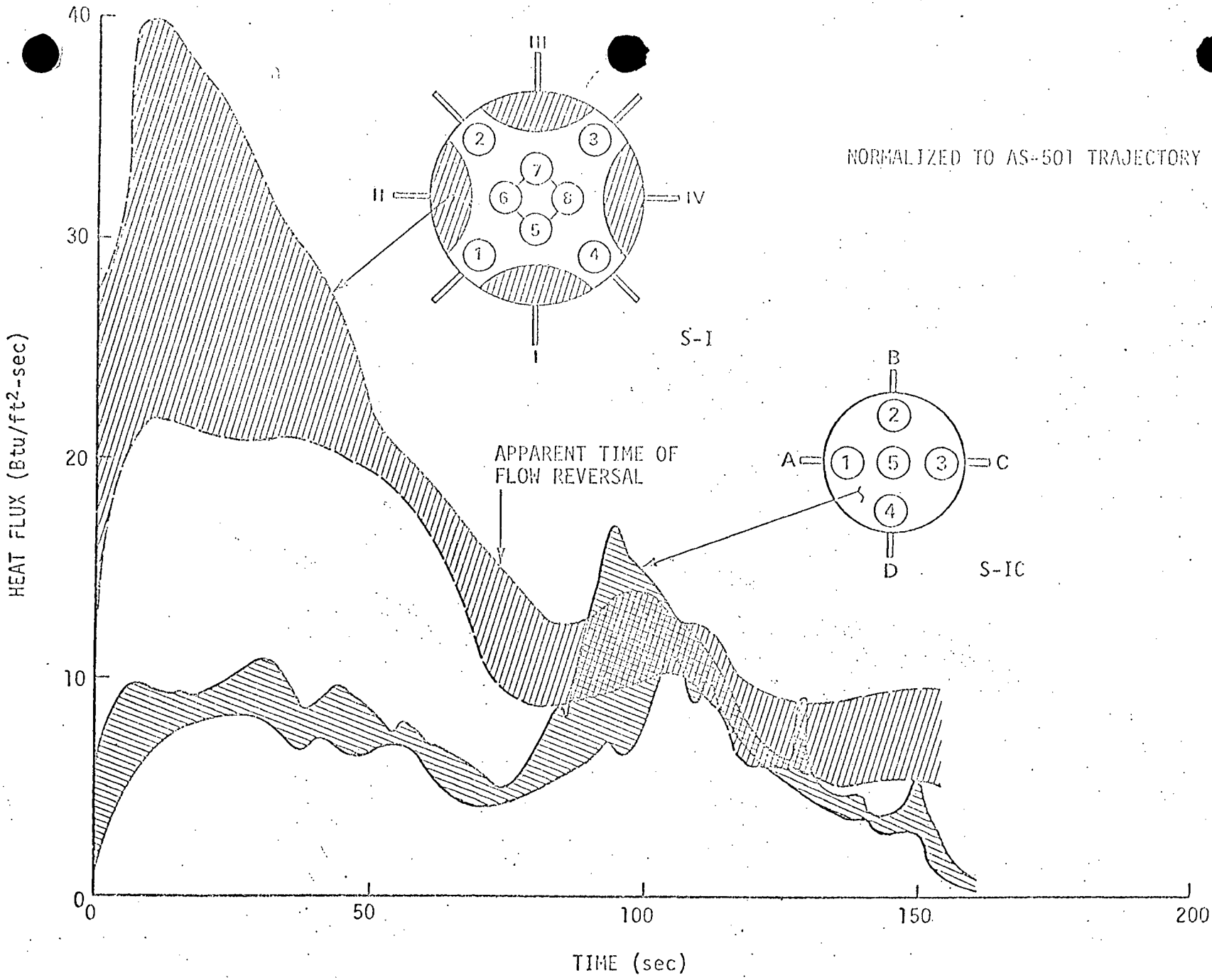

FIGURE 4-7. SATURN I, BLOCK II, AND SATURN V, S-IC RADIANT FLUX

region (see Figure 4-3) and, to a lesser degree, in the heat shield region. This is thought to be caused by the start of full flow reversal and will be discussed later.

A comparison of the Saturn I and S-IC total heat flux is shown in Figure 4-8. The total heat flux is somewhat indicative of the overall thermal environment since the area under the curve represents the net energy input to the surface. In light of the latter, a comparison of the Saturn I and S-IC total flux of Figure 4-8 would indicate that the S-IC heat shield environment was slightly less severe than the Saturn I.

In convective heat transfer, the flow velocity is an important parameter. In compressible flow the velocity can be computed if the gas temperature, total pressure, and static pressure are known (see Equation 2-9). In order to measure the static and total pressure, pitot static tubes were located in the base region of the Saturn S-IC vehicle. The results measured at two locations in the S-IC base region are shown in Figures 4-9 and 4-10. The measured results shown in the figures indicate that the freestream ambient air would flow into the base region during the first half of the flight (i.e., the base pressure being lower than the ambient pressure indicates inward flow). Likewise the base pressure being greater than the ambient pressure after 75 seconds indicates reversed flow back into and out of the base region. The evaluation of the base flow velocity will be discussed later.

4.2.3 Saturn S-IV Flight Test Results

Two of the Saturn upper stages had clustered engine arrangements and both used LOX/hydrogen as the propellants. The Saturn I upper stage consisted of six RL-10 engines clustered about a common center. The instrumentation in the base region consisted of black and gold-coated heat flux meters and static pressure probes. Because of the LOX/hydrogen propellants, the radiant flux in the base region was negligible

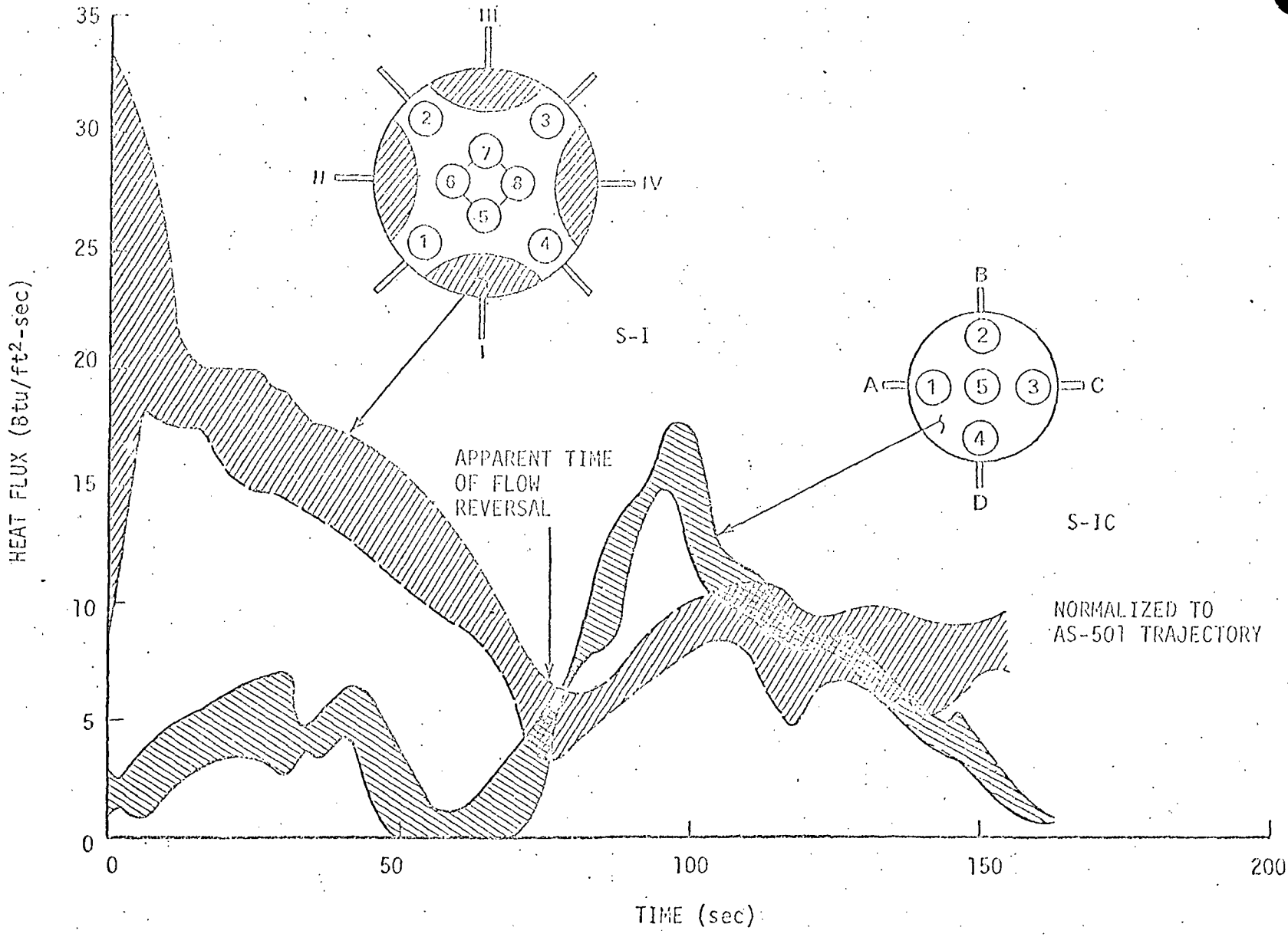

FIGURE 4-8. SATURN I, BLOCK II, AND SATURN V, S-IC TOTAL FLUX

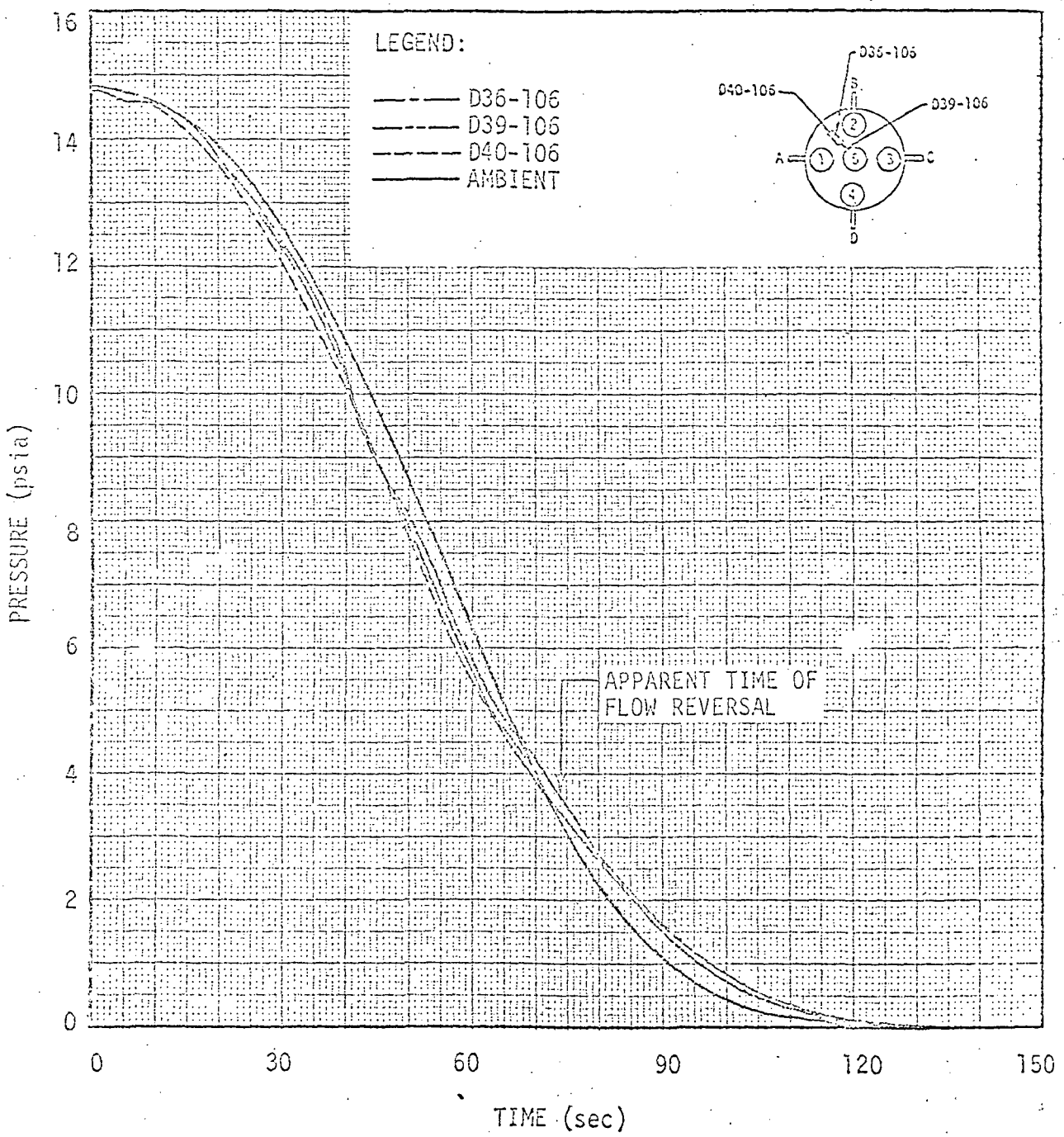

FIGURE 4-9. SATURN V, S-IC STAGE, HEAT SHIELD PITOT PRESSURES

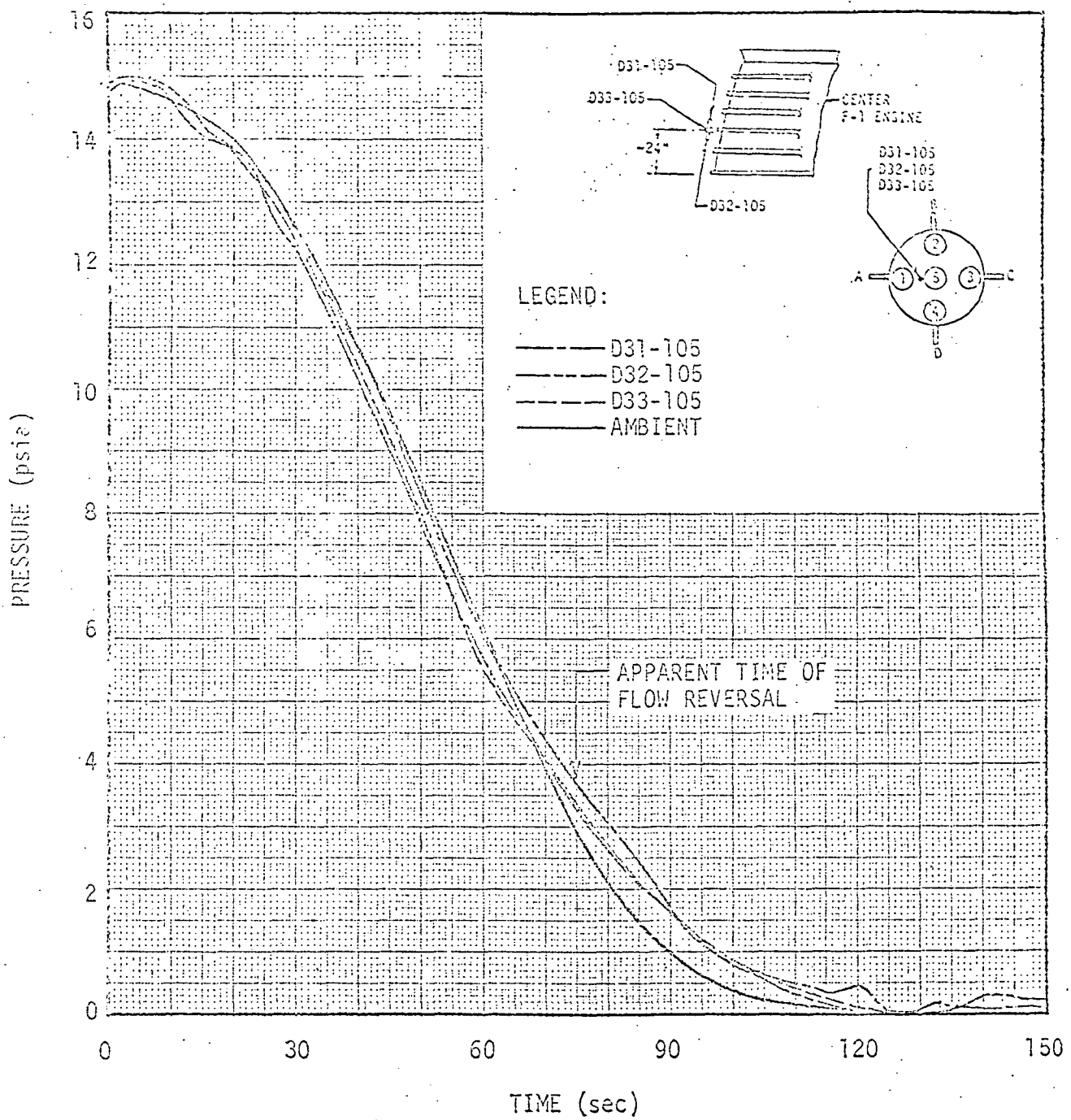

FIGURE 4-10. SATURN V, S-IC STAGE ENGINE PITOT PRESSURE

and could not be detected by combining the two different type heat flux meters. Engine ignition occurred at such a high altitude that the choked flow condition was established almost immediately. The heat shield heat flux measured at various radial distances from the center are shown in Figure 4-11. Because of the very low density of the base gas at these extreme altitudes, the base heating rates are less than 2 Btu/ft^2-sec. Another factor which also affected the base environment on this stage was the location of a helium heater nozzle in the center of the heat shield. The purpose of the helium heater was to warm the helium which was stored in the liquid hydrogen tank for use in pressurizing the liquid oxygen tank. The heater consisted of a low temperature combustion chamber/heat exchanger combination attached to a small nozzle. The nozzle discharged gas into the base region at a flow rate of 0.05 lb/sec and a temperature of 800°F. The secondary flow from this helium heater nozzle had some effect upon the base convective heating. The effect would appear to be a reduction in the heating rates.

Shown in Figure 4-12 are heat shield static pressures measured at various radial locations during one of the S-IV stage flight tests. As shown in the figure, the pressures are low and indicate that the choked flow condition is reached shortly after ignition.

4.2.4 Saturn S-II Flight Results

Shown in Figures 4-11 through 4-19 are typical gas temperatures, heating rates, and pressures measured in the base region of the Saturn V, S-II upper stage. This vehicle had five LOX/hydrogen fueled J-2 engines. The environment measured in the base region of this stage shown in Figure 4-11 consisted of approximately 3 Btu/ft^2-sec total heat flux, a 1 Btu/ft^2-sec radiant flux, and a 1000°F gas temperature. The resulting convective flux is shown in Figures 4-14 and 4-15. A cylindrical interstage with a diameter the same as the basic vehicle extended approximately 7 inches below the engine exit plane. This

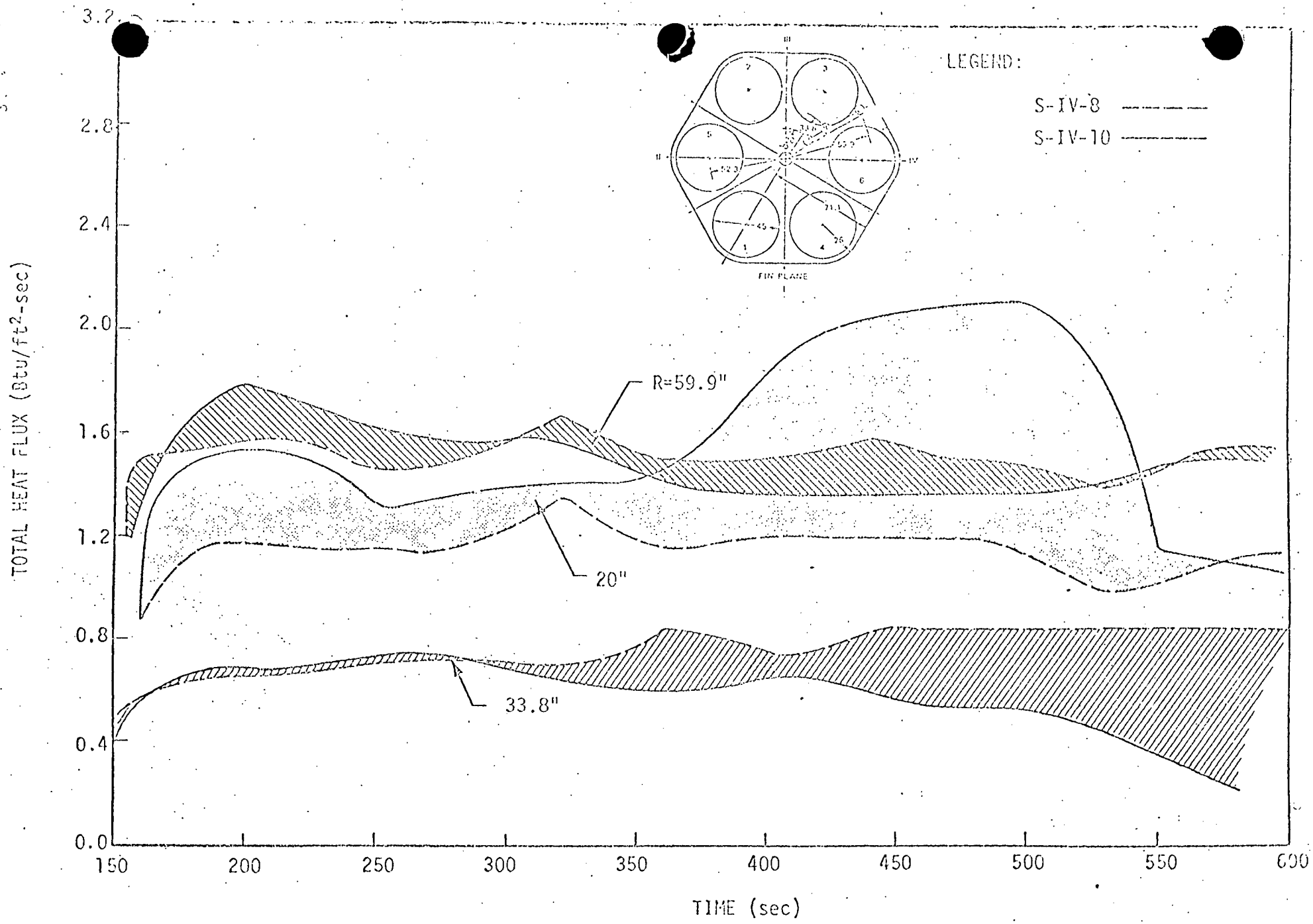

FIGURE 4-11. S-IV STAGE BASE HEAT FLUX

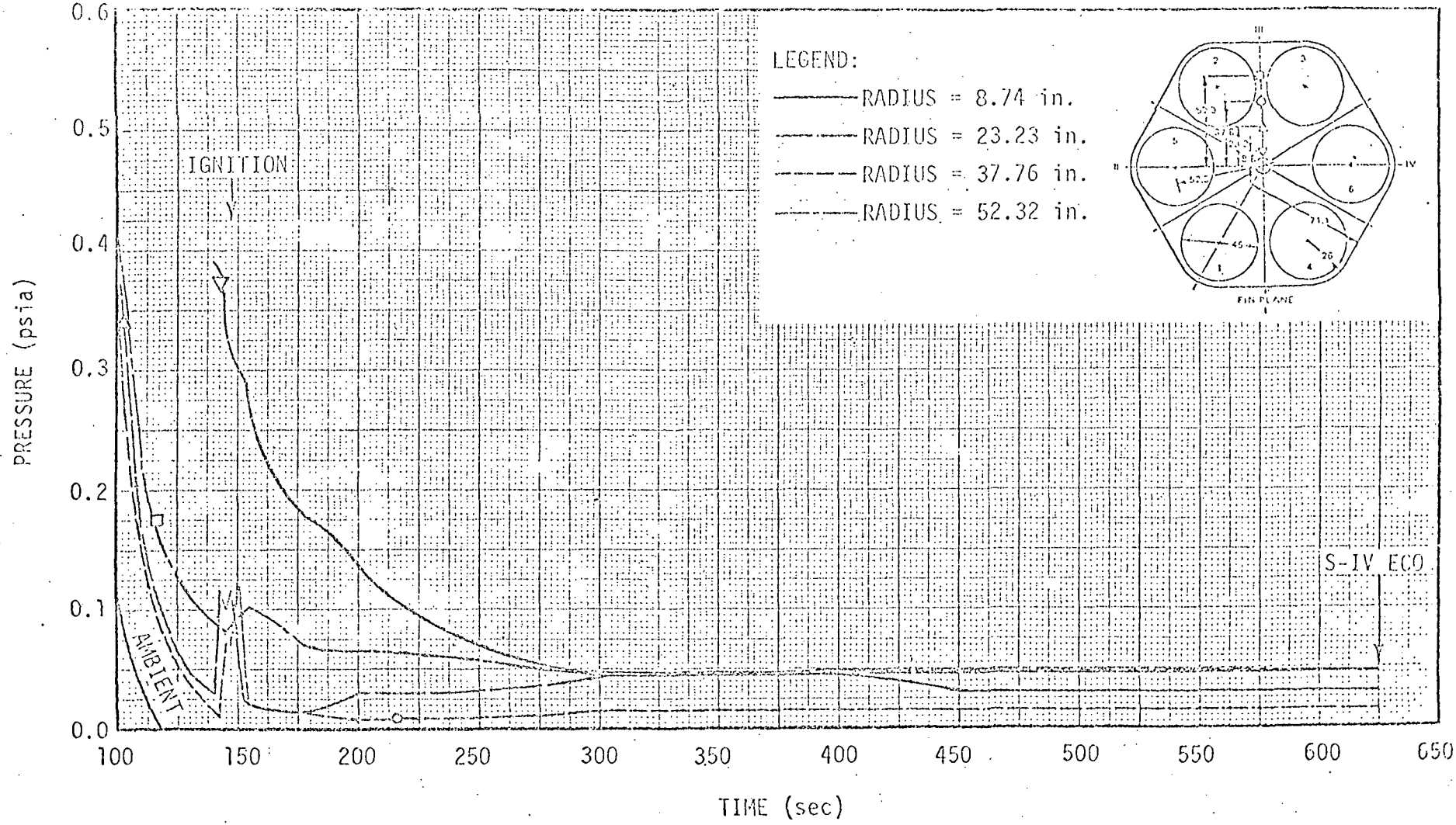

FIGURE 4-12. SATURN I, S-IV-8, HEAT SHIELD PRESSURE

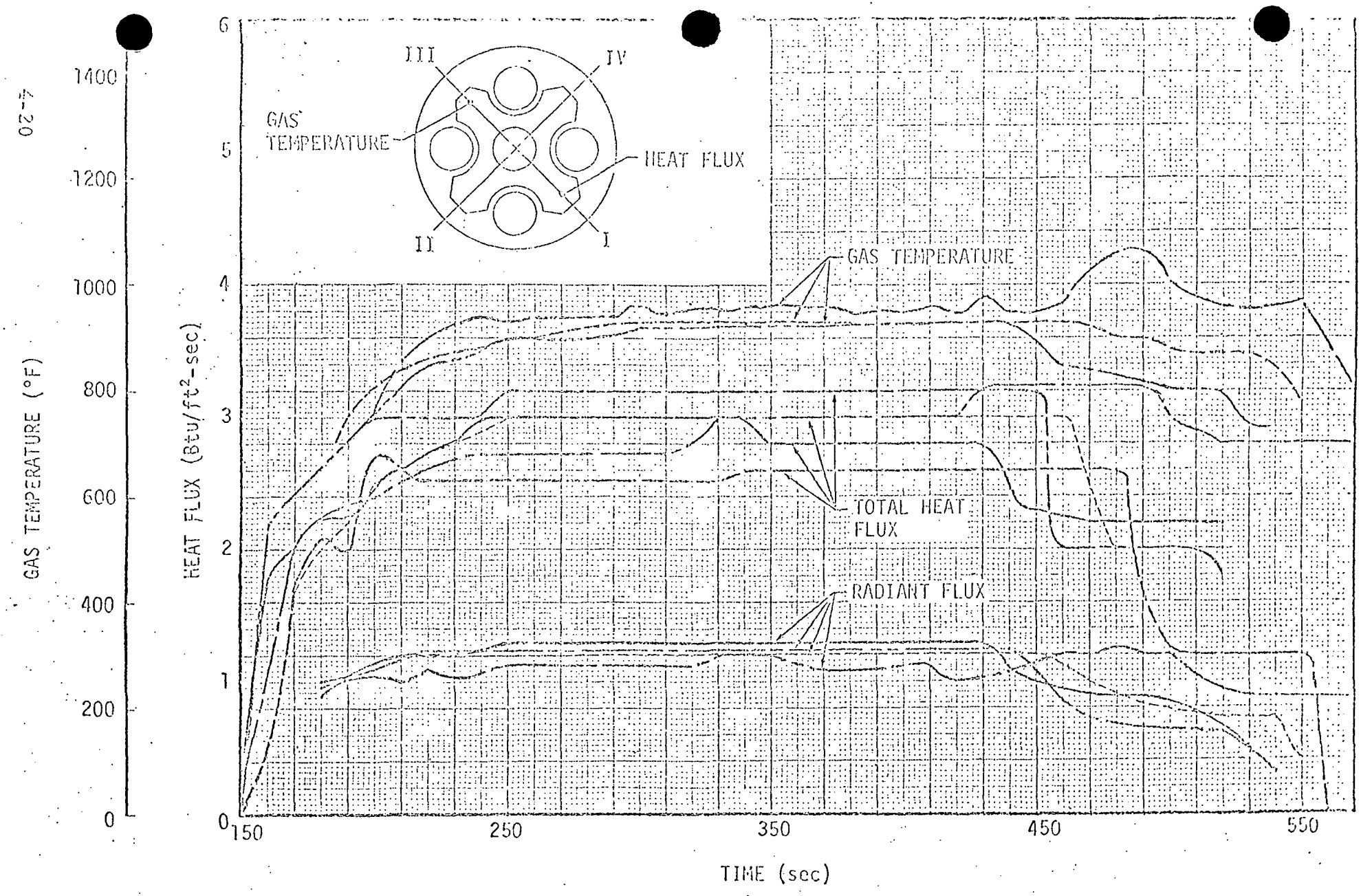

FIGURE 4-13. S-II STAGE BASE ENVIRONMENT

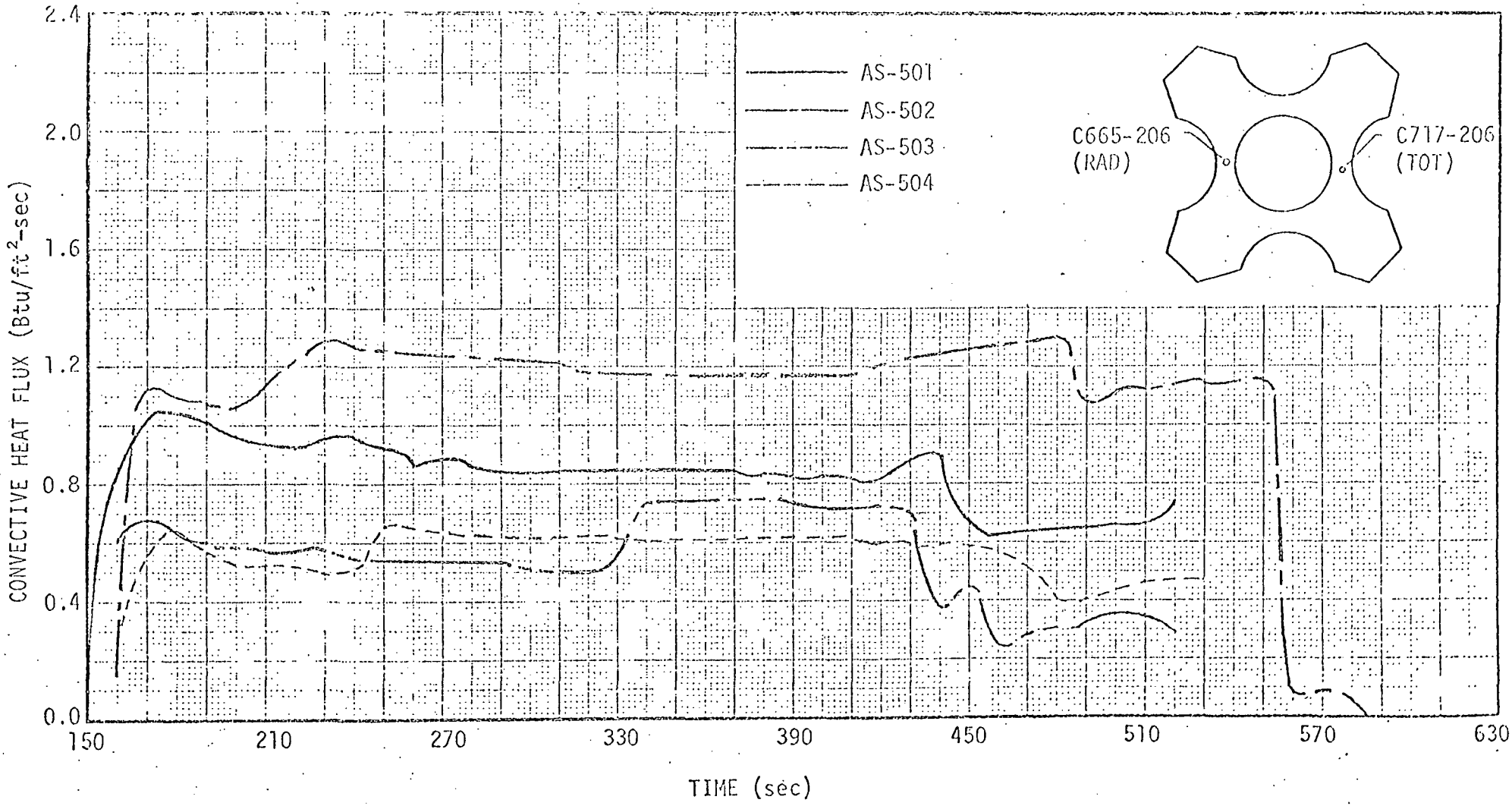

FIGURE 4-14. SATURN V, S-II, HEAT SHIELD HEAT FLUX FROM C665-206 AND C717-206

Page Intentionally Left Blank

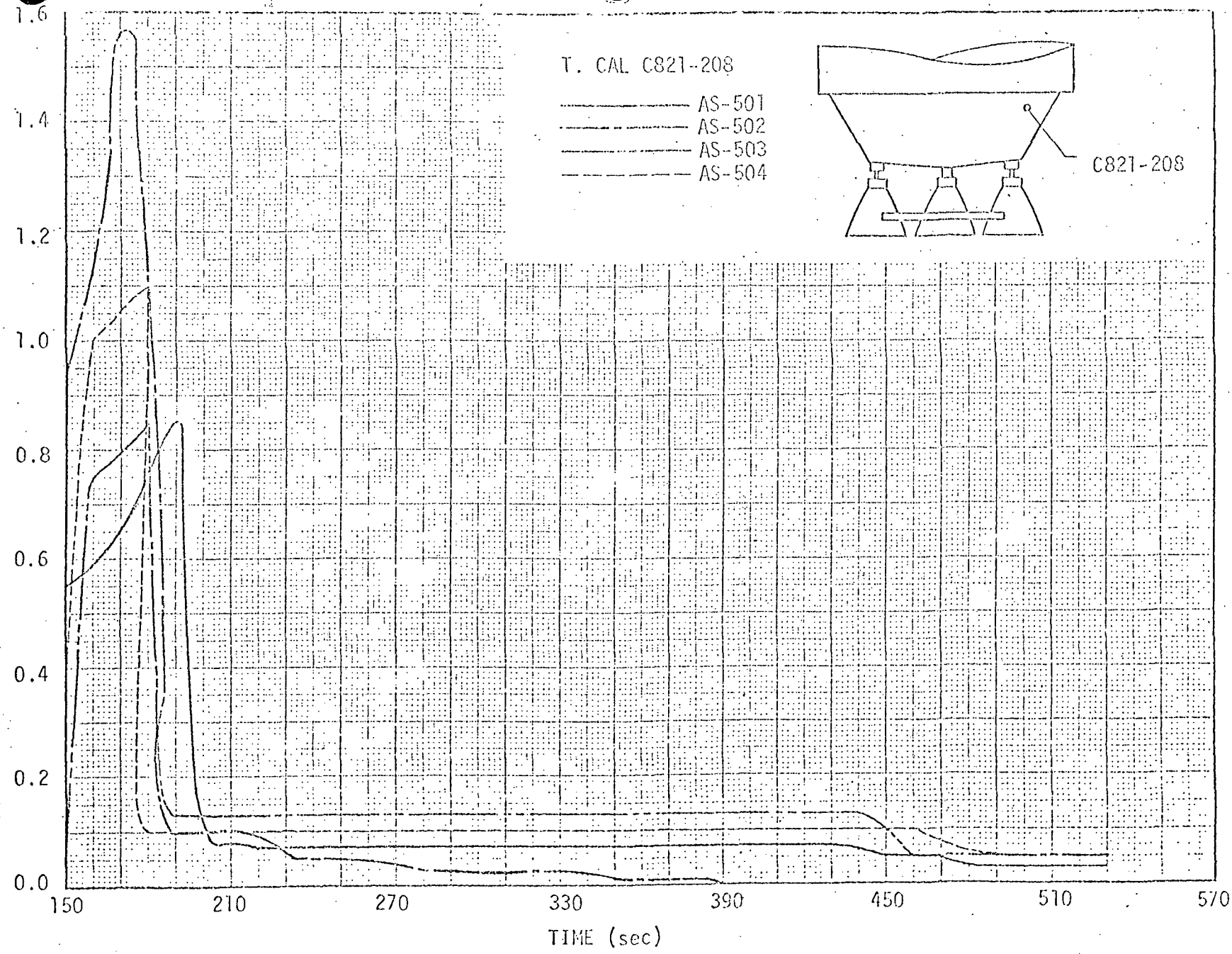

FIGURE 4-16. SATURN V, S-II STAGE THRUST STRUCTURE TOTAL HEAT FLUX

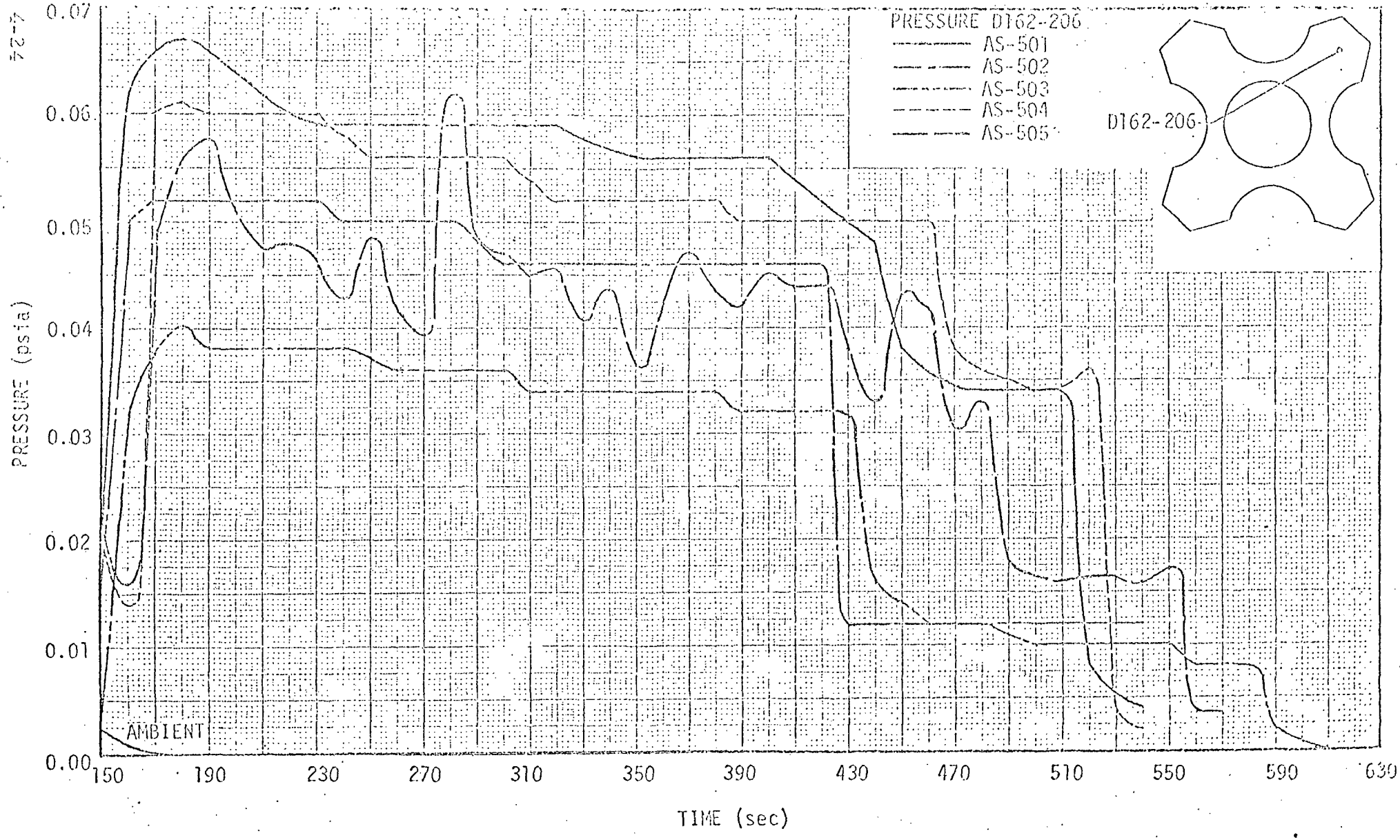

FIGURE 4-17. SATURN V, S-II STAGE STATIC PRESSURE

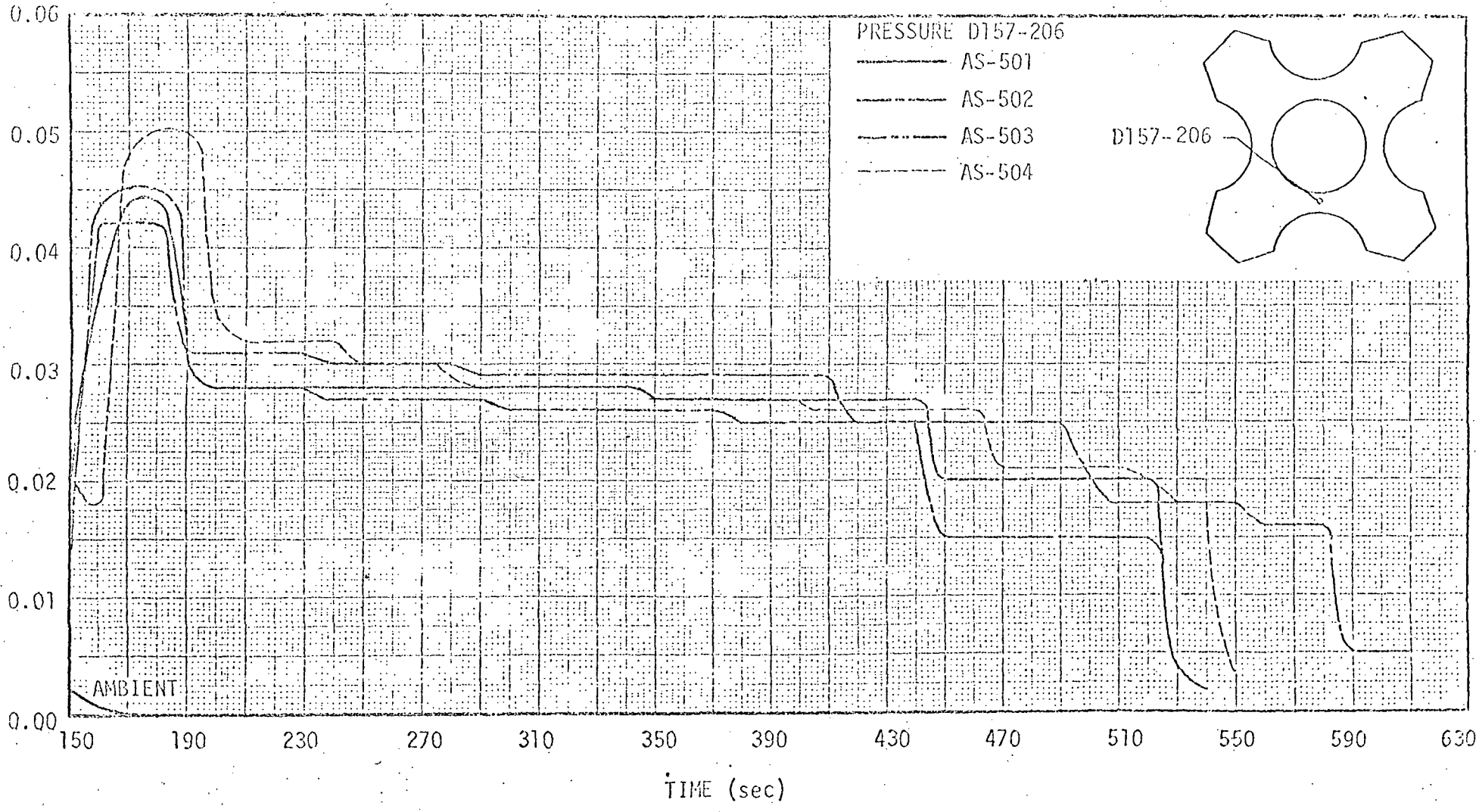

FIGURE 4-18. SATURN V, S-II STAGE HEAT SHIELD PRESSURE

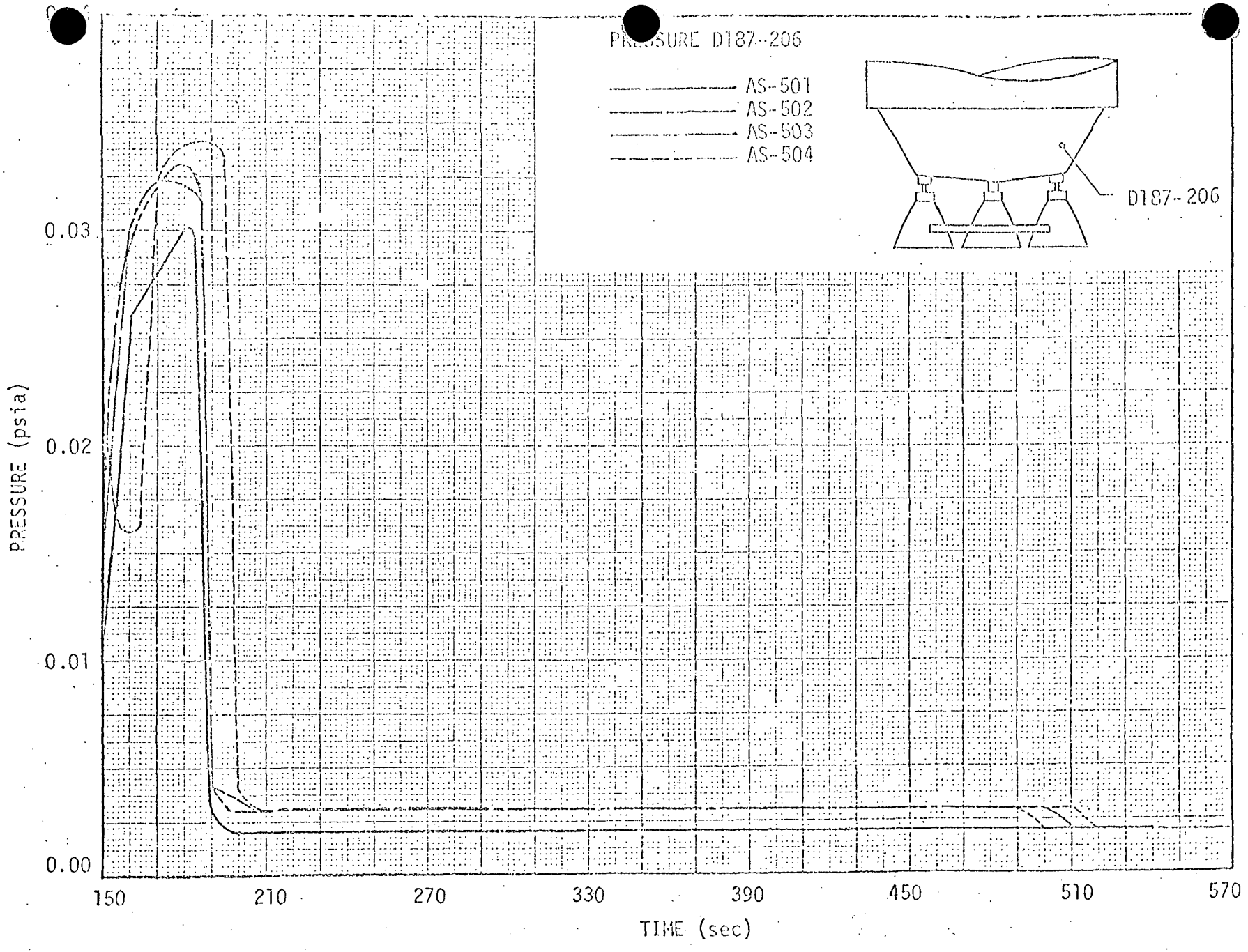

FIGURE 4-19. SATURN V, S-II STAGE THRUST STRUCTURE PRESSURE

interstage was jettisoned after the first 30 seconds of the flight. The effects of the interstage on the base thermal environment can be seen in the figures. The heating rates and pressures above the heat shield tended to be higher with the interstage on the vehicle and dropped drastically when it was jettisoned (see Figures 4-16 and 4-19). The pressure on the heat shield was also higher during this period (see Figure 4-18). The heat shield gas temperature and total heat flux were slightly lower with the interstage on than with it off (see Figure 4-15).

Another characteristic which can be seen in these figures is the decrease in heating rates and pressures associated with the shift in mixture ratio. The J-2 engine mixture ratio was shifted from the initial O/F = 5.5 to an OF = 4.7 late in each flight. The decreases can be seen in the figures at flight times corresponding to 400/450 seconds.

4.3 ANALYSIS AND CORRELATION OF THE MEASURED RADIANT FLUX

The radiation measured in the base region during the Saturn booster stage test flights was correlated. The correlation consisted of determining the ratio of radiation measured at any time during the flight to the measured ground level value. The ground level value was chosen after the vehicle had cleared the launch pad so that the effects of the flame deflector could be eliminated. The resulting ratios are presented as a function of vehicle altitude in Figures 4-20 through 4-23. Figure 4-20 shows the dimensionless radiation ratio obtained from the Saturn I measured data for two different zones of the heat shield. The Saturn I, Block I (SA-1 through SA-4) and Saturn I, Block II (SA-5 through SA-10) are both shown in this figure. The radiation ratio obtained from the Saturn S-IB flight test data is shown in Figure 4-21.

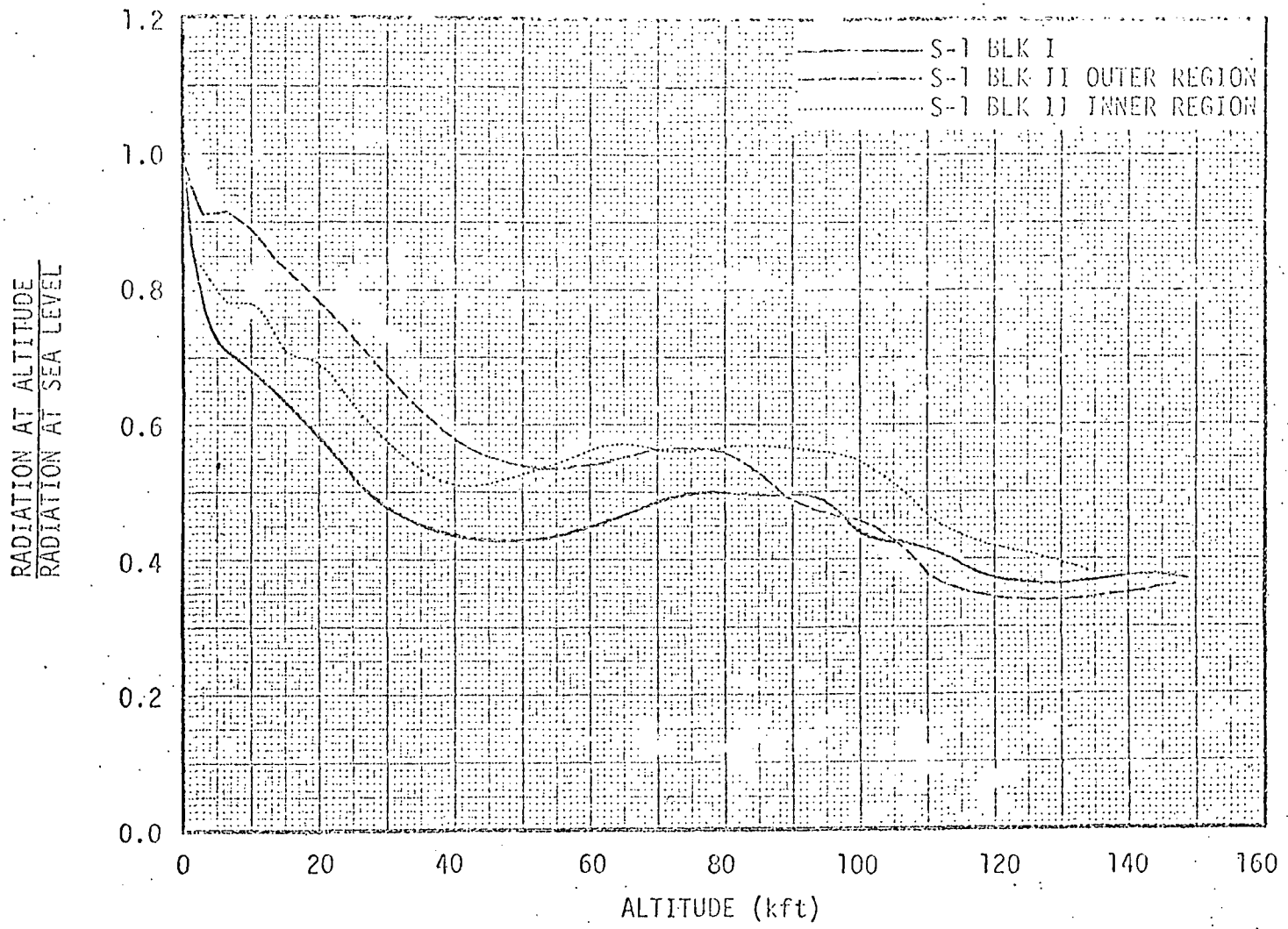

FIGURE 4-20. FRACTION OF GROUND LEVEL RADIATION, SATURN I

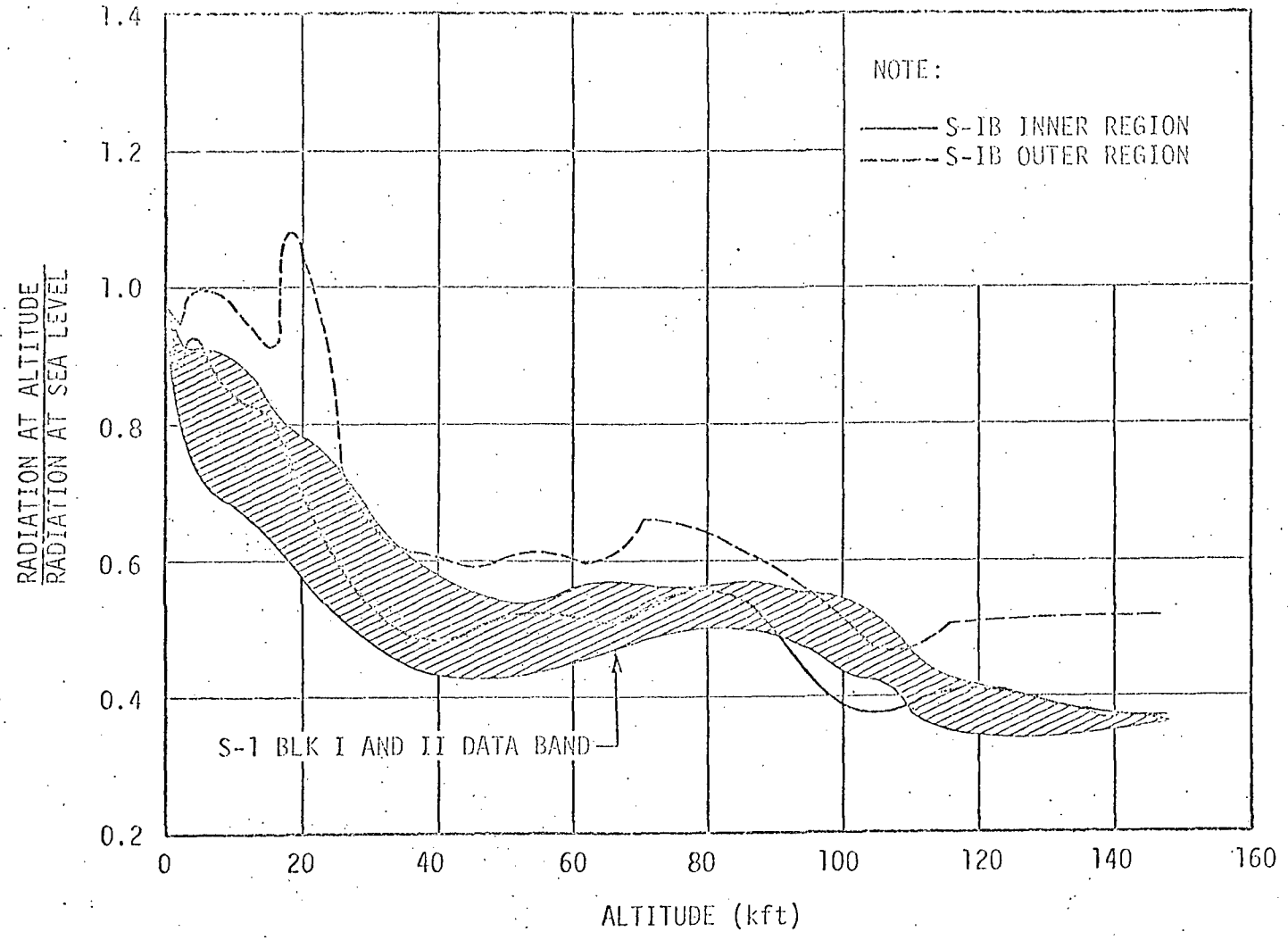

FIGURE 4-21. FRACTION OF GROUND LEVEL RADIATION, SATURN-IB

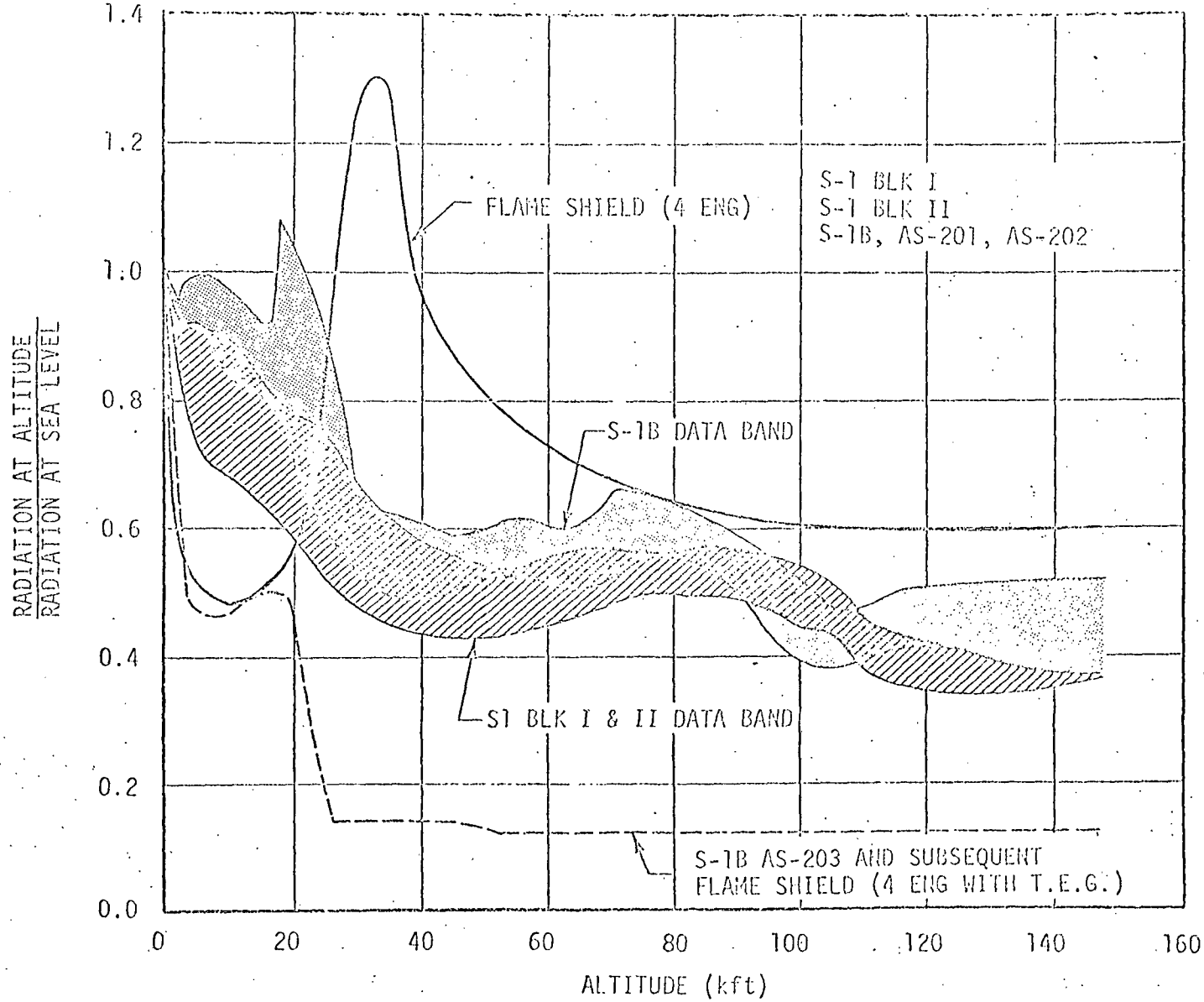

FIGURE 4-22. FRACTION OF GROUND LEVEL RADIATION, SATURN I, S-1B FLAME SHIELD

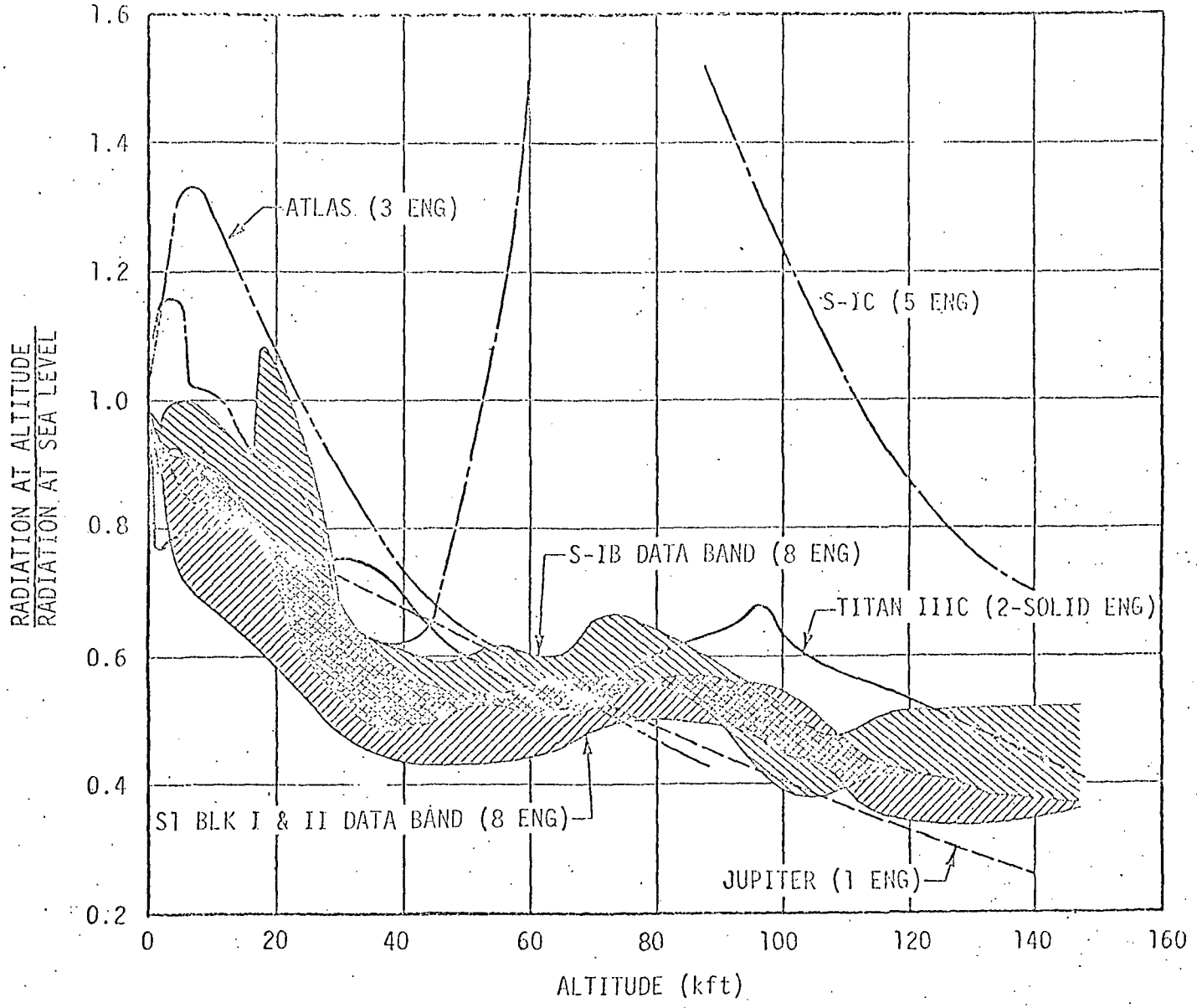

FIGURE 4-23. FRACTION OF GROUND LEVEL RADIATION, SATURN S-IC AND OTHER VEHICLES

Also shown in this figure is the Saturn I, Blocks I and II data band. In studying the data, a slight upward trend appears to be indicated in going from the Saturn I, Block I vehicle radiation decay to the Saturn IB results. This trend was probably caused by slight changes in the vehicle configuration and the uprating of the engine from 165,000-pound thrust, Block I, (578-psia chamber pressure) to 200,000-pound thrust, S-IB, (689-psia chamber pressure).

Figure 4-22 shows the radiation ratio for the Saturn S-I and S-IB flame shield regions. The heat shield data bands are also shown in this figure. As seen in this figure, the Saturn S-I and S-IB flame shield radiation ratios are approximately the same up to an altitude of approximately 15,000 feet and decrease at a much faster rate than the heat shield radiation. Beyond 15,000 feet a completely different trend is indicated. This difference can be explained and resulted from changes in the turbine exhaust gas discharge. The Saturn I turbine exhaust gas was discharged overboard through ducts on the sides of the vehicle. This was changed on the third Saturn S-IB and subsequent vehicles. For these vehicles, the turbine exhaust was discharged into the flame shield area. The sharp increase in radiation shown for the S-I flame shield coincides with the beginning of flow reversal. This same trend (i.e., slight hump in the curve), but less significant, can be seen in the heat shield radiation as well. This indicates that the radiation is being influenced by the flow reversal.

Shown in Figure 4-23 are the radiation ratios for the Saturn S-IC heat shield, the ATLAS, the JUPITER, the TITAN III-C, and the Saturn S-I and S-IB heat shield data bands. The S-IC vehicle had five LOX/RP-1, F-1 engines. The ATLAS had three engines in-line, and the two outboard

engines were the same as the Saturn S-I engines. The JUPITER vehicle had only one engine, which was also the same as the Saturn S-I engines. The TITAN III-C had two solid propellant engines. Two of the interesting trends shown in this figure are the JUPITER and Saturn S-IC results. Because the JUPITER had only one engine, flow reversal between engine exhaust jets did not exist. The JUPITER radiation ratio decreases constantly throughout most of the flight. Because the engines were the same, comparing the JUPITER results to the Saturn S-I results gives some indication of the engine clustering effects. The Saturn S-IC results are approximately the same as the Saturn S-I up to an altitude of 35,000 feet. Beyond this altitude, the S-IC radiation ratio shows a sharp increase to a value well above the ground level radiation. This also coincides with the beginning of flow reversal.

Because of the very complex nature of the problem, accurate radiation predictions are very difficult to make. The technique used in predicting the base radiation for the Saturn boosters was a semi-empirical method which depended strongly upon experimental results. The radiation at sea level was computed using Equation 2-17. The emissive powers and plume shapes were obtained from measurements and photographs taken during captive engine test firings. The radiation at altitude was predicted by extrapolating from one class of vehicles to the next using results similar to those shown in Figures 4-20 through 4-23. If it had not been for using conservative estimates of the sea level radiation, this technique would have led to serious underpredictions of the radiation at higher altitudes. An example of this can be seen in Figure 4-23 by comparing the Saturn S-IB radiation decay to the Saturn S-IC radiation.

By considering Equations 2-15 through 2-17 the problems with this technique can be discussed. When the ratio of radiation-at-altitude to radiation-at-sea level is plotted as a function of altitude, this essentially shows how the radiation varies with ambient pressure. When this ratio is used to extrapolate the radiation from one vehicle to the next, the assumption that is being made is that the plume emissive power and view factor will vary with pressure in the same general way. This, in turn, is assuming that the plume temperature, emissivity, and shape will vary with ambient pressure in this same general way. By considering Figure 4-23, this is obviously not a valid assumption. By comparing the radiation characteristics of the JUPITER and Saturn S-I and S-IB (Figure 4-23) and the Saturn S-I flame shield (Figure 4-22) where the engines were nearly the same, it is seen that clustering has a significant effect upon the radiation at higher altitude. Furthermore, considering the Saturn S-I flame shield radiation when flow reversal starts (approximately 20,000 ft) and Equation 2-17, it appears that the afterburning is either flushed back into the flame shield or starts to burn much closer to the engine exits at this time. In comparing the Saturn S-I flame shield radiation to the Saturn S-IB with the flame shield turbine exhaust discharge, it would appear that dumping this relatively large amount of unburned fuel into this region prevented the afterburning from taking place. In comparing these results to the S-IC radiation shown in Figure 4-23, it appears that afterburning and flow reversal effects also caused the increase in radiation on this vehicle. In comparing the Saturn S-IC radiation ratio to the Saturn S-I heat shield radiation in Figure 4-23, where the clustering arrangement is not too dissimilar, it must be concluded that afterburning and flow reversal effects take place in very complex ways. It must also be concluded that extrapolating the radiation from one vehicle configuration to another should be approached with caution.

4.4 EVALUATION AND COMPARISONS OF THE SATURN S-IC CONVECTIVE HEATING

Correlating and normalizing experimental data is a necessary step in solving a convective heating problem which has not been previously solved. However, the serious instrumentation-related problems associated with much of the Saturn flight data have made the correlation of the flight results very difficult. Such results as gas temperatures indicating convective heating simultaneously with the heat flux meters indicating cooling are factors which require serious explanation in correlating the flight data. The S-IC flight results are typical of the problems which are encountered.

Figure 4-24 shows the base gas temperatures measured during a typical S-IC flight test. The results shown are from probes which were mounted through the heat shield with the sensing element located from 0.25 to 2.5 inches below the heat shield surface. Also shown in the figure is the center temperature of the total calorimeter membrane. The membrane center temperature was computed from the measured total heat flux and the calorimeter sink temperature using the following equation,

$$T_c - T_o = q_t \frac{r_o^2}{4K\delta} \qquad (4\text{-}1)$$

where

T_c - foil calorimeter center temperature

T_o - foil calorimeter sink temperature

r_o - radius of the foil

K - thermal conductivity of the foil

δ - foil thickness.

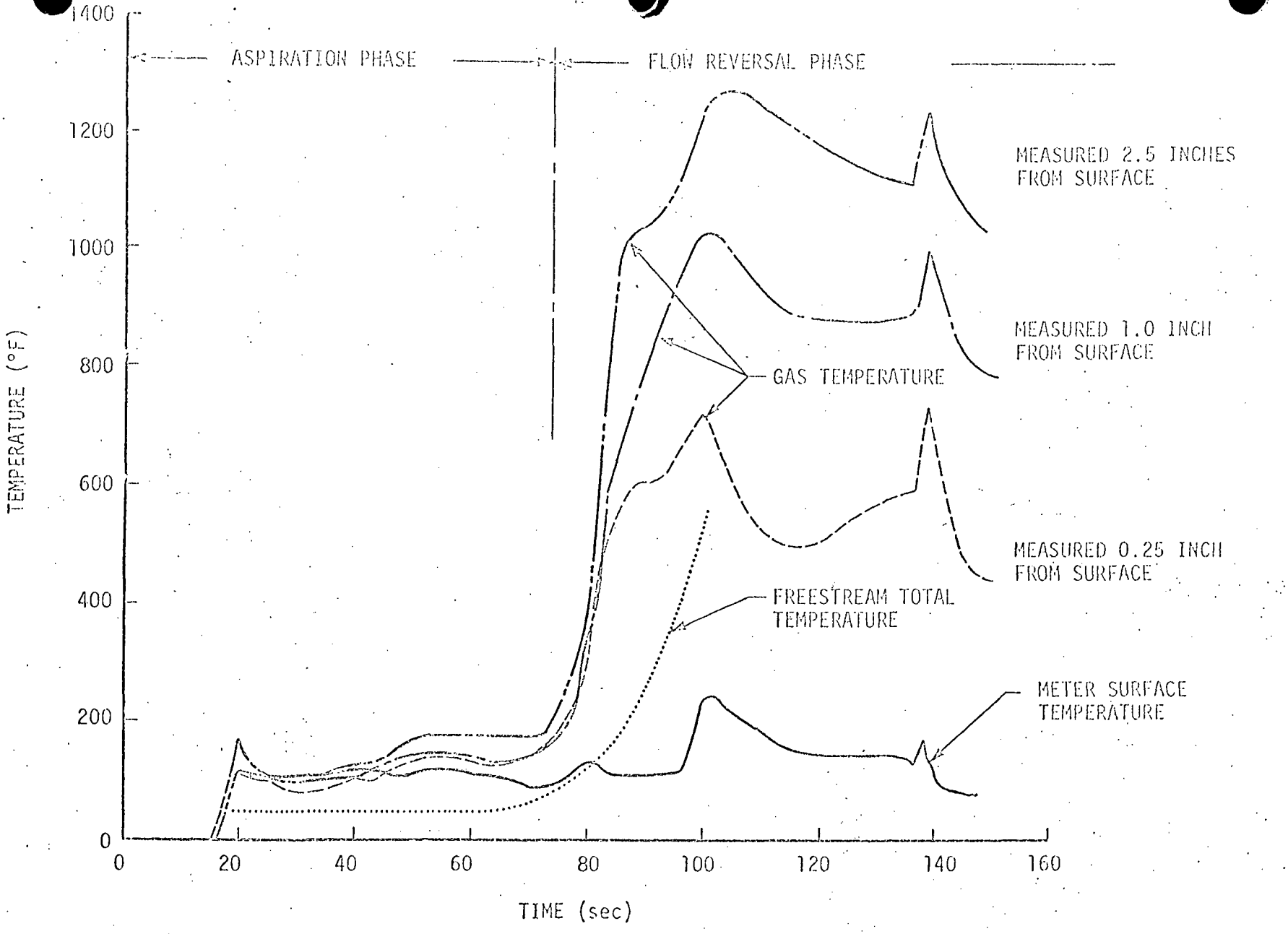

FIGURE 4-24. S-IC HEAT SHIELD GAS TEMPERATURES

Also shown in the figure is the total (i.e., stagnation temperature of the freestream).

Shown in Figure 4-25 are the bands of radiant and total heat flux measured by the one set of heat shield calorimeters during the first five S-IC flight tests. Included in Figure 4-25 is the adjunction (denoted by plus signs) in the radiation band which would account for the error in measured radiation resulting from angular variation in window transmissivity (see Section 3.4.2).

Shown in Figures 4-26 and 4-27 are the convective heating rates (with some of the obviously erroneous data deleted) evaluated from the heat flux meters at two locations on the S-IC heat shield. The convective flux is shown for both the uncorrected radiation (i.e., as measured) and for the measured radiation corrected for angular variation in window transmissivity.

By comparing the results of Figure 4-24 to Figures 4-25, 4-26, and 4-27 during the aspiration phase of the flight, the disagreement in measured data becomes obvious. Figure 4-24 shows the measured gas temperature to be higher than the highest temperature of the calorimeter beyond 40 seconds. Prior to 40 seconds, the measured gas temperature is approximately equal to the calorimeter temperature. The implied result would be convective heating of the calorimeter at least beyond 40 seconds. However, the result obtained by evaluating the convective flux using the measured heating rates is just the opposite, i.e, significant convective cooling during the first 75 seconds of flight (see Figures 4-26 and 4-27).

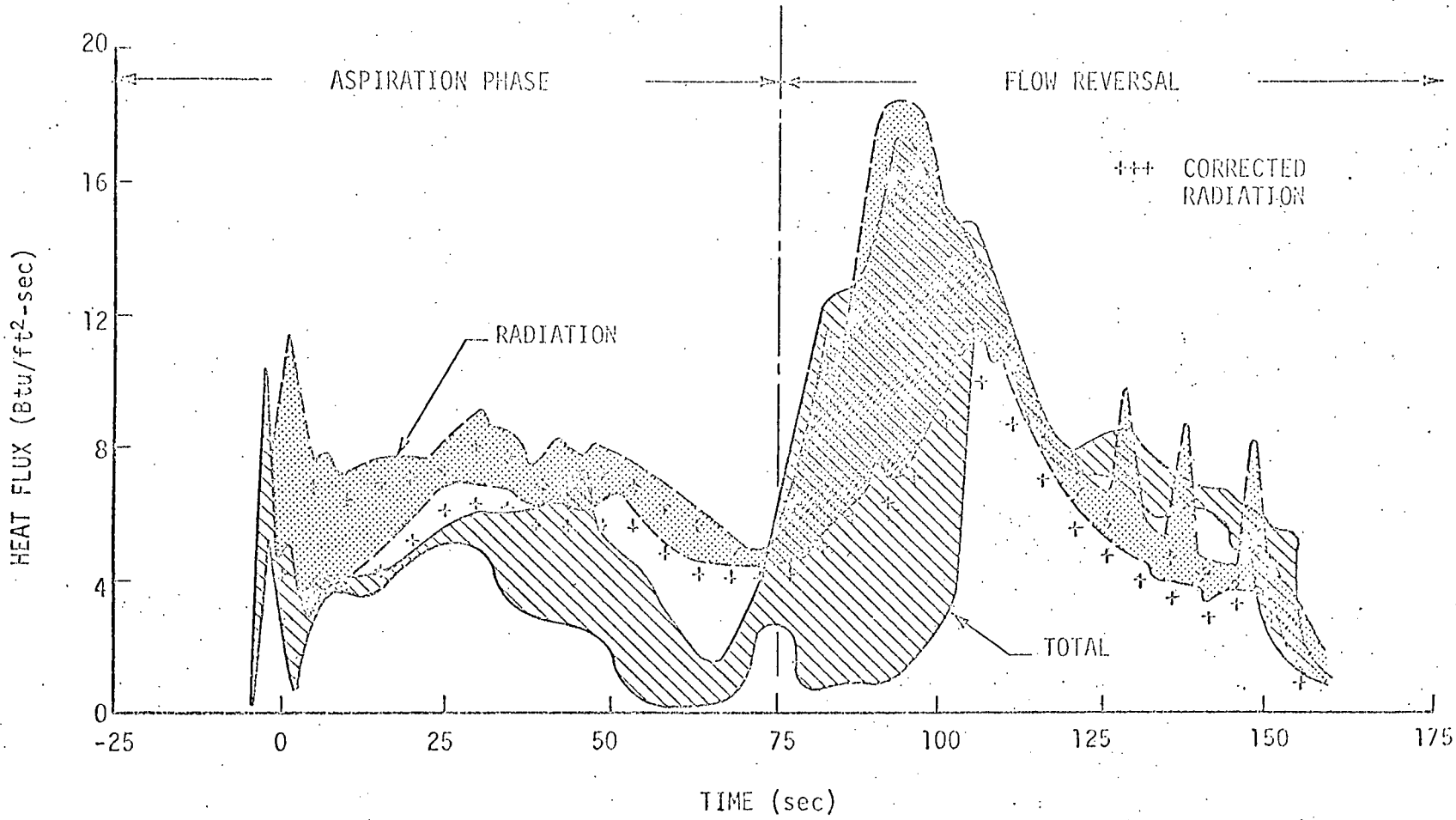

FIGURE 4-25. S-IC HEAT SHIELD RADIANT AND TOTAL HEAT FLUX

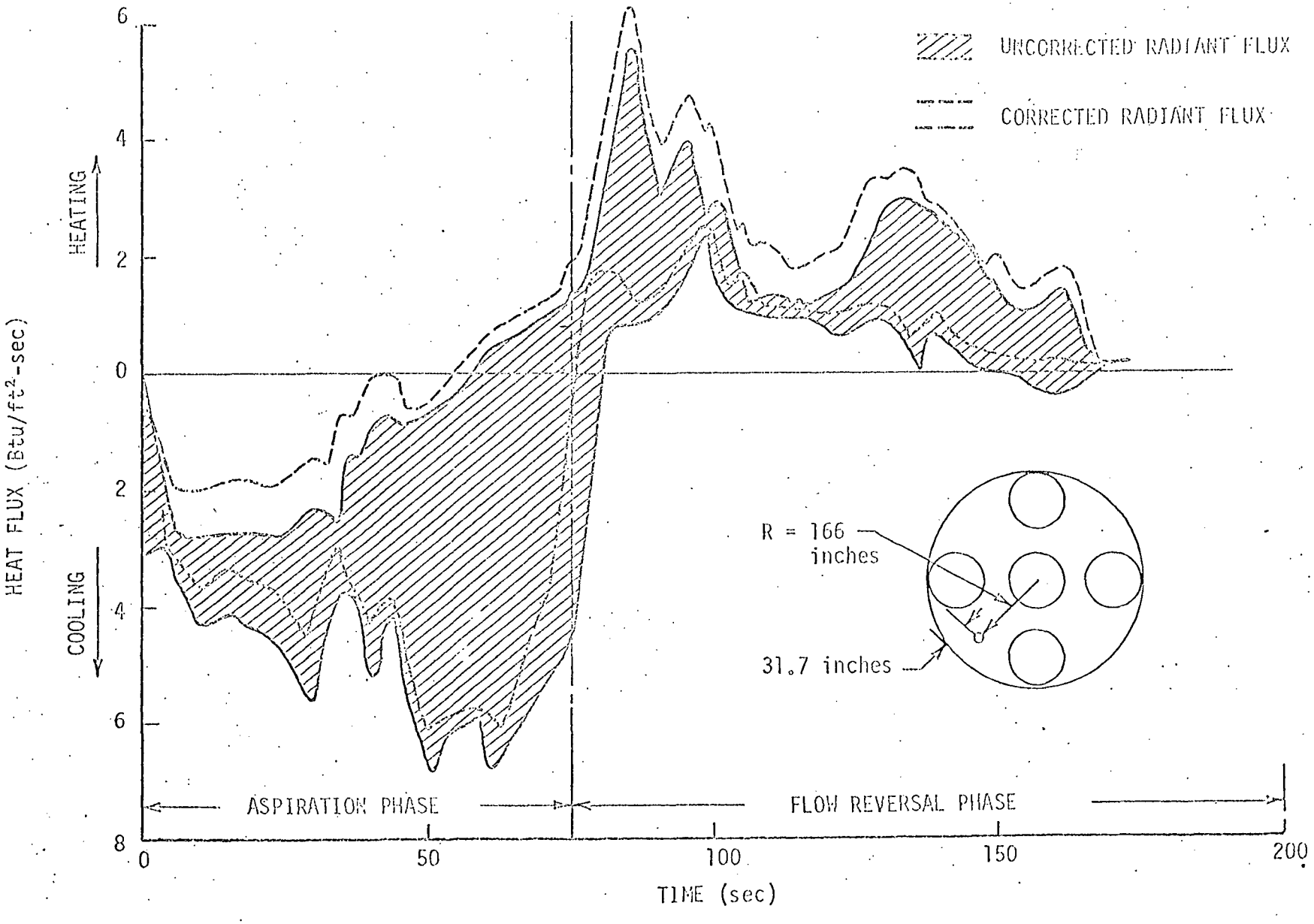

FIGURE 4-26. S-IC HEAT SHIELD CONVECTIVE FLUX TO TOTAL CALORIMETER C25-106

Page Intentionally Left Blank

This disparity must be explained before it is possible to correlate the flight test data. Some possible reasons are:

- Because of the sensitivity of the gas temperature probes to incident radiation, the temperature measured by the probes was higher (during the aspriation phase) than the actual base gas temperature.
- If the incident radiation beyond λ = 5-μm were negligible (i.e., plume radiation significantly different from a greybody), then an additional error in the measured radiant flux would exist (see Section 3.4.2).
- The possibility of moisture vaporized from the heat shield condensing on the total calorimeter surface exists and could have caused a low indicated total flux (see Section 3.3.4).

The possibility of explaining the disagreement on the basis of the surface temperature mismatch has also been suggested. This reasoning has been rejected. Using the semi-empirical solutions which have been derived for computing the heat transfer coefficient across a surface temperature discontunity, negative heat transfer coefficients can be computed for specified conditions. However, negative heat transfer coefficients cannot exist in reality because of violating the first law of thermodynamics. The situation which probably exists is that the recovery temperature of the boundary layer fluid which influences the heat transfer near the discontinuity is also changing. These changes in recovery temperature have not been included in the solutions of the surface temperature mismatch heat transfer. If this could be included in the solutions, negative heat transfer coefficients should not be possible.

Of the reasons proposed, none can be conclusively ruled out. However, available spectral radiation measurements [Refs. 4-3 and 4-4 (also see Figure 6-13b)] indicate that large LOX/RP-1 fueled rocket engine plumes do tend to emit greybody type radiation. Condensation of

moisture on the surface of the calorimeter is apparently a real possibility; however, the degree to which it could have reduced the measured total heat flux is speculative.

The desired goal of any correlation of convective heat transfer is the development of a dimensionless Stanton number, Prandtl number-Reynolds number relation. These correlations usually provide the basis for selecting the coefficients C, m, and n and the characteristic dimension, x, of Equation 2-13. Another advantage of this correlation is that it provides a direct means of comparing the convective heating for different geometric bodies and flow fields. A dimensionless correlation of the Saturn S-IC base heat shield convective heat tranfer during the aspriation phase of the flight was developed using the following assumptions:

- The freestream total temperature (see Figure 4-24) was used as the base gas recovery temperature.
- The transport properties of air (i.e., C_p, μ, k) were used and evaluated at the film temperature [i.e., $(T_r + T_w)/2$].
- The base flow velocity was evaluated as discussed in Section 3.5.2 (see Figure 3-35).
- Because the flow was into the base region during this phase of the flight, the characteristic dimension was taken as the distance from the edge of the base to the heat flux meter.
- The convective heat transfer was evaluated every 5 seconds for each heat flux meter and the results joined by a straight line in Figures 4-28 and 4-29.

Before correcting the measured radiation, most of the Saturn flight results appear to fit between lines A and B shown in Figure 4-28. The resulting correlation equations obtained for Lines A and B are:

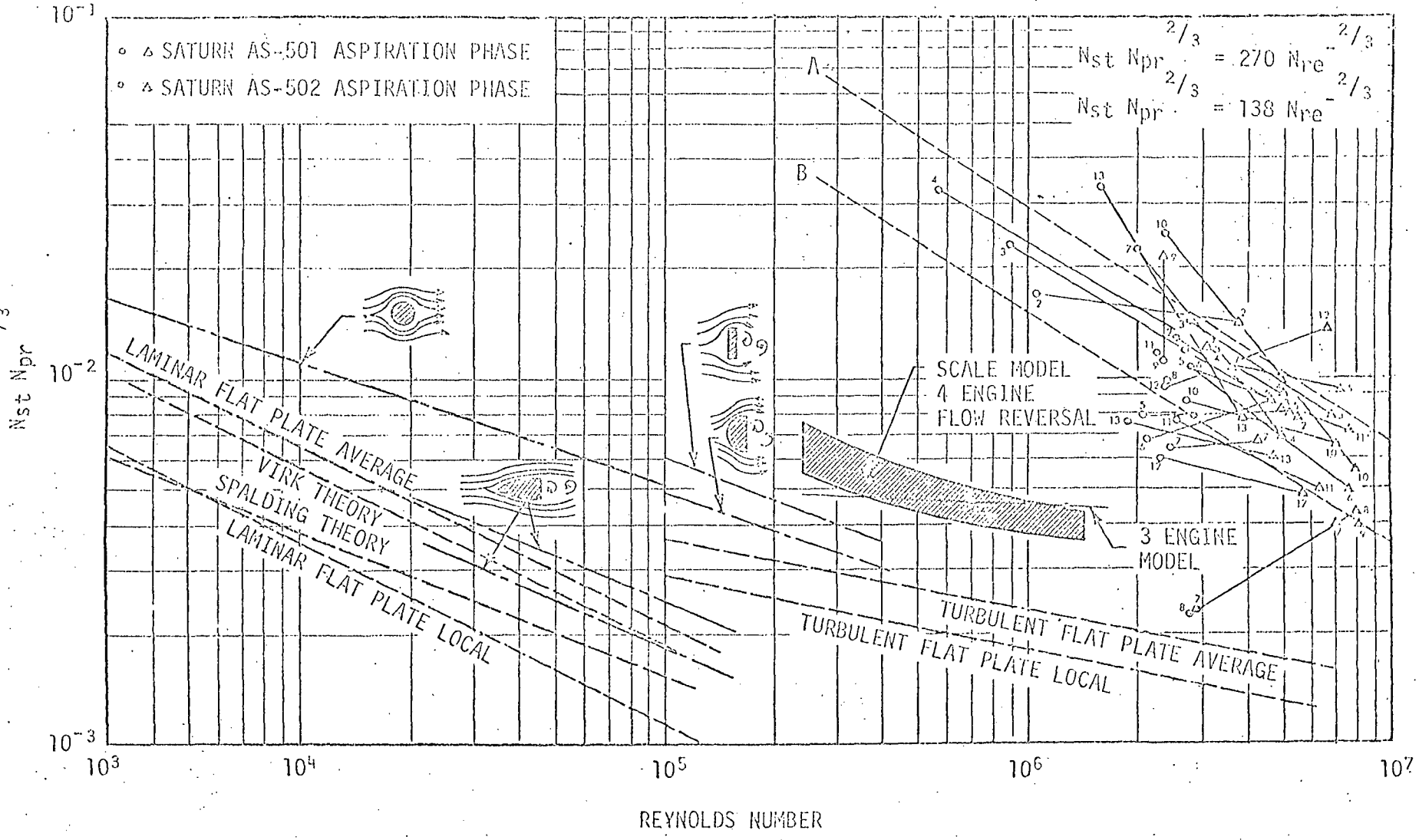

FIGURE 4-28. BLUFF BODY AND SATURN S-IC FLIGHT TEST STANTON NUMBER -- REYNOLDS NUMBER CORRELATIONS USING UNCORRECTED RADIATION RESULTS

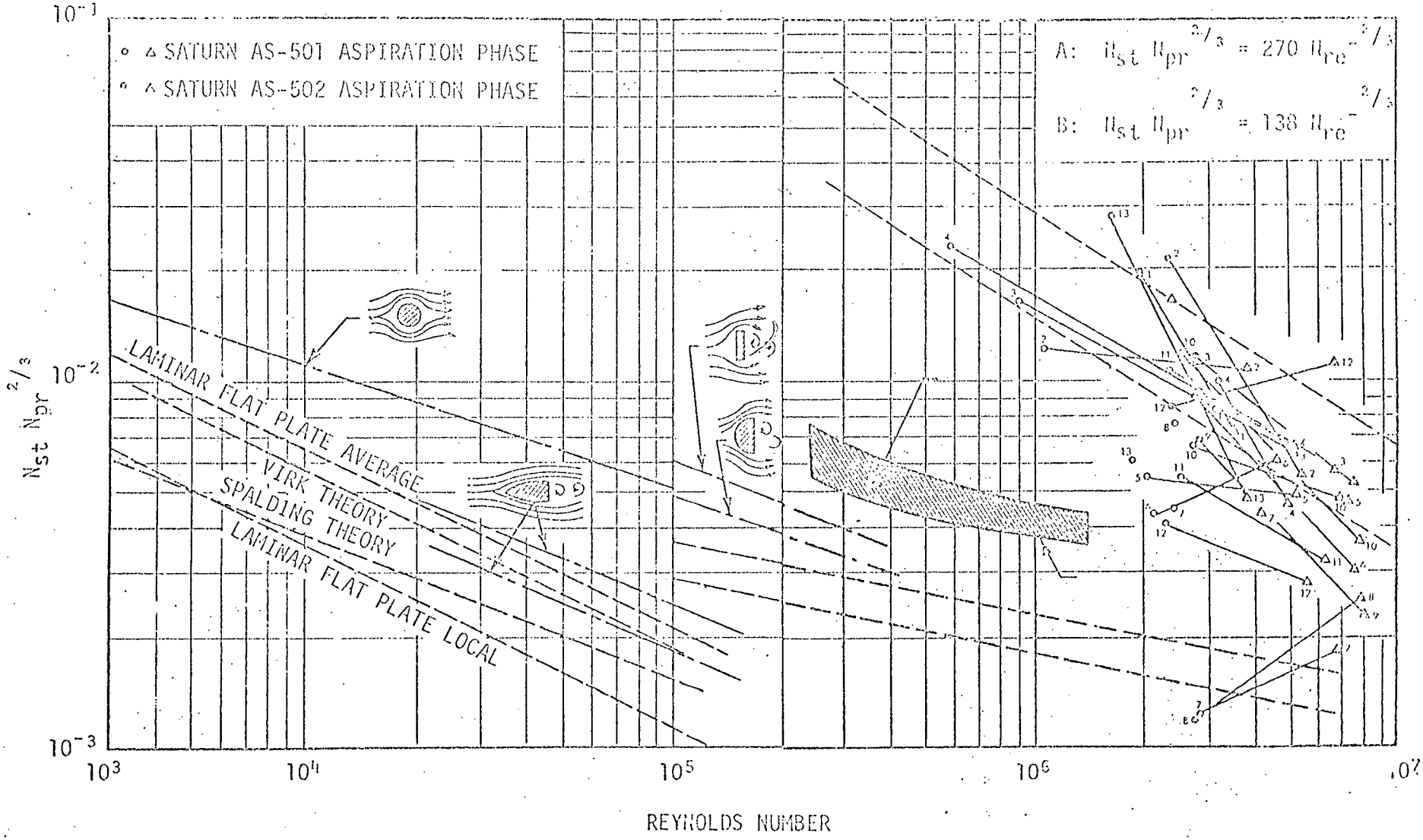

FIGURE 4-29. BLUFF BODY AND SATURN S-IC FLIGHT TEST STANTON NUMBER -- REYNOLDS NUMBER CORRELATIONS USING CORRECTED RADIATION RESULTS

$$A: \quad N_{st} N_{pr}^{2/3} = 270 N_{re}^{-1/3}$$

$$B: \quad N_{st} N_{pr}^{2/3} = 138 N_{re}^{-1/3} \qquad (4\text{-}2)$$

As opposed to this, the correlation equations which were obtained for the other bodies shown in Figures 4-28 and 4-29 range as shown in Table 4-1.

TABLE 4-1. CORRELATION EQUATIONS FOR SEPARATED REGIONS

REFERENCE	BODY TYPE	CORRELATION EQUATION
4-7	Cylinder, cross flow	$N_{st} = 0.19\ N_{re}^{-1/3}$
4-8	Flat Plate, normal	$N_{st} = 0.28\ N_{re}^{-1/3}$
4-8	Hemisphere	$N_{st} = 0.22\ N_{re}^{-1/3}$
4-6	Wedge, side plates	$N_{st} = 0.135\ N_{re}^{-0.4}$
4-6	Wedge	$N_{st} = 0.23\ N_{re}^{-1/3}$
4-9	Theory (Spalding)	$N_{st} = 0.15\ N_{re}^{-0.4}$
4-10	Theory (Virk)	$N_{st} = 0.59\ N_{re}^{-0.5}$

Obviously, the correlation equations obtained from the base heating flight test data are much higher than those associated with any of the similar convective heating problems shown in the figure.

When the measured radiation is corrected for the effects of variation in angular transmissivity of the calorimeter window, the correlated flight data changes to that shown in Figure 4-29. As seen in the figure, the corrected Saturn flight test data indicates that convective heating is 2 to 10 times higher than that of a flat plate in parallel flow or in the separated regions of similar bodies. Further reduction in the

flight data might be justified by the calorimeter-heat shield surface temperature mismatch. If the measured results shown in Figure 3-16 are typical for membrane calorimeters, the flight data might be reduced by a factor of up to 1.5. Condensation heat transfer caused by the vaporized heat shield moisture could also account for the higher heat transfer shown for the flight data.

Because cooling exists during the aspiration phase of the flight, use of the correlation equations for a flat plate would give conservative heat shield design data.

4.5 CONCLUSIONS REGARDING THE FLIGHT TEST RESULTS

Some of the conclusions regarding the flight test results are as follows:

- Useful qualitative trends and characteristics can be obtained from the flight test data by comparing similar parameters over a series of flights and between similar vehicles.

- The attainment of quantitative values and comparisons directly from the measured flight data should be considered with caution in light of the instrumentation-related errors and problems.

- Because all necessary convective heat transfer parameters must be evaluated and included and because the results can be compared directly to similar convective heat transfer problems, the development of the Stanton-Prandtl-Reynolds number relation should be the ultimate goal of any base-heat transfer evaluation. At present, the inability to measure the necessary parameters accurately on flight vehicles makes this correlation difficult and requires liberal interpretation of the measured data. However, until these correlations can be made using flight-related data, serious questions regarding the measured data will continue to exist.

- The measured radiation results for vehicles using hydrocarbon and solid propellants appear to indicate the existence of an empirical relationship between the reduction in radiation with decreasing ambient pressure. This pattern may offer a simple method for making good engineering estimates of the inflight radiation from measurable ground level conditions.

- Since the most serious problems with the flight test results appear to be those associated with the instrumentation errors, additional effort could be well spent in this area. In light of the Space Shuttle vehicle, the most pressing need is for the development of accurate, reliable base parameter measurement techniques. The alternatives are

  - Spend the time and money necessary to develop new instruments with improved accuracy

  - Calibrate (i.e., to the degree possible) the existing instrumentation and evaluate the base thermal parameters approximately.

5. SCALE MODEL TESTING OF BASE HEAT TRANSFER

5.1 INTRODUCTION

In addition to the problem areas associated with rocket exhaust plume/vehicle interactions is the requirement for knowledge of the complete integrated system performance characteristics throughout the flight trajectory. Such information is often required both during the desig stages for purposes of optimizing new vehicle designs and later during flight test phases to account for variations between observed and predicted performance.

The testing of vehicle models which have been scaled down to some convenient size and operated in a simulated flight environment is one of the techniques which has been employed in the acquisition of performance data for studying the base heating problem.

Certain limitations exist in scale modeling such as the size and operating capabilities of available facilities and the degree to which the full-scale vehicle can be modeled. The limitations are compounded by the lack of understanding of the base heating problem which results in the inability to fully define all the necessary scaling laws. Two different test techniques were employed for the Saturn scale model test program. These were designated as the long-duration and short-duration techniques. The long-duration technique consisted of mounting a scaled model of the vehicle in a wind tunnel test section and operating the model at some simulated flight condition. In order to carry out such model experiments on a continuous (or semi-continuous) flow basis, complicated and difficult engineering problems encountered in the fueling, combustion, cooling, ignition, etc. of small rocket engines had to be solved. Also, maintaining a continuous high altitude

environment during the test duration required an extensive vacuum pumping capability. This technique was found to be too complex and costly to be considered for normal laboratory testing of Saturn vehicles. Because of the difficulties with a continuous flow rocket test, a short-duration technique was developed by Cornell Aeronautical Laboratory (CAL). The short-duration technique consists of mounting only a scale model of the base region in a vacuum chamber and testing at a simulated altitude. The actual test time for this technique is in the order of a few milliseconds, compared to the several seconds of the long-duration tests, based upon results which show that the base heating rates and pressures reach a quasi steady-state condition in less than a millisecond. Steady combustion is maintained during the time required for the expansion waves created by the rupture of a diaphragm to travel the length of the supply tubes and return to the combustion chamber.

One of the advantages of the short-duration technique is the nearly instantaneous establishment of a hot, steady flow, lasting for a few milliseconds, which has permitted the use of simple models without cooling.

Overall, the short-duration techniques appears to give the same results but at a lower price. Saturn I long-duration tests cost from $50 to $150 thousand each (Ref. 5-1), whereas short-duration tests cost approximately 10 per cent of this amount.

5.2 MODEL SCALING CONSIDERATIONS

To illustrate model scaling, consider some arbitrary differential area in the base region as was shown in Section 2.1, Figure 2-1. An energy balance shows that the total heat flux (q_t) must equal the convective flux (q_c) plus the absorbed radiant flux (αq_{ir}), i.e.,

$$q_t = q_c + \alpha q_{ir} \tag{5-1}$$

The convective and radiant flux can likewise be written as

$$q_c = h(T_r - T_w) \tag{5-2}$$

and

$$q_{ir} = \int_{A_p} E_p dF_{dA_1 \rightarrow dAp} = \int_{A_p} \epsilon_p \sigma T_p^4 \, dF_{dA_1 \rightarrow dAp} \tag{5-3}$$

The definition of these terms can be found in Sections 2.2 and 2.5, Equations 2-5 and 2-16, respectively.

For the sake of brevity Equation 5-3 has been simplified and written as if the plume radiation were a surface phenomenon. In some cases, the radiation can be treated as a surface phenomenon; however, in general, it is a gaseous problem and must be treated as such.

In model heat transfer testing, the obvious objective is to reduce the physical dimensions of the prototype to some size which can be conveniently tested. A relationship between the model and prototype can be established to relate the model heat transfer to that of the prototype. However, with heat transfer problems as complex as base heating, the scaling becomes exceedingly complicated. To identify some of the problems which exist, the following is a discussion of factors which must be considered.

5.2.1 Convective Modeling

In scale modeling the base heat transfer problem, it is usual to make the idealizing assumption that the model is an identical scaled version of the prototype and differs only in physical size. Furthermore, the convective heat transfer in the base region of both the model and prototype must satisfy the well-known Nusselt equation (discussed in Section 2.2).

$$N_{nu} = C\, N_{re}^{\,m}\, N_{pr}^{\,n} \qquad (5\text{-}4)$$

where

N_{nu} - Nusselt Number = hx/k

N_{re} - Reynolds Number = $\rho ux/\mu$

N_{pr} - Prandtl Number = $\mu C_p/k$

C, m, n - Empirical constants.

The ideal model assumption leads to the further assumption that the base gas density (ρ), velocity (u) and transport properties (k, μ, c_p) are also identical or very similar. Thus when the model and flight vehicle convective heating rates are compared using Equation 2-7, a relationship is established, giving

$$\frac{h_{model}}{h_{flight}} = \left(\frac{x_{flight}}{x_{model}} \right)^{1-m} \qquad (5\text{-}5)$$

which shows that the ratio of the heat transfer coefficients from model and flight vehicle are inversely related to the ratio of their respective characteristic lengths (x) to the 1-m power. Now, from Newton's law of cooling, i.e.,

$$q_c = h(T_r - T_w) \quad ,$$

an additional relation follows. Since h is not directly measured it is convenient to express Equation 5-5 in terms which are measurable. Equation 5-5, using Newton's law of cooling, becomes

$$\frac{q_{model}}{q_{flight}} = \left(\frac{x_{flight}}{x_{model}} \right)^{1-m} \quad . \tag{5-6}$$

It has been assumed that the temperature differences for model and flight are equal, i.e.,

$$(T_r - T_w)_{model} = (T_r - T_w)_{flight} \quad .$$

When dealing with convective modeling in the past, it was assumed that the base region could be approximated by a flat plate (Refs. 5-2 and 5-3). Under this assumption, the Colburn equation (Equation 2-6) for turbulent flow over a flat plate is used (Ref. 5-4). This equation has the Reynolds number raised to the 4/5 power (i.e., m = 4/5). Equation 5-6 then becomes

$$q_{flight} = q_{model} \left(\frac{X_{model}}{X_{flight}} \right)^{0.2} \tag{5-7}$$

where x_{model}/x_{flight} is the scale of the model used in the test.

As an example, a summary of the models used in the Saturn program is shown in Table 5-1. By using Equation 5-7 and the scale given for each model, the following scaling factors result:

TABLE 5-1. SUMMARY OF SATURN MODEL BASE HEATING

VEHICLE	STAGE	BASE CONFIGURATION	SCALE	TEST FACILITY	TYPE TEST	TEST CONDITIONS: MACH RANGE	TEST CONDITIONS: ALTITUDE BASED (ft)	MODEL PROPELLANTS	MODEL ROCKET EXHAUST SIMULATION
SATURN I (BLOCK I & II)	S-I		5.47	AEDC-PWT 16 foot Transonic	Long Duration-Hot Flow	0.6 - 1.5	10,000-40,000	LOX/RP-1	GH_2
			5.47	AEDC-RTF	Long Duration-Hot Flow	0.8, 1.5	16,000-27,500	LOX/RP-1	GH_2
			5.47%	AEDC-PTF	Long Duration-Hot Flow	1.63 3.07	33,000-45,000 70,000-80,000	LOX/RP-1	GH_2
	S-IV	 4 Engine  6 Engine	1/10	AEDC-RTF/T-3 (4 Engine)	Long Duration-Hot Flow	No External Flow	117,500-152,500	GO_2/GH_2	Helium Heater Simulation
			1/27.75	AEDC-RTF (4 Engine)	Long Duration-Cold Flow	No External Flow	150,000	AIR	
			1/10	CAL Altitude Chamber (4 Engine)	Short Duration-Hot Flow	No External Flow	140,000-200,000	H_2O_2/H_2	Ambient H_2
			1/10	CAL Altitude Chamber (6 Engine)	Short Duration-Hot Flow	No External Flow	190,000-220,000	GO_2/GH_2	Predicted N_2-H_2 Mixture
SATURN IB	S-IB		5.47%	AEDC-RTF/T-1	Short Duration-Hot Flow	1.18 1.63	30,000 40,000	GOX/ETHYLENE	Cold H_2
	S-IVB				No Testing				
SATURN V	S-IC		1/45	CAL 8 x 8 Transonic	Short Duration-Hot Flow	0.6 - 1.2	13,000-34,000	GOX/ETHYLENE	GH_2
			1/45	LeRC 8 x 6 Transonic	Short Duration-Hot Flow	0.2 - 1.65	8,000-50,000	GOX/ETHYLENE	GH_2
			1/45	LeRC 10 x 10 Supersonic	Short Duration-Hot Flow	2.0 - 3.5	51,000-95,000	GOX/ETHYLENE	GH_2
			1/45	CAL High Altitude Chamber	Short Duration-Hot Flow	No External Flow	125,000-205,000	GOX/ETHYLENE	GH_2
	S-II		1/25	CAL High Altitude Chamber	Short Duration-Hot Flow	No External Flow	150,000-265,000	GO_2/GH_2	GH_2
			1/25	MSFC Impulse Base Flow Facility	Short Duration-Hot Flow	No External Flow	150,000-265,000	GO_2/GH_2	GH_2
	S-IVB				No Testing				

Page Intentionally Left Blank

result, when the prototype is scaled, the optical path length is also scaled, leading to a change in the emissive power and therefore the incident radiant flux, q_{ip}. The latter assumes that the plume temperature profile is not altered in the scaling process. As opposed to this the exhaust plume of a rocket engine operating at a low altitude has an afterburning mantle which affects the radiation. Because liquid rocket engines operate most efficiently when the propellant ratio is fuel-rich, the exhaust products contain unburned fuel. At some distance downstream of the engine exit, the exhaust products have sufficiently mixed with the ambient air such that the unburned fuel ignites and forms the afterburning mantle (see Figure 2-1). The distance downstream required to mix the exhaust products and ambient air appears to depend upon the size of the engine, but this is not a linear relation. As a result the afterburning characteristics of a prototype engine and a scaled engine appear to be quite different. This again leads to differences in the plume emissive power for the scale model and the prototype. In addition to the above, other factors such as carbon particle generation associated with the hydrocarbon propellants, the engine and plume chemical kinetics, and plume boundary layer development enter into the radiation problem and could be expected to affect the scaling. In conclusion the relationship between the radiation associated with a scale model and that of the prototype would appear to be difficult to establish at present.

5.2.3 Gas Temperature Modeling

Because of instrumentation difficulties, the recovery temperature on the model cannot be determined directly. Therefore, some techniques have been developed that give an indirect method of determining the gas recovery temperature. One example of these techniques is the

PRECEDING PAGE BLANK NOT FILMED

"Hot-Base Technique" (see Ref. 5-5). This particular technique is based upon Newton's law of cooling, which is

$$q_{conv.} = h(T_r - T_w) .$$

The basic premise of the technique is that h is constant, that is, independent of temperature. Under this assumption a direct means of determining T_r becomes evident, i.e., by varying T_w, the base temperature, over a wide range in order to produce a significant change in the measured $q_{conv.}$. Now, since the gas recovery temperature is identical to the adiabatic wall temperature, T_r can be found by extrapolating the test data to a value of zero $q_{conv.}$

Actually, h is a function of the temperature; therefore, a lower value of T_r would be indicated ($T_{r_{act}}$). This technique, however, does give a good indication of the gas temperature and can be used to indicate trends and possibly magnitudes.

5.3 SOME APPARENT LIMITATIONS IN SCALE MODELING

In practice, realistic limitations exist insofar as what can be scaled and what is beneficial to scale. Some examples of these limitations will now be discussed.

Certain functional parts and components of the engine and vehicle are not duplicated. Examples would be the wall thickness of the rocket engines which, if scaled accurately, would not contain the flow passages inside the wall. Therefore, the engines were generally larger than the ideal scale.

Base gas temperature is related directly to nozzle boundary layer which, in turn, is related to the engine size, contour, and operating characteristics.

Turbine exhaust gas discharge varies between model and prototype. For example, ethylene turbine exhaust would more nearly simulate the actual gas condition on the prototype; however, to obtain a steady level of turbine exhaust flow during combustion, the turbine exhaust would have to be initiated prior to ignition. Also, for a few low-altitude runs where ethylene was used it was found to burn and coat the heating gages with soot. For these reasons, hydrogen gas was preferred over ethylene as the turbine exhaust gas.

Regenerative cooling of nozzle wall is not simulated in the scale model engines. This is expected to be a serious limitation in the case of the upper stage engines (i.e., J-2 engines), where the effects of condensation on the inside nozzle wall can greatly influence the amount of energy which is reversed into the base region.

Additional discrepancies which exist between scale model and prototype include the use of gaseous propellants as opposed to liquids, combustion chamber injector design, and the omission of an external flow in some of the booster stage runs.

It appears that with the present state of the art of scale model testing, one model which successively reproduces, or models, both the convective and radiation heating phenomenas is not available. One can be simulated only at the expense of the other. Therefore, in modeling vehicles, two different criteria need to be considered: one for radiation and the other for convection.

5.4 TRENDS ESTABLISHED BY SCALE MODELING

The ability to correctly scale model test data to the full-scale vehicle requires an understanding of the heat transfer mechanisms in the base region as mentioned in the previous section. It has been assumed that the heat transfer can be correlated with an equation of the Colburn-Nusselt type:

$$N_{nu} = C\, N_{re}^{n}\, N_{pr}^{m} \quad .$$

For similar surface flow processes between rocket nozzles and base region, it can be shown that a functional relationship of the forms

$$q_{base} \propto P_{cham}^{n}$$

and (5-8)

$$q_{base} \propto P_{base}^{n}$$

exists and might be used to predict the base convective heat flux.

The major disadvantage of this method of correlating data from scale model tests is that it is only true for the same engine shape and configuration. An example where the proportionality has been used in scaling thermal design criteria was in the base regions of the S-I, and S-IV vehicles. The H-1 engines used on the vehicles went through a development stage that increased its thrust from 165,000 lbf on the S-I, Block I, to a thrust of 200,000 lbf on the S-IB.

From data taken by the Cornell Aeronautical Laboratory (CAL) (Ref. 5-6) on a four-engine configuration, the correlation obtained using Equation 5-8 was as shown in Figures 5-1 and 5-2. From

Figure 5-1, the exponent (n) of Equation 5-8 is seen to vary between 0.75 to 0.98. The common value of the exponent associated with turbulent heat transfer over a flat plate is 0.8. Figure 5-2 shows the second correlation in Equation 5-8. The apparent power of 1.02 is greater than the 0.8 power which is well established for flat plate turbulent flow.

Therefore, it is seen that Equation 5-6 does not accurately represent the base region of the vehicle. This is believed to be caused by the assumption that the recovery temperature is independent of chamber pressure in the development of these relationships. The recovery temperature as a function of chamber pressure for the same data represented in Figures 5-1 and 5-2 is shown in Figure 5-3. It shows that there exists a relationship of the form $T_R \propto P_C^n$ where for this particular case the average exponent is seen to be 0.20. Thus, the assumption that recovery temperature was constant in developing Equation 5-8 was apparently incorrect.

In light of these discrepancies, the model data was replotted using the Nusselt-Colburn type equation with Pr = 1. These results are shown in Figure 5-4. Figure 5-4 indicates a turbulent variation ($N_{Re}^{0.8}$) in heat transfer with Reynolds number over a major portion of the base region. However, the scatter in the data at the lower values of N_{Re} indicates a possible correlation with laninar flow theory where $N_{Nu} \propto N_{Re}^{0.5}$. A similar anomaly was observed on the five-engine S-II model test.

As an attempt to better understand the flow phenomena occurring during full flow reversal, some very detailed model studies have been conducted. The results of one such investigation are reported in Reference 5-7. During these tests probes were inserted into the base region of a four-engine configuration. These probes measured the static and impact pressure as well as velocities. The

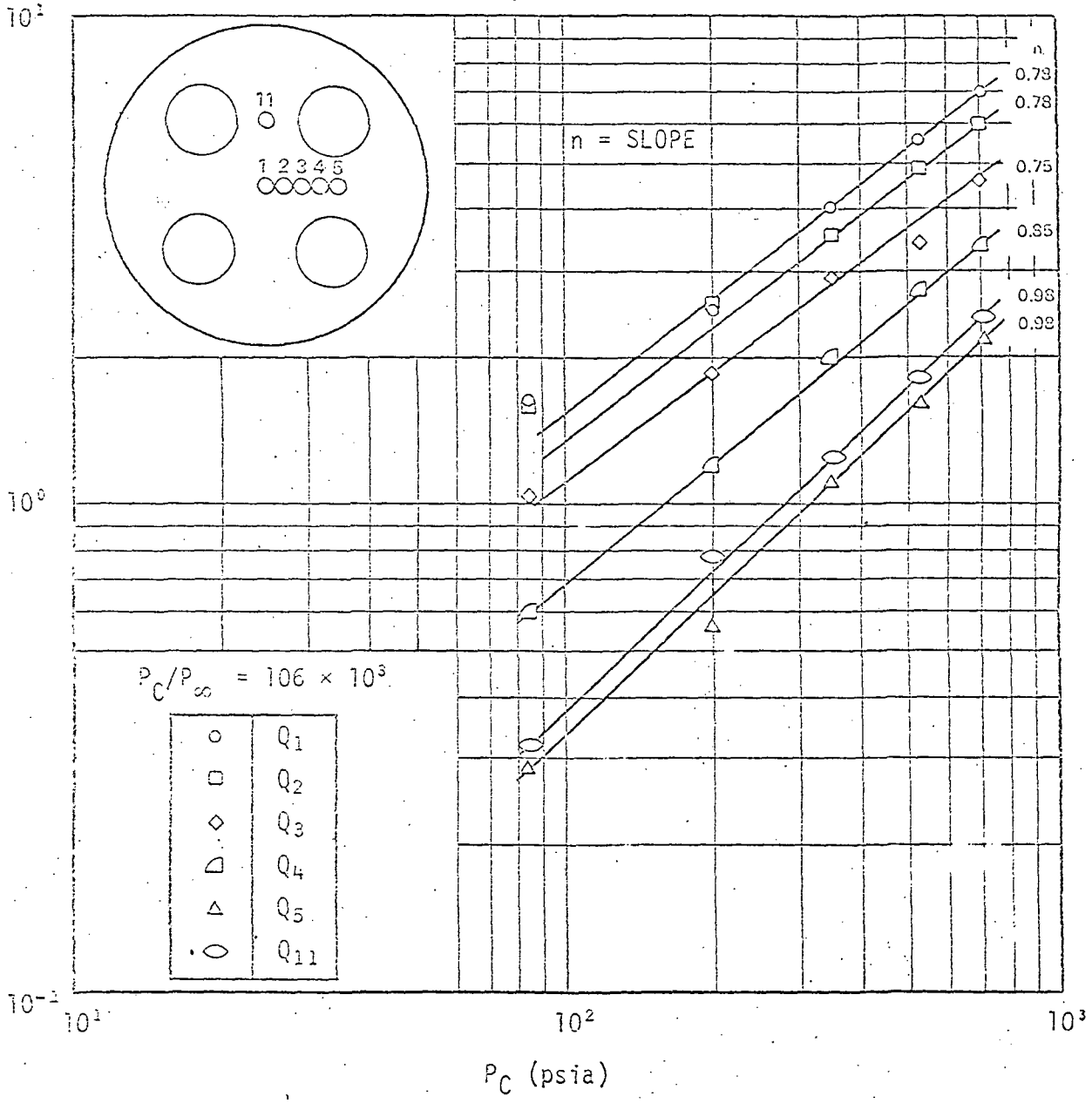

FIGURE 5-1. EFFECT OF CHAMBER PRESSURE ON HEAT TRANSFER RATE (from Ref. 5-6)

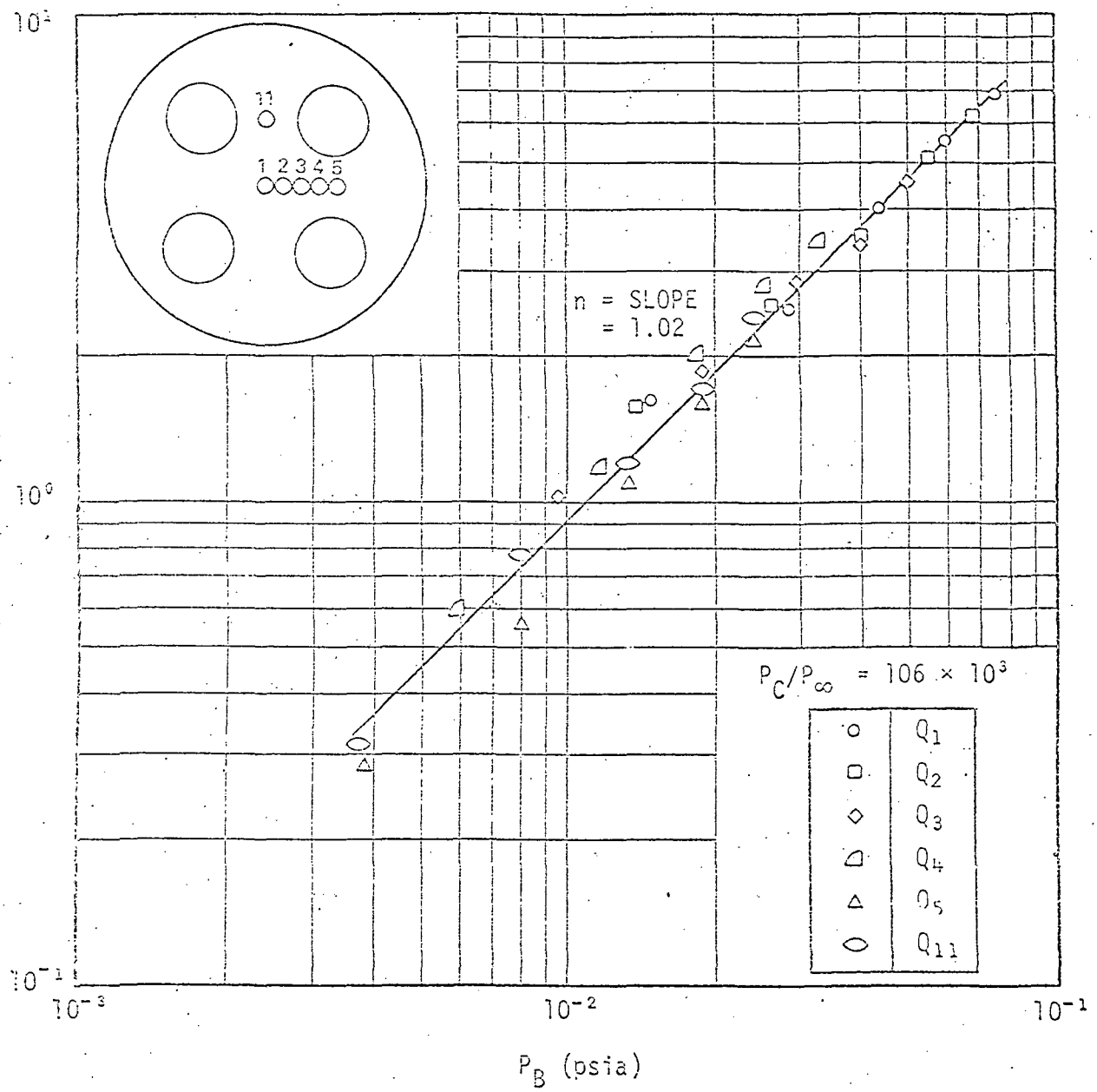

FIGURE 5-2. CORRELATION OF HEAT TRANSFER RATE WITH LOCAL HEAT SHIELD PRESSURE (from Ref. 5-6)

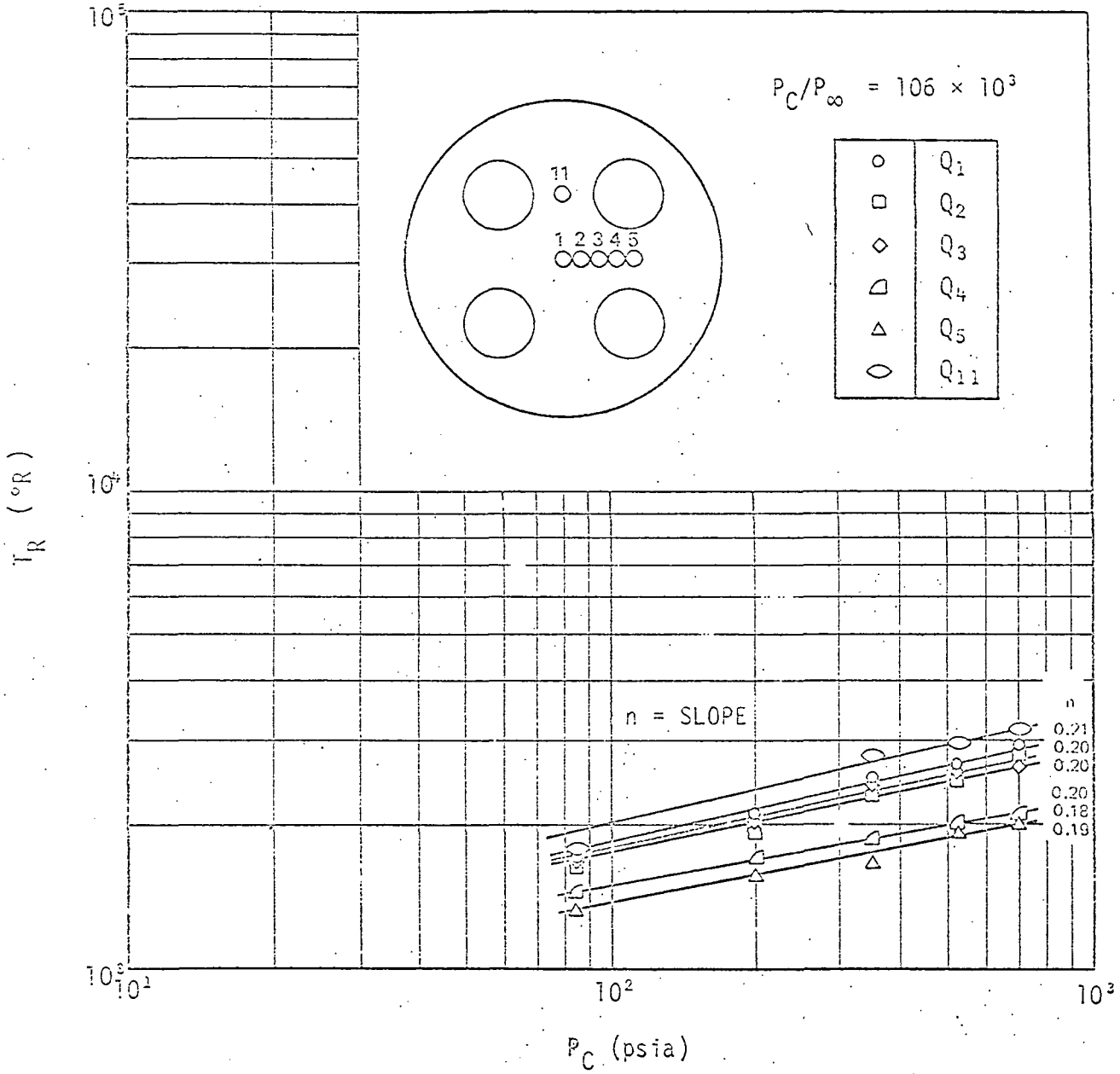

FIGURE 5-3. EFFECT OF CHAMBER PRESSURE ON RECOVERY TEMPERATURE (from Ref. 5-6)

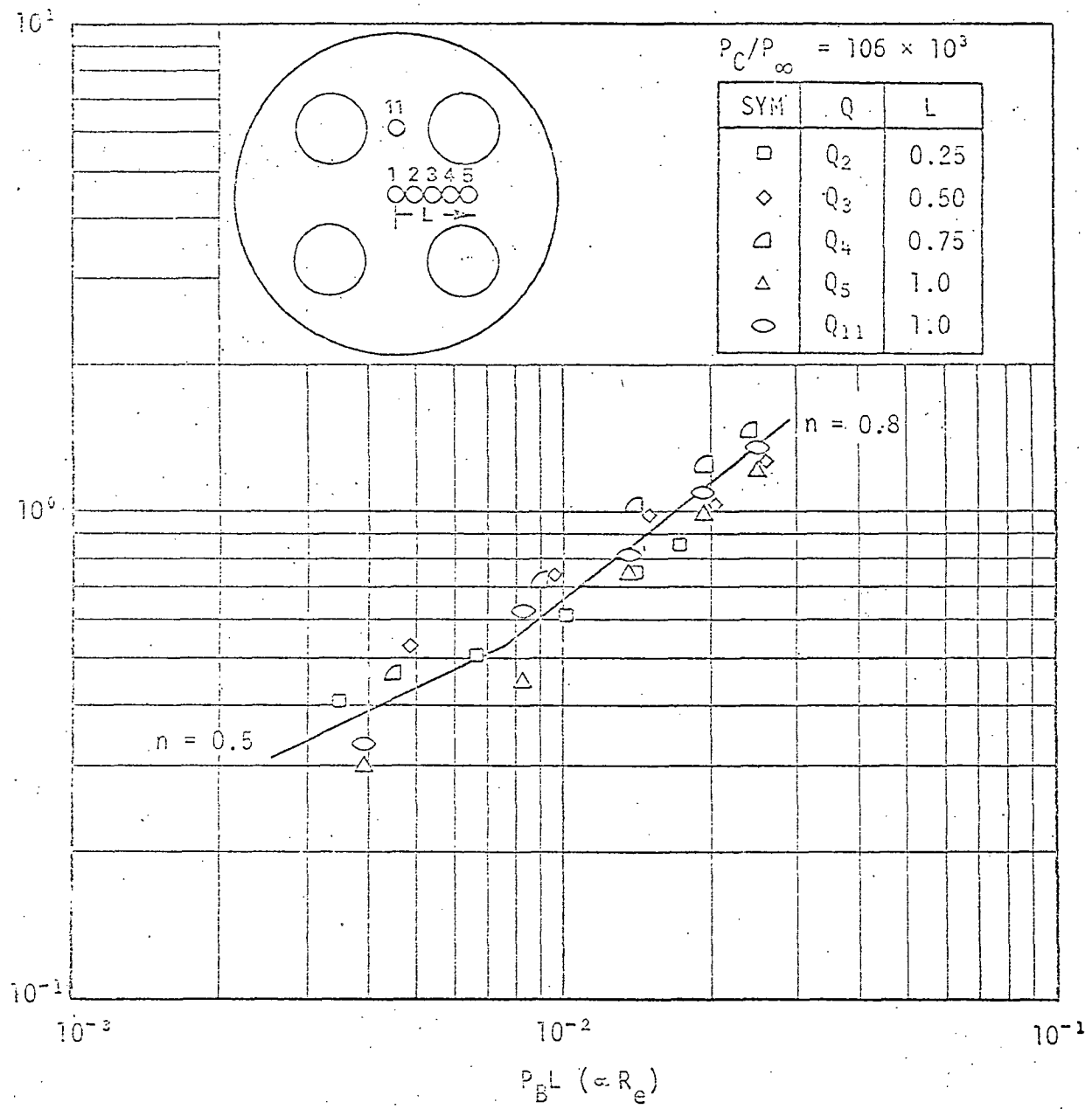

FIGURE 5-4. CORRELATION OF HEAT TRANSFER AND LOCAL HEAT SHIELD PRESSURE (from Ref. 5-6)

velocities were measured using hot wire anemometers. Some typical results of these tests are shown in Figures 5-5 through 5-7. These figures show the static and impact pressures and the resulting Mach number obtained by combining these results.

Several interesting observations can be made in studying these figures. Figure 5-7 shows that supersonic flow can apparently exist in the base region. The static pressure shown in Figure 5-5 shows a sharp increase as the flow approaches the heat shield (e.g., compare the 0.5-inch curve with the 1.0-inch curve in Figure 5-5). This trend, if not the magnitude, is in agreement with what would be anticipated with supersonic flow conditions (i.e., a standing shock above the heat shield). Measurements taken along the base plate also indicated sonic velocities as the flow approached the vent area. Efforts to show the existence of the base plate standing shock using a laser-Doppler technique (Ref. 5-8), however, did not provide concrete results to confirm the existence of the shock.

Another interesting factor which can be obtained from these results is the following. Isentropic flow is normally assumed in the base region, and isentropic flow relations are used in the analytical models. In isentropic flow, no change in total pressure occurs unless the flow is supersonic and moves through a shock wave. As the flow moves through the shock, the entropy changes. In checking the data shown in Figures 5-5 through 5-7, one would expect to find the entropy changes indicated by the change in impact pressure to correspond to the entropy change across a normal shock. What is found, however, are entropy changes which are 3 to 10 times greater than the entropy change across a normal shock. This could mean that the flow in the base region has much larger viscous losses associated with it than has previously been assumed.

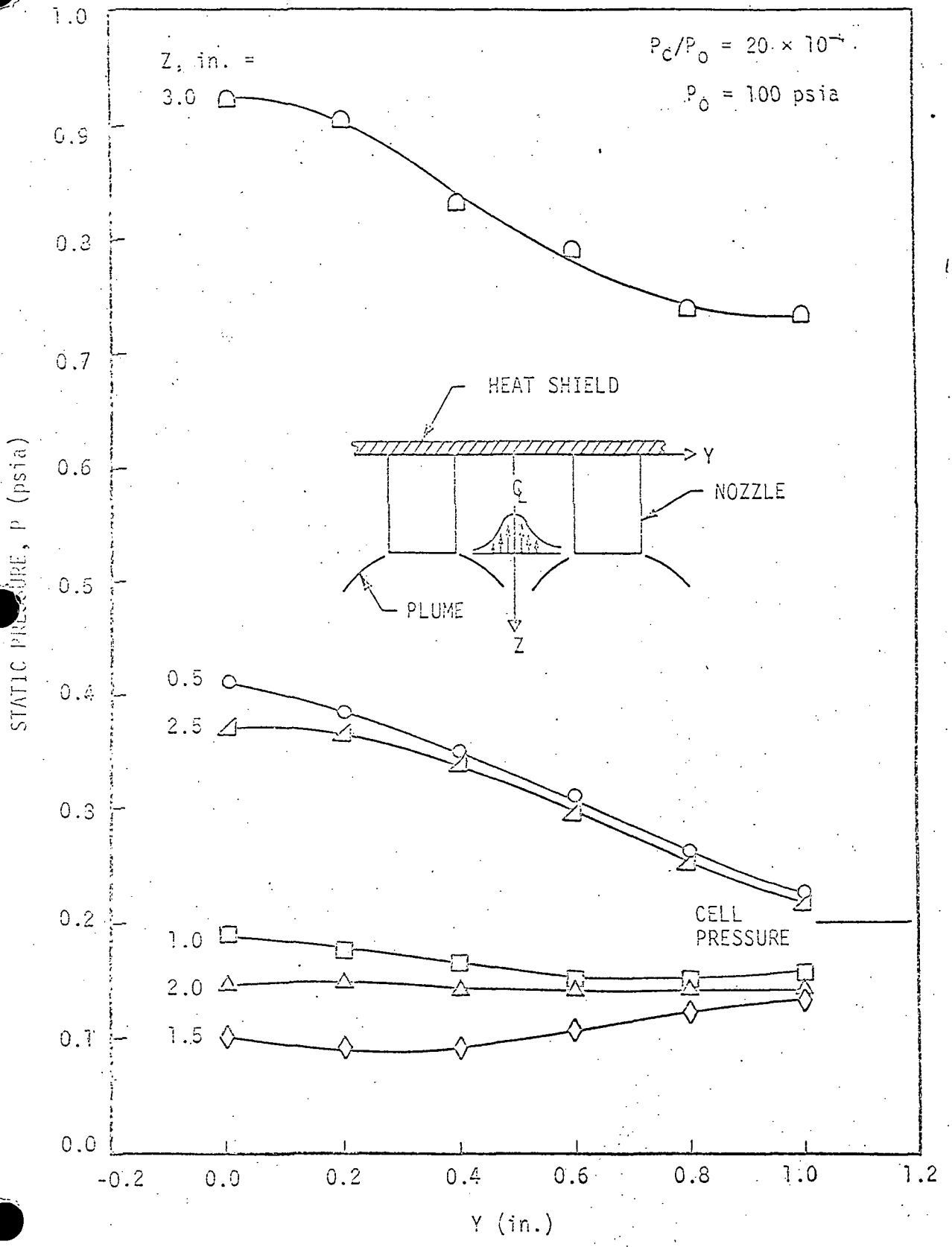

FIGURE 5-5. STATIC PRESSURE IN REVERSE JET (from Ref. 5-7)

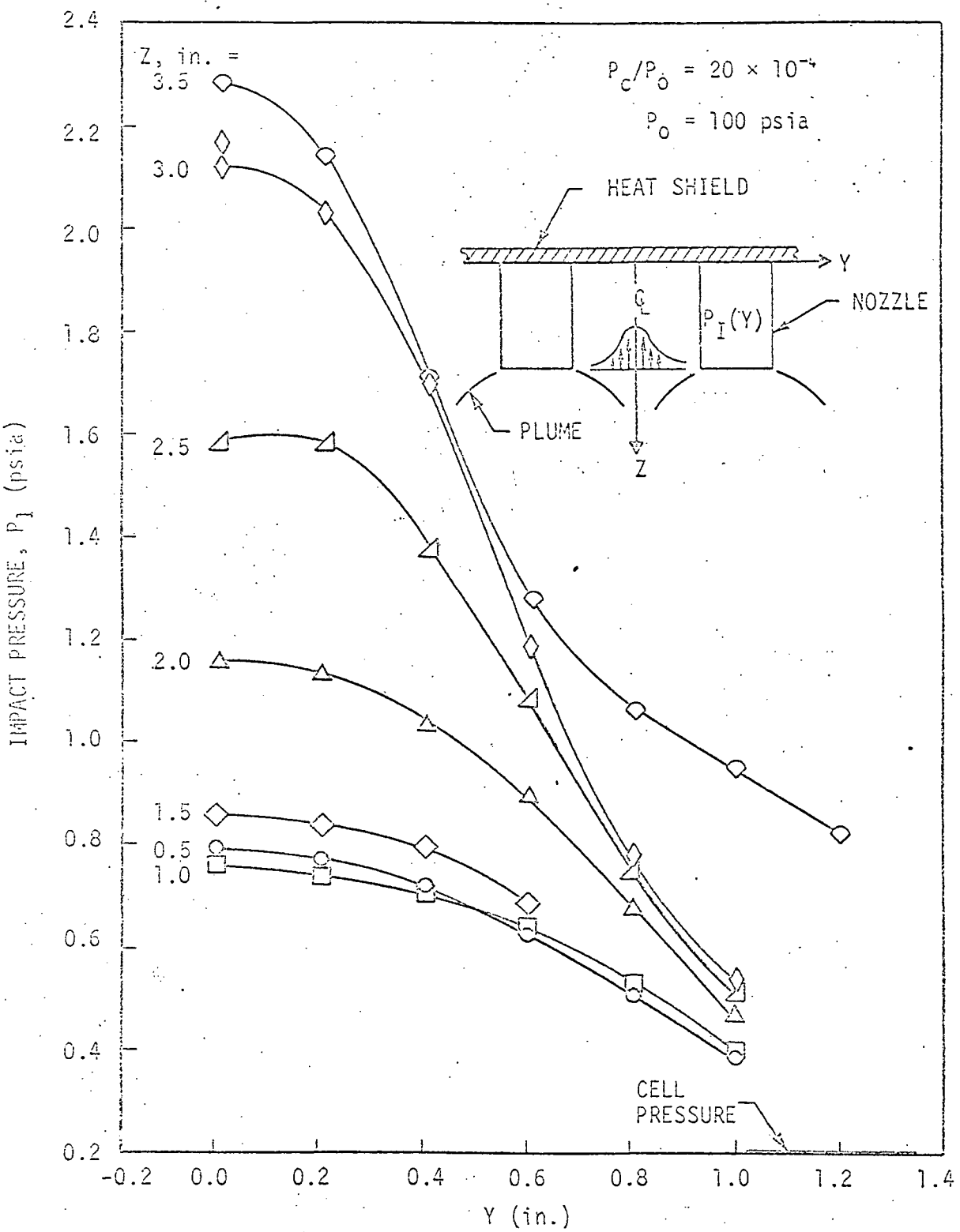

FIGURE 5-6. IMPACT PRESSURE IN REVERSE JET (from Ref. 5-7)

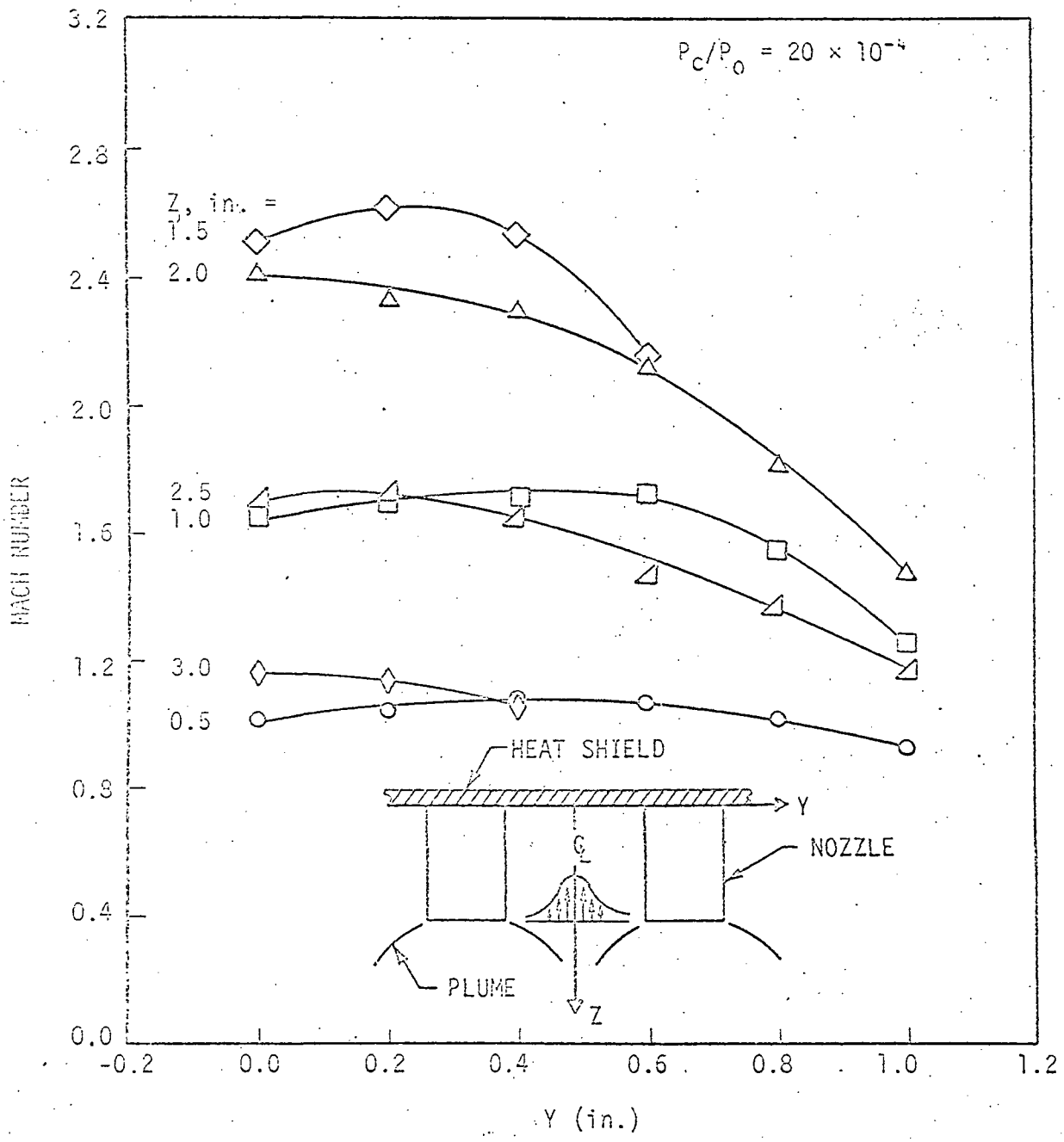

FIGURE 5-7. MACH NUMBER IN REVERSE JET (from Ref. 5-7)

As mentioned earlier the five-engine S-II scale model test exhibited the same abnormalities as did the four-engine scale models. However, from studies on four- and five-engine configurations (Refs. 5-7 and 5-9), it is interesting to note the dissimilarities between the two. Figure 5-8 shows a graphical representation of the velocity profiles which appear to exist. The typical velocity profile of the four-engine cluster appears to resemble that of a jet impinging on a flat plate; however, the five-engine case shows that a major portion of the flow appears to leave the base region before stagnation on the base plate occurs.

5.5 MODEL DATA AND FLIGHT DATA COMPARISON

5.5.1 S-IC Stage Model Test Results

A model test program was initiated early in 1962 to aid in predicting the base heating environment on the Saturn V/S-IC stage. A short-duration (shock tube) test technique was chosen because it provided a much simpler and cheaper method of testing. Confidence in the technique had been obtained earlier by the favorable comparison between the long and short duration test results. A 1/45th scale model of the S-IC stage base region was designed by Cornell Aeronautical Laboratory (CAL).

Tests were conducted in CAL's high-altitude chamber at altitudes between 125,000 and 205,000 feet with no external flow and in the CAL transonic tunnel between Mach 0.6 and 1.2. The NASA/Lewis Research Center transonic and supersonic tunnels were used to obtain model data in the Mach 0.4 to 3.5 range.

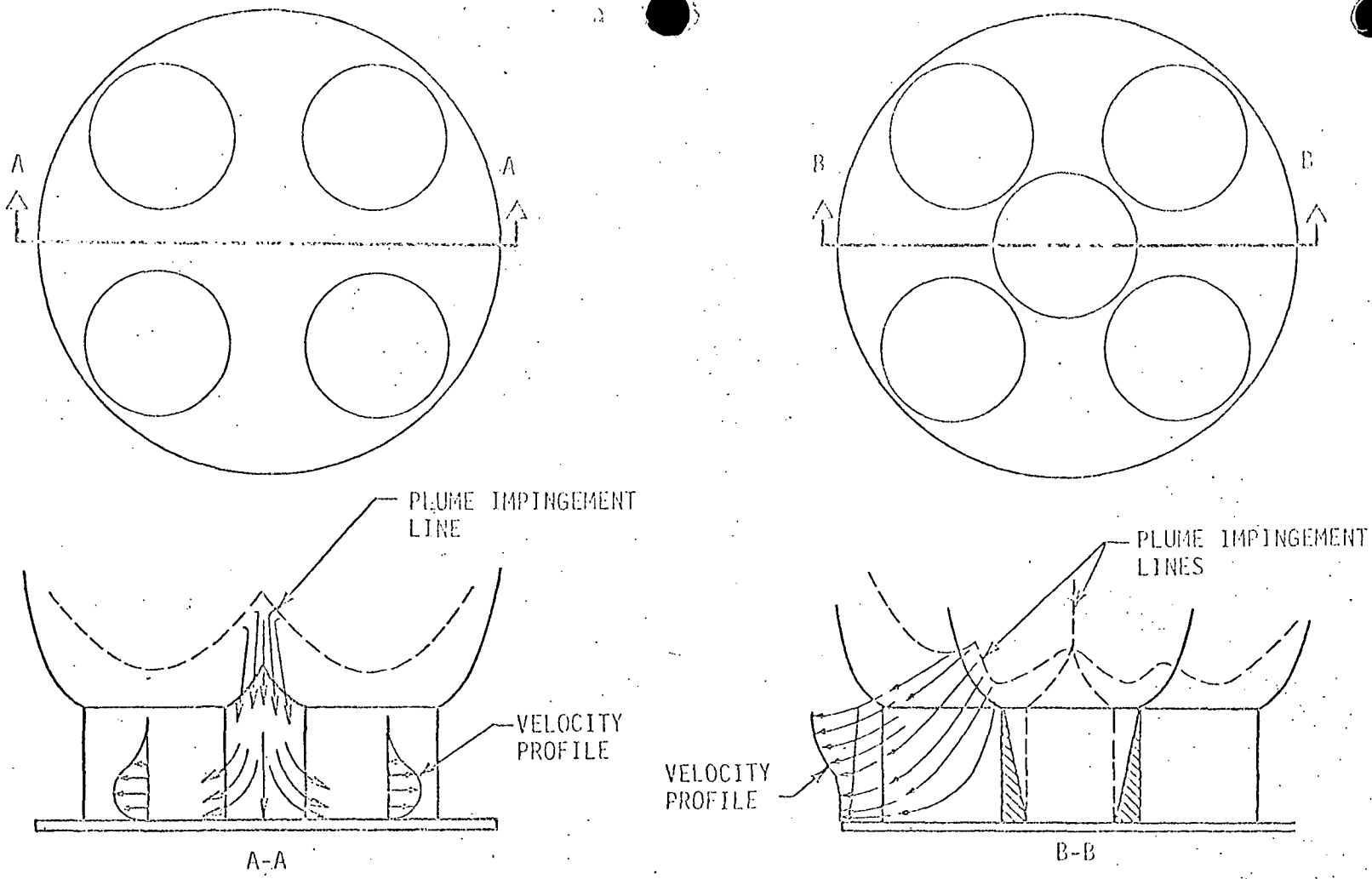

a. FOUR-ENGINE FLOW FIELD

b. FIVE-ENGINE FLOW FIELD

FIGURE 5-8. APPARENT BASE FLOW FIELD WITH FOUR AND FIVE ENGINES

The model used GOX/ethylene to simulate LOX/RP-1 propellants. Hydrogen was injected into the main exhaust flow inside each of the nozzles at the 10:1 area ratio point to simulate the turbine exhaust.

Thin-film heat transfer gages (calorimeters) were employed for the measurement of short-duration heating. Because of the short-time duration of the model test, the gages were recording a cold wall heating rate.

As shown in Figure 5-9, the scale model radiation heating rates were negligible as compared to those measured during the flight tests. This difference is probably due to the lack of particulate carbon (soot), the smaller radiating gas volume, and the afterburning mantle location that is associated with the scale model engine plumes.

Model data total heating is shown in Figure 5-10 for the heat shield. It is made up almost totally of convective heating and follows the trend of the flight data. The model convective heating presented in Figure 5-11 is observed to be much greater than the flight data. The scaling factor for convective heating discussed in the previous section was applied to the model data and is also shown in Figure 5-11. The model data did not indicate the convective cooling which took place on the flight vehicle early in flight; however, the tests did indicate the trends (increases and decreases) in the base region for later times in flight. For comparison purposes the convective heating values obtained from the aspiration model and the flow reversal model developed at Teledyne Brown Engineering are presented.

Base pressure measurements from model and flight are compared in Figure 5-12. The shapes of the curves are very similar; however, the model base pressures have not been corrected for the differences in efficiency between model and flight engines, scoops, and flow deflectors.

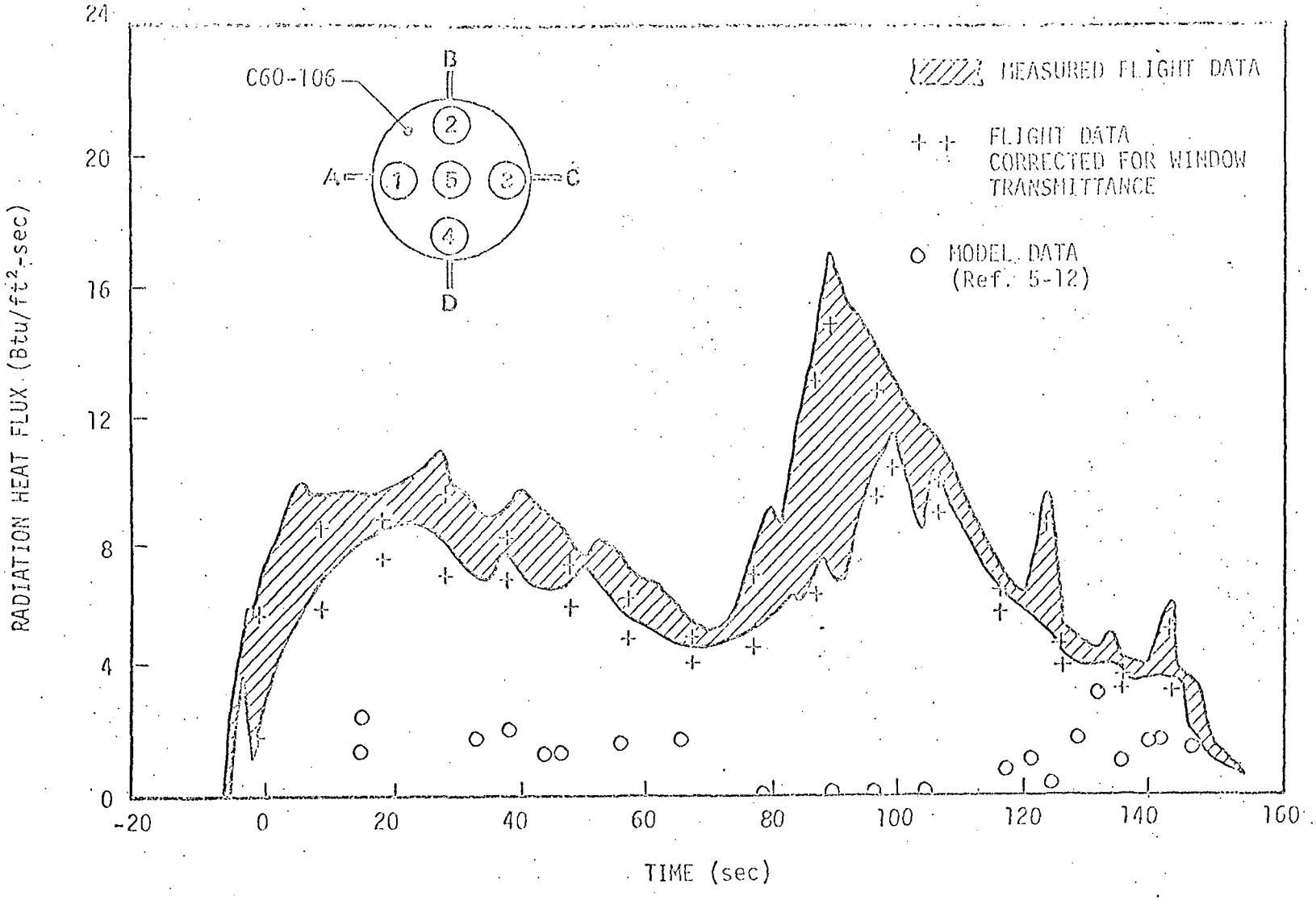

FIGURE 5-9. S-IC FLIGHT AND MODEL RADIANT FLUX

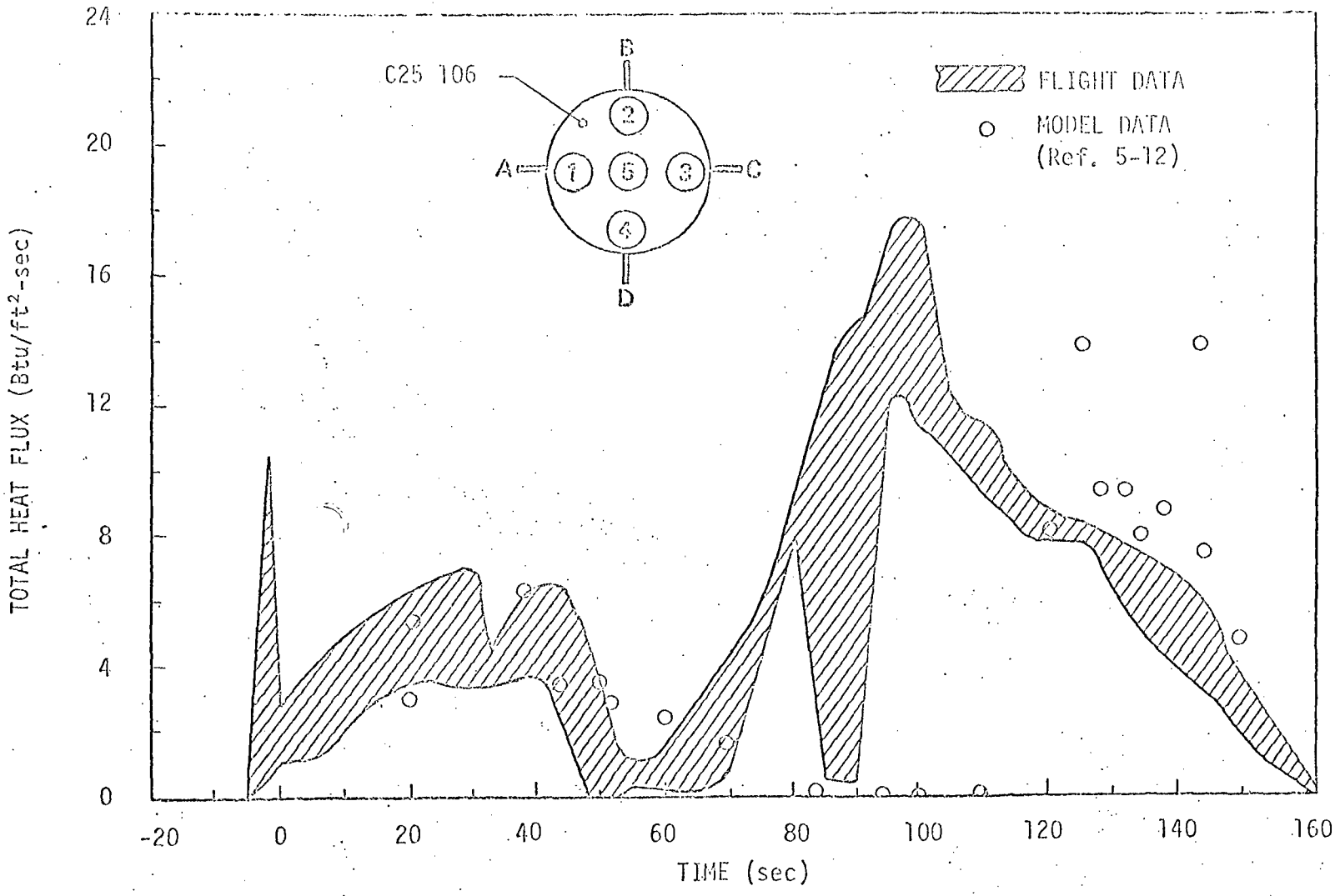

FIGURE 5-10. S-IC FLIGHT AND MODEL TOTAL HEAT FLUX

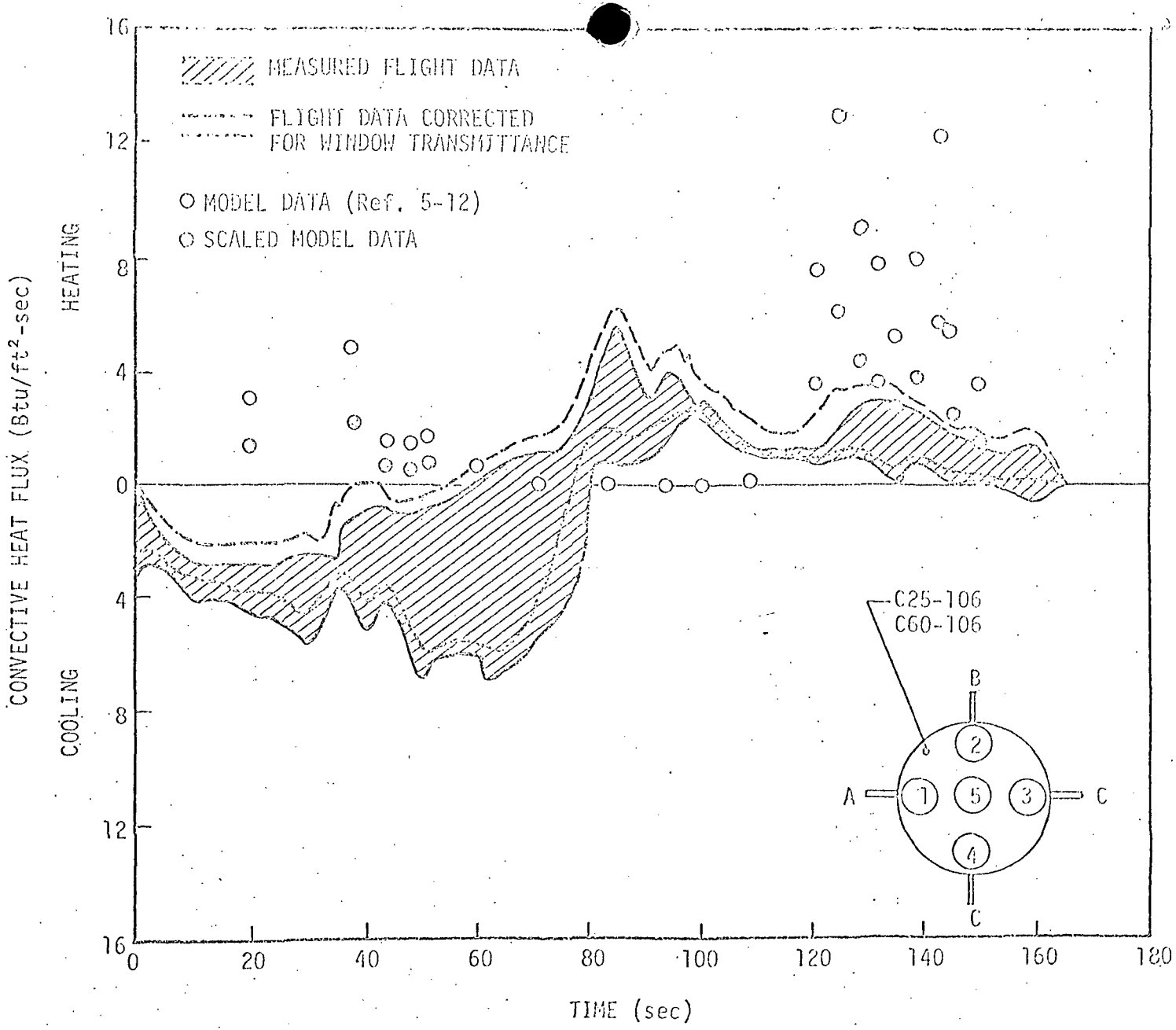

FIGURE 5-11. S-IC FLIGHT AND MODEL CONVECTIVE HEAT FLUX

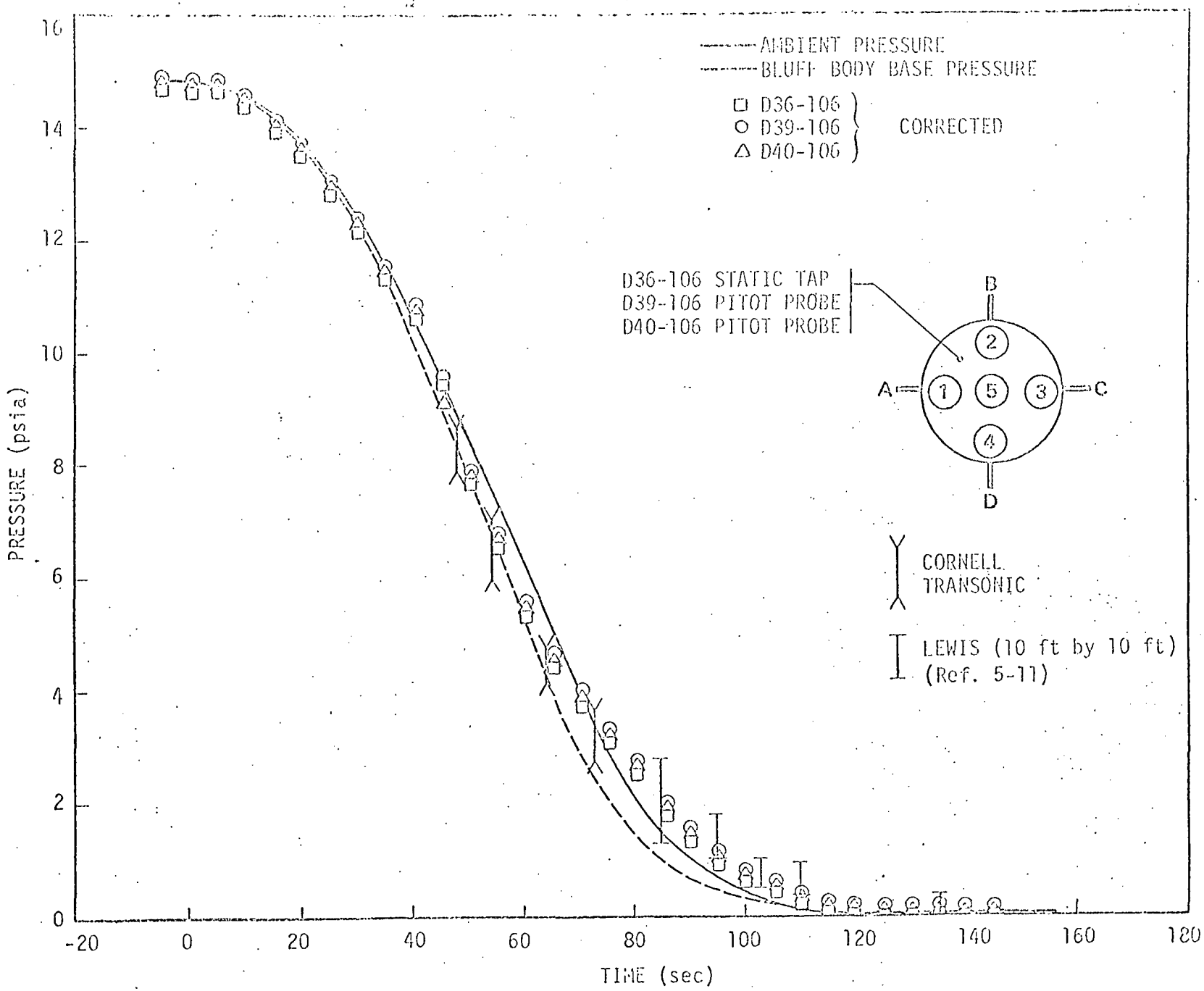

FIGURE 5-12. S-IC FLIGHT AND MODEL BASE PRESSURE

Flight and model gas temperatures are compared in Figure 5-13. The flight data shows large gradients in the gas temperature near the heat shield. The variations in the model data are significant, however, it is evident that the flight and model data have comparable magnitudes of gas temperature at the higher altitudes. Data for the lower altitudes (or Mach numbers) were not reported, since CAL felt that the data obtained for these conditions were not reliable.

5.5.2 S-IB Stage Model Test Results

A model test program on a 5.47 percent scale of the S-IB stage booster was conducted at Arnold Engineering Development Center (AEDC) to determine the effect of turbine exhaust gases on base heating. Short-duration techniques were used in the test program. Tests were conducted at Mach numbers of 0.8, 1.18, and 1.63; however, because of tunnel flow disturbances caused by the mass flow addition of the rockets into the tunnel, the data at Mach 0.8 was believed unreliable and omitted. Therefore, only data for Mach 1.18 (30,000 feet) and 1.63 (40,000 feet) is available. GOX/ethylene was used to produce the main engine exhaust, and hydrogen gas at 100°F was used to simulate the fuel-rich turbine exhaust gases.

On the S-IB stage there are two areas of importance in studying the base thermal environment: the heat shield and the flame shield. For this reason the comparison will be broken into these two categories.

The same difficulties mentioned in the preceding section on the S-IC stage, in simulating the base heating, also apply here.

The total heating rate and radiation heating on the heat shield are presented in Figures 5-14 and 5-15. The heat shield thermal environment of the model was relatively unaffected by the turbine exhaust configuration (i.e., whether the turbine exhaust is exhausted

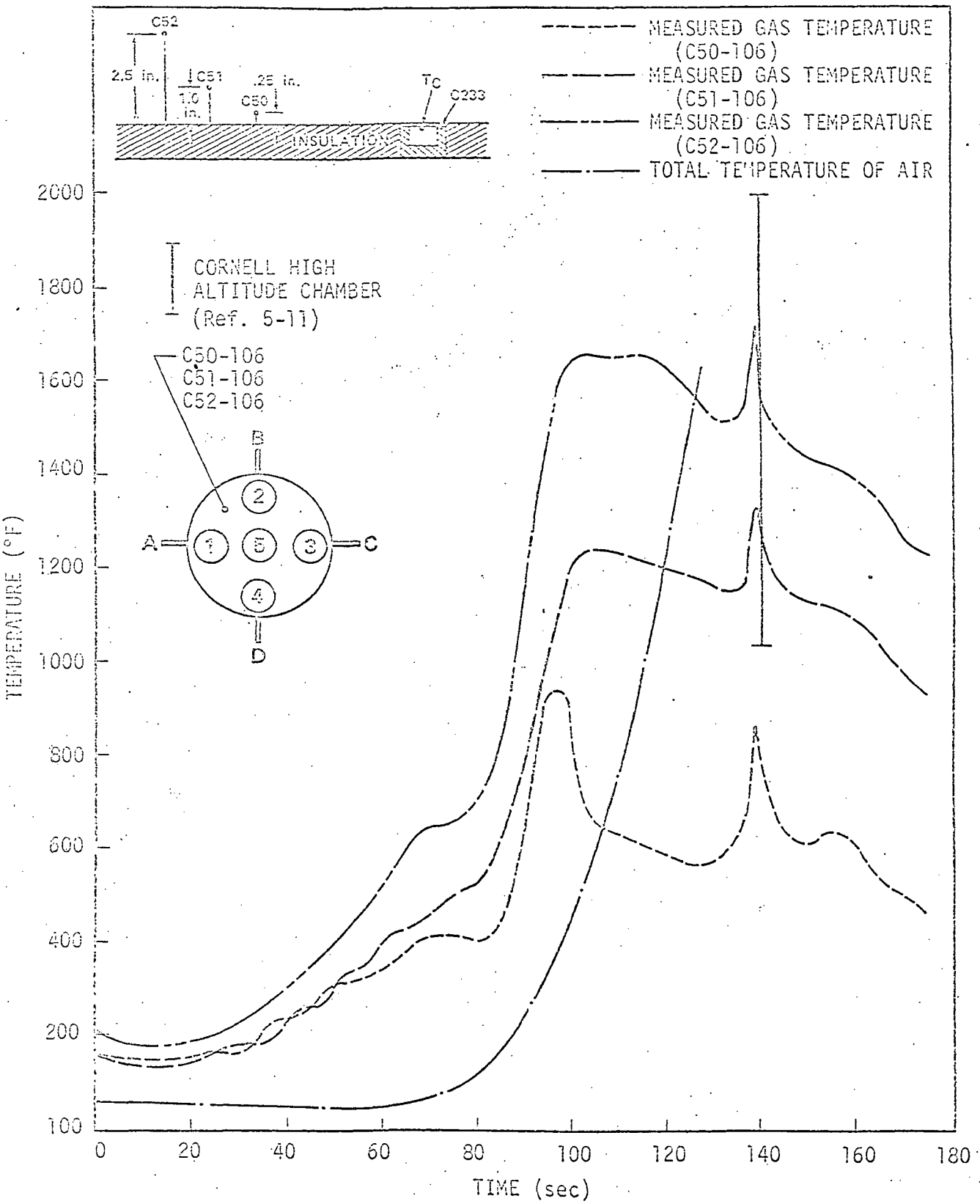

FIGURE 5-13. S-IC FLIGHT AND MODEL BASE GAS TEMPERATURE

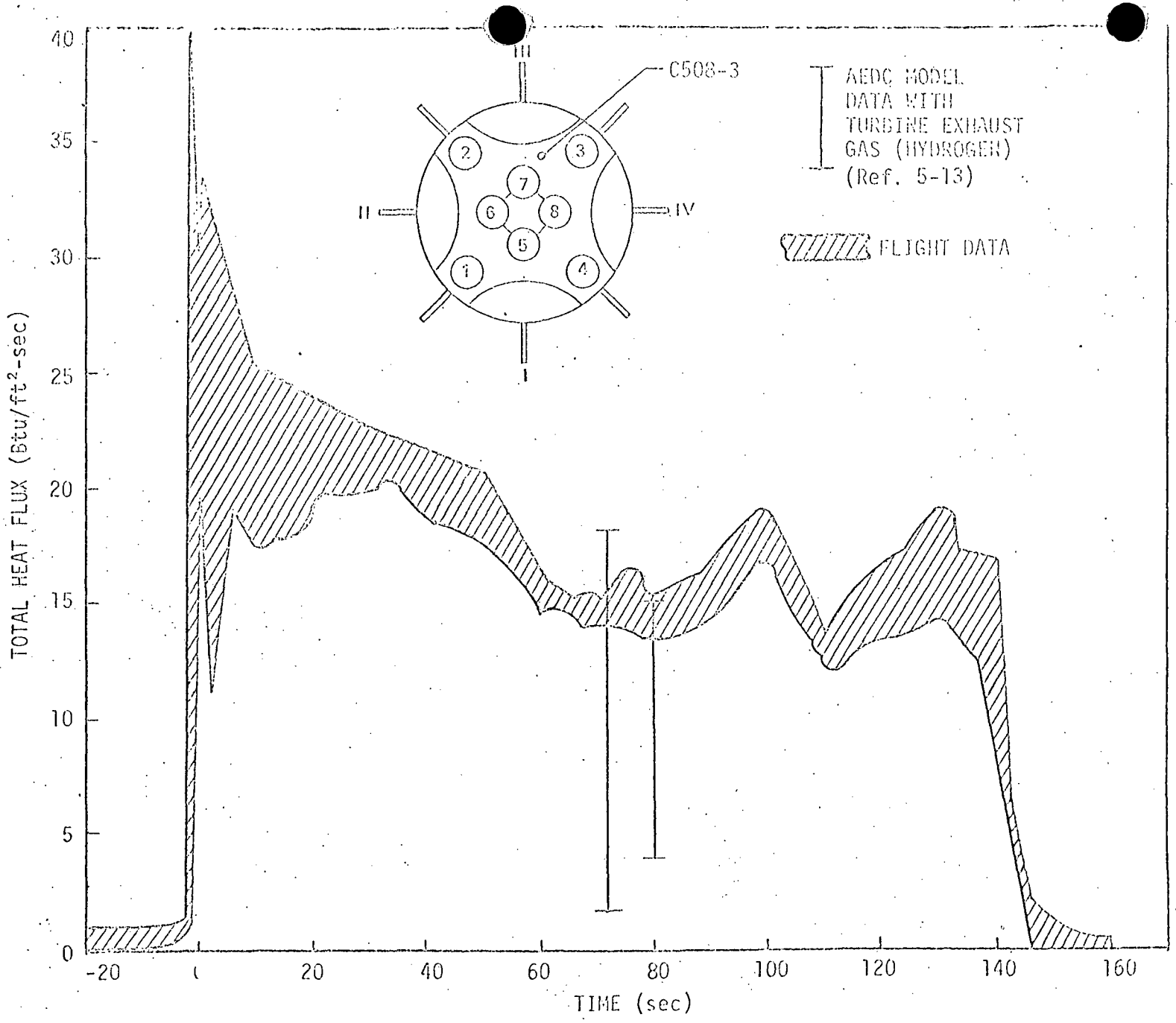

FIGURE 5-14. SATURN I FLIGHT AND MODEL HEAT SHIELD TOTAL HEAT FLUX

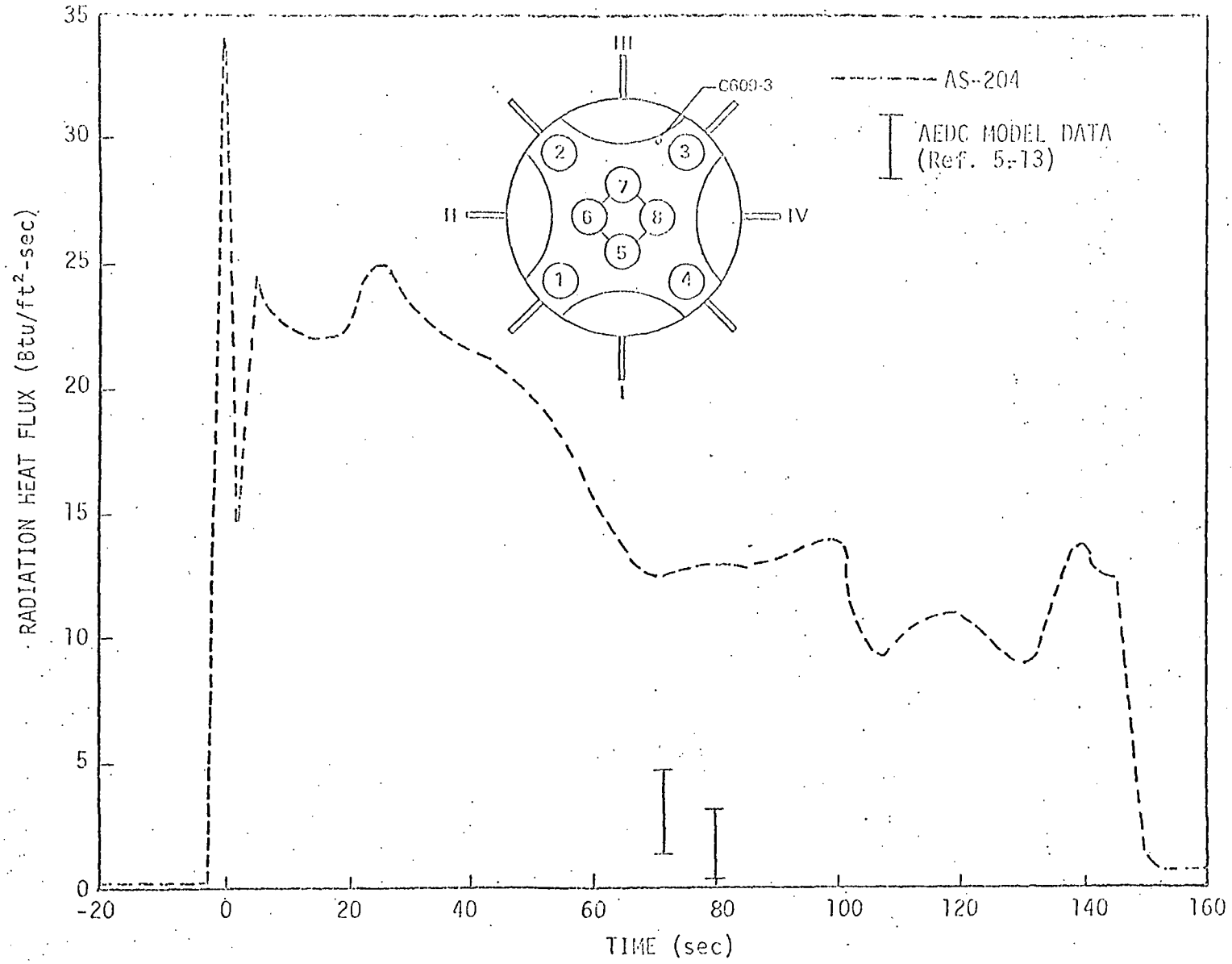

FIGURE 5-15. SATURN I FLIGHT AND MODEL HEAT SHIELD RADIANT FLUX

at the four inboard engines, or exhausted outboard through the stub fins).

Figure 5-16 shows the convective heating obtained from Figures 5-14 and 5-15 for the heat shield. The scaling factor was applied to the model data and this is also presented in Figure 5-16.

In Figures 5-17 and 5-18 the comparison between the flight and model total and radiation heating data is presented. As illustrated in Figure 5-17, the simulated turbine exhaust gas has a definite effect on the total heating value. The hydrogen gas used to simulate the turbine exhaust was at 100° F, whereas the flight vehicle's turbine exhaust is approximately 1, 500° F. Therefore, in the case when the turbine exhaust is exhausted around the flame shield, the gas has a cooling effect in the model where it may actually have a heating effect in flight.

No appreciable difference was found in the model's radiation heating, with or without simulated turbine exhaust gases, or because of different configurations used to dump the turbine exhaust gases (Ref. 5-3).

5.5.3 S-II Stage Model Test Results

Parametric model tests were conducted by CAL in 1962 using a 1/25 scale model of the S-II stage and short-duration techniques. The model made provisions for variation in engine pitch circle, heat shield location, and interstage skirt location.

The model was moved from CAL to the larger altitude chamber at Marshall Space Flight Center (MSFC). This move was required in order that the thrust structure heating rates could be better analyzed. In the CAL test, shock reflections from the tank walls disturbed the flow within 3.4 milliseconds.

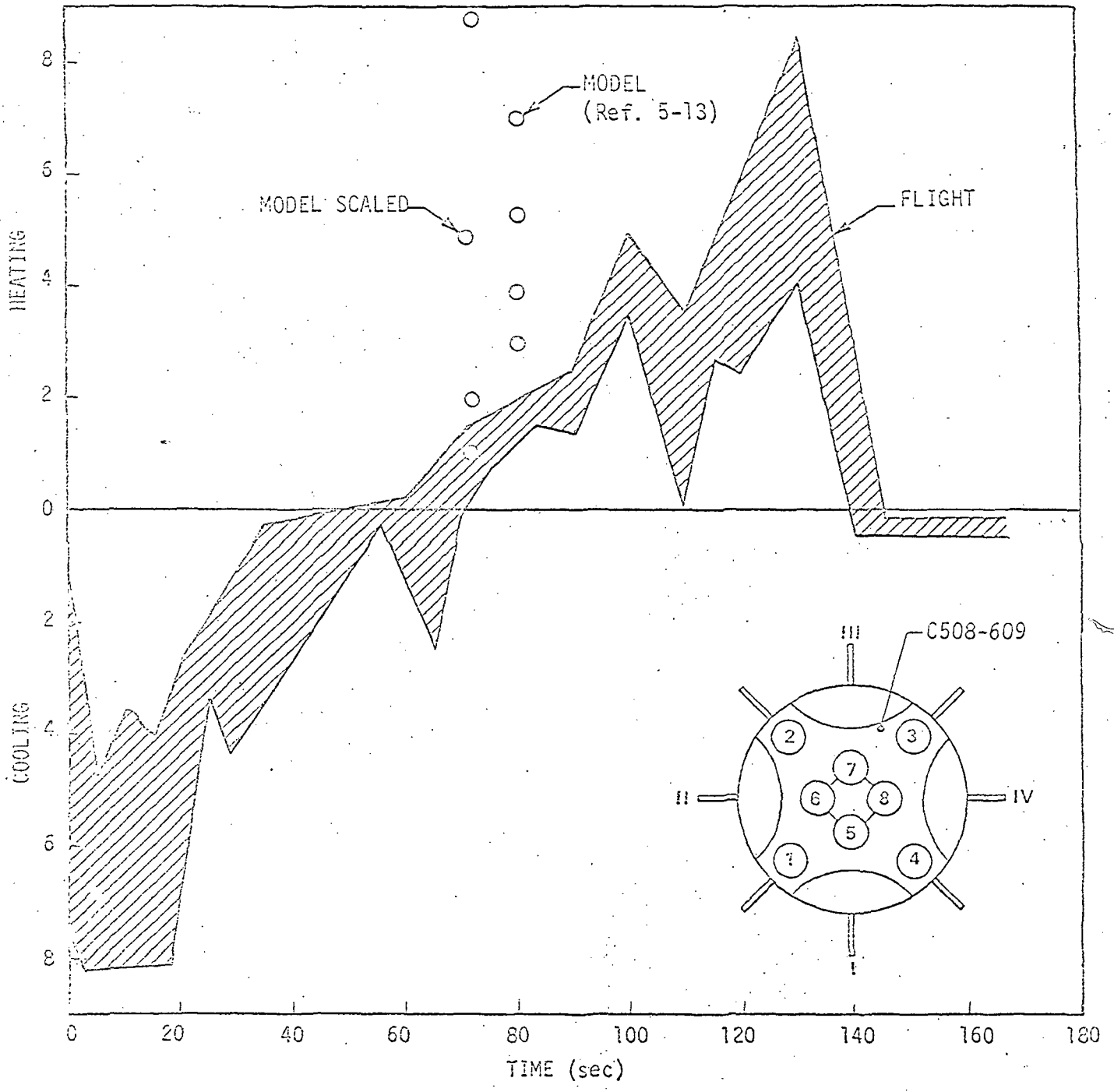

FIGURE 5-16. SATURN I FLIGHT AND MODEL HEAT SHIELD CONVECTIVE FLUX

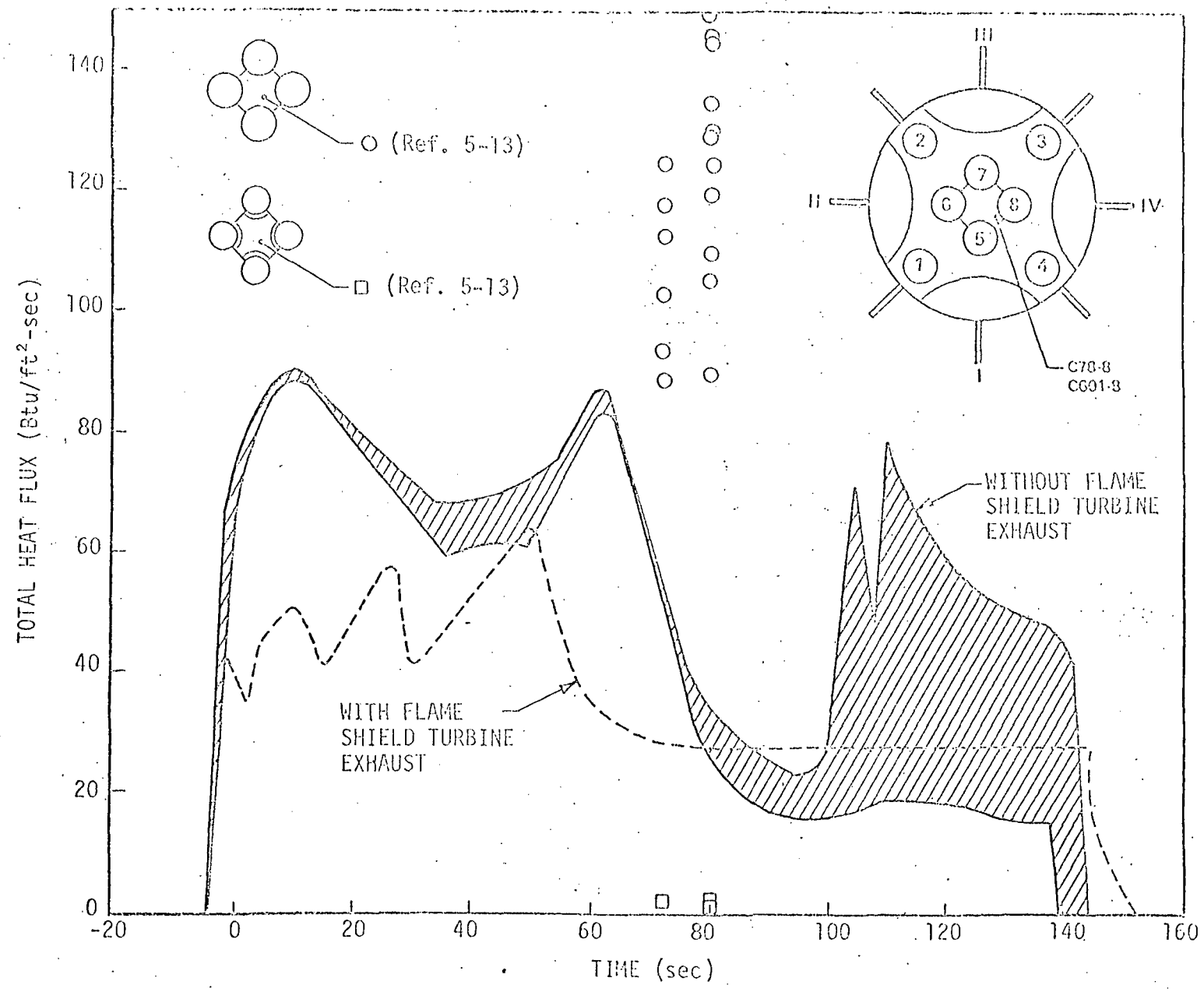

FIGURE 5-17. SATURN I FLIGHT AND MODEL FLAME SHIELD TOTAL HEAT FLUX

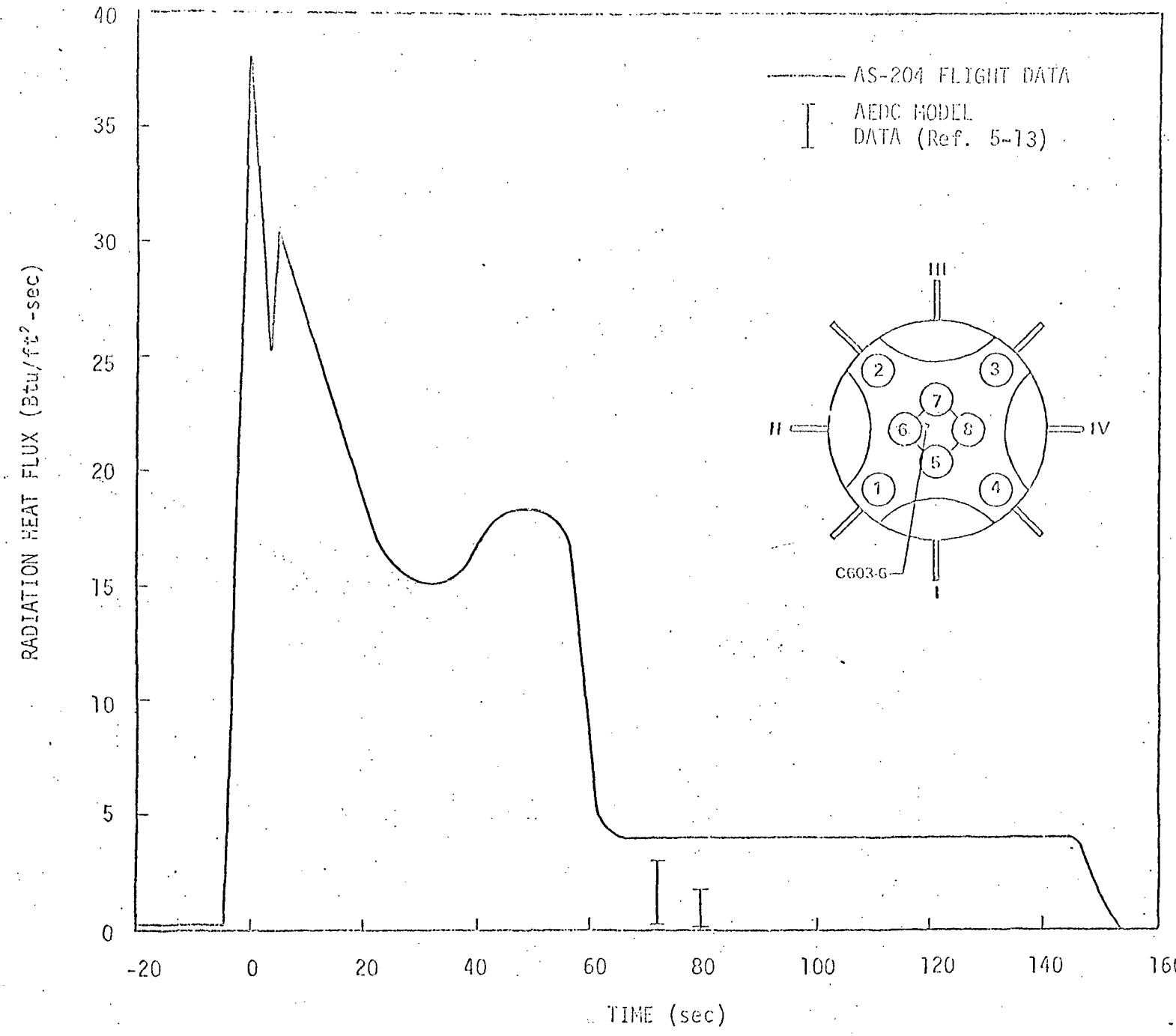

FIGURE 5-18. SATURN I FLIGHT AND MODEL FLAME SHIELD RADIANT FLUX

In this time interval the thrust structure heating rates did not have adequate time to stabilize. At MSFC, the larger tank provided test times in the order of 6 to 7 milliseconds before flow disturbance.

The test on the S-II stage was limited to the capabilities of the chambers. The CAL chamber has a vacuum capacity of approximately 6 microns of mercury (266, 500 feet) which is only 170 seconds into flight. This represents 10 to 20 seconds of S-II stage flight time. Because of the limitations imposed by these facilities, a simulated altitude of only 266, 500 feet was obtainable.

The comparison of base heating data for the S-II stage can be presented as follows: 1) Heat shield thermal environment, and 2) Thrust cone thermal environment. Figures 5-19 and 5-20 compare flight and model data on the heat shield, and Figures 5-21 and 5-22 compare data on the thrust cone. As shown in these figures the heat shield experiences a more severe heating environment than the thrust cone. Looking at the flight data, the thrust cone is seen to have a negligible convective heating rate during flight (approximately 0.02 to 0.04 Btu/ft^2-sec).

Figure 5-23 presents a comparison of the flight and model convective heating rates for the heat shield. The model data has been scaled assuming a flat plate correlation. As shown, once the model data is scaled, it is in better agreement with the flight data. The analytical value is also presented for comparison.

Some typical test data for the S-II scale model obtained by CAL are presented in Figure 5-24. As noted, the values for heat shield heat transfer and pressure level off after about 0.5 millisecond. The

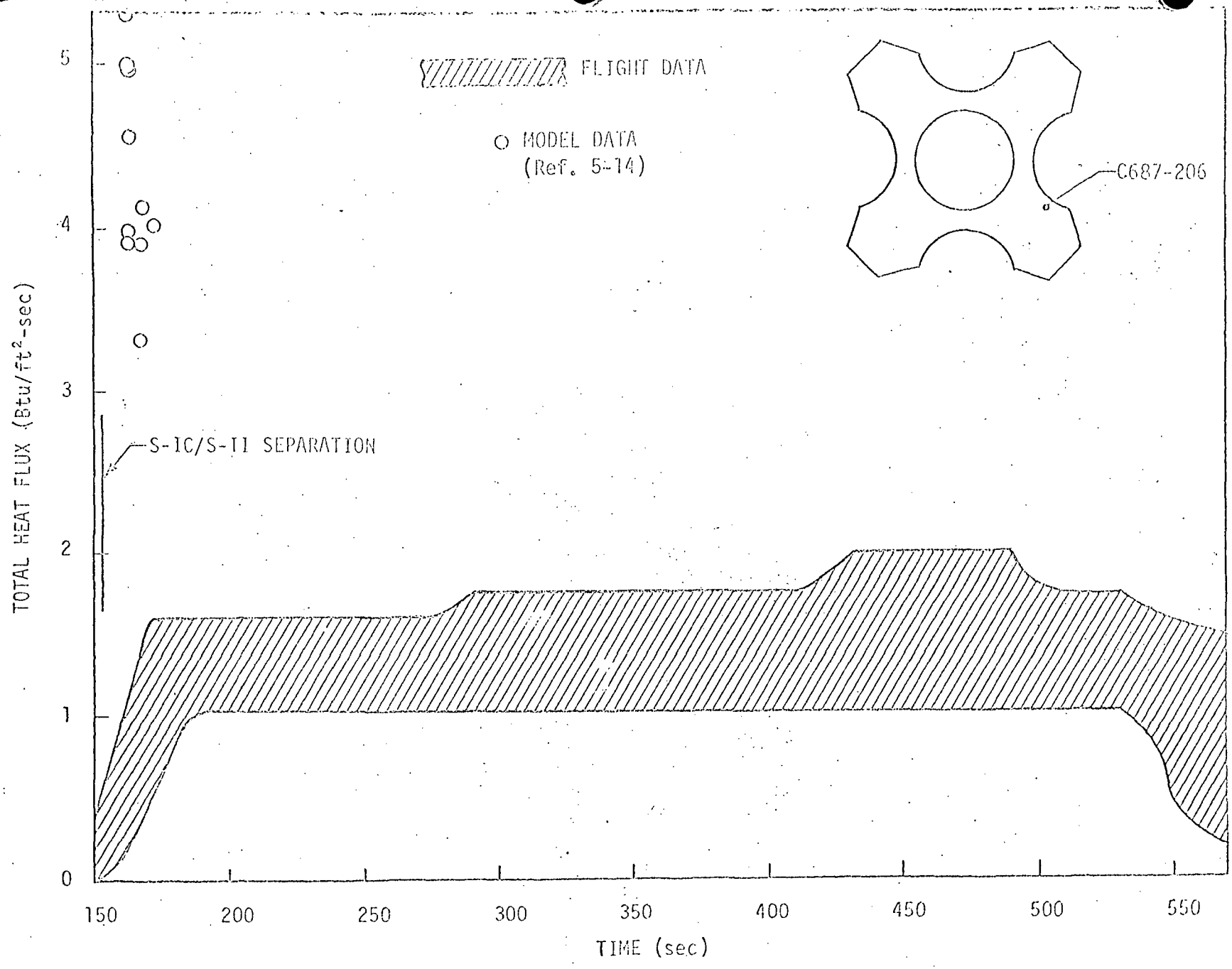

FIGURE 5-19. S-II STAGE FLIGHT AND MODEL HEAT SHIELD TOTAL HEAT FLUX

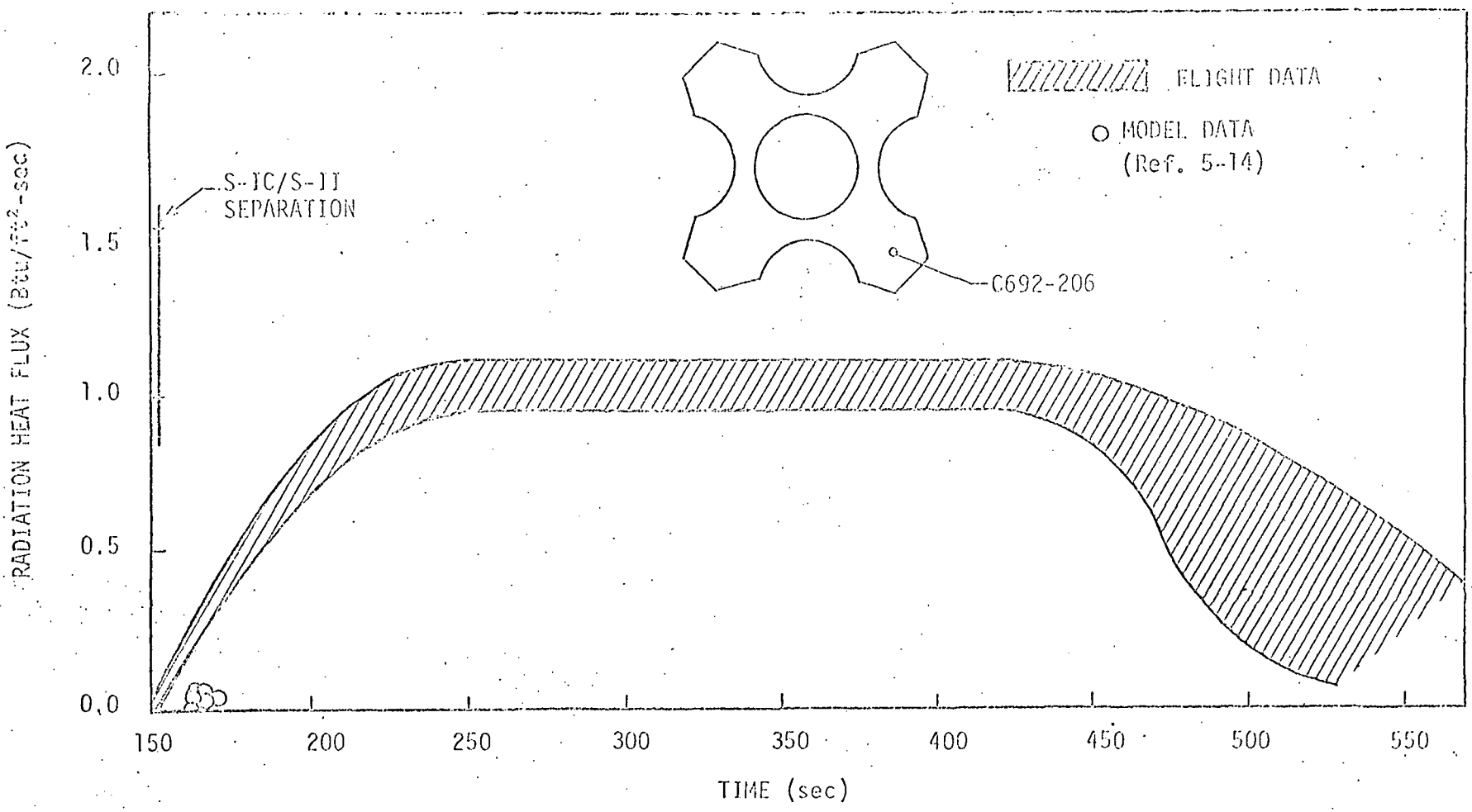

FIGURE 5-20. S-II STAGE FLIGHT AND MODEL HEAT SHIELD RADIANT FLUX

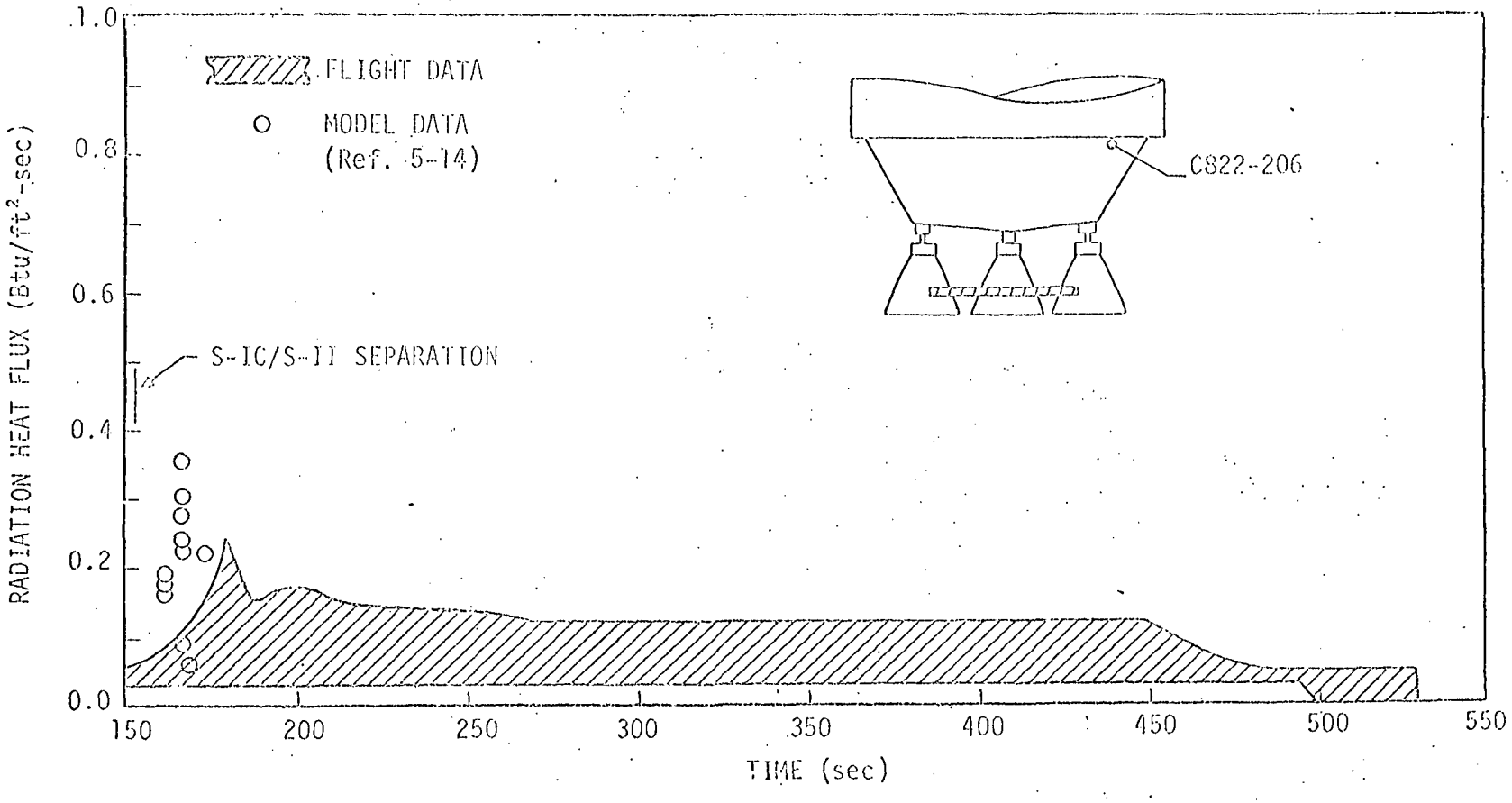

FIGURE 5-21. S-II STAGE FLIGHT AND MODEL THRUST CONE RADIANT FLUX

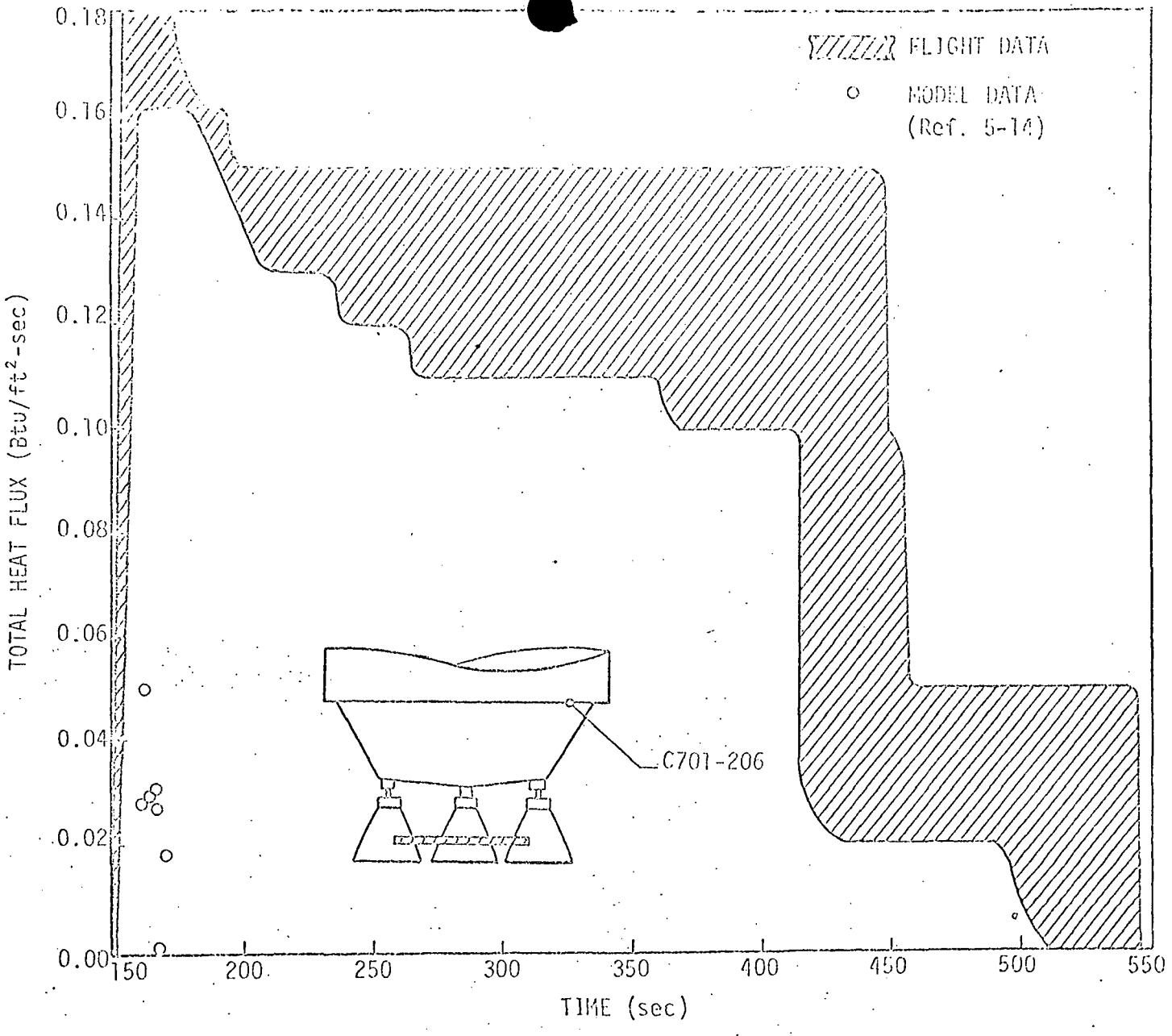

FIGURE 5-22. S-II STAGE FLIGHT AND MODEL THRUST CONE TOTAL HEAT FLUX

Page Intentionally Left Blank

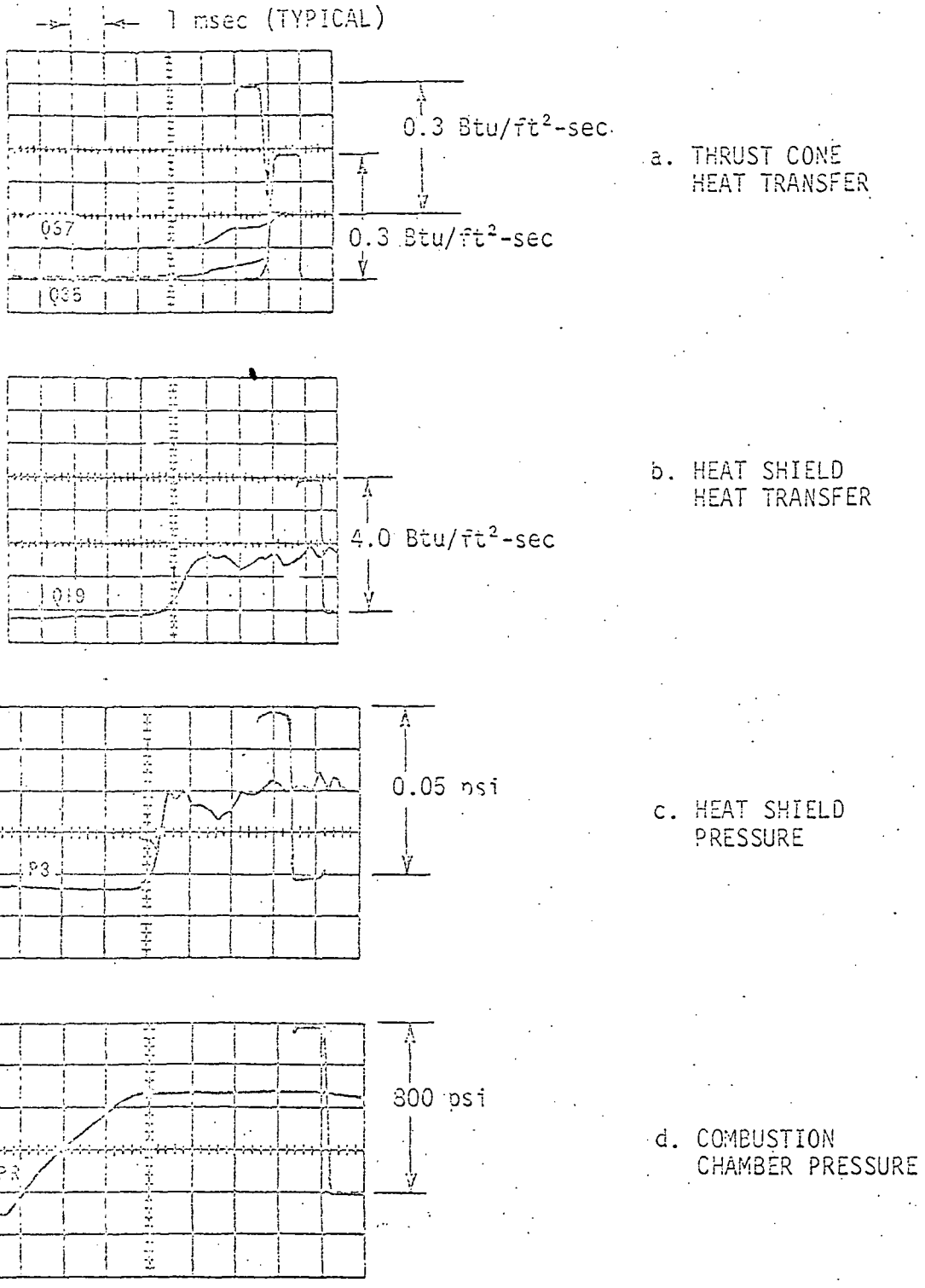

FIGURE 5-24. TYPICAL S-II STAGE TEST DATA

thrust cone heating rates on the other hand do not appear to reach a steady-state condition during the test. This is thought to be caused by the size limitation of the chamber. The test apparatus was moved to NASA/MSFC to investigate the thrust cone in more detail. Results of this test compared to CAL's data are shown in Figure 5-25. The CAL data gives the impression that it might rise to a higher heating level if it were not interrupted by the returning shock. The fact that heating rates rise at a slower rate in the larger tank makes it appear that the heating rate may be caused by a flow phenomenon characteristic of the chamber rather than the effect of exhaust gas reversal from the model.

5.6 CONCLUSIONS REGARDING MODEL TEST RESULTS

Some conclusions of the scale model testing are listed below.

- In general, measurements obtained directly from tests performed on the model appear to indicate a higher base thermal environment than that measured during the flight.
- The application of scaling factors to the convective flux gives better agreement between the model and the full-scale flight results. Thus, it appears that the model results should be scaled; however, the exact scaling laws that apply are unknown and are probably more complex than those which have been used.
- Judicious interpretation of the results of model testing appears to be required, as evidenced by the wide scattering of test data and by the methods used in certain tests (e.g., simulation of the turbine exhaust gases of the S-IB flame shield).
- In most cases, the trends with respect to configuration changes appear to be indicated correctly.

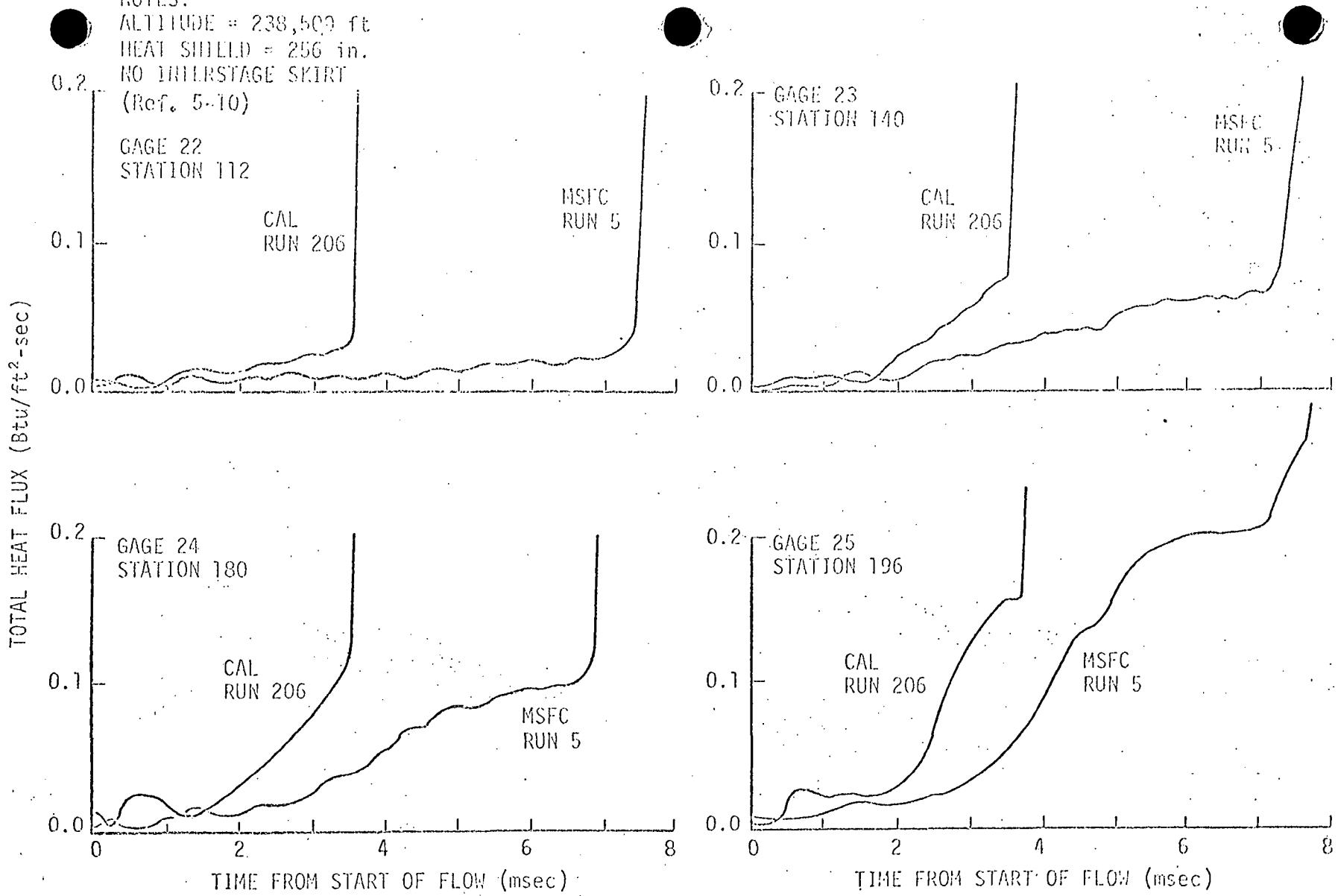

FIGURE 5-25. COMPARISON OF VACUUM TANK EFFECTS ON THRUST STRUCTURE HEATING RATES

- With respect to the Saturn model test, the following points were noted:
  - The base pressures were predicted fairly accurately and correlations have been developed using model and flight data in other references (Ref. 5-11).
  - The convective cooling that was evident early in the S-IC flights was not indicated by the model.
  - Model heating rates that were obtained for the upper stages were in better agreement with the flight results; however, the gas temperatures that were indicated by the hot base technique were significantly above those indicated during the flight tests.
- Some of the problems and inaccuracies in scale model testing appear to be caused by limitations in the facilities and the lack of simulation of certain functional details of the vehicle, rather than by the test technique itself.
- A problem appears to exist in translating scale model test data into effective flight vehicle design criteria. In order to predict vehicle surface temperatures, it is necessary to know the convective heat transfer coefficient, the recovery temperature, and the incident radiation. The exception to this is when the total heat flux is of such a magnitude that the surface reradiation will cause equilibrium to exist at a temperature below the limit of the material. The latter was the situation for most of the Saturn upper stages. For all of the booster stages and for many specific problems on upper stages, it was necessary to estimate the probable gas temperature and heat transfer coefficients. The desired design criteria could be established much more conclusively if these parameters could be obtained from the scale model test results. Therefore, the following is recommended:

- More effort should be devoted to developing techniques for measuring base recovery temperatures and evaluating convective heat transfer coefficients from scale model test results.

- More basic studies such as those represented by References 5-7 and 5-9 should be carried out to investigate basic parameters such as base flow fields, velocities, recovery temperature, and convective heat transfer coefficients.

- A more thorough experimental investigation of the scale model to flight vehicle scaling laws should be pursued.

REFERENCES - SECTION 5

5-1. Danm, W. K., "Relevances of Laboratory Experiments to Actual Radiating Flows", NASA TM-X-53711, Given in Specialist Conference on Molecular Radiation and Its Application to Diagnostic Techniques, NASA/MSFC, p. 459, October 5 and 6, 1967

5-2. Jones, I. P., Jr., "Summary of Base Thermal Environment Measurements on the Saturn I Block I Flight Vehicles", NASA/MSFC Technical Memorandum TM-X-53326, September 3, 1965

5-3. Sergeant, R. J., "Base Heating Scaling Criteria for a Four-Engine Rocket Cluster Operating at High Altitudes", AIAA Paper No. 65-826, December 1965

5-4. Kreith, F., Principles of Heat Transfer, 2nd ed., International Textbook Company, Scranton, Pennsylvania, 1965

5-5. Sergeant, R. J., "The Application of Short-Duration Techniques to the Experimental Study of Base Heating, Part II: A Study of Reynolds Number and Temperature Effects on Base Heating for a Four-Engine Hot Rocket Configuration Operating at High Altitude", CAL Report No. HM-1510-Y-1(II), April 1965

5-6. Czeck, E. A., "An Investigation of the Base Environment of the Saturn S-IC Booster at Low Altitudes Using Short-Duration Experimental Techniques", CAL Report No. HM-2045-Y-2, February 1966

5-7. Brewer, E. B. and C. E. Craven, "Experimental Investigation of Base Flow Field at High Altitude for a Four-Engine Clustered Nozzle Configuration", NASA TN-D-5164, May 1969

5-8. Brewer, E. B., Private Communications, 1972

5-9. Craven, C. E., "Optical Measurement of Multiplume Interaction", Lockheed Missile and Space Company, TM 54/20-236, LMSC/HREC D 148854, August 1969

5-10. "Minutes of a Meeting to Discuss S-II Thrust Cone Base Heating Test Data", Memo No. R-AERO-AT-64-22, June 17, 1964

REFERENCES (Concluded)

5-11. Pierce, T. G., "Preliminary Base Pressure Correlations, S-I Model and Flight Test Data", Boeing Coordination Sheet, AERO-N-046, November 28, 1962

5-12. Mullen, C. R., "Analysis of Saturn S-IC Base Heating Environment", Boeing Document No. D5-11287, November 1964

5-13. Davis, G. L., "Saturn IB Turbine Exhaust Reroute Study on a 5.47 Percent Scale Model at Mach Numbers 1.18 and 1.63", CCSD TN-AP-66-25, May 1, 1966

5-14. Rickard, W. D., "High Altitude Investigations on the Saturn S-II Stage Using Short-Duration Techniques, Part II: Prototype Base Environment", CAL Report No. HM-1510-Y-17(II), April 1965.

6. BASE HEAT TRANSFER DIAGNOSTIC AND PREDICTION TECHNIQUES

6.1 ASPIRATION PHASE MODEL

The Saturn flight test results have indicated that aspiration of ambient air into the base region exists during the first part of the flight. During this phase, ambient air flows into the base region. If the radiant flux is high, the relatively low temperature ambient air provides convective cooling. It should be noted that the Saturn I and S-IB flame shield region was an exception to the above. A semi-empirical analytical model which approximates the base convective environment during this phase has been devised and is described below.

In Section 2 it was shown that in order to predict the convective flux the following parameter must be determined:

$$q_c(\tau) = f[h(\tau),\ T_r(\tau)] \tag{6-1}$$

$$h(\tau) = f[c,\ m,\ n,\ P_o,\ P_S,\ T_o,\ x] \tag{6-2}$$

$$T_r(\tau) = f[T_o(\tau)] \tag{6-3}$$

where

q_c - convective flux

h - convective heat transfer coefficient

T_r - gas recovery temperature

P_o - stagnation pressure

P_S - static pressure

T_o - stagnation temperature

x - characteristic dimension

c, m, n - experimentally determined coefficients.

Figure 6-1 is a simplified schematic of the proposed model. In this model, the flow is shown to make a 90-degree turn at the edge of the base region and flow radially into the center. In reality, the flow would become detached at the edge and probably vortices would be shed into the base region. This flow model was selected partially for the following reasons:

- The supersonic engine exhaust jets produce a definite aspiration effect upon the rocket base, tending to draw the ambient air into the region.
- The use of peripheral scoops on some of the vehicles tended to divert air into the base region.
- Probably as a result of the above, measurements of rocket base heat transfer indicate an inverse function of the base radius. This can best be explained by a flow which is radially inward across the base.

Using this simplified model the parameters of Equations 6-1 through 6-3 can be approximated as follows. The trajectory of the vehicle is always known; therefore, the freestream ambient conditions are also known. The most utilitarian model of the base aspiration phase heat transfer would be one which relates the base heating to the freestream parameters.

Figure 6-2 shows the experimentally determined pressure in the separated flow region of a bluff body and a back step taken from References 6-1 and 6-2. Figure 6-3 shows how the bluff body base pressure agreed with the corrected pressure measured in the base region

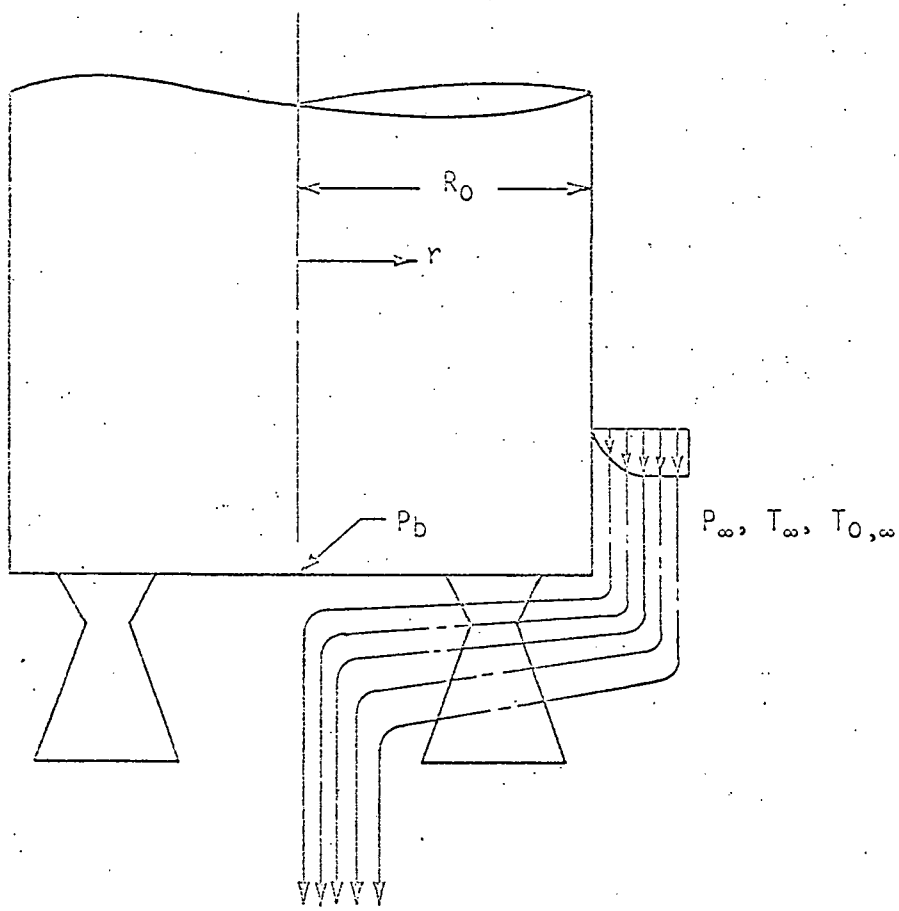

FIGURE 6-1. SIMPLIFIED ASPIRATION FLOW FIELD

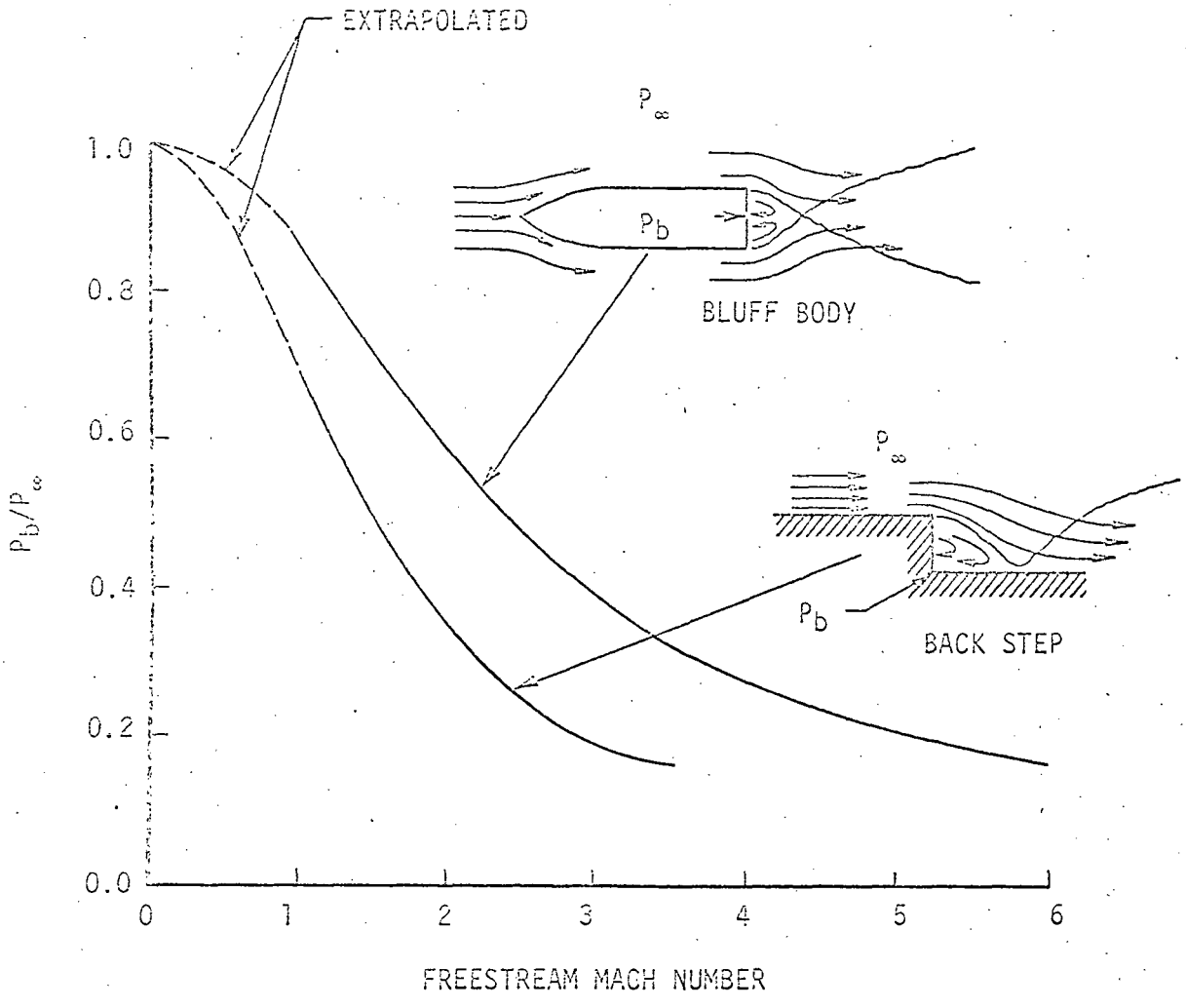

FIGURE 6-2. EXPERIMENTAL BASE TO AMBIENT PRESSURE RATIO

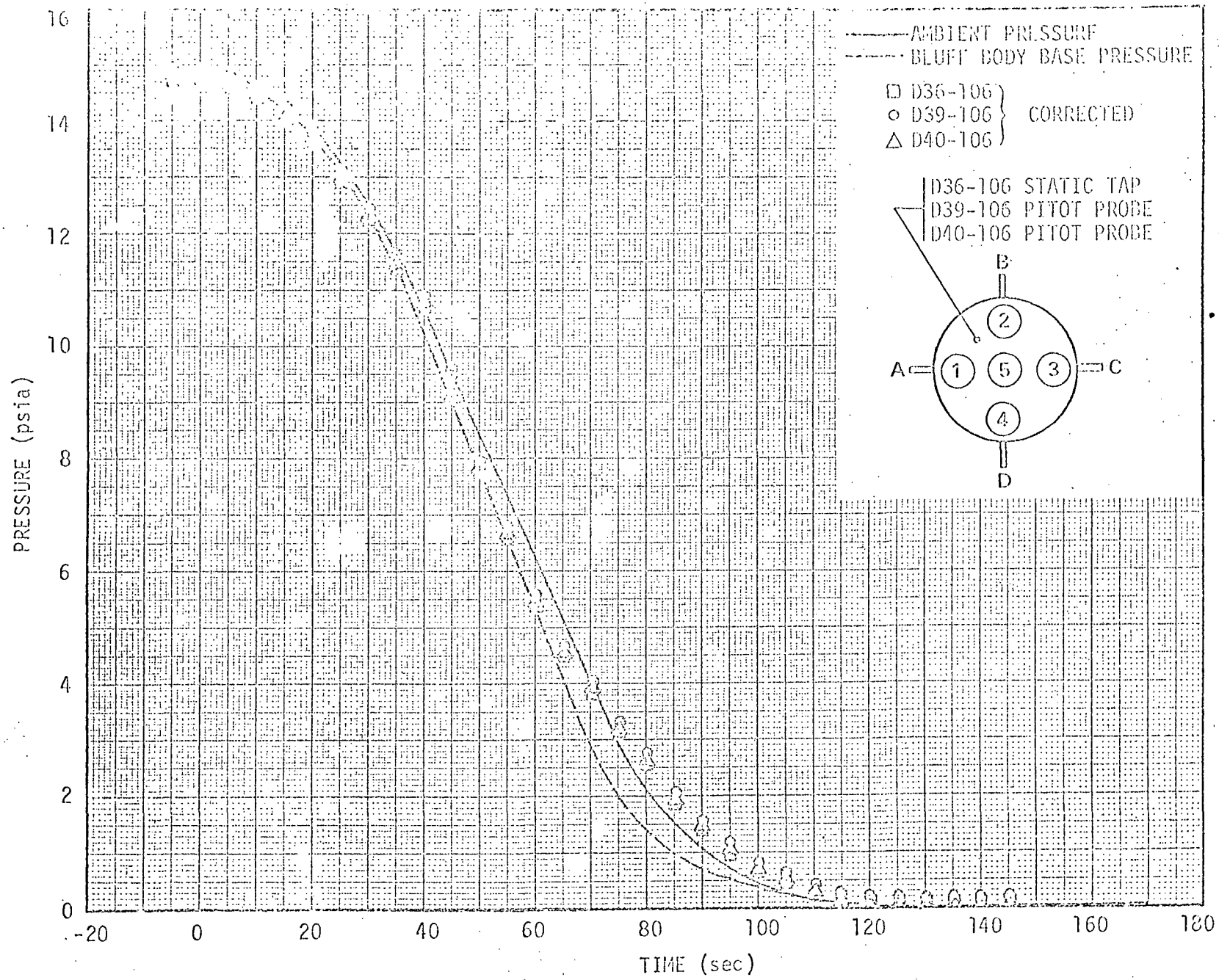

FIGURE 6-3., AS-501 CORRECTED BASE PRESSURES

of the Saturn AS-501 flight. By letting the ambient and bluff body base pressure represent, respectively, the stagnation and static pressure of the radial component of flow into the base region, a base flow Mach number can be computed from

$$M_b^2(\tau) = \frac{2}{\gamma - 1} \left\{ \left[\frac{P_\infty(\tau)}{P_b(\tau)} \right]^{\frac{1-\gamma}{\gamma}} - 1 \right\} \qquad (6\text{-}4)$$

where

$M_b(\tau)$ - Mach number of the radial inward base flow at time τ

$P_b(\tau)$ - center base pressure at time τ

$P_\infty(\tau)$ - local freestream ambient pressure at time τ

γ - specific heat ratio of the ambient air.

To assist in evaluating the base-to-ambient pressure ratio, the bluff body base pressure curve shown in Figure 6-2 was curve-fit between freestream Mach numbers $0 \leqq M_\infty \leqq 1.5$ to obtain

$$\frac{P_b(\tau)}{P_\infty(\tau)} = 1 - 0.135\, M_\infty^{1.75} \quad , \qquad 0 \leqq M_\infty \leqq 1.5 \quad . \qquad (6\text{-}5)$$

Figure 6-4 shows the comparison between the base flow Mach number obtained using Equations 6-4 and 6-5 and that evaluated from the Saturn AS-501 and AS-502 measured pressures. The figure illustrated that the computed Mach number agrees reasonably well with that obtained from the measured data during the aspiration phase.

Based on Saturn S-IC flight results, the stagnation temperature in the base region is assumed to be the same as the freestream; thus,

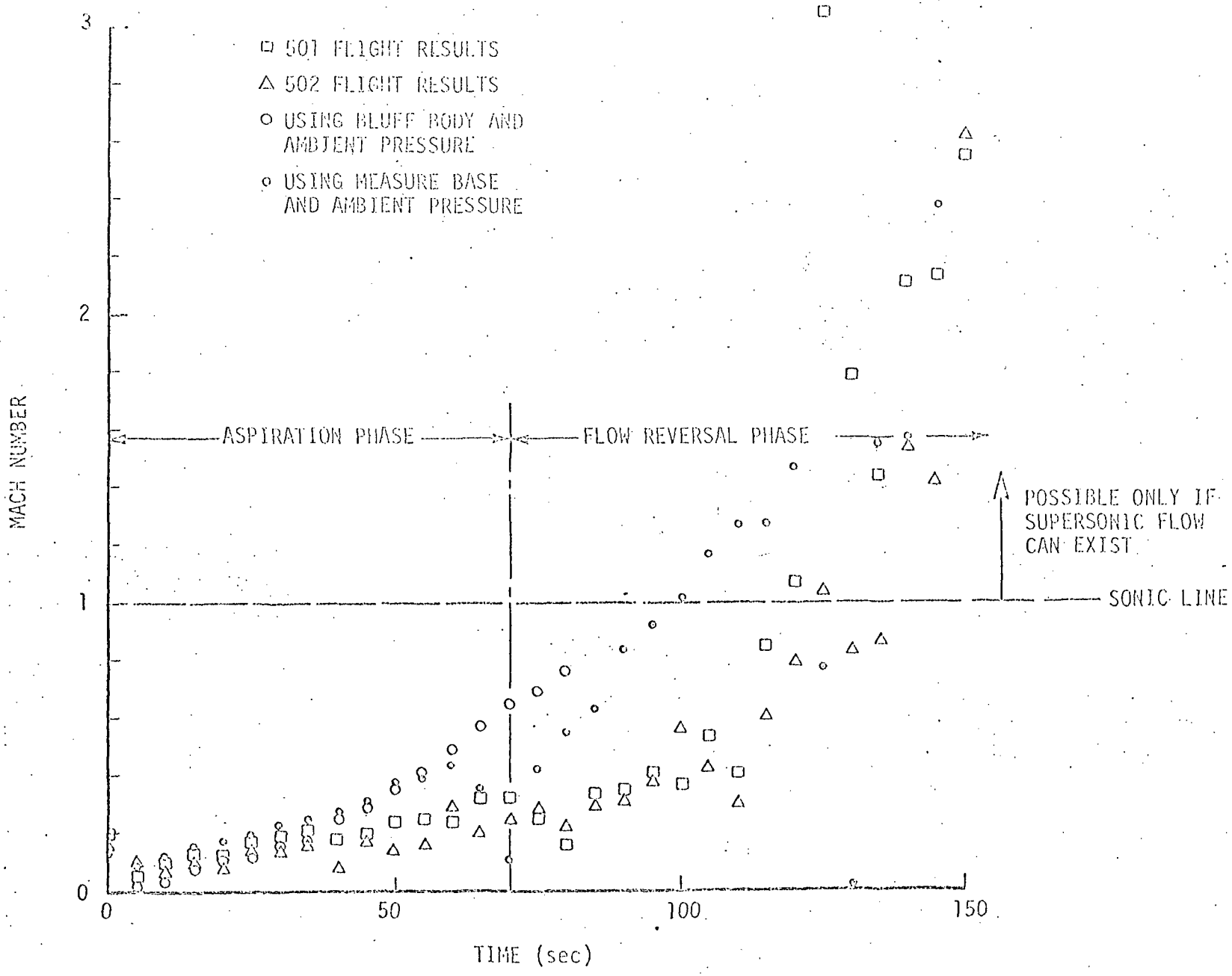

FIGURE 6-4. BASE FLOW MACH NUMBER

$$T_o = T_\infty \left(1 + \frac{\gamma - 1}{2} M_\infty^2\right) \quad . \qquad (6\text{-}6)$$

The base recovery temperature can be obtained from

$$T_r = T_\infty \left(1 + r' \frac{\gamma - 1}{2} M_\infty^2\right) \quad . \qquad (6\text{-}7)$$

Sogin (Ref. 6-3) found that a recovery factor, $r' = 0.1$, gave good agreement with heat transfer measured in base regions of bluff bodies. Thus, using $r' = 0.1$ and $\gamma = 1.4$, the recovery temperature can be obtained from

$$T_r = T_\infty \left(1 + 0.02 M_\infty^2\right) \quad . \qquad (6\text{-}8)$$

When evaluating transport properties, the static temperature of the base gas can be obtained from

$$T_S = T_o \left(1 + \frac{\gamma - 1}{2} M_b^2\right)^{-1} \quad . \qquad (6\text{-}9)$$

Combining Equations 6-9 and 6-6 gives

$$T_S = T_\infty \frac{\left(1 + \frac{\gamma - 1}{2} M_\infty^2\right)}{\left(1 + \frac{\gamma - 1}{2} M_b^2\right)} \quad . \qquad (6\text{-}10)$$

The transport properties for air should be evaluated at the film temperature given by

$$T_f = \frac{T_S + T_w}{2} \qquad (6\text{-}11)$$

where

T_S - gas static temperature

T_w - surface temperature .

Based upon the simplified flow model of Figure 6-1, the characteristic dimension is taken as

$$x = R_o - r \quad . \tag{6-12}$$

Using the equation derived in Section 2, i. e.,

$$q_c = h(T_r - T_w) \tag{2-5}$$

where

$$h = C\left(\frac{C_{p_f}^{\,n}\,\kappa_f^{\,1-n}\,\rho^m\,u^m}{\mu_f^{\,m-n}}\right) x^{m-1} \tag{2-7}$$

and coefficients m = 0.8; n = 0.333; the convective flux to the S-IC heat shield calorimeters C25-106 and C26-106 was computed. The computed results, compared to the measured convective flux, are shown in Figures 6-5 and 6-6. The coefficient C = 0.03 is equivalent to flat plate, parallel turbulent flow heat transfer. For the aspiration phase convective cooling, using C = 0.03 would give conservative design results. Based on the results shown in Figures 4-28 and 4-29 and Table 4-1 for the heat transfer in separated regions, a higher coefficient may be justified. Therefore, the convective heat transfer was computed using coefficients C = 0.06 and C = 0.09. These results are also shown in Figures 6-5 and 6-6.

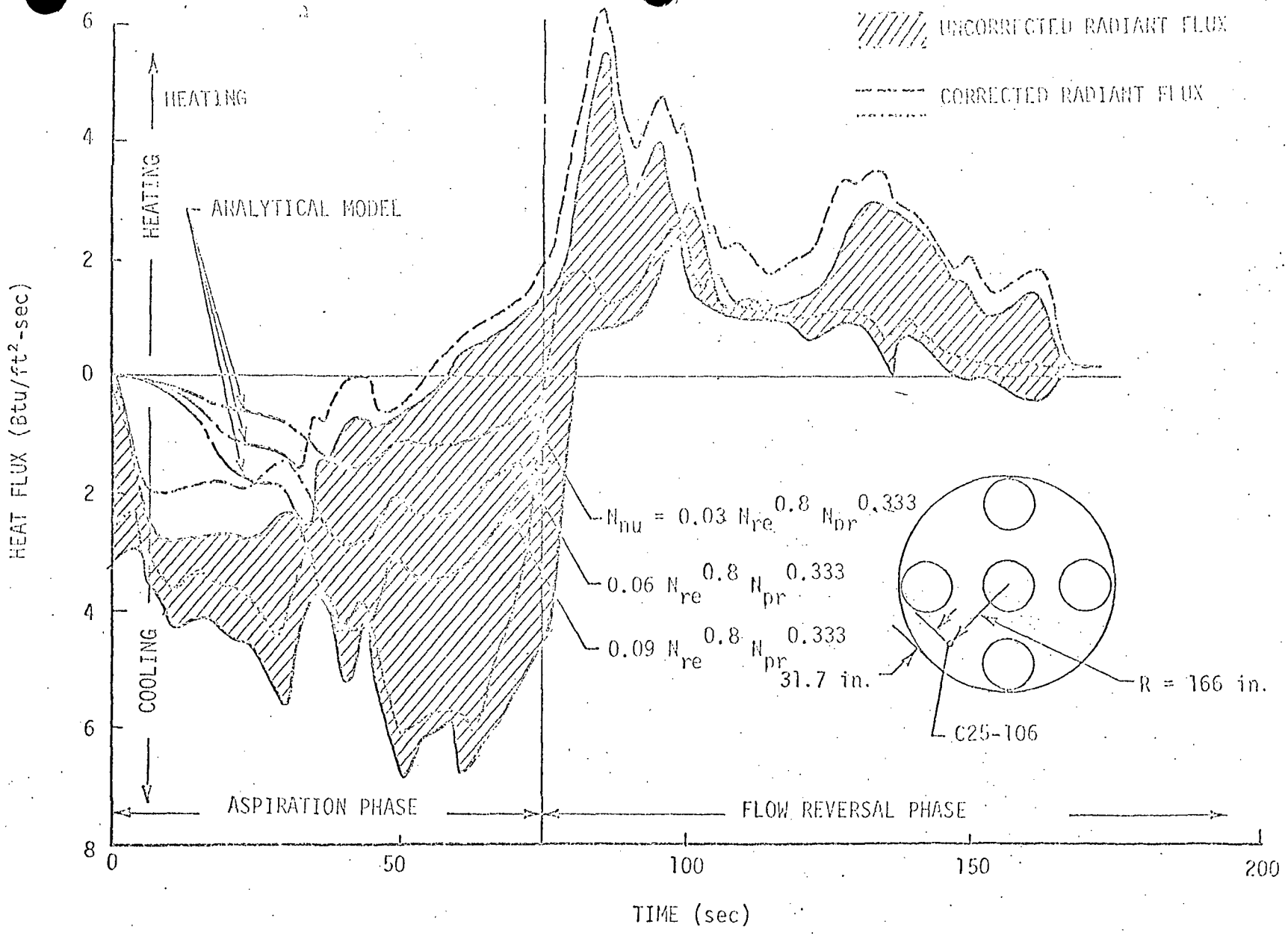

FIGURE 6-5. S-IC HEAT SHIELD ANALYTICAL MODEL AND MEASURED CONVECTIVE FLUX TO TOTAL CALORIMETER C25-106

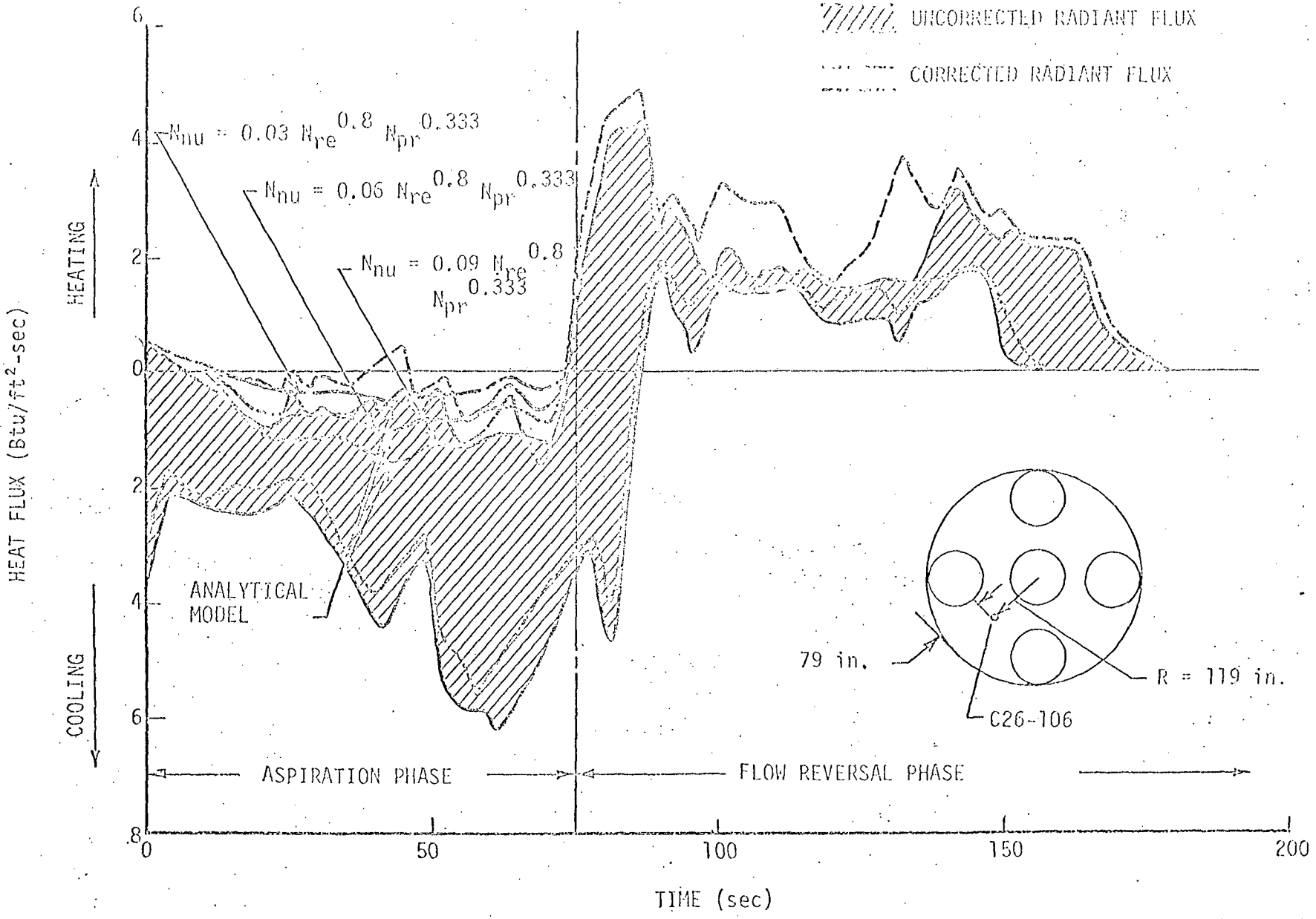

FIGURE 6-6. S-IC HEAT SHIELD ANALYTICAL MODEL AND MEASURED CONVECTIVE FLUX TO TOTAL CALORIMETER C26-106

The figures illustrate that the convective flux computed using the aspiration phase analytical model is in reasonably good agreement with the measured flux evaluated for calorimeters C25-106 and C26-106; however, the computed flux is in better agreement with the results for C25-106 than for C26-106. The figures also show that the aspiration phase analytical model will yield conservative design criteria.

6.2 PLUME AND AFTERBURNING EFFECTS

In studying booster base heating and related problems, the shapes of the engine exhaust plumes become important for several reasons. Such factors as the time and/or altitude at which flow reversal starts and the apparent coincidence of increases in radiant flux during this period are related to the plume shapes and interactions. To further understand these relations, a cursory study of actual plume shapes, predicted inviscid shapes, and adjacent plume interactions was initiated with the following preliminary results.

At present, several methods of predicting inviscid plume shapes are available. Throughout this study an approximate method developed by Charwat (Ref. 6-4) has been used. Comparisons have indicated that this approximation gives good results compared to the more involved method of characteristics.

Figure 6-7 shows a dimensionless plot of a single plume boundary which was calculated using the method mentioned above for an F-1 engine with a 3:1 area ratio. Two different types of input were used in the calculations. The first utilized the NASA/Lewis Thermochemical Program to evaluate the nozzle exit conditions, whereas the second used the one-dimensional isentropic flow theory to obtain the exit conditions. From photographs taken during static tests of this same engine, the

actual plume boundary has been scaled and nondimensionalized and is shown in Figure 6-7 along with the inviscid plume shapes. It can be seen in the figure that the inviscid plume boundary predictions are substantially less than the real plume boundary, especially in the afterburning mixing zone.

To show how this affects the base heat transfer, the gas temperatures and pressures measured in the flame shield and heat shield regions during one of the Saturn I flight tests are shown in Figures 6-8 and 6-9. As shown in Figure 6-8, flame shield flow reversal appears to start at approximately 25 seconds, whereas the heat shield flow reversals start at approximately 60 seconds. (Note. These results have not been normalized to AS-501 trajectory.) Figure 6-9 shows the corresponding pressures to be approximately 10.2 and 3.4 psia, respectively. Figure 6-10 shows the dimensionless plume shapes of the Saturn engines predicted using Charwat's method for various pressures. The centerlines between adjacent engines are also shown in the figure. By studying Figure 6-10, it can be seen that the inviscid plume prediction would not have predicted plume interaction corresponding to the flame and heat shield pressures of 10.2 and 3.4 psia, respectively. Apparently, the thick mixing and afterburning layers are interacting and reversing much earlier in flight than would be indicated by the inviscid plume predictions. Therefore, using plume shapes which have been generated using inviscid flow theories to predict plume impingement may not be representative of the real condition. Further analytical work to incorporate the mixing zone in the prediction of plume shapes is indiciated here.

A similar analysis can be conducted on the F-1 (Saturn V, S-IC) engine. The analytical plume shapes for several altitudes, for the F-1, are presented in Figure 6-11.

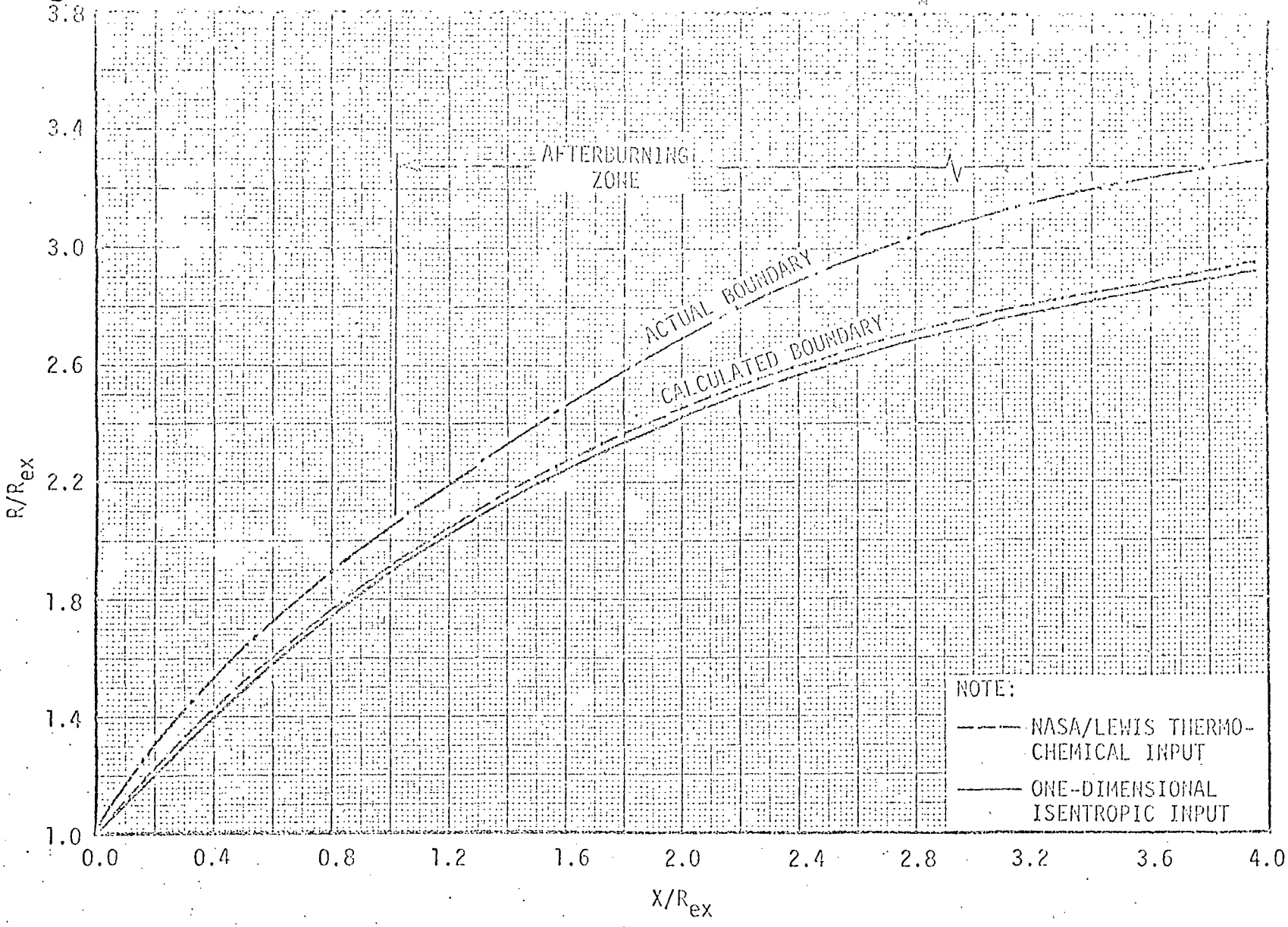

FIGURE 6-7. F-1 ENGINE PLUME (A/A* = 3) AT SEA LEVEL

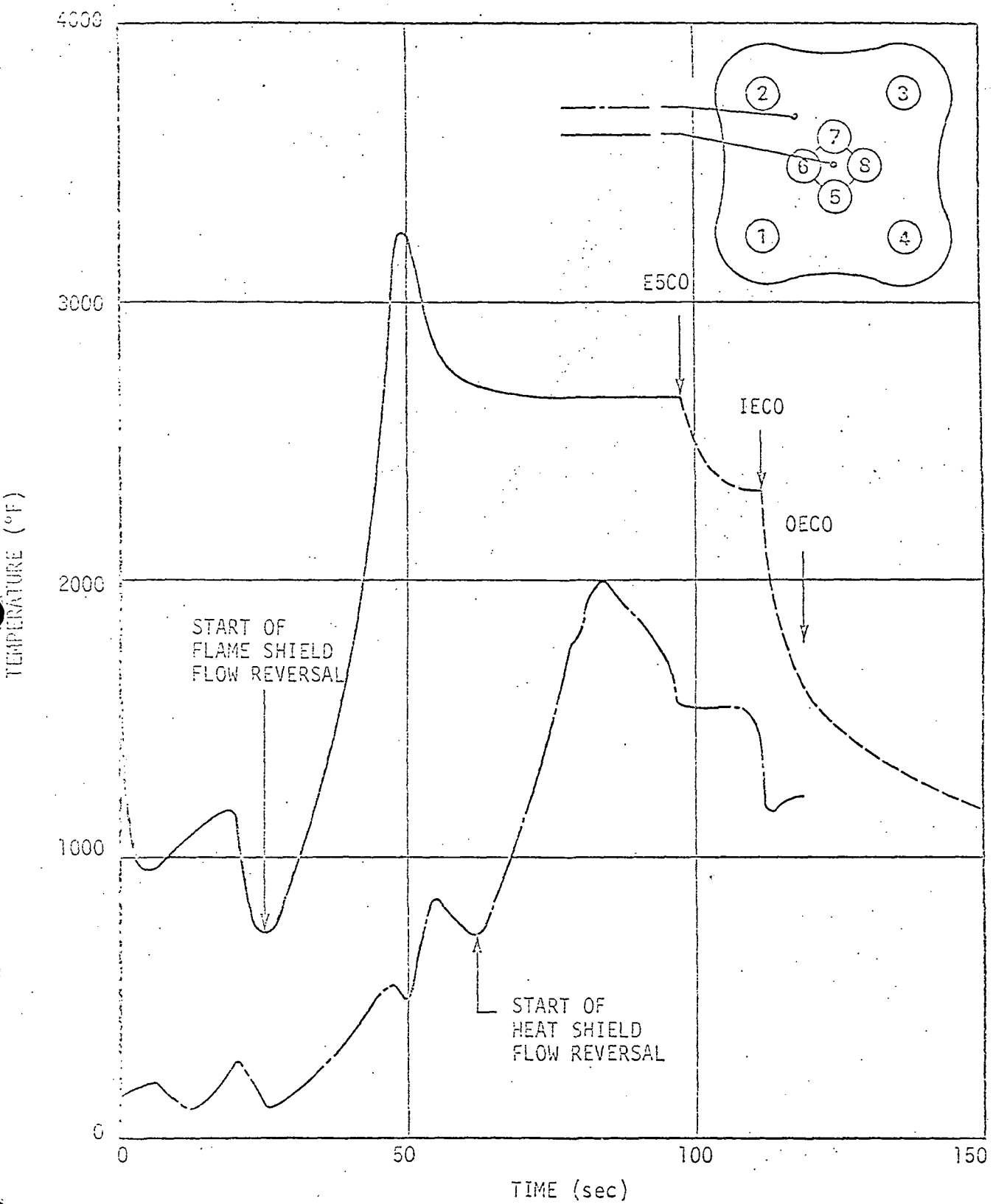

FIGURE 6-8. SATURN I GAS TEMPERATURE

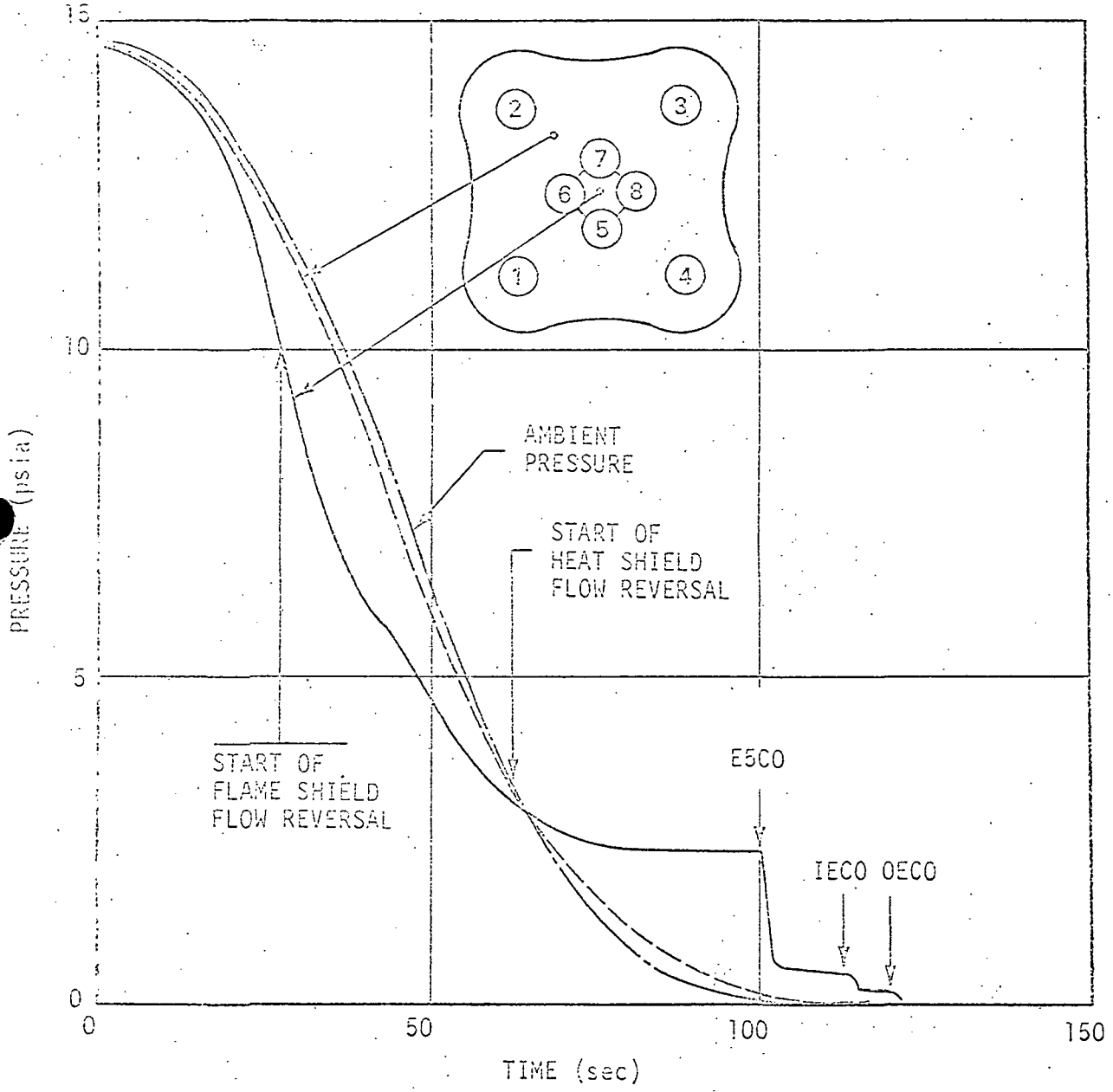

FIGURE 6-9. SATURN I PRESSURES

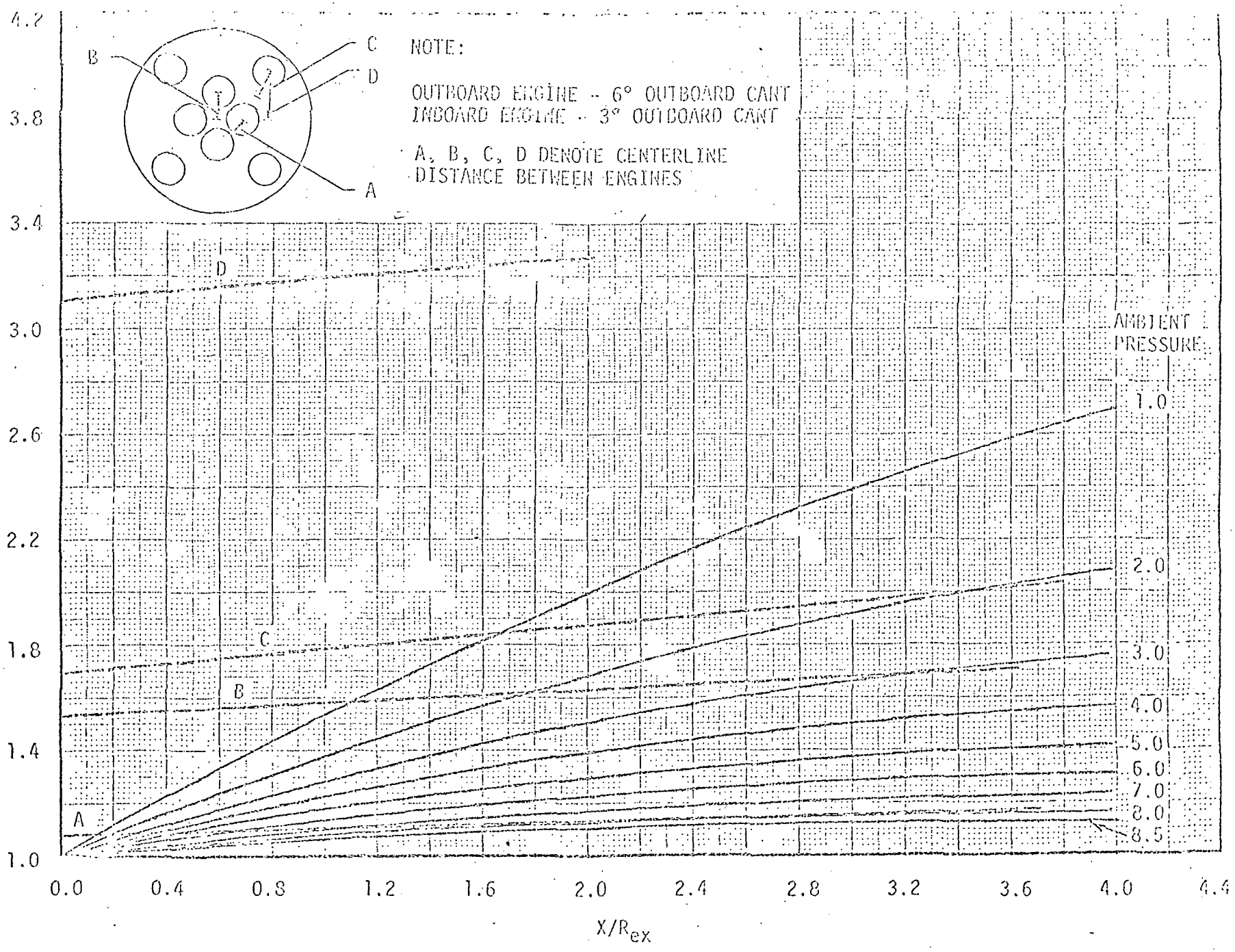

FIGURE 6-10. H-1 ENGINE PLUME SHAPE

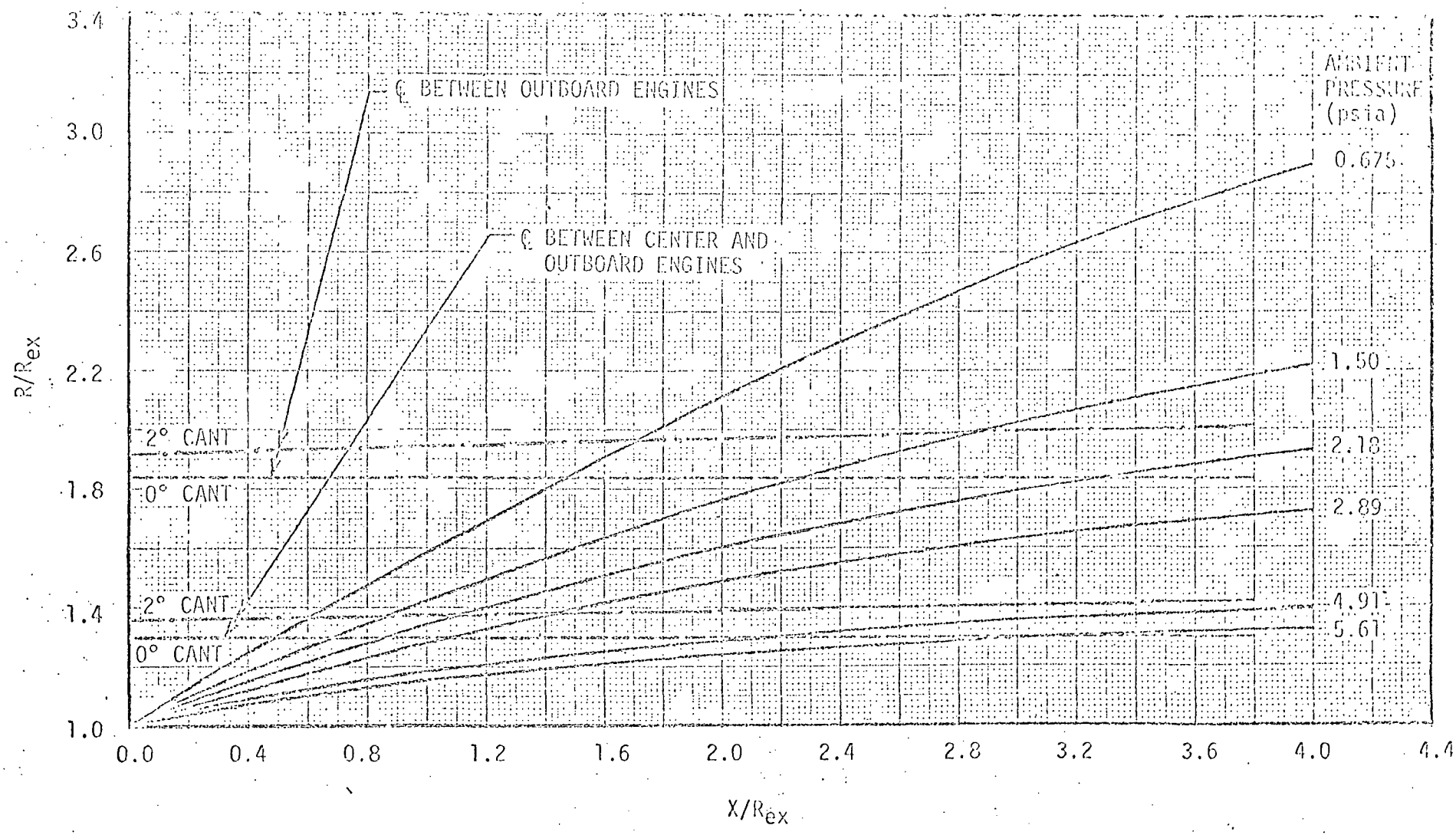

FIGURE 6-11. F-1 ENGINE (A/A* = 16) PLUME SHAPE

Single engine plume shapes for the J-2 (S-II stage) engine have been calculated and are presented in Figure 6-12. Afterburning is not a problem on the upper stages, as it is for boosters. Therefore, it should be mentioned that the inviscid plume shapes should be more valid for upper stages.

6.3 BASE RADIATION

As discussed in Section 2, rocket exhaust plumes are nonisothermal, nonisobaric, and nonhomogeneous gas bodies. The equation which governs the radiation from such bodies is

$$q_{ir} = \int_{\nu} \int_{\omega} \int_{S} \rho \, \kappa_{\nu} \, I_{b\nu} \exp \left(- \int_{S} \rho \, \kappa_{\nu} \, dS' \right) \times \cos \phi \, dS \, d\omega \, d\nu \quad , \tag{6-13}$$

where

q_{ir} - incident radiant flux

ρ - local density

κ_{ν} - spectral absorption coefficient

$I_{b\nu}$ - Planck function

S - optical path

ω - solid angle

ν - wave number

ϕ - polar angle (Figure 2-2).

For conditions where the radiation can be considered a surface phenomenon, the equation for radiation between a finite radiating plume surface element and a differential receiver is

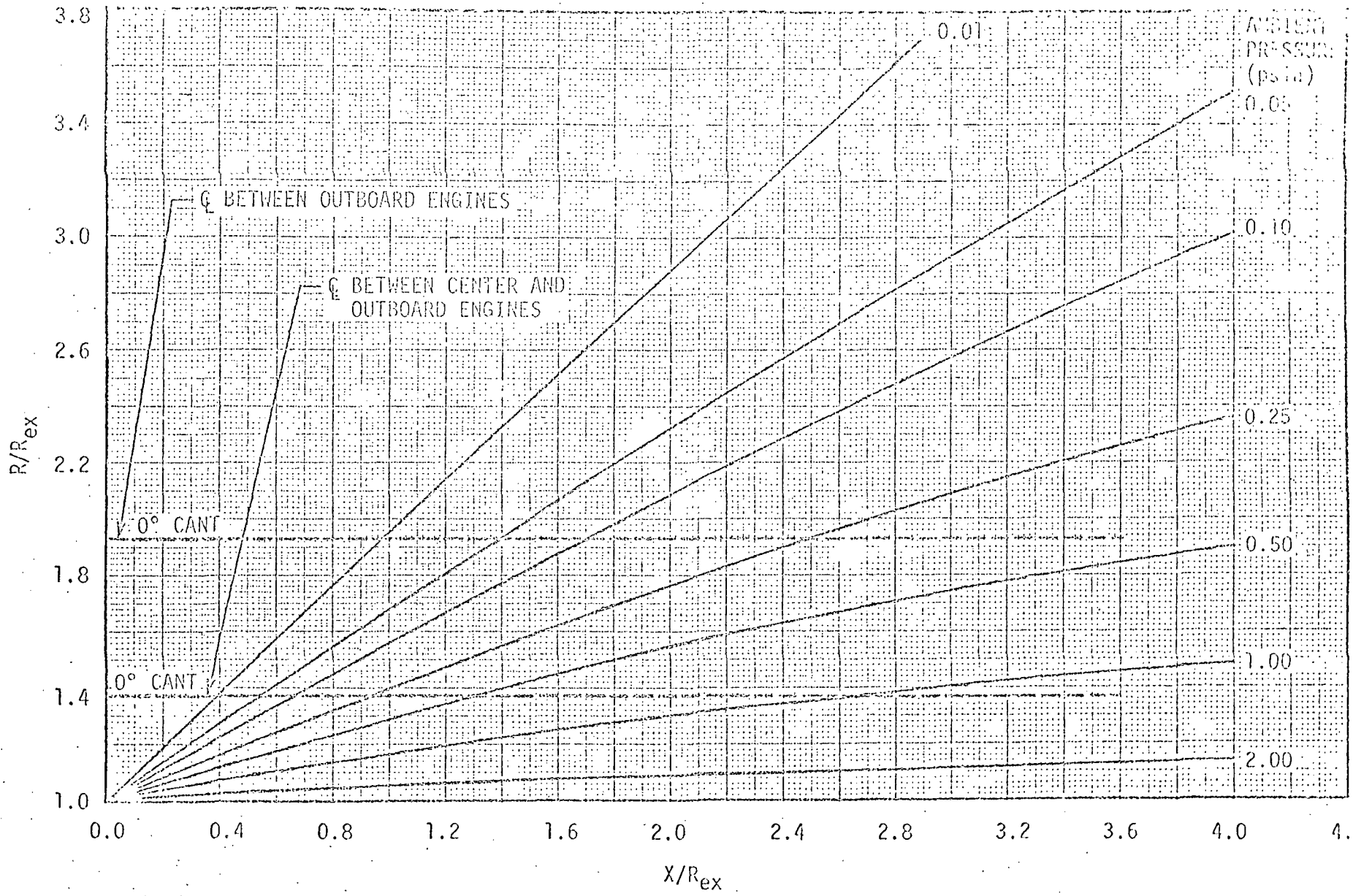

FIGURE 6-12. J-2 ENGINE PLUME SHAPE

$$q_{ir} = \sum_{p} E_p F_{\Delta A_S - \Delta A_p} \qquad (6\text{-}14)$$

where

$E_p = \sigma T_p^4$ - plume blackbody emissive power

$F_{\Delta A_S - \Delta A_p}$ - view factor between ΔA_S and ΔA_p

6.3.1 Gaseous Radiation

A number of methods have been developed for predicting gaseous radiation, and Reference 6-5 contains an excellent literature survey on this subject. The most successful method involves the use of several computer programs and was developed for or by the MSFC Aero-Astrodynamics Laboratory over a period of years. Briefly, the calculations are carried out in the following way.

The chemical composition of the reacting propellants is obtained using a thermal-chemical computer program similar to that described in Reference 6-6. This program generates the chemical composition of the gases as an input to the method-of-characteristics flow program.

A method-of-characteristics (Ref. 6-7) flow program in conjunction with the thermal-chemical program is used to generate the inviscid flow fields of the engine and plumes. This program can also generate the internal shock structure of the plumes to a limited degree. Since the method-of-characteristics is restricted to supersonic flows, the Riemann waves (normal shocks) which are known to exist at points along the plume axis cannot be generated with this program. Also, no computer program is known to exist which can readily generate the three-dimensional shock waves which would exist as a result of the plume/plume interactions. In some cases, approximations of the shock structure in these regions have been used and patched into the inviscid supersonic flow fields with some success.

Since the method-of-characteristics program output is the thermodynamic and flow properties at a point where right- and left-running characteristic lines cross, it is not usually suitable for direct input into the gaseous radiation programs. A separate computer program called JUGGLE (Ref. 6-8) is used to prepare the method-of-characteristics output for use in the radiation program. This program generates a systematic map of plume thermodynamic properties as a function of axial distance downstream of the exit and radial distance from the axis. This is accomplished by iterating between the four nearest points of the method-of-characteristics output.

If afterburning along the plume boundary is significant and is to be included in the radiation problem, the thermodynamic and chemical composition of the afterburning mantle must also be supplied. One of the many techniques which have been developed for this purpose is discussed in Reference 6-9. This technique uses the stream tube approach, viscous mixing, and finite rate chemical reactions to compute the temperature and gas properties of the mixing boundary layer. This layer is then superimposed on the inviscid flow field.

Once the thermodynamic properties and chemical species are spatially defined, the thermal radiation can be computed. The radiation calculations are essentially the numerical integration of Equation 6-13. Reference 6-10 describes a computer program which has been developed for this purpose. This program is a volumetric integration from an arbitrarily oriented differential area through the plumes and surrounding media along each line of sight. The program uses band-averaged absorption coefficients (κ_ν in Equation 6-13) and the Curtis-Godson method of approximating nonhomogeneous gas properties.

The techniques just outlined are theoretically sound and appear to be the most advanced if not the only complete technique presently available for computing plume radiation from basic knowledge.

Figure 6-13, which was extracted from Reference 6-11, shows some typical results which can be obtained using this method to predict the radiation from a single plume. Given the complexities associated with the three-dimensional flow field and shock structure of multiplumes, chemical reactions in free boundaries and the unknown nature of particle sizes, concentrations, and densities, it would appear that these techniques would not easily lend themselves to a simple solution to the problem. However, reasonably accurate predictions of the incident flux to a point in the base region can be obtained provided the expenditure of the time and effort implied in using these techniques is not prohibitive. As is so often the case, a simple engineering method (i.e., one which is reasonably accurate most of the time and simple to use) would be very beneficial in solving this problem.

6.3.2 Surface Radiation Approximation

For certain conditions, it is possible to treat the plume as a diffusely radiating surface. The physical implication of this approximation is that the absorption coefficients associated with the gas in the outer layers of the plume are so large that the gas is essentially opaque for any significant thickness. This situation exists when the gas is heavily laden with particulate materials.

By treating the radiating plumes in this manner, the problem becomes mathematically simple as shown by Equation 6-14. The problem with this approximation is that the spatial variation in emissive power of the plume must be known in order to predict the incident heat flux. Often this can be deduced from radiation measurements taken during engine static test firings.

To aid in calculating the heat transfer between a diffusely radiating plume and an arbitrarily located area in the base region, a computer program has been developed (Ref. 1-6). The details of

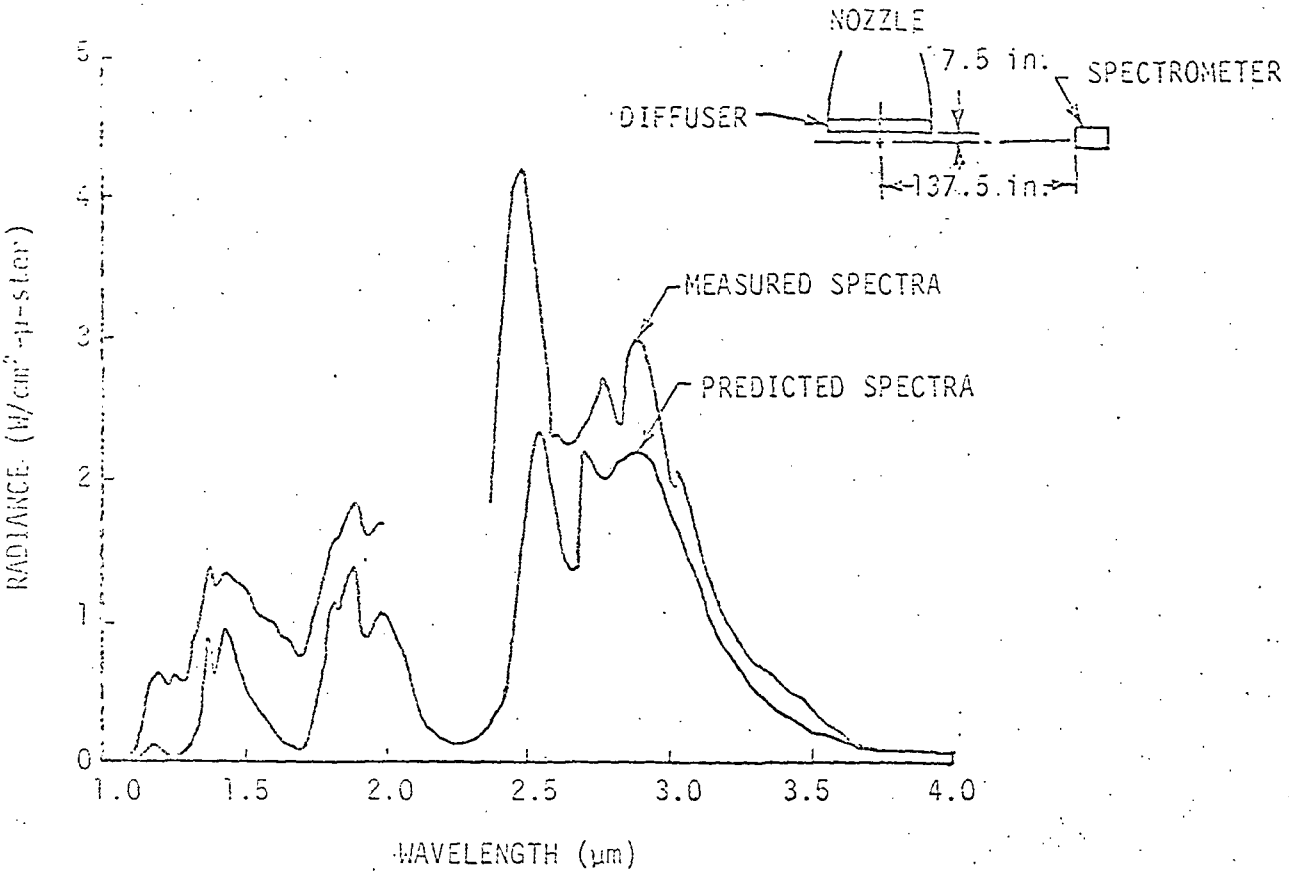

a. LOX/LH_2

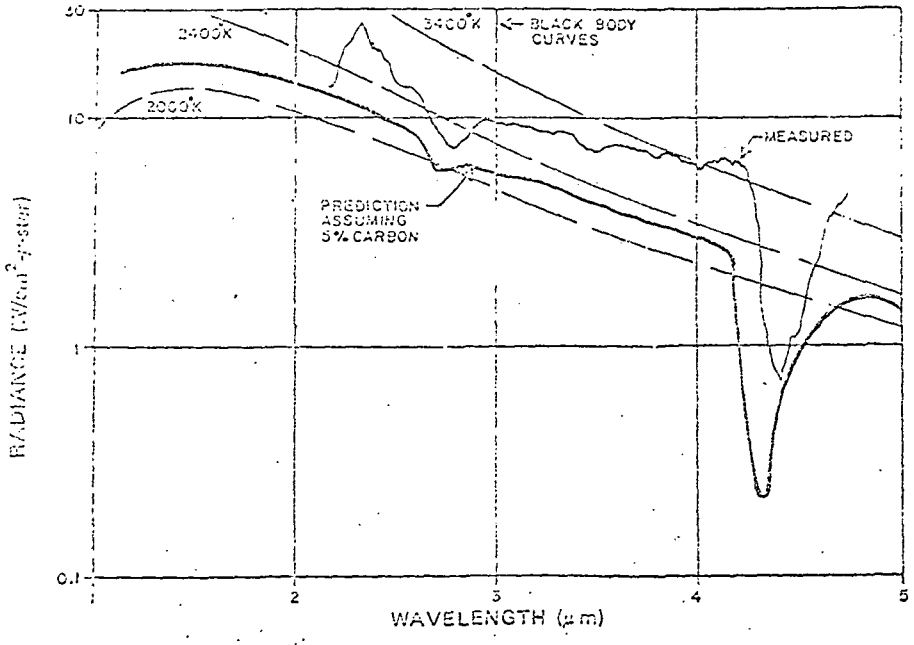

b. LOX/PR-1 (hydrocarbon)

FIGURE 6-13. ENGINE EXHAUST PLUME NEAR SEA LEVEL

of this program are given in the appendix. The program has the capability to compute the radiation from multiple plumes, including any blockage by intervening plumes or nonparticipating surfaces.

To show how well the calculated radiation agrees with the measured radiation, comparisons were made with the Saturn S-IC flight test results and are shown in Figures 6-14 through 6-21. The F-1 engine plume emissive power, shown in Figure 6-14, was obtained by extrapolating measured results taken during static tests of an H-1 (Saturn S-I) engine. In extrapolating the H-1 engine plume emissive power to the F-1 engine plume, it was assumed that the dimensionless distance, X/D, would be the same for both engines. The only justification for this is that both engines used the same propellants (LOX/RP-1) and the afterburning appeared to start at approximately $X/D \approx 1$ for both engines. It is anticipated that better agreement would have been obtained if the actual F-1 emissive power were available. The plume shape was obtained from photographs taken during the static tests. The plumes were divided into short cylindrical segments over which the emissive power could be assumed constant as shown by the dashed line in Figure 6-14. Since the available literature indicated two possible levels of the plume emissive power (Figure 6-14), both of these were used in the computations. The sea-level radiant flux was computed for two heat shield locations corresponding to the heat flux meters, C60-106 and C61-106 shown in Figure 6-15, and three engine locations corresponding to C57-101, C58-105, and C150-101 shown in Figures 6-15 and 6-16. The calculated and measured results are shown in Figures 6-17 through 6-21. For the calculated results, the upper and lower parts of the band shown in the figures correspond to the upper and lower emissive power curves of Figure 6-14. Because of launch pad deflections of the F-1 engine plumes, the computed flux should be compared with the flight heat flux measured after lift-off (possibly 5 to 15 seconds).

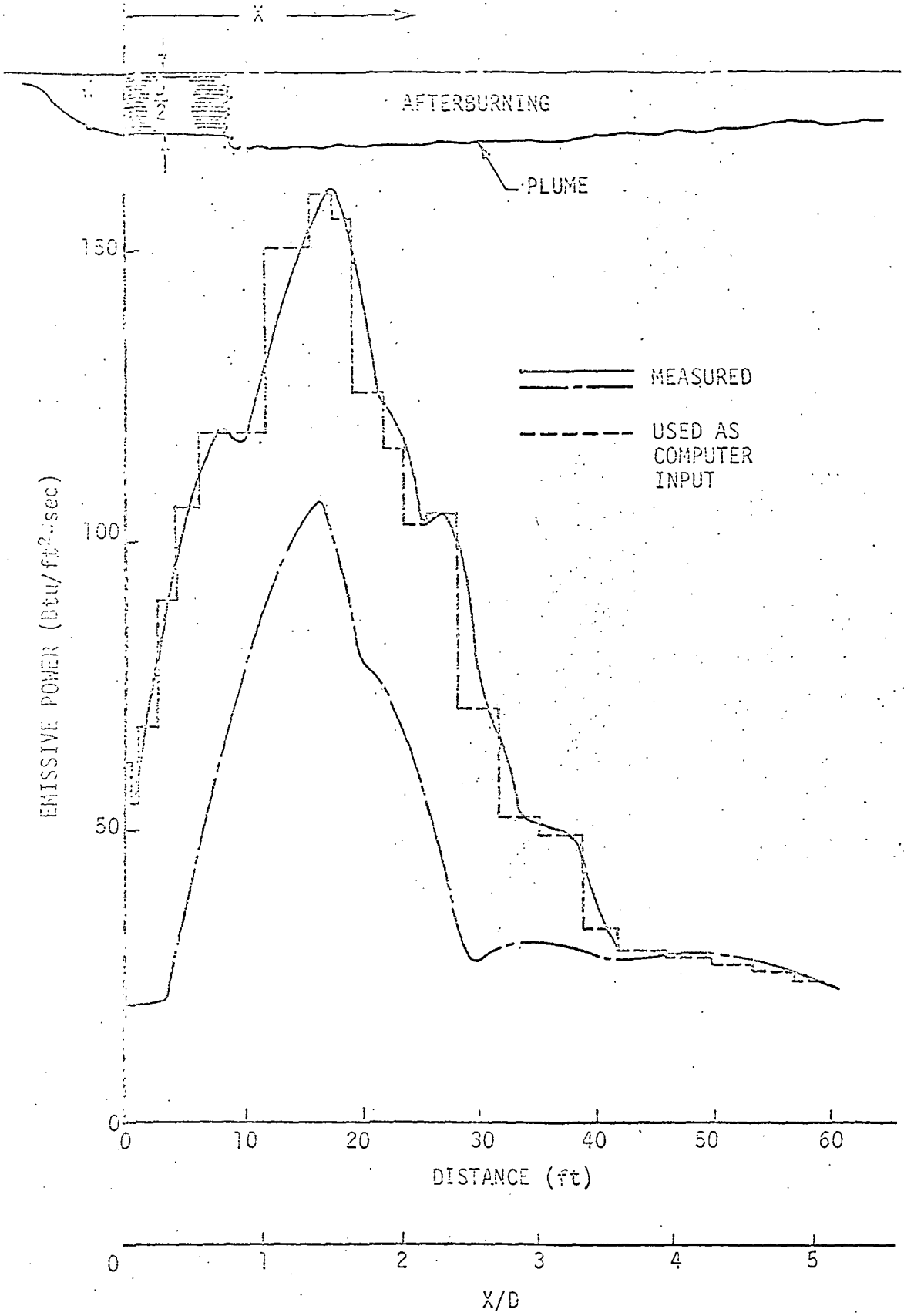

FIGURE 6-14. F-1 ENGINE PLUME EMISSIVE POWER

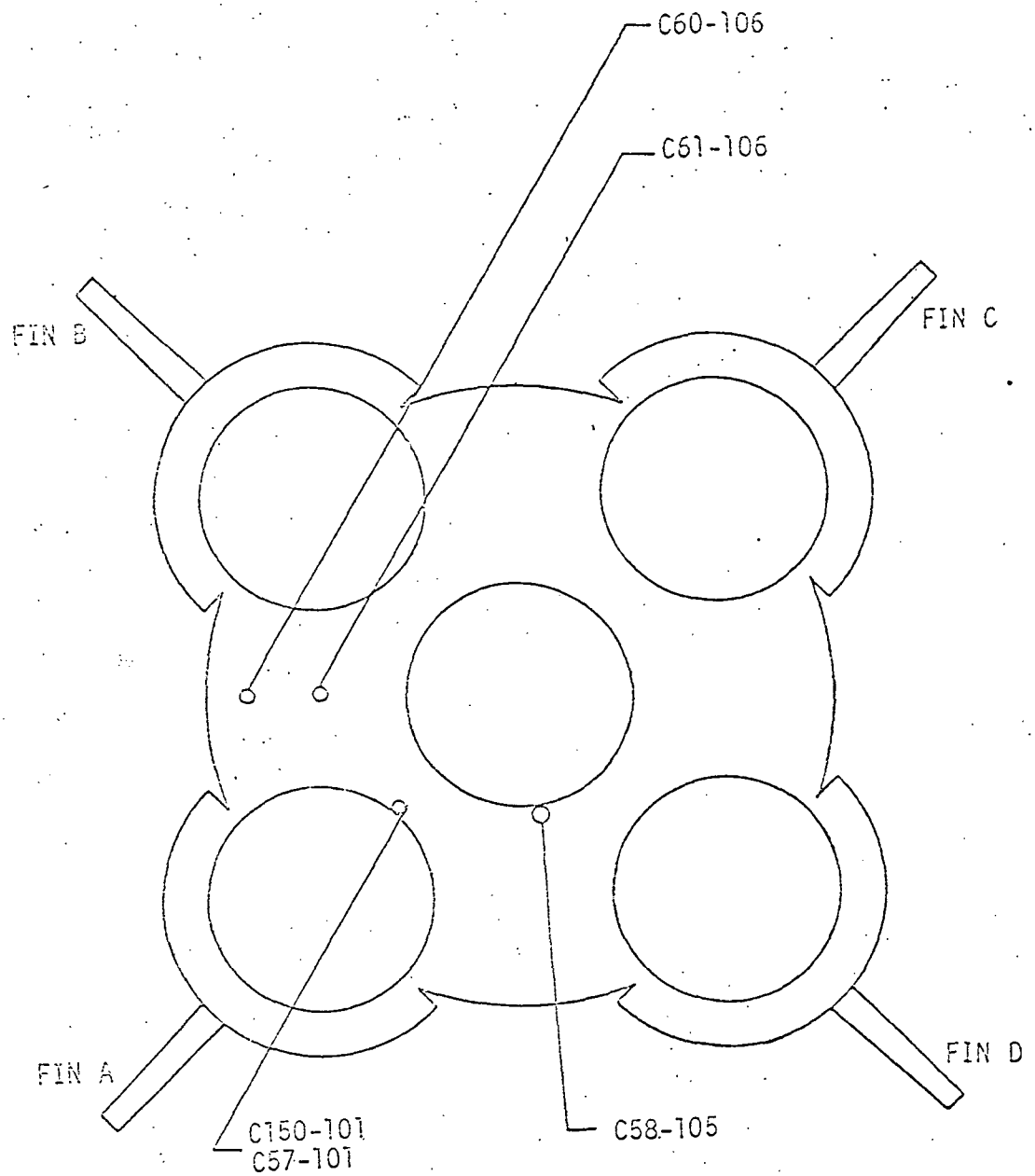

○ RADIATION CALORIMETER LOCATIONS

FIGURE 6-15. S-IC RADIATION CALORIMETER LOCATIONS

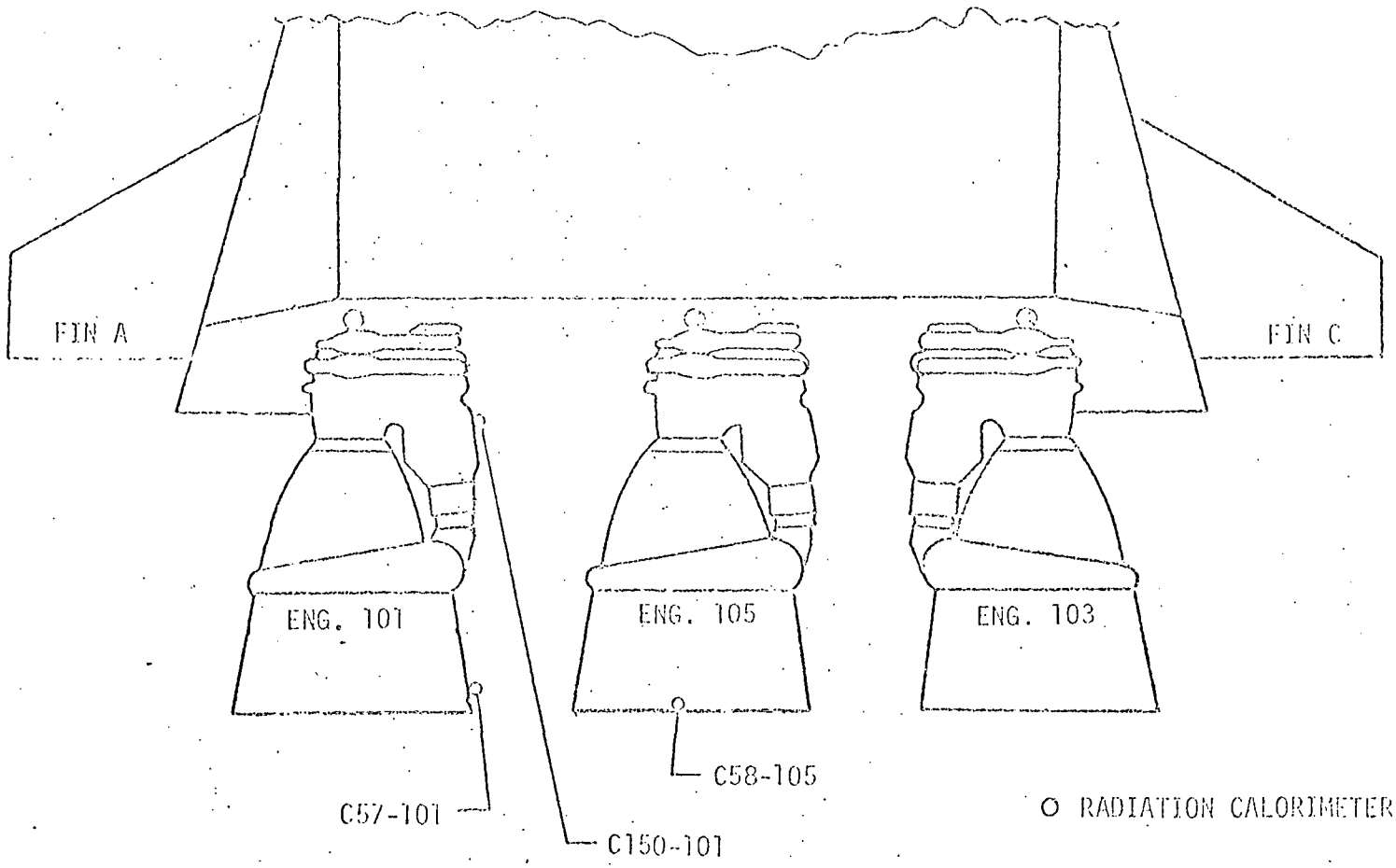

FIGURE 6-16. F-1 ENGINE RADIATION CALORIMETER LOCATIONS

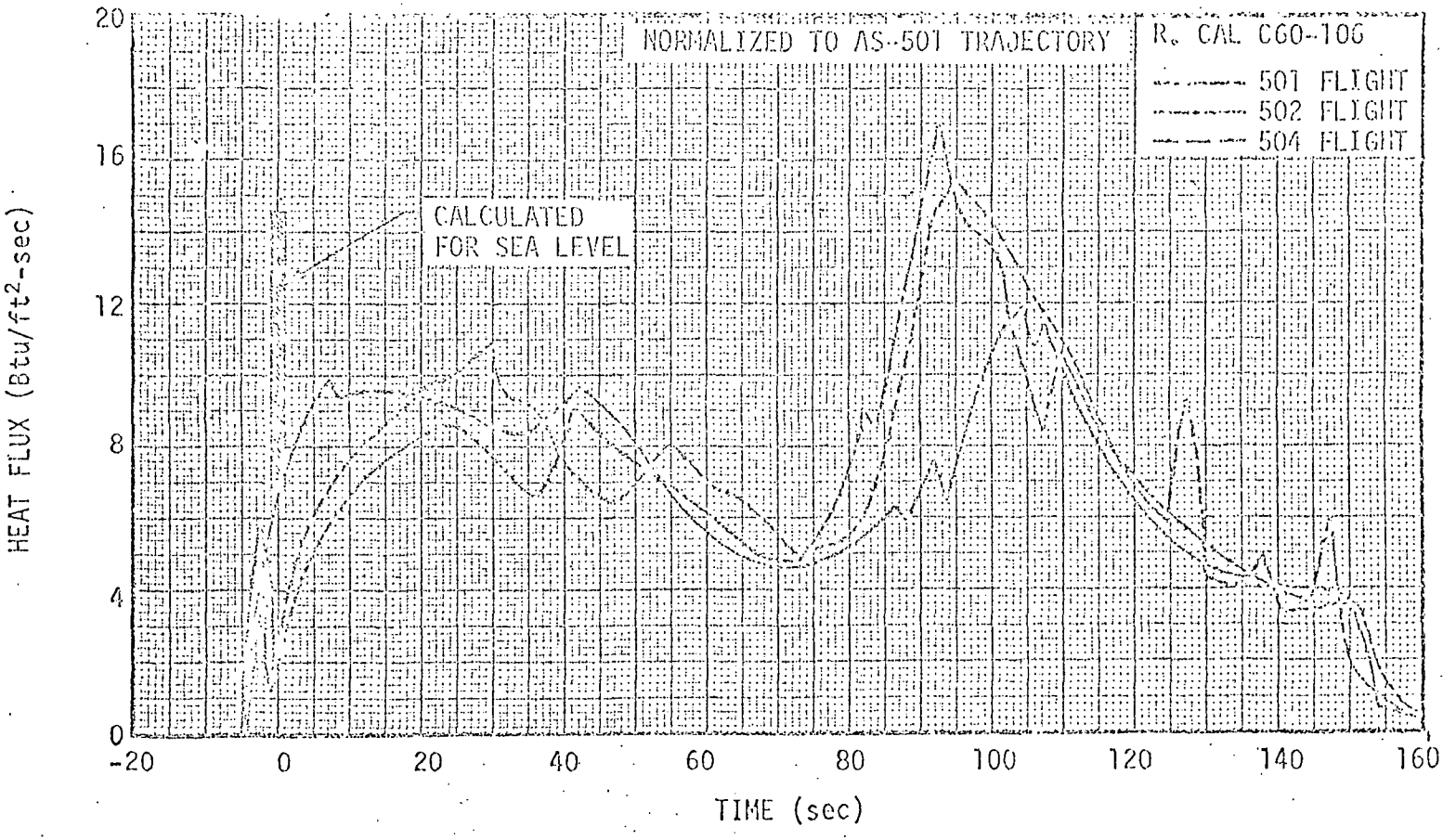

FIGURE 6-17. S-IC MEASURED AND CALCULATED SEA LEVEL RADIANT FLUX AT C60-106

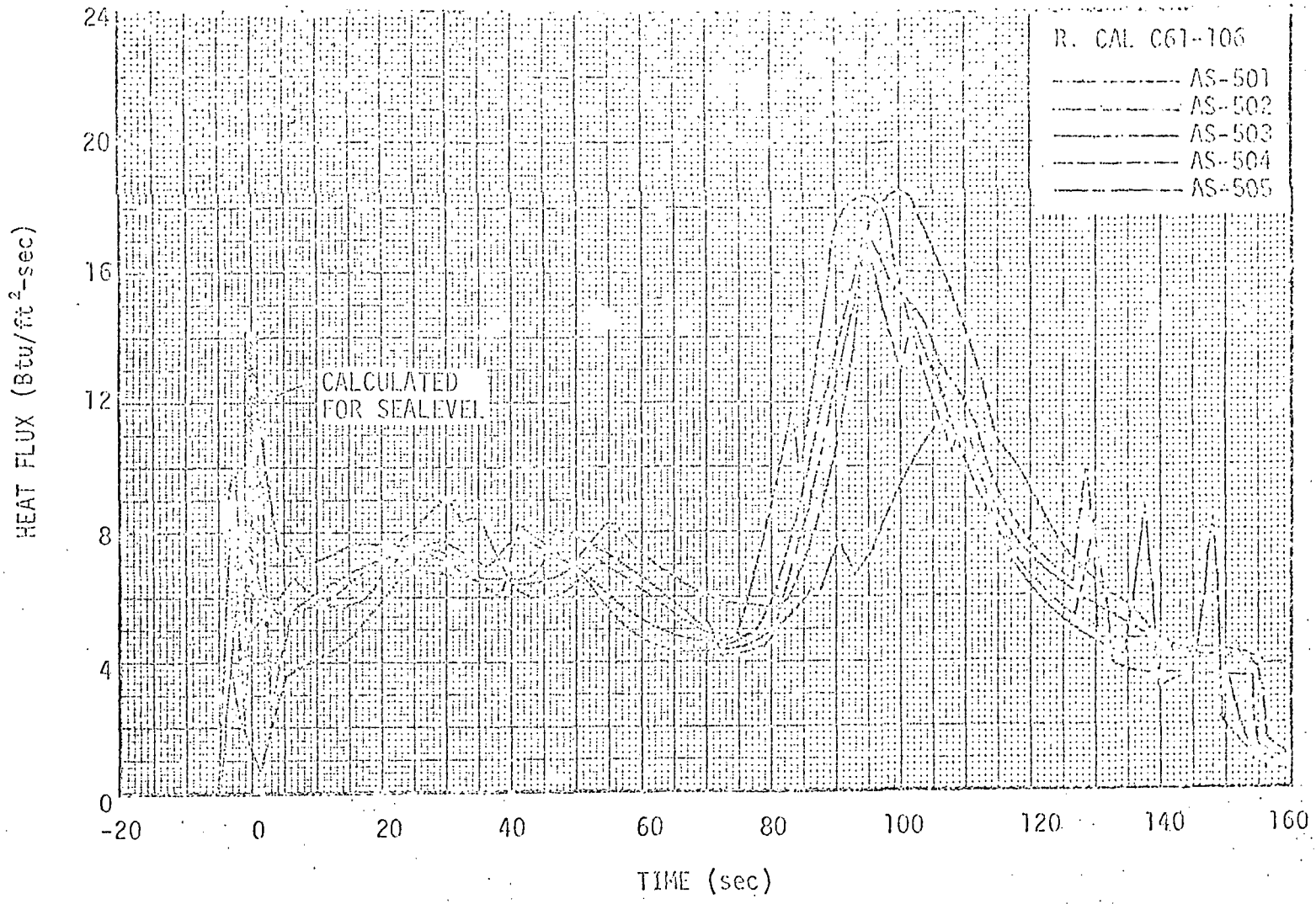

FIGURE 6-18. S-IC MEASURED AND CALCULATED SEA LEVEL RADIANT FLUX TO C61-106

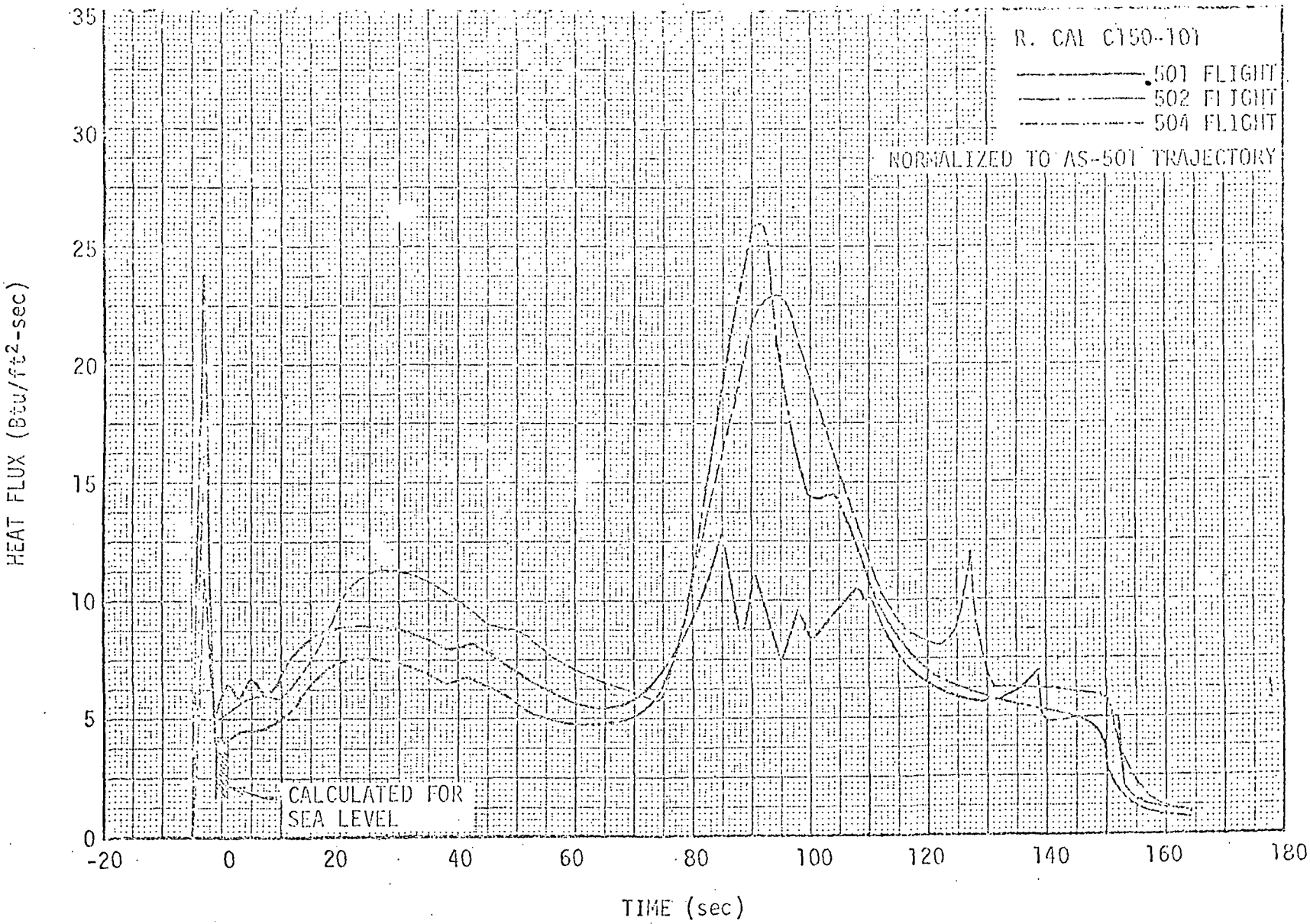

FIGURE 6-19. S-IC MEASURED AND CALCULATED SEA LEVEL RADIANT FLUX TO C150-101

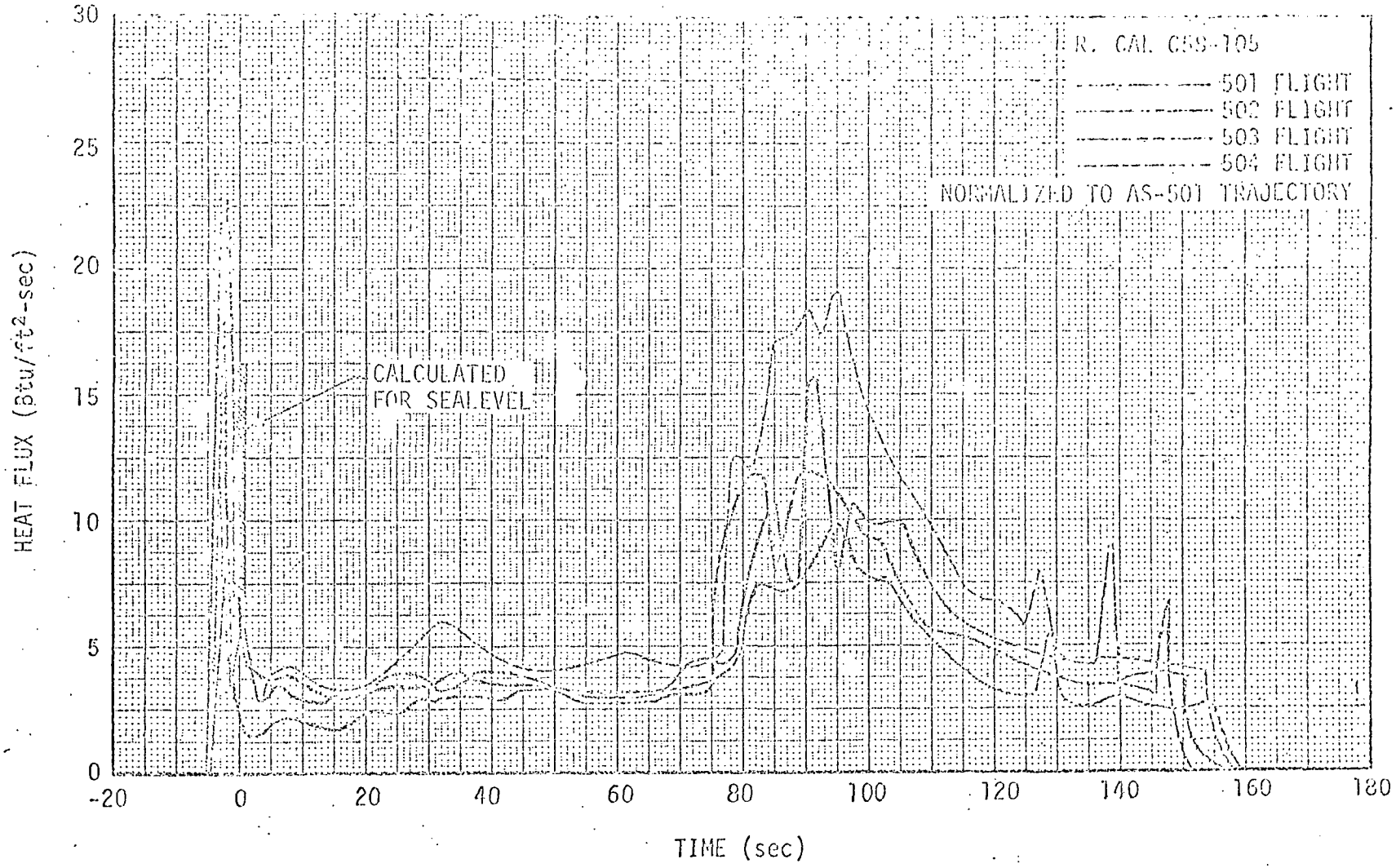

FIGURE 6-20. S-IC MEASURED AND CALCULATED SEA LEVEL RADIANT FLUX TO C58-105

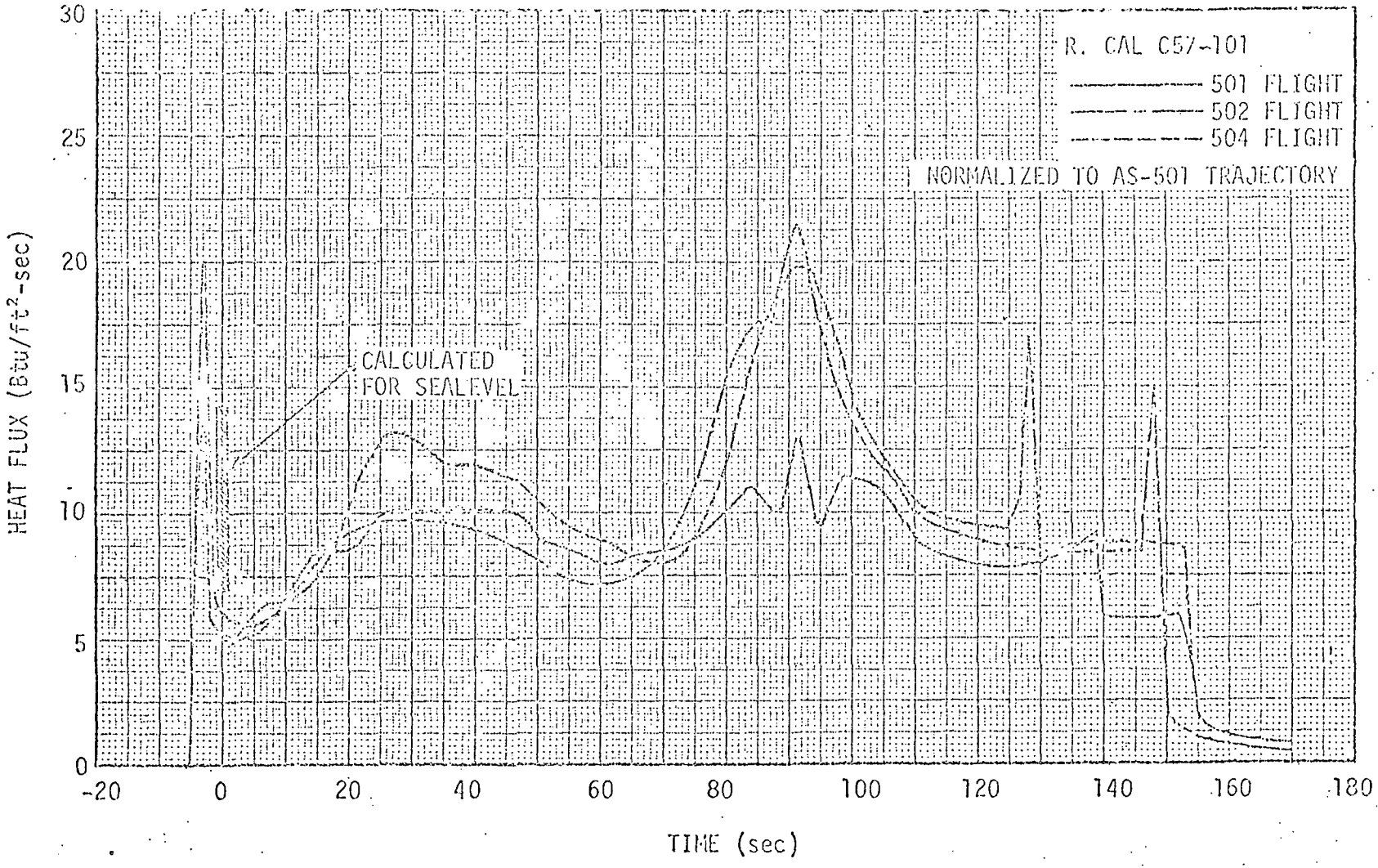

FIGURE 6-21. S-IC MEASURED AND CALCULATED SEA LEVEL RADIANT FLUX TO C57-101

As previously stated, the shortcoming of this method is its reliance on the measured plume emissive power. Ideally the plume emissive power would be measured with a scanning radiometer from a position which offered complete visibility of the plume. However, the accessibility of the plume and the environment often make this impossible. As a result, heat flux meters located in close proximity to the engine exit and measuring only the irradiation to a point must be relied upon to estimate the emissive power. The emissive power is estimated by iterating to determine what emissive power as a function of distance will give agreement with the measured incident flux.

6.3.3 Radiation at Altitude

Because of the empirical nature of the surface radiation model and its dependence upon radiation measured during static testing of a single engine at sea level, it is not applicable to higher altitudes. One empirical technique which was used with reasonable success in predicting the Saturn booster base radiant flux is the so-called "radiation decay method". This method consists of predicting the radiation at an altitude on the basis of previous flight test results. Some of the limitations associated with this technique have been discussed previously in References 1-4 and 1-5. The general idea in using this technique is to select a vehicle with a configuration and propellants which are similar to those of the vehicle to be designed. Fortunately the inflight radiation characteristics in the base regions of enough dissimilar vehicles have been measured to make this possible most of the time. The base radiation characteristics, as a function of altitude of several vehicles, are shown in Figures 6-22 and 6-23.

Because of the similarity between some of the current space shuttle configurations and the Titan IIIC, it is anticipated that the base radiation characteristics will be similar to those shown for the Titan

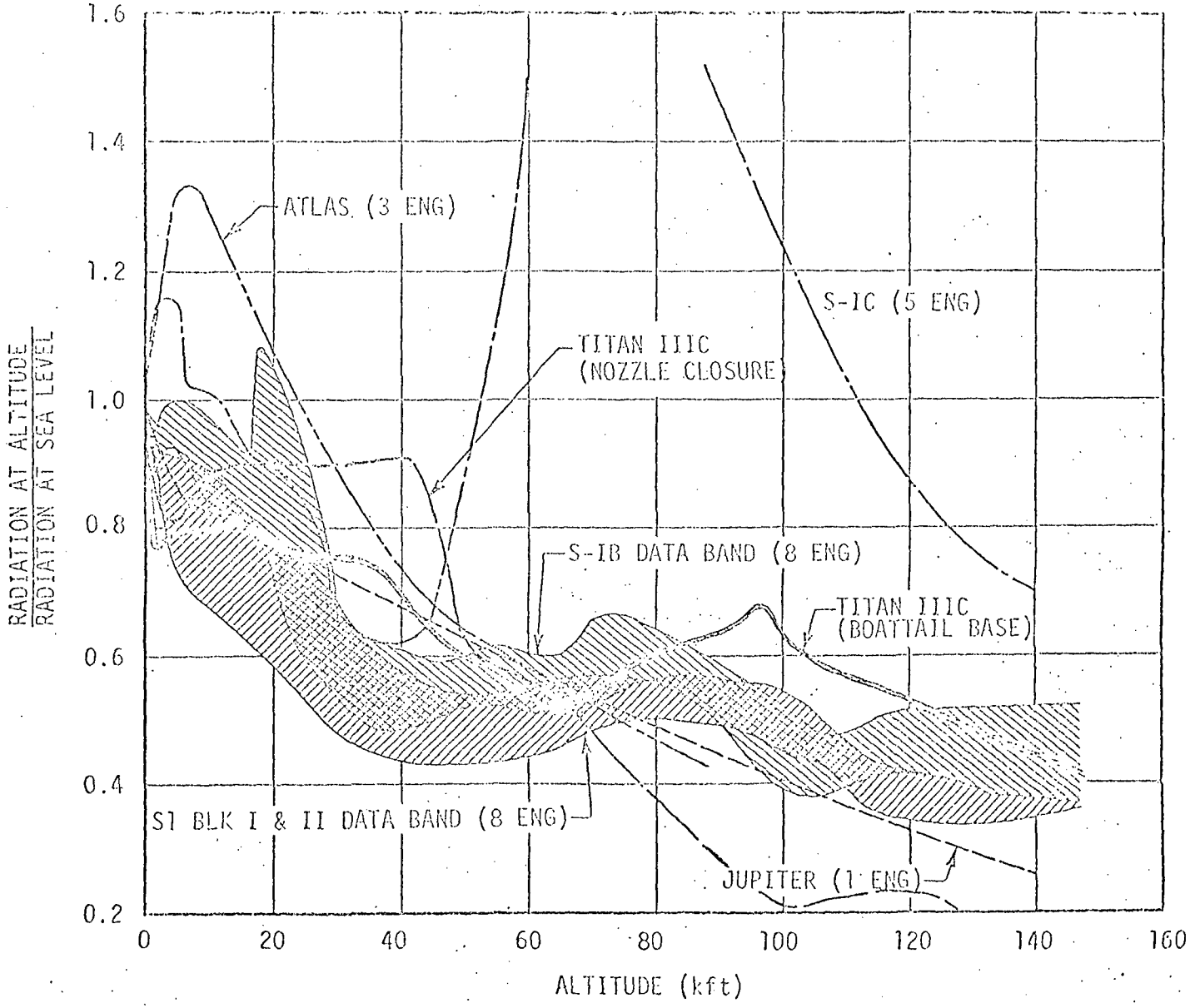

FIGURE 6-22. FRACTION OF GROUND LEVEL RADIATION, SATURN I, IB, S-IC, JUPITER, TITAN IIIC, AND ATLAS

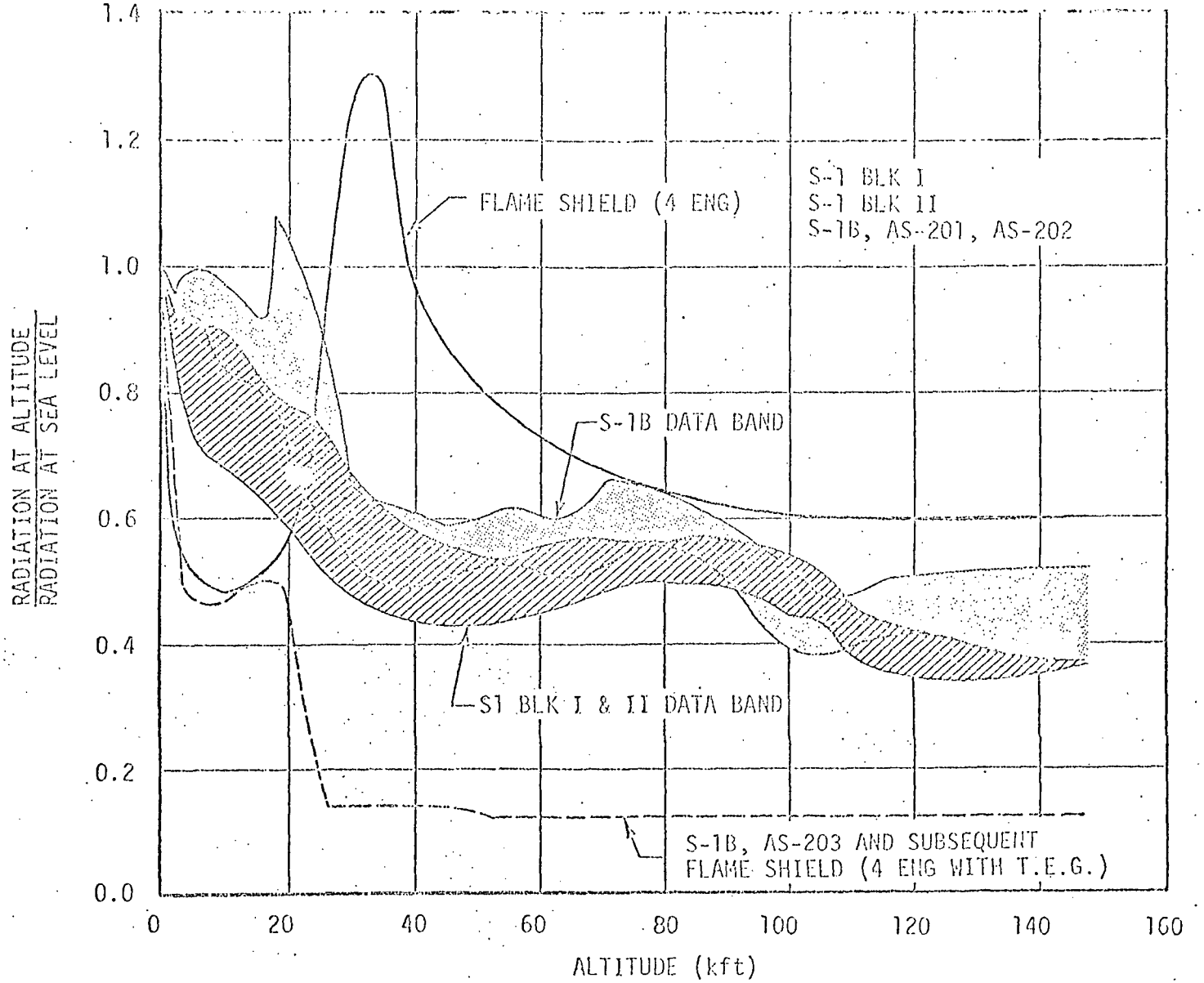

FIGURE 6-23. FRACTION OF GROUND LEVEL RADIATION, SATURN I, IB FLAME SHIELD

IIIC in Figures 6-22 and 6-23. Although the Space Shuttle radiation is still being investigated, an indication of the level can be seen in the comparison between the Saturn I, S-IC, and Titan IIIC (Ref. 3-8) measured radiant flux shown in Figure 6-24.

6.4 ENGINE CRYOPROPELLANT EFFECTS

With respect to the base heating problem, engine cryopropellant effects are those effects which are caused by the extremely low-temperature cryogenics. The most interesting example of this effect was noted during the vacuum chamber test firings of the J-2 engine. Film taken during the tests indicated that a condensed liquid and ice layer existed near the wall at the exit of the J-2 engine. At first it was thought to be inconceivable that condensation could exit, considering the engine chamber temperature (and therefore the gas total temperature) of approximately 5,700° F which is several thousand degrees above the temperature at which condensation can be formed. However, considering the J-2 engine cooling circuit (Figure 6-25) in which liquid hydrogen at a temperature of -423° F is forced through the wall of the engine, it was concluded that condensation was not only possible but probable. In conjunction with this problem, a cursory analysis of the effect the condensation could have upon the S-II stage base heating was undertaken. The results of this analysis were documented in Reference 1-2.

Figure 6-26 shows how and where engine condensation occurs and the internal wall temperature of the J-2 engine. At a point approximately 40 inches downstream of the engine throat the wall temperature drops sharply. The hydrogen inlet to the cooling circuit and the turbine exhaust gas outlet are both near this location and contribute to the sharp

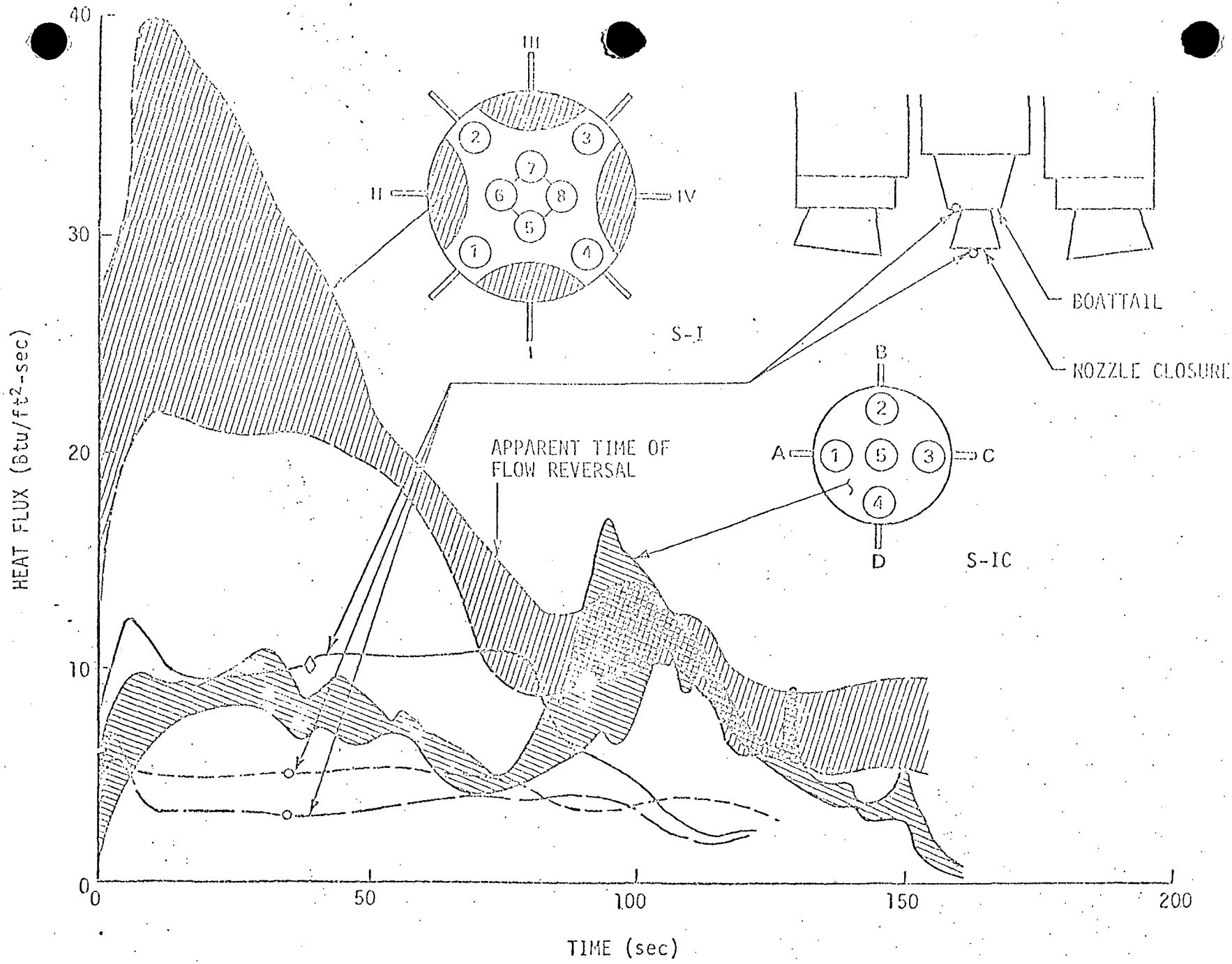

FIGURE 6-24. SATURN I, BLOCK II, SATURN S-IC AND TITAN IIIC RADIANT FLUX

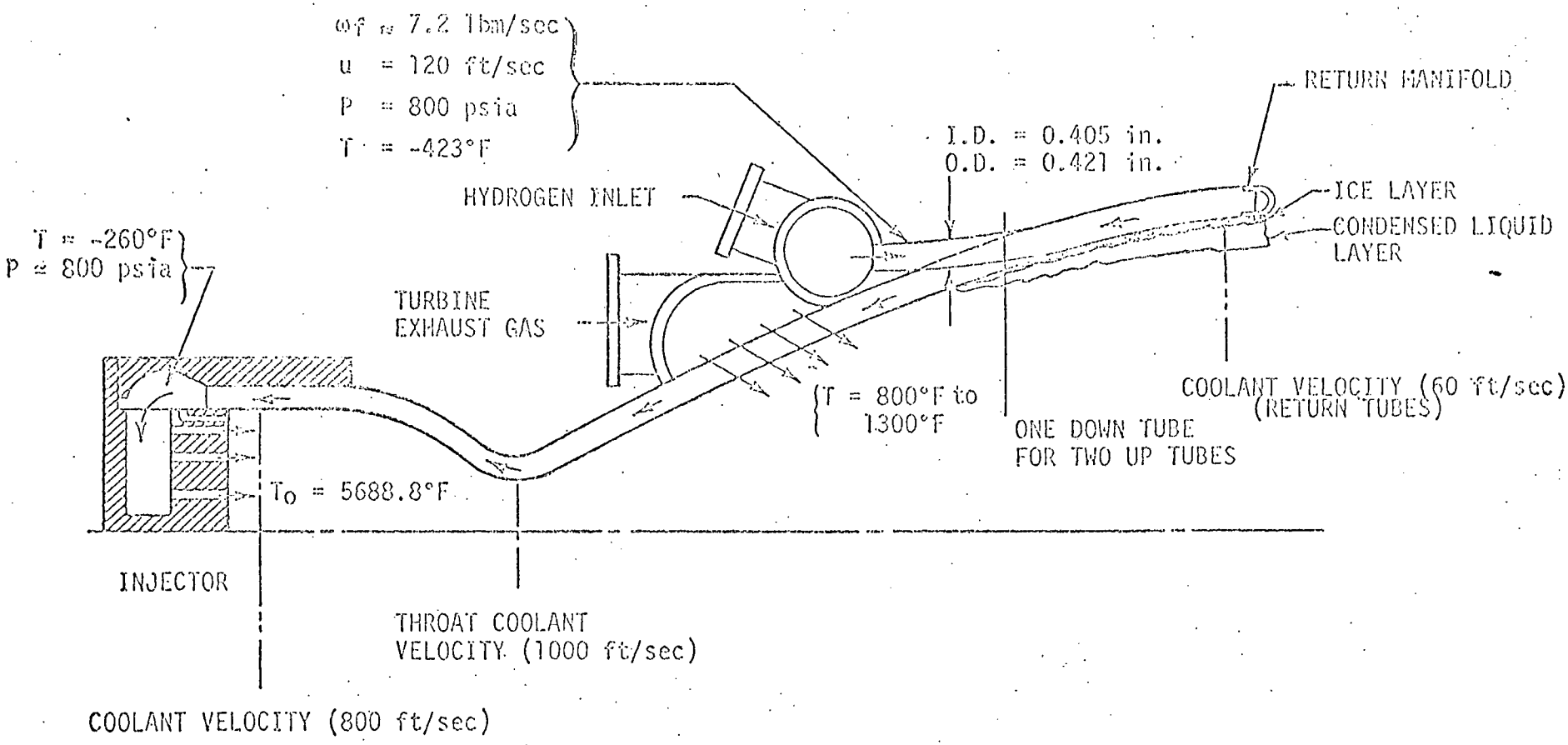

FIGURE 6-25. THRUST CHAMBER COOLANT CIRCUIT

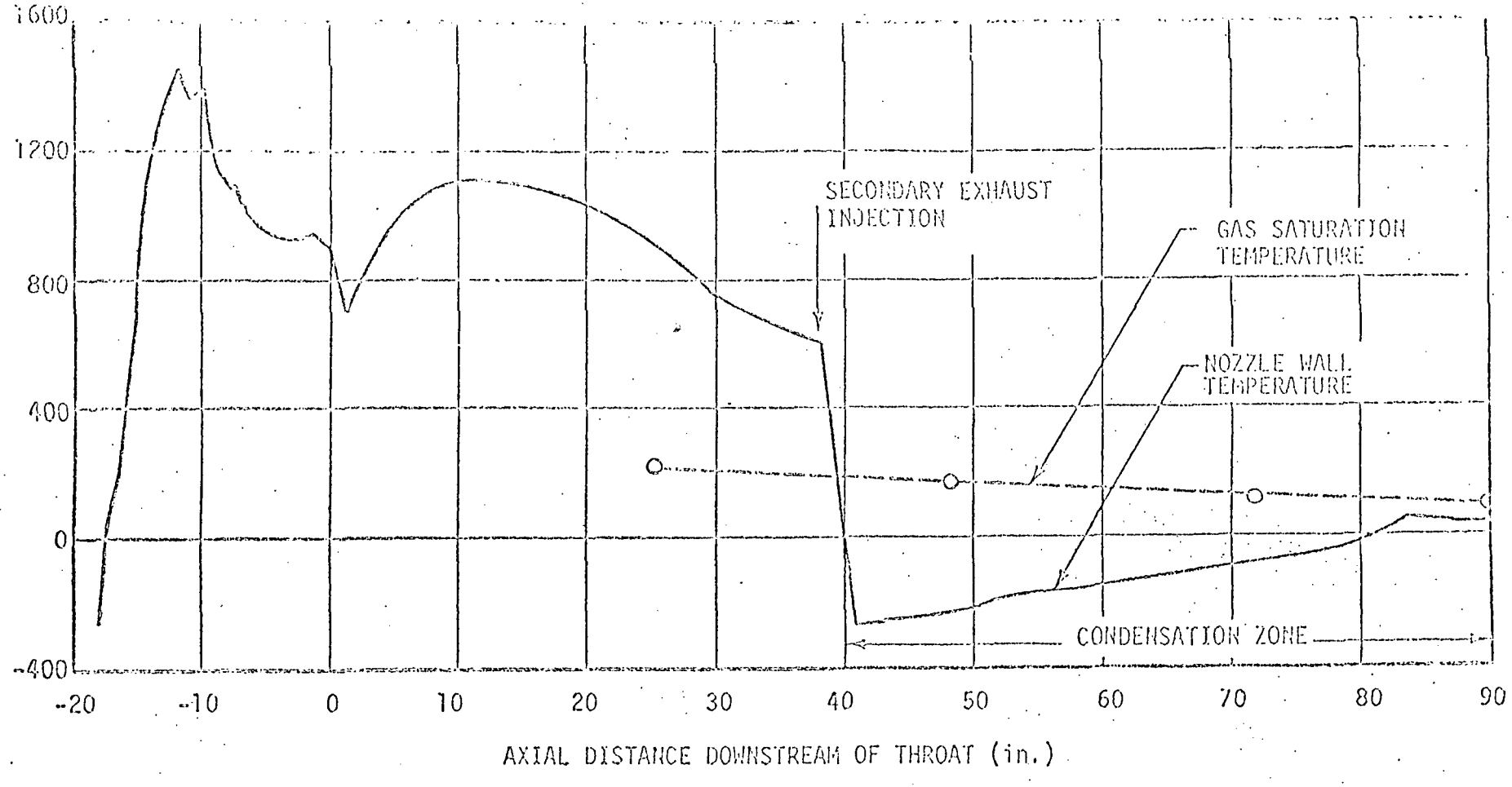

FIGURE 6-26. WALL TEMPERATURE DISTRIBUTION AND GAS SATURATION TEMPERATURE FOR J-2 ENGINE

decrease in wall temperature. Also shown in Figure 6-2 is the saturation temperature of the exhaust gases. Since the wall temperature is below the saturation temperature of the gas, condensation can occur.

The study of the effect condensation could have on the S-II stage base heating was undertaken because of the difference in gas temperature predicted by the scale model test (~2500°F) and the in-flight measured temperature (~1000°F). Since the source of the reversed flow is a small portion of the fluid which was originally in the nozzle boundary layer, it was postulated that if a condensed liquid layer existed it could revaporize upon leaving the nozzle and significantly reduce the base gas temperature. Other factors such as the energy loss to external engine surfaces and to the heat shield were also considered. The results of the study are indicated in the following paragraph.

The energy loss to the external surfaces of the engine could have reduced the mean temperature of the base gas a maximum of approximately 200°F. The heat transfer to the heat shield could have reduced the mean temperature of the base gas a maximum of 100°F. To reduce the mean temperature of the base gas an additional 1200°F would require a 28 to 43 percent moisture content in the reversed mass flow. Using a laminar flow theory (the only technique presently available for computing condensation for the J-2 engine conditions), it was shown that more than the desired amount of condensation could have been produced in the J-2 engine. As a result, it was concluded that engine wall condensation could have affected the S-II stage gas temperatures and heating rates.

The possibility that the Space Shuttle engines might produce condensation in amounts which could also affect the base heat transfer has been considered briefly. The latest Space Shuttle engine wall temperature

predictions, obtained from Rocketdyne (Ref. 6-13), indicate that condensation of the exhaust gases along the internal wall can occur when the engine is operating at reduced power levels. Figure 6-27 shows the predicted engine internal wall temperature when the engine is operating at the normal, emergency, and minimum power levels. Also shown in this figure are the corresponding saturation temperatures of the H_2O exhaust gases (i.e., temperature at which condensation of the gas will start).

Since the wall temperature during normal and emergency power operation is above the saturation temperature, no condensation would be anticipated. However, as shown in Figure 6-27, the wall temperature during minimum power level operation is below the saturation temperature and, therefore, condensation of the exhaust gases in the engine wall boundary layer would be expected. The significance of the condensation is its tendency to reduce the base region gas recovery temperature and convective heat transfer.

6.5 FLOW REVERSAL PHASE ANALYTICAL MODEL

An analytical model of multi-engine flow reversal was developed and evaluated as a part of this study. Details of the computer program and modification are discussed in Volume III of this report. Included in Volume III are parametric studies of the Saturn base heat transfer and comparisons between scale model test results and the flow reversal program.

Shown in Figures 6-28 through 6-36 is a comparison of the flight and scale model measured parameters and the analytical results obtained from the flow reversal program.

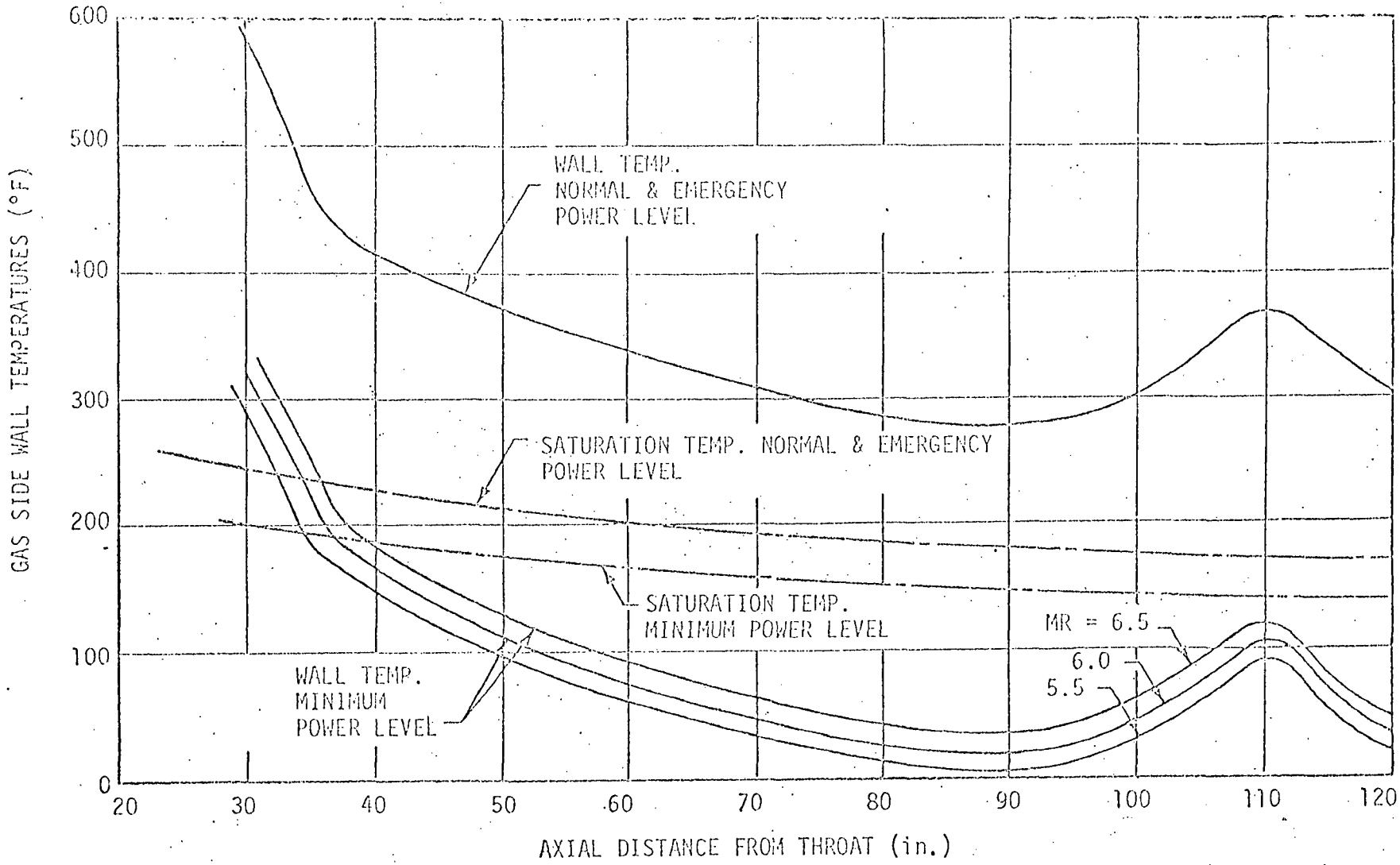

FIGURE 6-27. WALL TEMPERATURE DISTRIBUTION AND GAS SATURATION TEMPERATURE FOR SPACE SHUTTLE ENGINE

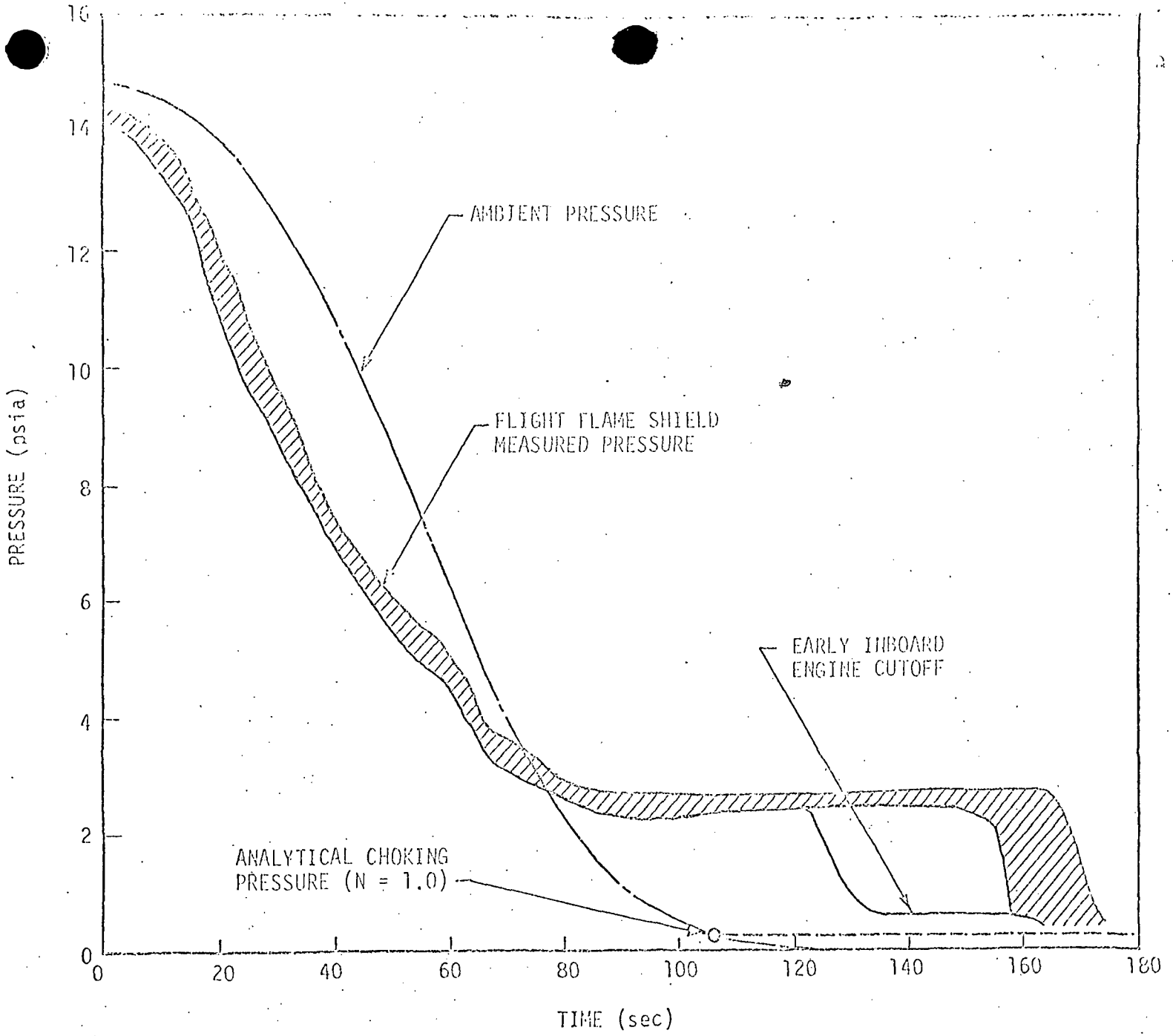

FIGURE 6-28. COMPARISON OF S-I FLAME SHIELD FLIGHT AND ANALYTICAL FLOW REVERSAL MODEL PRESSURE

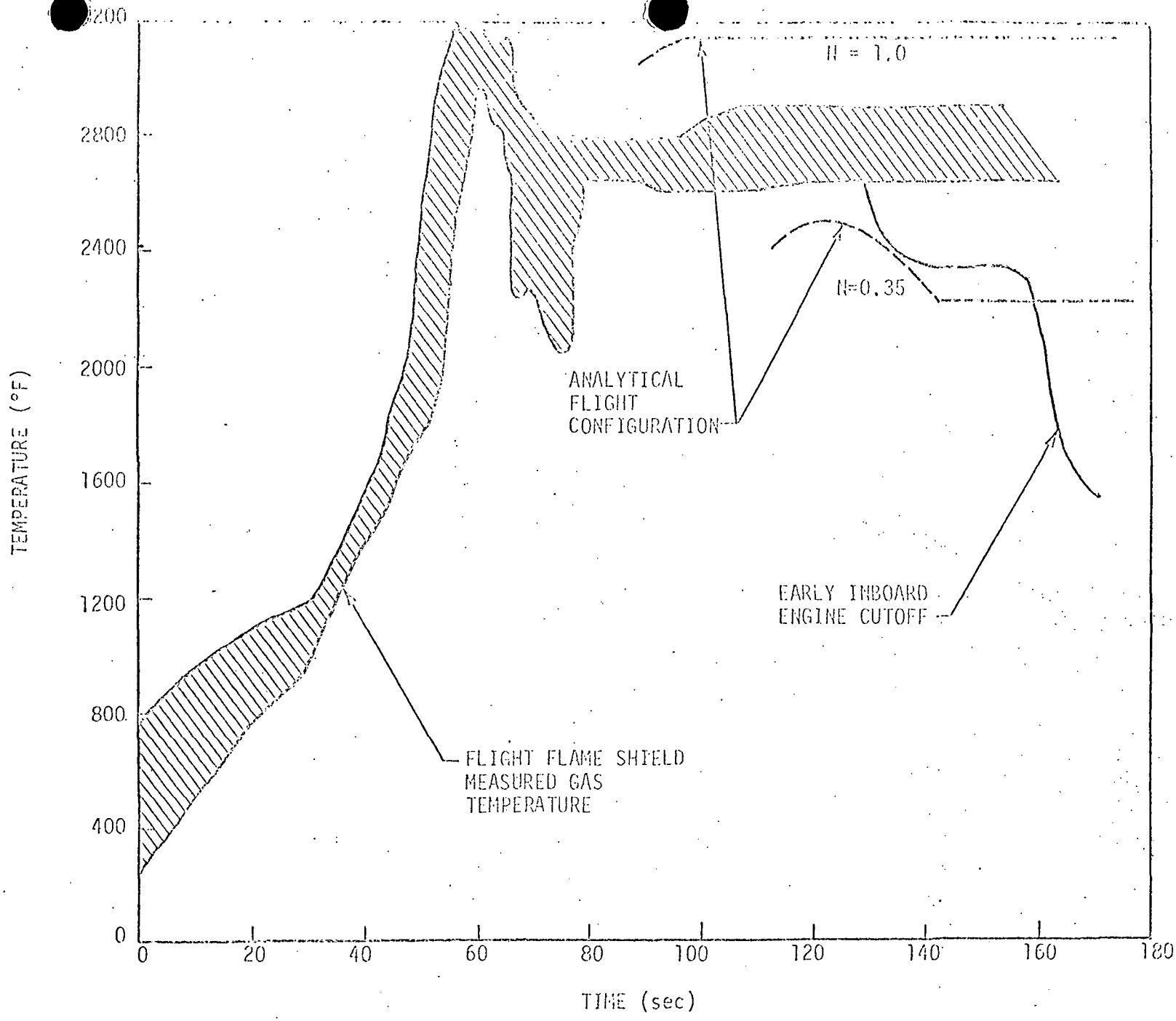

FIGURE 6-29. COMPARISON OF S-I FLAME SHIELD FLIGHT AND ANALYTICAL FLOW REVERSAL MODEL GAS TEMPERATURE

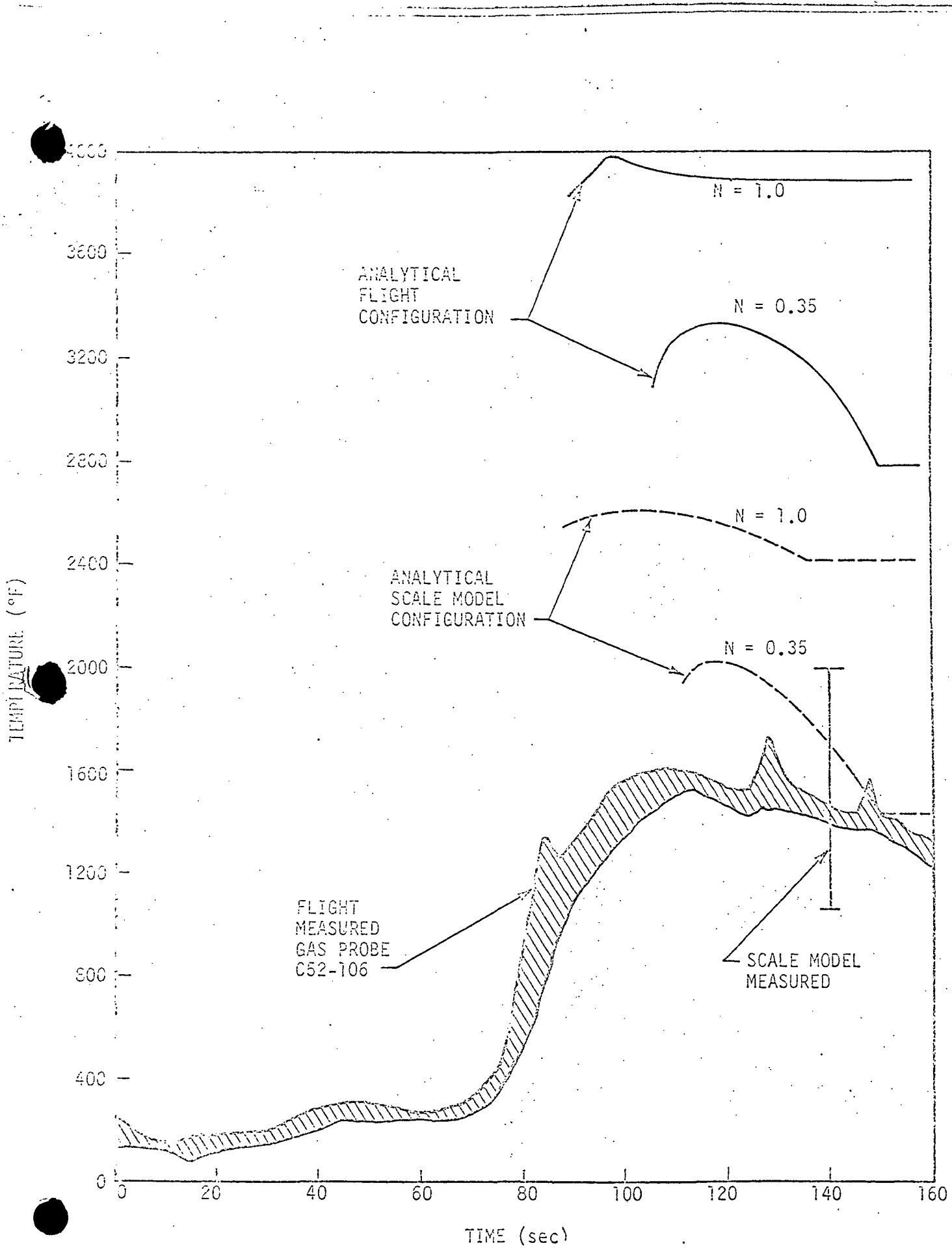

FIGURE 6-30. COMPARISON OF S-IC FLIGHT, MODEL, AND ANALYTICAL FLOW REVERSAL MODEL GAS TEMPERATURE

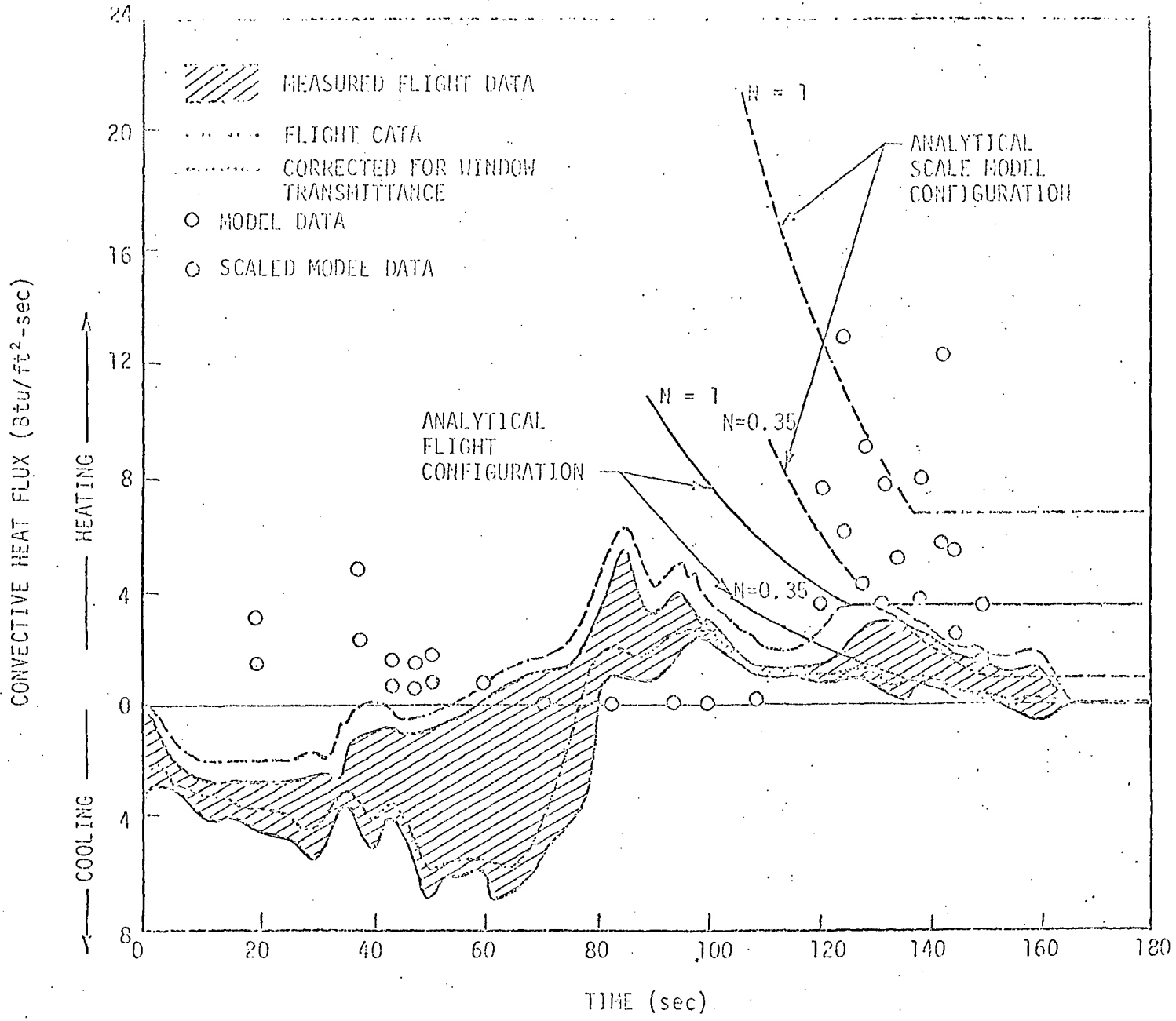

FIGURE 6-31. COMPARISON OF S-IC FLIGHT, MODEL, AND ANALYTICAL FLOW REVERSAL MODEL CONVECTIVE HEAT FLUX

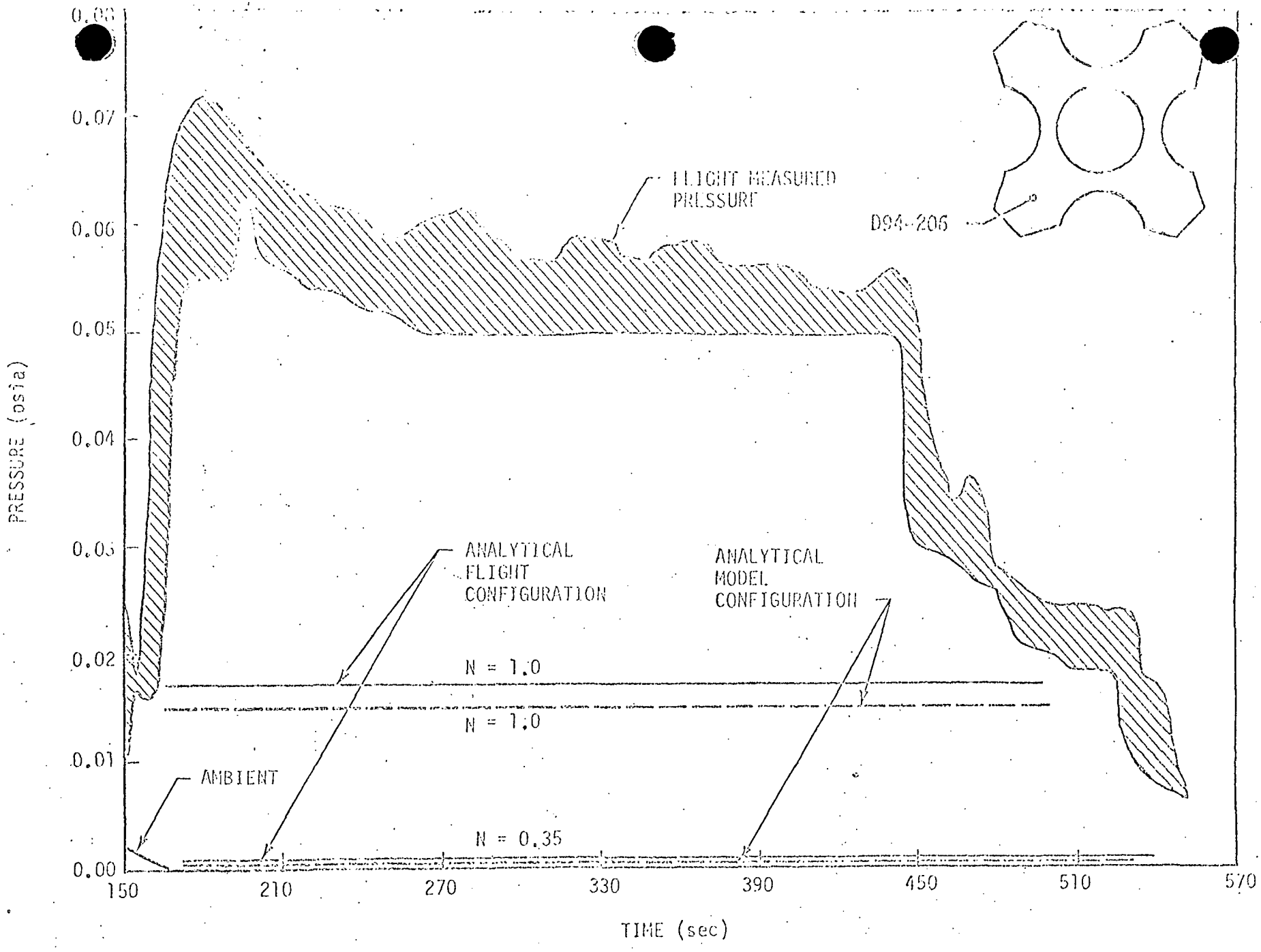

FIGURE 6-32. COMPARISON OF S-II HEAT SHIELD FLIGHT ANALYTICAL FLOW REVERSAL MODEL PRESSURE

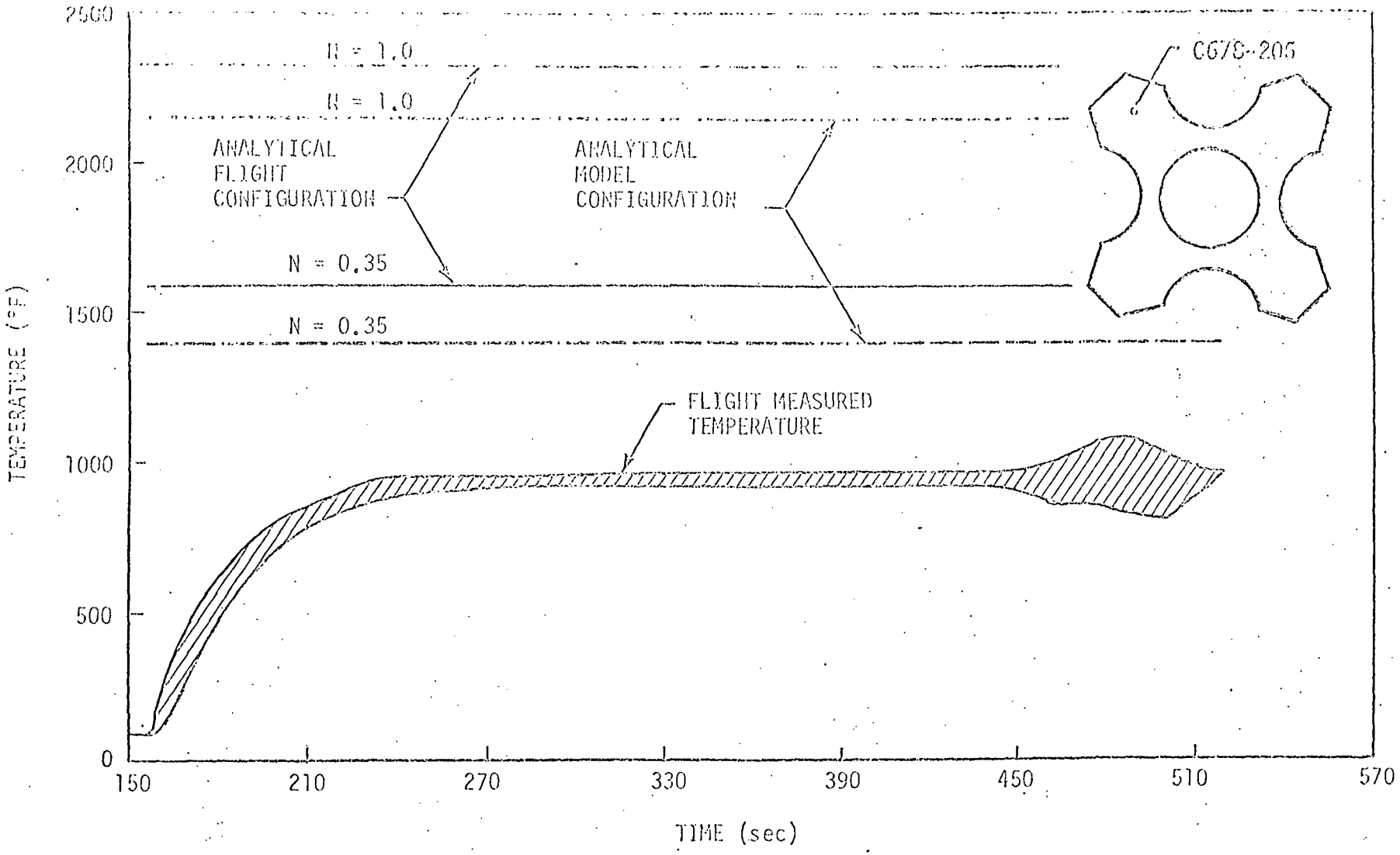

FIGURE 6-33. COMPARISON OF S-II HEAT SHIELD FLIGHT AND ANALYTICAL FLOW REVERSAL MODEL GAS TEMPERATURE

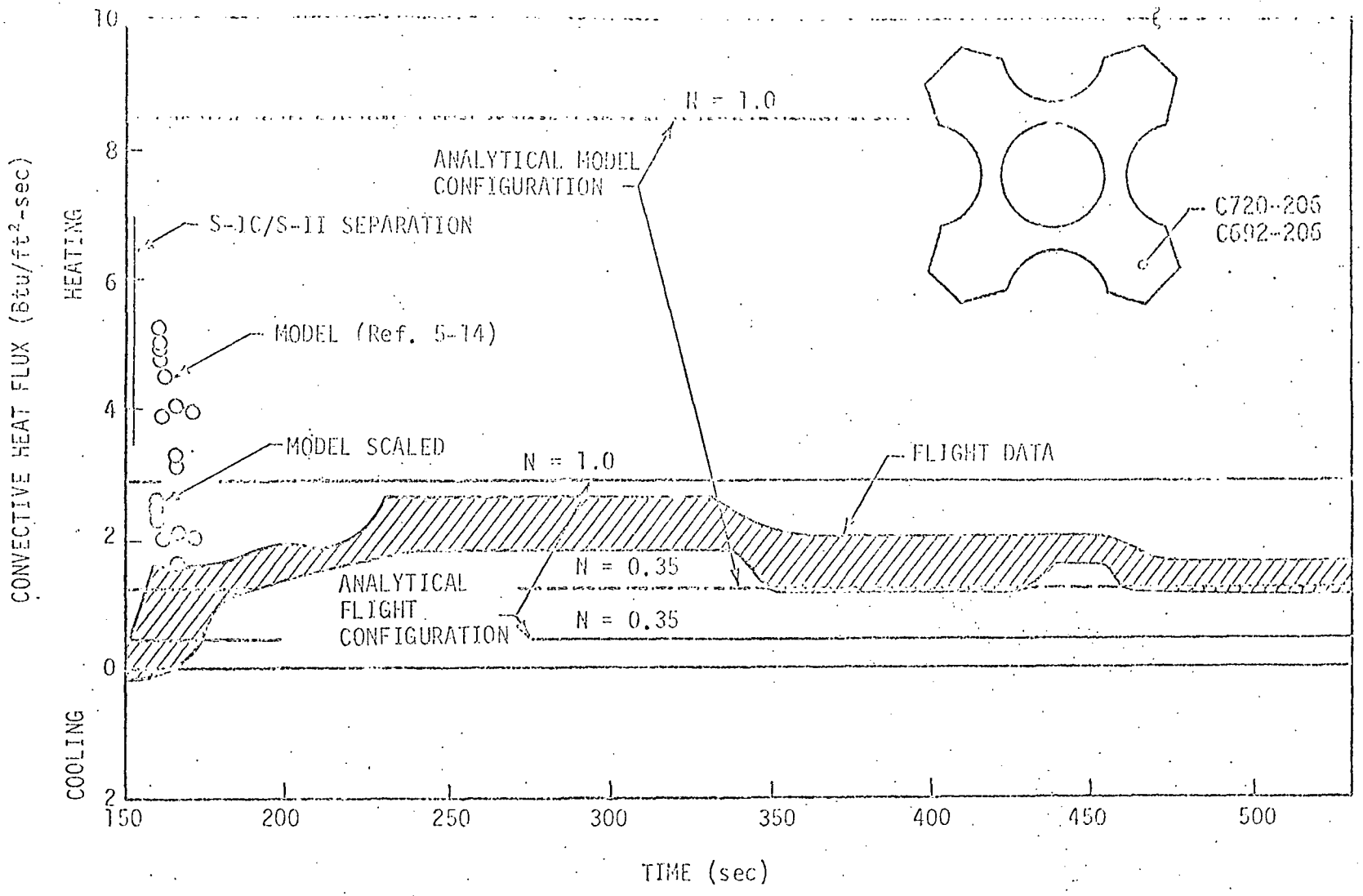

FIGURE 6-34. COMPARISON OF S-II FLIGHT, MODEL, AND ANALYTICAL FLOW REVERSAL MODEL CONVECTIVE HEAT FLUX

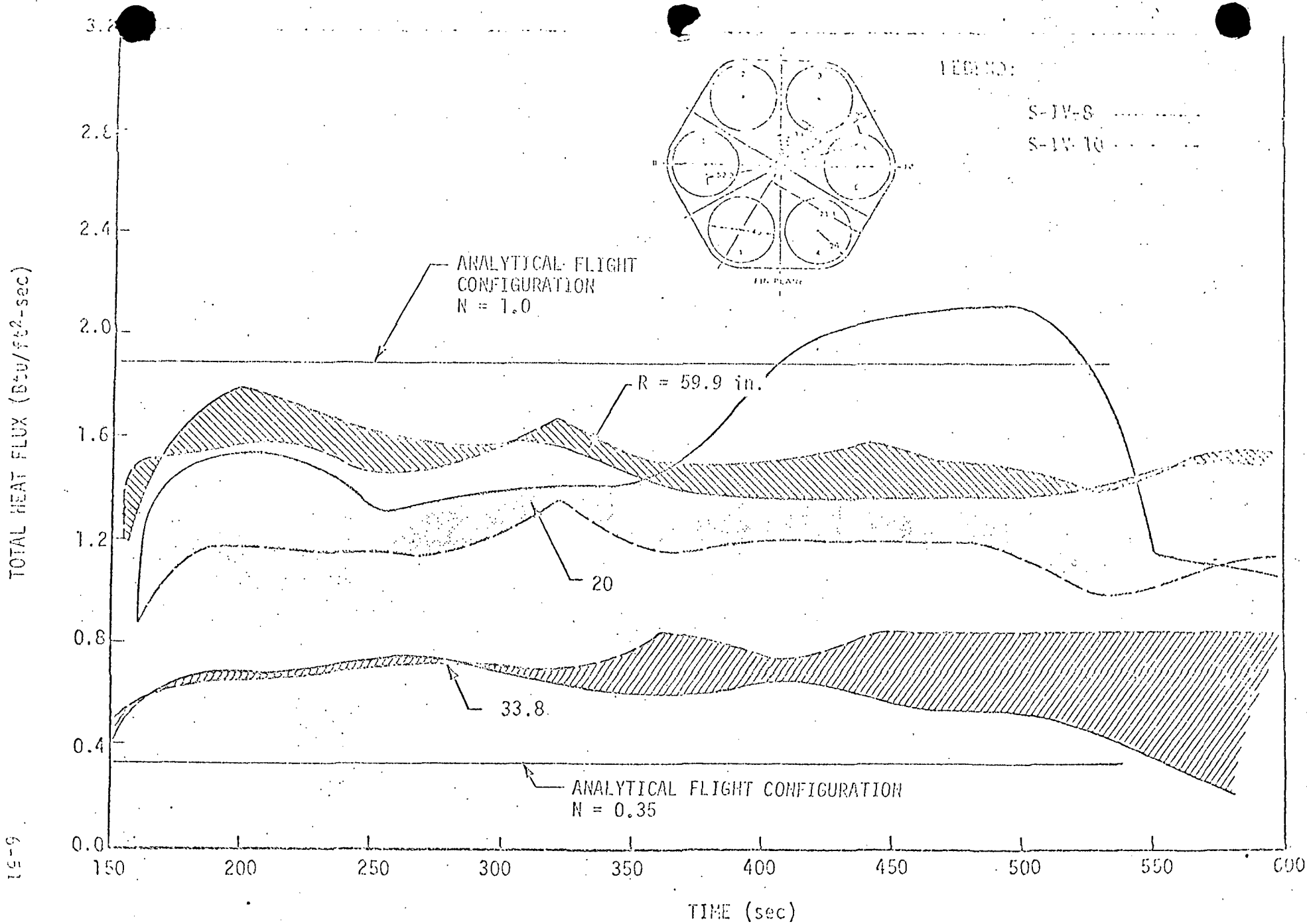

FIGURE 6-35. COMPARISON OF S-IV FLIGHT TOTAL HEAT FLUX AND ANALYTICAL FLOW REVERSAL MODEL CONVECTIVE HEAT FLUX

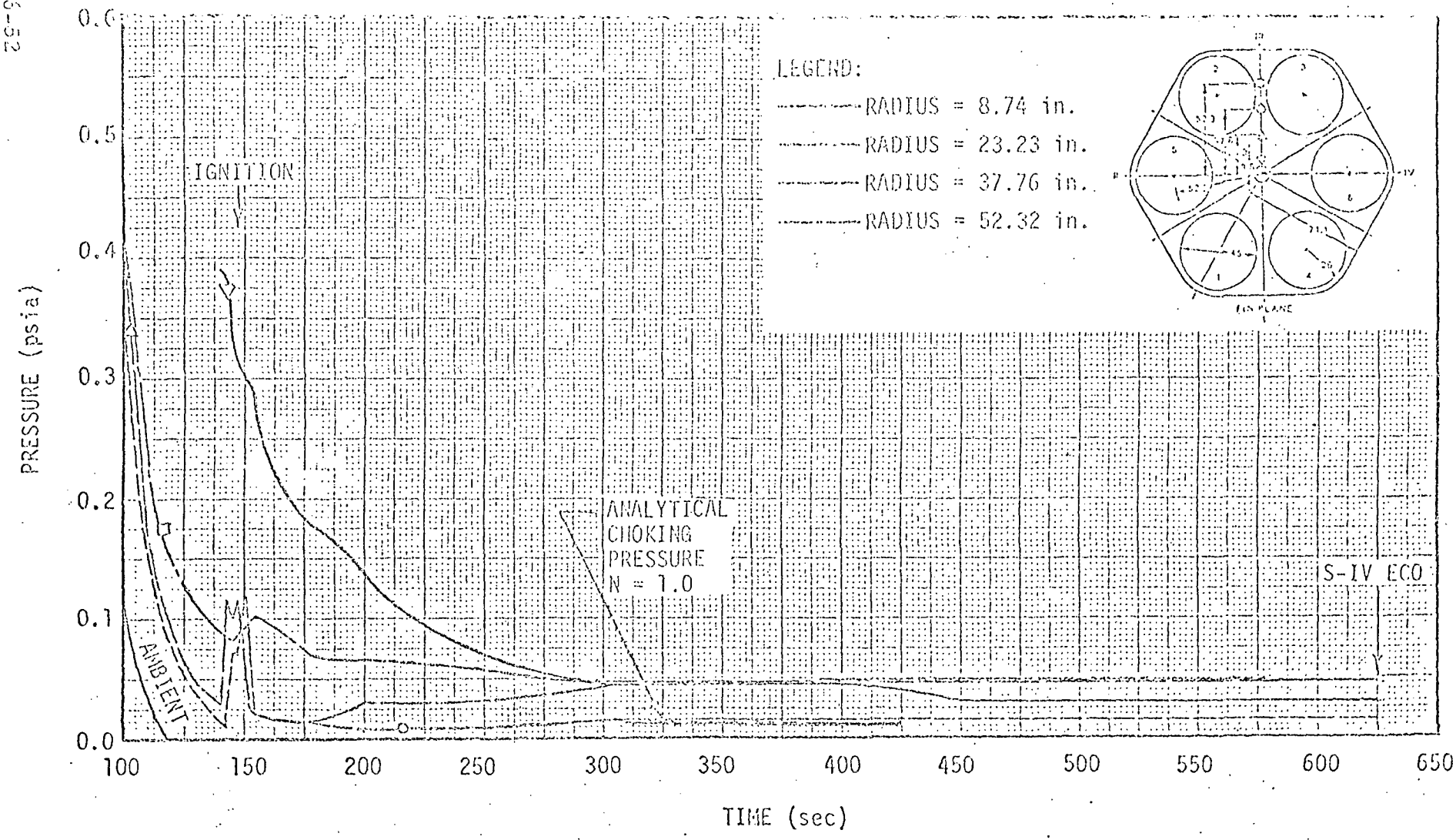

FIGURE 6-36. COMPARISON OF S-IV HEAT SHIELD FLIGHT AND ANALYTICAL FLOW REVERSAL MODEL PRESSURE

Figure 6-28 shows the pressure measured in the Saturn flame shield region. Also shown in the figure is the analytically computed choking pressure. Choking pressure is the pressure at which the flow through the vents becomes choked and no further change in ambient pressure produces a change in the flow reversal conditions. As can be seen in Figure 6-28, the choking pressure measured during the flight was approximately 2.7 psia. With one of the four center engines cutoff the choking pressure was reduced to approximately 0.7 psia. The choking pressure computed, using the flow reversal program, is approximately 0.24 psia. The analytical choking pressure was computed using a Nash factor of unity. The Nash factor controls the amount of boundary layer fluid which is assumed to be reversed. A Nash factor of unity essentially assumes that the maximum amount of fluid which can be reversed will be reversed. Likewise, a Nash factor of less than unity assumes that some of the fluid which might reverse will not be reversed.

The computed choking pressure is significantly less than the measured choking pressure (Figure 6-28). This appears to be a common characteristic of the flow reversal program and, at present, cannot be explained; however, several possibilities can be suggested. Since the computed pressure is lower than the measured pressure, this indicates that more fluid is actually reversed during flight than that which is being computed. In Section 6.2, it was shown that the actual plume expanded more upon leaving the nozzle than was inidicated by the inviscid flow approximations (Figure 6-7). This suggests that either the inviscid prediction of the plume boundary is not accurate for large liquid engines or a thicker mixing layer exists along the outer periphery of the plume. Either of these conditions would cause more gas to be reversed into the base region resulting in a higher choking pressure.

Figure 6-29 shows the measured and computed Saturn S-I flame shield gas temperature. The computed values shown are for Nash factors of 1.0 and 0.35. In Figure 6-29 the computed gas temperature agrees well with the measured gas temperature; however, this is not characteristic of the program. As will be seen in later comparisons, the computed gas temperatures tend to be higher than the measured temperatures.

The Saturn S-IC flight and scale model measured base gas temperatures and the computed gas temperatures are shown in Figure 6-30. The flight temperatures are those measured by the heat shield probe (2.5 inches below the surface) C52-106. Because of the scale of the model, different recovery temperatures are obtained from the flow reversal program for the model and the flight vehicle. In Figure 6-2? the computed gas temperature is approximately twice as high as the flight measured temperature. The gas temperature computed for the scale model shows better agreement. As discussed in Section 3, the flight gas temperature probes had the potential for error, which might explain a portion of the difference between the computed temperatures and the measured values; however, it is unlikely that the full difference could be attributed to probe errors.

Shown in Figure 6-31 is the comparison of the S-IC heat shield flight, scale model, and analytical flow reversal program convective heat flux. The computed results show good agreement with both the flight and scale model measured heating rates. Both the magnitude of the heat flux and the trend predicted for the scale model, with respect to the flight configuration (i.e., scale model convective heating higher than the flight convective heat flux), show good agreement. Apparently, the high predicted gas temperature and the low predicted pressure tend to compensate each other when the convective flux is computed.

Shown in Figure 6-32 is the comparison of the Saturn S-II upper stage flight and analytical flow reversal program computed heat shield pressures. The predicted choking pressures indicated choked flow would occur at an altitude prior to the altitude at which S-II flight stage engine ignition occurred. This simply means that the flow in the S-II base region is predicted to choke immediately after engine ignition and remain choked throughout the flight. As can be seen in Figure 6-32, the computed base pressure is approximately the same for both the model and flight configurations. The computed pressures are significantly lower than those measured during the flight. During the flight the measured pressure varied between 0.05 psia and 0.06 psia. The pressure computed using the flow reversal program varied between 0.017 for N = 1 and 0.001 for N = 0.35. The difference cannot be explained at this time except for the reasons suggested for the Saturn S-I flame shield.

The flight measured and computed S-II stage base gas temperatures are shown in Figure 6-33. As with the S-IC stage, the computed temperatures are approximately twice as high as the measured gas temperatures.

Shown in Figure 6-34 is a comparison of the S-II stage flight, scale model measured, and computed convective heating rates. As with the S-IC stage the computed heating rates appear to show reasonably good agreement with both the scale model and flight test results.

Figures 6-35 and 6-36 show comparisons between the S-IV stage in-flight measured and the flow reversal model computed heating rates and pressures. These results indicate approximately the same trend established by the previous comparison.

6.6 CONCLUSIONS REGARDING THE DIAGNOSTIC AND PREDICTION TECHNIQUES

Some conclusions arrived at regarding the diagnostic and prediction techniques are the following:

- Though not as important as the other sources of heat transfer it appears that the base convective cooling during the aspiration phase can be predicted to an acceptable degree.

- The inability to predict the actual plume boundary (including the viscous mixing and reacting layer) prevents establishing the onset of flow reversal. A thicker and less energetic plume boundary layer could also explain some of the apparent problems with the analytical prediction of flow reversal.

- The use of gaseous radiation techniques and band models will probably eventually lead to appropriate methods for predicting plume radiation. However, at the present time, these methods appear to be complex, time-consuming, and limited (except for special computation) to single plumes. The latter is related to the inability to completely define the very complicated impinging plume thermodynamic properties and not to the radiation computation techniques, per se.

- For engineering computations, the use of the radiation decay method appears to give acceptable results; however, this method requires that the plume ground level radiation be known.

- Studies of engine cryopropellant effects indicate that condensation of the engine exhaust products can occur when the wall temperature is below the saturation temperature of the exhaust gas. The effects of condensation on the base environment could be significant.

- The analytical flow reversal program appears to overpredict the base gas temperature and underpredict the base pressure; however, these effects appear to be

offset when predicting the base convective heat transfer. The program appears to offer an alternate means of making acceptable predictions of the convective heat transfer during flow reversal.

- The inability of the flow reversal program to accurately predict the gas temperature and pressure appears to be related to insufficient reversed mass from the jet. This, in turn, could be related to the inability to accurately predict the expanded plume mixing layer. Further research in this area is recommended. Emphasis should be placed on defining the thermodynamic and flow fields in the mixing zones of jet plumes of large rocket engines. The effects of turbine exhaust gas discharge and cold walls on the nozzle boundary layers should be included.

REFERENCES - SECTION 6

6-1. Sims, J., "Base Pressure at Supersonic Speeds on Two-Dimensional Airfoils and Bodies of Revolution with and Without Fins Having Turbulent Boundary Layers", NACA-TN-3819

6-2. Horst, H. H., et al, "Research on Transonic and Supersonic Flow of a Real Fluid at Abrupt Increases in Cross Section", University of Illinois, Report ME-TR-397-5, December 1959

6-3. Sogin, H. H., et al, "Heat Transfer in Separated Flows", Aeronautical Research Laboratory, Report ARL 4 (AD No. 254681), January 1961

6-4. Charwat, A. F., "Boundary of Underexpanded Axisymmetric Jets Issuing into Still Air", AIAA Journal, Vol. 2, No. 1, January 1964

6-5. Rochelle, W. C., "Review of Thermal Radiation from Liquid and Solid Propellant Rocket Exhausts", NASA-TMX-53576, 1967

6-6. Gordon, S. and B. J. McBride, "Computer Program for Calculation of Complex Chemical Equilibrium Composition, Rocket Performance, Incident and Reflected Shocks, and Chapman-Jouguat Detonations", NASA SP-273, NASA-Lewis Research Center, Cleveland, Ohio, 1971

6-7. Ratliff, A. W., et al, "Rocket Exhaust Plume Computer Program Improvement Volume I - Final Report", LMSC-HREC D162220-I, Lockheed Missile and Space Company, Huntsville, Alabama, January 1972

6-8. Smith, S. D., "Description of a Computer Program to Prepare an Axisymmetric Flowfield Tape for the Gaseous Radiation Program", LMSC-HREC D225762, Lockheed Missile and Space Company, Huntsville, Alabama, March 1972

6-9. Graham, R. F. and R. V. S Valamanchili, "Mixing and Combustion in Exhaust Gases", Nortronics - Huntsville Tech., Report No. 371, March 1968

REFERENCES - SECTION 6 - Concluded

6-10. Huffaker, R. M. and M. J. Dash, "A General Program for the Calculation of Radiation from an Inhomogeneous, Nonisobaric, Nonisothermal Rocket Exhaust Plume", NASA-TMX-53622, 1967

6-11. Reardon, J. E. and R. M. Huffaker, "Radiative Heat Transfer Calculations for Saturn Exhaust Plumes", Paper presented at "Specialist Conference on Molecular Radiation and Its Application to Diagnostic Techniques", NASA-TMX-53711, October 1967

6-12. Kramer, O. G., "Evaluation of Thermal Radiation from the Titan III Solid Rocket Motor Exhaust Plumes", AIAA Paper 70-842, July 1970

6-13. Private Communication with Mr. R. R. Kossner, Aerothermodynamics Unit, Advanced Programs, Rocketdyne, North American Rockwell